# Défauts topologiques dans les films mince de cristal liquide smectic A

Jean de Dieu Niyonzima

SORBONNE UNIVERSITÉ
ÉCOLE DOCTORALE PHYSIQUE ET CHIMIE DES MATERIAUX
UMR 7588 CNRS-Institut des NanoSciences de Paris
Physico-chimie et dynamique des surfaces

# TOPOLOGICAL DEFECTS IN SMECTIC A LIQUID CRYSTAL THIN FILMS

Par Jean de Dieu Niyonzima

Thèse de doctorat de Physique

Dirigée par Emmanuelle Lacaze

Présentée et soutenue publiquement le 8 Décembre 2023

Devant un jury composé de :

| | | |
|---|---|---|
| Mme Marianne Impéror | Directrice de recherche au LPS – Orsay | Rapportrice |
| M. Frédéric Nallet | Professeur à l'Université de Bordeaux | Rapporteur |
| M. Christophe Blanc | Chargé de recherches au laboratoire Charles Coulomb | Examinateur |
| M. Laurent Michot | Directeur de recherche au PHENIX-Paris, Sorbonnne University | Examinateur |

## Acknowledgement

First and foremost, my heartfelt thanks belong to Almighty, the Creator, who has guided me in this journey of three years. He has shown me infinite possibilities beyond the wall of impossibility. He has provided me with the well-being, power, and people to whom I express my sincere gratitude for their direct or indirect contributions to the completion and success of this thesis. The first person I would like to express my deepest gratitude is my supervisor, Emmanuelle Lacaze. Your guidance from the first day we communicated until the last day of this thesis. It isn't easy to express how your personality has inspired me. Your dynamics, courage, optimism, and patience have been my anchor in this journey. From the first introduction you made to some researchers in our corridor to the last remark you made about me, it was incredible and inspiring. One of the powerful characteristics I learned from you is how you invest all your time in ensuring your student's success daily, discussing, searching, and providing scientific opportunities. I would like to say I have been trained by the exact researcher I longed for in my career dream. Through your scientific networks, I met various world-class scientists in our field of research. For the realization and success of this work, I would like to gratefully acknowledge the research group of Emmanuelle Lacaze. I express my sincere gratitude and appreciation to Bernard Croset. I recognize especially the endless support and fruitful scientific discussions we have had from the beginning to the end of this. Thanks for the keys to unlock mysteries about X-ray scattering. I appreciate your support for the interpretation and calculations about X-ray scattering. I was inspired by the way you understand and explain physics. I am also grateful for proofreading my manuscript. You were always there for me. Haifa Jeridi, you are one of the first people I met in our group, and you showed some techniques that would be very helpful in the next three years. I am grateful for your contribution to this thesis, particularly your know-how in sample preparation and scientific advice. Lamya Essaoui and Caterina Tosareli, you have been kind to me since you joined our team. I am grateful for that and acknowledge your incredible contribution to sample preparation. I want to thank Isabelle Trimaille for the proofreading. Thank you for what you have done. Sébastien Royer, thank you for always being ready for optical microscopy and during synchrotron beam time. This work is the result of the collaboration between the team of Professor Emmanuelle Lacaze, Bernard Croset, Haifa Jeridi, Michel Goldmann (INSP), the colleagues of SIXS beamline (Alina Vlad, Yves Garreau, and Alessandro Coati), David Baboneau and Doru Constantin. I want to acknowledge your scientific contribution throughout the three years of this thesis. The days and nights we spent together at the beamline and all the discussions we have had together have borne sweet fruits. The warm welcome I received upon my arrival at INSP, particularly from the PHYSUF team and the moments I have had in this laboratory are engraved deep in my heart. It is an excellent scientific seed that has undoubtedly started to bear fruit. I remember when a group of PHYSUF researchers gathered together, and my supervisor requested them to recommend the best literature I should begin with; everyone was willing to propose. During the whole time of my thesis, one of the essential things that I needed was "Bonjour Jean de Dieu". I appreciate everyone for it. One of my great memories is the time of INSP day; many people have always prepared delicious vegan food. I am thankful for your kind heart, thinking about me, and taking your time, energy, and money just for the simple soul of Jean de Dieu. It showed me the reality of your kindness. I would like to thank all PhD candidates, postdocs, and permanent researchers whom we have met in one way or another. Making an exhaustive list of all INSP members couldn't be easy. However, some names are worth mentioning, particularly Geoffroy Prévot for the encouragement and Romain Bernard. I appreciate your kindness. Luis Lechaptois, Guillaume Diot, and Claire Abadie, thank you for being good colleagues throughout my time at INSP. I am thankful to all INSP administration and academic staff for how you have made my life smooth. I was impressed by your ways of functioning.

I would like to thank Professor Blaise Tchapnda, the Academic Director of the African Institute for Mathematical Sciences ( AIMS-RWANDA ), for having confidence in me and recommending me for this opportunity.

The motivation, mentoring, and encouragement from Doctor Ntahompagaze Joseph, Professor Safari Bonfils, Doctor Emmanuel Nshingabigwi, Doctor Innocent Nkurikiyimfura, and Professor Paul R. Berman are worth to be gratefully acknowledged.

The miraculous contact that has transformed into our perpetual friendship, Mr. M. Mwin-Maalou Frédéric Dabire, thank you for always being there for me. You know it was an indescribable and memorable moment we

spent together. I don't want to open again the bond theory between past, present, and future... Thank you for introducing me to the Veronique family and Anne-Sophie Boutry. Thank you, Mr. Bizimana Eric, Kwizera Amose, and Chika Kennedy Ajede, for being good friends and my family. Emmanuella Serwaa and Faith Nganyi, thank you for joining me in presenting my supplication to our God. He has surely understood and replied accordingly. Alexis Marie Marthe, thank you for the excellent moment we spent together.

My heartfelt thanks go to the family of Dr. Iyandemye Samuel; without you, I would be telling another story. Thank you for ensuring my well-being and completing my doctoral studies in good condition.

Finally, I sincerely thank my grandparents and aunt, who have always been there for me throughout my studies.

## Funding

I am grateful to the French Embassy in Rwanda which has not only provided with me this full scholarship for PhD studies but also has been regularly following up its execution ensuring my well-being. I would also like to gratefully acknowledge Centre national de la recherche scientifique (CNRS) for providing with the finance to accomplish this thesis.

# Contents

# General Introduction

The aim of this thesis is to study the intimate structure of the topological defects and smectic layers distortion in smectic A liquid crystal thin films. We focused on the 1D patterns, the so-called oily streaks which were created by confining thin films between uniform planar anchoring imposed by the rubbed PVA substrate and homeotropic anchoring imposed by air. The material that we studied is the well known (8CB) in smectic A phase. The layered structure of the 8CB allows us for a study using X-ray scattering. Moreover, we have studied the evolution of the oily streaks structures as function of the thicknesses of the smectic A liquid crystal thin film. My PhD aims at reconstructing the intimate internal structure of the oily streaks using a nanoscale resolution.

Due to the ubiquitous nature of topological defects, they have been of interest to both theoreticians and experimentalists. In condensed matter physics, they play a crucial role in mechanical and electrical properties of various materials such as superconductors [1], insulators[2] and superfluids [3]. The dislocation defects are responsible for the plastic deformation of crystalline material such as metal [4]. In cosmology, liquid crystals has been used as a remarkably useful laboratory test bed of the dynamics of cosmologically relevant defects [5]. Liquid crystals defects have been explored from the perspective of technological applications including self-assembly of nanomaterials [6, 7, 8, 9], optical vortex generation [10] and in tunable plasmonic metamaterials [11]. Recently it has been mathematically shown that the topological defects in liquid crystals resemble to quantum bit, which would help in the development of practical quantum computer [12].

However, this technology based on the liquid crystal topological defect requires a precise understanding of their intimate structures. In particular, Michel et al. [13] has demonstrated that the 1D patterns of defects could be created when smectic liquid crystals were distorted in arrays of hemicylinders, the so-called oily streaks. Various experimental works have been performed to attain a precise understanding of the intimate structure of these hemicylinders [14, 15, 16]. Xia et al. [17] have worked on the structural landscape of the oily steaks and have developed a free energy model suitable for finite element simulation allowing to propose a preliminary structure for the oily streaks. These oily streaks intimate structure is currently interesting for mathematicians. For instance, Ball, Canevari, and Stroffolini [18] have reported a mathematical model to describe the oily steak structure.

From a more applied point of view, Wu et al. [19] have demonstrated that new unprecedented oily streak structures can emerge in a predictable manner from the combination of various flexible defect engineering. They have also shown that a lateral electric field can manipulate the width and the orientation of the oily streaks. 1d patterns can also rotate as much as $12^\circ$ near the N-SA transition when 8CB is doped with a chiral dopant. Recently Missaoui et al. [20] have reported an experimental work on a new way of strictly localize oily streaks on a substrate and of distorting them in a controllable manner. Understanding how to be able to modify the defects requires to understand them in the simplest unidirectional situation in a first step. Also many works have demonstrated that topological defects trap and confine nanoparticles within the defect cores [21, 22, 23, 24, 25]. The result is that oriented topological defects can create unique assemblies of nanoparticles perfectly oriented by the defect orientation [26, 27, 28, 29, 30, 31].Understanding the interaction between defect cores and nanoparticles is thus crucial to be able in the future to control better these assemblies of nanoparticles. However this requires first a perfect control on the nature of the defects, on their structure and localization .

Despite of the ample works both theoretically and experimentally on the structure of the topological defects, their intimate structure is yet to be attained. It is in this perspective that in this thesis we have used the 4-n-Octyl-4'-Cyanobiphenyl ( 8CB ) smectic A liquid crystal to study the intimate internal structure of the oily streaks using synchrotron X-ray scattering.

This thesis is made of six chapters:

In chapter 1, we have focused on the state-of the-art of the liquid crystals, in particular the smectic A phases. We have reviewed the models developed for the free energy of the liquid crystals and the topological defects in this smectic A phase. We have given a review on the works that have been done by our team on the smectic A thin films where they have shown that the oily streaks are made of an array of topological defects. We have detailed

the current understanding of the structure of the oily streaks. Finally we have explained the preparation of the oily streak thin films and their typical observation by Optical Microscopy.

Chapter 2 of this thesis concerns the X-ray diffraction of smectic liquid crystals. The layered structure of the 8CB smectic A liquid crystal allows for possible X-ray study of its structure. We have first described the X-ray diffraction of the 3D crystals and then of the smectic liquid crystal. We have firstly focused on a system made of perfectly flat layers. We have presented the effects of the famous Peierls-Landau instability on the smectic liquid crystals. In the ideal system, this instability replaces the Bragg peaks with algebraic decay singularities, whereas in the real system, for instance for samples of finite size, the X-ray scattered intensity is made up of significantly large Bragg peaks accompanied by tails. We have then reviewed different works of smectic A liquid crystals where X-ray diffraction scattering has been used. We have reviewed in particular the previous studies on the structure of the oily streaks performed by our group.

Chapter 3 was devoted to the experimental technique and data analysis. In this chapter, we have described in detail the methodology that we have developed for a new analysis of our data. We have described how to take into account the refraction effects of our thin 8CB films. We presented an unprecedented measurement technique to ascertain the Bragg condition while measuring the intensity scattered by the smectic layers inside the oily streaks. For this we have combined theoretical calculation and experimental measurements at different incident angles of the scattering of the smectic hemicylinders. We demonstrated how to extract the value of the wave vector transfer and of its full width at half maximum in order to use them as new parameters in the understanding of the intimate structure of the oily steaks. We have also presented a technique to correct the effects of misorientation-based asymmetry of the sample.

Chapter 4 describes in details the results on the X-ray scattering study of the intimate structure of the smectic A oily streaks. We have focused on a film of thickness $180\ nm$. We have demonstrated that the integrated intensity is not directly proportional to the number of scattering layers in contrast to the system of perfectly flat layers that we have seen in chapter 3. A new relationship between the integrated intensity and the number of the scattering smectic layers was therefore presented. This has allowed for an interpretation of the intensity scattered by the curved smectic layers. The presence of disclinations has thus been demonstrated. We have also evidenced the presence of chevrons in the middle of the flattened hemicylinders. In order to explain the origin of these chevrons, we have presented a calculation of the energy minimization for the rotating smectic layers which has also finally revealed new features of dilation of the rotating smectic layers close to the center of curvature of the oily streak.

In chapter 5, we present the results from the study of the evolution of the structure that was previously described in chapter 4 as a function of film thickness. The dominating role of the disclination on the oily streak structure when the thickness increases has been demonstrated.

We then give a general conclusion with perspectives in chapter 6.

**Keywords—** liquid crystals, smectic A phase, topological defects, disclinations, wall defect, film thickness.

# Bibliography


[1] Rudolf Podgornik. "Principles of condensed matter physics". In: *Journal of Statistical Physics* 83.5 (June 1996), pp. 1263–1265. ISSN: 1572-9613. DOI: 10.1007/BF02179565. URL: https://doi.org/10.1007/BF02179565 (cit. on p. 9).

[2] Joel E. Moore. "The birth of topological insulators". en. In: *Nature* 464.7286 (Mar. 2010), pp. 194–198. ISSN: 0028-0836, 1476-4687. DOI: 10.1038/nature08916. URL: https://www.nature.com/articles/nature08916 (visited on 11/07/2023) (cit. on p. 9).

[3] G E Volovik. *Exotic properties of superfluid helium 3*. WORLD SCIENTIFIC, 1992. DOI: 10.1142/1439 (cit. on p. 9).

[4] "Dislocations in Solids. Plastic Relaxation". en. In: *Soft Matter Physics: An Introduction*. Ed. by Maurice Kleman and Oleg D. Lavrentovich. Partially Ordered Systems. New York, NY: Springer, 2003, pp. 261–299. ISBN: 978-0-387-21759-8. DOI: 10.1007/978-0-387-21759-8_8. URL: https://doi.org/10.1007/978-0-387-21759-8_8 (visited on 01/27/2022) (cit. on p. 9).

[5] Isaac Chuang et al. "Cosmology in the Laboratory: Defect Dynamics in Liquid Crystals". en. In: *Science* 251.4999 (Mar. 1991), pp. 1336–1342. ISSN: 0036-8075, 1095-9203. DOI: 10.1126/science.251.4999.1336. URL: https://www.science.org/doi/10.1126/science.251.4999.1336 (visited on 11/07/2023) (cit. on p. 9).

[6] Syou-P'Heng Do. "Composites cristaux liquides/nanoparticules, synergies entre matière molle et propriétés électroniques de nanoparticules". Theses. Sorbonne Université, Jan. 2019. URL: https://theses.hal.science/tel-03137919 (cit. on p. 9).

[7] Haifa Jeridi et al. "Unique orientation of 1D and 2D nanoparticle assemblies confined in smectic topological defects". en. In: *Soft Matter* 18.25 (June 2022). Publisher: The Royal Society of Chemistry, pp. 4792–4802. ISSN: 1744-6848. DOI: 10.1039/D2SM00376G. URL: https://pubs.rsc.org/en/content/articlelanding/2022/sm/d2sm00376g (visited on 08/17/2022) (cit. on p. 9).

[8] Yunfeng Li et al. "Periodic assembly of nanoparticle arrays in disclinations of cholesteric liquid crystals". In: *Proceedings of the National Academy of Sciences* 114.9 (Feb. 2017). Publisher: Proceedings of the National Academy of Sciences, pp. 2137–2142. DOI: 10.1073/pnas.1615006114. URL: https://www.pnas.org/doi/10.1073/pnas.1615006114 (visited on 11/07/2023) (cit. on p. 9).

[9] Christophe Blanc, Delphine Coursault, and Emmanuelle Lacaze. "Ordering nano- and microparticles assemblies with liquid crystals". In: *Liquid Crystals Reviews* 1.2 (Dec. 2013). Publisher: Taylor & Francis, pp. 83–109. ISSN: 2168-0396. DOI: 10.1080/21680396.2013.818515. URL: https://doi.org/10.1080/21680396.2013.818515 (cit. on p. 9).

[10] Péter Salamon et al. "Tunable Optical Vortices Generated by Self-Assembled Defect Structures in Nematics". en. In: *Physical Review Applied* 10.4 (Oct. 2018), p. 044008. ISSN: 2331-7019. DOI: 10.1103/PhysRevApplied.10.044008. URL: https://link.aps.org/doi/10.1103/PhysRevApplied.10.044008 (visited on 09/20/2022) (cit. on p. 9).

[11] John J. Sandford O'Neill et al. "Electrically-tunable positioning of topological defects in liquid crystals". en. In: *Nature Communications* 11.1 (Dec. 2020), p. 2203. ISSN: 2041-1723. DOI: 10.1038/s41467-020-16059-1. URL: http://www.nature.com/articles/s41467-020-16059-1 (visited on 07/23/2022) (cit. on p. 9).

[12] Žiga Kos and Jörn Dunkel. "Nematic bits and universal logic gates". In: *Science Advances* 8.33 (Aug. 2022). Publisher: American Association for the Advancement of Science, eabp8371. DOI: 10.1126/sciadv.abp8371. URL: https://www.science.org/doi/10.1126/sciadv.abp8371 (visited on 04/21/2023) (cit. on p. 9).

[13] Jean-Philippe Michel et al. “Optical gratings formed in thin smectic films frustrated on a single crystalline substrate”. en. In: *Physical Review E* 70.1 (July 2004), p. 011709. ISSN: 1539-3755, 1550-2376. DOI: 10.1103/PhysRevE.70.011709. URL: https://link.aps.org/doi/10.1103/PhysRevE.70.011709 (visited on 10/20/2021) (cit. on p. 9).

[14] Jean-Philippe Michel et al. “Structure of smectic defect cores: X-ray study of 8CB liquid crystal ultrathin films”. In: *Physical review letters* 96.2 (2006). Publisher: APS, p. 027803 (cit. on p. 9).

[15] Delphine Coursault et al. “Self-organized arrays of dislocations in thin smectic liquid crystal films”. en. In: *Soft Matter* 12.3 (2016), pp. 678–688. ISSN: 1744-683X, 1744-6848. DOI: 10.1039/C5SM02241J. URL: http://xlink.rsc.org/?DOI=C5SM02241J (visited on 01/17/2023) (cit. on p. 9).

[16] Bruno Zappone et al. “Self-ordered arrays of linear defects and virtual singularities in thin smectic-A films”. en. In: *Soft Matter* 7.3 (2011), pp. 1161–1167 (cit. on p. 9).

[17] Jingmin Xia et al. “Structural Landscapes in Geometrically Frustrated Smectics”. In: *Physical Review Letters* 126.17 (Apr. 2021). Publisher: American Physical Society, p. 177801. DOI: 10.1103/PhysRevLett.126.177801. URL: https://link.aps.org/doi/10.1103/PhysRevLett.126.177801 (visited on 09/17/2023) (cit. on p. 9).

[18] J. M. Ball, G. Canevari, and B. Stroffolini. “A free discontinuity model for smectic thin films”. en. In: *Liquid Crystals* (Apr. 2023), pp. 1–10. ISSN: 0267-8292, 1366-5855. DOI: 10.1080/02678292.2023.2192183. URL: https://www.tandfonline.com/doi/full/10.1080/02678292.2023.2192183 (visited on 10/16/2023) (cit. on p. 9).

[19] Sai-Bo Wu et al. “Smectic Defect Engineering Enabled by Programmable Photoalignment”. en. In: *Advanced Optical Materials* 8.17 (2020), p. 2000593. ISSN: 2195-1071. DOI: 10.1002/adom.202000593. (Visited on 03/23/2022) (cit. on p. 9).

[20] Amine Missaoui et al. “Energetics of topographically designed Smectic-A oily streaks”. In: *Soft Matter* 19.20 (2023). Publisher: The Royal Society of Chemistry, pp. 3733–3738. DOI: 10.1039/D3SM00306J. URL: http://dx.doi.org/10.1039/D3SM00306J (cit. on p. 9).

[21] Delphine Coursault et al. “Linear self-assembly of nanoparticles within liquid crystal defect arrays”. In: *Advanced Materials* 24.11 (2012). tex.eprint: https://onlinelibrary.wiley.com/doi/pdf/10.1002/adma.201103791, pp. 1461–1465. DOI: https://doi.org/10.1002/adma.201103791. URL: https://onlinelibrary.wiley.com/doi/abs/10.1002/adma.201103791 (cit. on p. 9).

[22] Hiroyuki Yoshida et al. “Nanoparticle-Stabilized Cholesteric Blue Phases”. en. In: *Applied Physics Express* 2.12 (Nov. 2009), p. 121501. ISSN: 1882-0778, 1882-0786. DOI: 10.1143/APEX.2.121501. URL: https://iopscience.iop.org/article/10.1143/APEX.2.121501 (visited on 08/30/2021) (cit. on p. 9).

[23] B Rožič et al. “Theoretical and experimental study of the nanoparticle-driven blue phase stabilisation”. In: *The European physical journal. E, Soft matter* 34.2 (Feb. 2011), p. 17. ISSN: 1292-8941. DOI: 10.1140/epje/i2011-11017-8. URL: https://doi.org/10.1140/epje/i2011-11017-8 (cit. on p. 9).

[24] George Cordoyiannis et al. “Different modulated structures of topological defects stabilized by adaptive targeting nanoparticles”. In: *Soft Matter* 9.15 (2013). Publisher: The Royal Society of Chemistry, pp. 3956–3964. DOI: 10.1039/C3SM27644A. URL: http://dx.doi.org/10.1039/C3SM27644A (cit. on p. 9).

[25] Eva Karatairi et al. “Nanoparticle-induced widening of the temperature range of liquid-crystalline blue phases”. en. In: *Physical Review E* 81.4 (Apr. 2010), p. 041703. ISSN: 1539-3755, 1550-2376. DOI: 10.1103/PhysRevE.81.041703. URL: https://link.aps.org/doi/10.1103/PhysRevE.81.041703 (visited on 11/09/2023) (cit. on p. 9).

[26] Julian S. Evans et al. “Optical generation, templating, and polymerization of three-dimensional arrays of liquid-crystal defects decorated by plasmonic nanoparticles”. en. In: *Physical Review E* 87.3 (Mar. 2013), p. 032503. ISSN: 1539-3755, 1550-2376. DOI: 10.1103/PhysRevE.87.032503. URL: https://link.aps.org/doi/10.1103/PhysRevE.87.032503 (visited on 11/09/2023) (cit. on p. 9).

[27] Julian S. Evans et al. “Optical generation, templating, and polymerization of three-dimensional arrays of liquid-crystal defects decorated by plasmonic nanoparticles”. In: *Physical Review E* 87.3 (Mar. 2013). DOI: 10.1103/PhysRevE.87.032503 (cit. on p. 9).

[28] Delphine Coursault et al. “Tailoring anisotropic interactions between soft nanospheres using dense arrays of smectic liquid crystal edge dislocations”. In: *ACS nano* 9.12 (2015). Publisher: ACS Publications, pp. 11678–11689 (cit. on p. 9).

[29] Brigita Rožič et al. “Oriented Gold Nanorods and Gold Nanorod Chains within Smectic Liquid Crystal Topological Defects”. In: *ACS Nano* 11.7 (July 2017). Publisher: American Chemical Society, pp. 6728–6738. ISSN: 1936-0851. DOI: 10.1021/acsnano.7b01132. URL: https://doi.org/10.1021/acsnano.7b01132 (cit. on p. 9).

[30] Syou-P’heng Do et al. “Interactions Between Topological Defects and Nanoparticles”. English. In: *Frontiers in Physics* 7 (2020). Publisher: Frontiers. ISSN: 2296-424X. DOI: 10.3389/fphy.2019.00234. URL: https://www.frontiersin.org/articles/10.3389/fphy.2019.00234/full (visited on 05/13/2021) (cit. on p. 9).

[31] Syou P’heng Do et al. “From Chains to Monolayers : Nanoparticle Assembly Driven by Smectic Topological Defects”. In: *Nano Letters* (Jan. 2020). Publisher: American Chemical Society. DOI: 10.1021/acs.nanolett.9b04347. URL: https://hal.archives-ouvertes.fr/hal-02450544 (visited on 10/03/2021) (cit. on p. 9).

Chapter 1

# Introduction to liquid crystals phase and topological defects

*La volonté trouve, la liberté choisit. Trouver et choisir, c'est penser*

– Victor Hugo

## Contents

## 1.1 Introduction

Generally crystalline solid materials are characterized by a long-range translational order and an orientation order. They are also anisotropic. When these solid materials transform into an isotropic liquid, the long-range translational order and the orientation order are lost. Between the solid crystalline state and the isotropic liquid there may be an intermediate state, called the liquid crystal. Liquid crystals correspond to a state of matter that exhibits properties intermediate between those of a conventional crystalline solids and those of an isotropic liquids. For example, a liquid crystal may flow like a liquid, but its molecules may be oriented in the same way as a crystalline solid.

Until the late nineteenth century, it was believed that there existed only three states of matter: solid, liquid and gas, and that a material could only change depending on temperature variation from one of these states to another. This has changed in 1888 by the observation of an Austrian Botanist and Chemist, Friedrich Reinitzer. While experimenting with the structure and behavior of cholesteryl benzoate, a molecule found in carrots, he observed that this chemical melted at $145^{\circ}C$ into a cloudy fluid which in turn melted at $179^{\circ}C$ into liquid. In addition to these two melting points, he also observed both reflection of polarized light and rotation of polarization of light [1]. These strange behaviors of the cholesteryl benzoate led him to contact a German Physicist Otto Lehmann who was recognized for optical microscopy measurements. Then he studied the cloudy fluid using polarized-light microscopy which enabled him to observe the liquid-like flowing of ordered rod-like molecular structure. He concluded that the cloudy fluid was an unprecedented phase of matter after having been convinced that the cloudy fluid had both crystalline and liquid characteristics. In 1889, he named this phase liquid crystal.

After a long polemic period among the scientific community on the discovery of Lehmann (it was considered incompatible with the existing understanding of matter) , it was until early in the Twentieth century, that a French physicist and mineralogist Georges Friedel published a conclusive work on the existence of the new state of matter and gave concrete classification of the liquid crystal structures into nematic, smectic, and cholesteric mesophases[2]. While the cholesteric was named after the pioneering discovery of Reinitzer on cholesterol esters, the name nematic comes from its thread-like structure, whereas the smectic comes from a Greek word smectos which means soap. This was due to the fact that it behaves like stacked layers that slide on one another like in a soapy film [3].

Most of the materials which can exhibit these liquid crystal phases can be found in natural systems such as proteins, cell membrane, DNA, soap, tobacco mosaic virus [4, 5, 6, 7, 8]. Very scarcely, liquid crystal can be found in inorganic system. There is ample of articles on mineral liquid-crystalline phases. For example semiflexible wires, such as $V_2O_5$ ribbons, imogolite nanotubes, or $Li_2Mo_6Se_6$ wires, form a nematic phase at large enough concentrations [9, 10, 11, 12, 13, 14, 15]. Liang-shi Li et. al. have shown the formation of liquid crystalline phases of CdSe semiconductor nanorods[16, 17]. Many other liquid-crystalline phases of mineral nanorods have been reported for example goethite nanorods[10, 18] sepiolite [19].

These liquid crystal materials exhibit intermediate physical and chemical properties between the conventional crystalline phase and liquid phase and they can be found in two categories of the liquid crystal phases depending on how the mesophase is produced: The first one corresponds to lyotropic liquid crystals which form only in the presence of a solvent such as water or oil. The stability of the existence of liquid crystalline properties depends on the concentration. Most of the amphiphilic molecules such as soap exhibit the lyotropic liquid crystal properties. The second one, which in fact has been our focus throughout the whole period of my thesis corresponds to thermotropic liquid crystals. The existence of liquid-crystalline properties depends on temperature. Their constituent molecules are anisotropic rigid rod-like or disc-like molecules which can be easily polarized.

An example of these rod-like molecules is the 4-n-Octyl-4'-Cyanobiphenyl, commonly known as 8CB( shown in figure 1.1), one constituent of the $n$CB families where $n$ is the number of carbon atoms in the alkyl chain on which the phase transition of such molecules depends [20]. This material has been our interest throughout my thesis. The 8CB is composed of two parts (figure 1.1): a long flexible non-polar alkyl chain characterized by a rigid polar head. The latter is formed by two highly polarizable biphenyl groups and a cyano group with a strong polar moment of $4.9D$. The formation of mesophases has resulted from this molecular antagonism which is characterized by very weak miscibility of the two molecular groups which form the 8CB. When two 8CB molecules interact the Van der Waals force is weak for the alkyl chains and it is strong for the rigid polar heads.

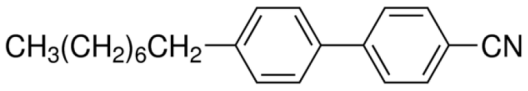


Figure 1.1: The 4-n-Octyl-4'-Cyanobiphenyl.

Due to their high sensitivity in responding to the external applied factor such as temperature and electric field, liquid crystal materials play a key role in displays and optical imaging technology among many existing others. Today, many studies on the development of liquid crystal based-technology are still currently being done around the world.

### 1.1.1 Nematic phase

When cooled from liquid state to $40.5°$, the 8CB liquid crystal reaches a nematic phase ( figure 1.4). In this phase, all molecules are orientated so that their long axis is parallel to the director $\vec{n}$ ( as shown in figure 1.3 ), a unit vector around which all molecules are preferentially orientated. This unit vector is along the optical axis. For 8CB the nematic phase is uniaxial. $\vec{n}$ and $-\vec{n}$ are equivalent. Nematic has orientation order, and the center of mass of molecules is randomly distributed like in the liquid phase. Unlike the solid phase, nematic has no positional order. The nematic phase is characterized by an order parameter, a degree of molecular alignment along the director.

$$S = \frac{1}{2} < 3\cos^2\theta_i - 1 > \tag{1.1}$$

where $\theta_i$ is angle of deviation between a molecular long axis and director $\vec{n}$ as (shown in figure 1.2). The value of the nematic order parameter varies between 0 and 1, with $S = 1$ corresponding to the perfect nematic order where all molecular are aligned parallel to $\vec{n}$. $S = 0$ corresponds to no long-range orientation order. $S$ therefore is used to describe the nematic-isotropic liquid phase transition.

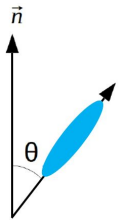


Figure 1.2: Nematic director

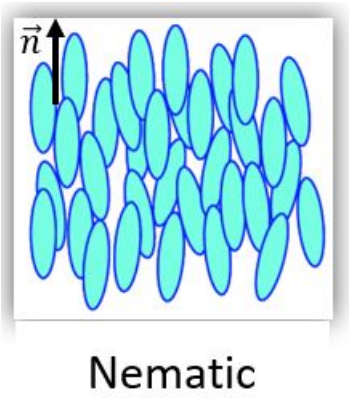


Figure 1.3: Uniaxial nematic type of ordering in thermotropic liquid crystal. $\vec{n}$ is the nematic director of the 8CB molecules depicted as in the blue ellipses

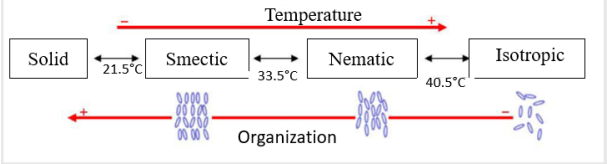


Figure 1.4: Phase transitions induced by temperature in 8CB molecules.

### 1.1.2 Smectic A phase

When the 8CB material cools down from the nematic phase, it reaches the smectic phase at temperature $33.5°$C. Generally, there are a diversified set of smectic phases which have intermediate properties between nematics and crystalline solids. Among these smectic phases, SmA and SmC are the two most widely found ones that are still thoroughly studied [21]. SmC is constituted by rod-like molecules organized in periodic layers of of interlayer spacing $d_o$ with their long axis being tilted to the layer normal. In the smectic A, the rod-like molecules are arranged in periodic layers of of interlayer spacing $d_o$ with their long axis being parallel to the layer normal as shown in figure 1.5. This material has a liquid character inside each smectic layer. This layered structure

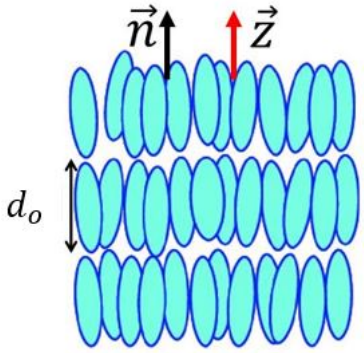


Figure 1.5: 8CB smectic A ordering in thermotropic liquid crystal. $\vec{n}$ is the smectic director and is parallel to the layer normal.

of the smectic A phase of the 8CB material is interesting in that it allows us to measure the materials with X-RAY diffraction which now can allow, with the use of synchrotron radiation a particularly accurate study of the corresponding structures, as I will try to show in this manuscript.

The smectic A liquid crystal phase is characterized by long-range orientational order and quasi-long-range 1-D translational order of rod-like molecules. The interlayer distance $d$ is constant. In the case of 8CB material, the value of $d_o$ is $31.6$ Å. Let's consider a smectic layer to be parallel to the X-Y-plane and the layer displacement $u(z) = u_z(r)$ is in the $z$ direction. In smectic phase, the mass density $\rho$ exhibits a periodic variation along the normal to the smectic layers, i.e., parallel to the z-direction (figure 1.5) . If we ignore the higher-order harmonic terms of its Fourier series, this density can be written as [22, 23, 24, 25]

$$\rho(z) = \rho_o + \rho_1 \cos[q_o \Phi(z)] \tag{1.2}$$

where $\Phi(z) = z + u(z)$ is the phase parameter and $\rho_o$ is the average density of the medium, $q_m = \frac{2\pi}{d_o}$ and $u(z)$ is the layer displacement from the position $z = nd_o$ where $n$ is an integer, with the origin is chosen at $z = 0$. When the smectic layers are rotating for example in our system as we will see later in this manuscript, we can write this in polar coordinates as

$$\rho(r) = \rho_o + \rho_1 \cos[q_o \Phi(r)] \tag{1.3}$$

where

$$\Phi(r) = r + u(r) \tag{1.4}$$

and $u(r)$ is the layer displacement in the direction $\vec{n}$ at the position $r = z^2 + \varrho^2$ with $\varrho^2 = x^2 + y^2$ from the equilibrium position $r = nd$, with $n$ integer and the origin is chosen at $r = 0$. The $u(r)$ which can for instance be the undulation (figure 1.6) due to the thermal fluctuation or some imposed deformation [23, 25].

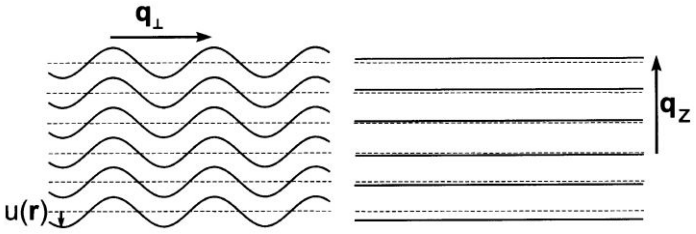


Figure 1.6: Undulation (left) and compression (right) of smectic layers with corresponding wave vector for the smectic-A phase. $u(r)$ is the one dimensional smectic layer displacement from its equilibrium position[25].

This layered structure system can give rise to linear defects such as dislocation and disclinations as in other crystalline systems. There is a large elastic energy associated with any deformation which changes the interlayer spacing in smectic A material. In the next section I will describe the distortion free energy in nematic and smectic A systems.

### 1.1.3 Nematic distortion free energy density

Distortion free energy density describes the increase in the free energy of a liquid crystal caused by distortions from its uniformly aligned configuration. Shearing, compression or dilatation, bending of the smectic layers, splay, and twist deformation are some of the distortions that can be applied to the liquid crystal system.

The distortion free energy density for a nematic is given by the Frank-Oseen energy density associated with the director field $\vec{n}$ deformation as shown in the equation 1.5.

$$f_d = \frac{K_1}{2}(\boldsymbol{\nabla} \cdot \vec{n})^2 + \frac{K_2}{2}(\vec{n} \cdot \boldsymbol{\nabla} \times \vec{n})^2 + \frac{K_3}{2}(\vec{n} \times \boldsymbol{\nabla} \times \vec{n})^2 + \frac{K_4}{2}\boldsymbol{\nabla} \cdot (\vec{n}\boldsymbol{\nabla} \cdot \vec{n} + \vec{n} \cdot \boldsymbol{\nabla} \times \vec{n}) \tag{1.5}$$

All the above Frank constants $K$ in the distortion-free energy are useful to describe how a liquid crystal materials responds to strain or deformation applied to it. Each of them is related to a specific pure deformation as displayed in figure 1.7. The constants $K_1$, $K_2$, and $K_3$ are associated respectively with the splay ,twist, and bend deformation of the director. The fourth constant $K_4$ is associated with the saddle-splay energy that describes the surface interaction. Generally, more than one of these deformations is often created. Since the free-energy density has the energy dimension per unit volume, these constants can be estimated as energy ($E$) of molecular interactions responsible for the orientation order divided by a molecular size ($l$). Their dimension is therefore $J/m$[26].

$$K = \frac{E}{l} \tag{1.6}$$

The magnitudes of these constants can be determined, and their order is often $K_3 > K_1 > K_2$. In most cases, the bending constant ($K_3$) is the largest because of the rigid-rod shape of molecules whereas the twist constant $K_2$ is the smallest. Consequently, the twist deformation is the most favorable in the nematic phase. For example, for the nematic 5CB, these values were found to be

$$K_3 = 1 \times 10^{-12}\mathrm{Jm}^{-1}; K_1 = 0.64 \times 10^{-12}\mathrm{Jm}^{-1}; K_2 = 0.3 \times 10^{-12}\mathrm{Jm}^{-1};$$

The value of all these constants strongly decreases as temperature increases and vanishes in isotropic phase [23, 27, 28].

The distortion-free energy of the nematic liquid crystal in equation 1.5 is most often written in terms of the first three terms. The fourth term contributes a surface term. Since the energies in the bulk of the liquid crystal are often greater than those due to the surface, the contribution of this term to the total free energy of the system is often neglected [20].

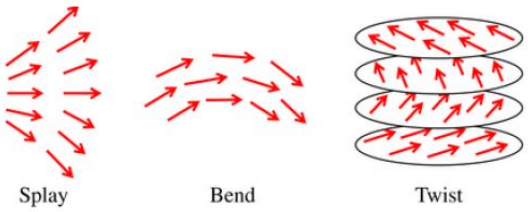


Figure 1.7

### 1.1.4 Smectic distortion free energy density

The smectic free energy can be changed by altering either the smectic medium's density or the smectic layer's thickness [24]. Moreover, since the director field, **n** is normal to the smectic layer, the bending of this layer can deform it.

The equation of total smectic distortion free energy per unit volume is formed by the contributions from the variation of the thickness of the layer, i.e., compression/dilation and the deformation of the director such as twist and bend. While the thickness of the layer is necessarily changed under the bend deformation, this is not the case when the deformation is the splay [24]. Let's now look at how this equation is derived from the two contributions.

#### Contribution from deformation of the smectic director

Applied to the smectic case, the constants $K_1$ in equation 1.5 is still associated with the splay deformation of the director. It corresponds to the total curvature of the layers.

$$\boldsymbol{\nabla} \cdot \vec{n} = \frac{1}{R_1} + \frac{1}{R_2} = \left( \frac{\partial^2 u(r)}{\partial x^2} + \frac{\partial^2 u(r)}{\partial y^2} \right) \tag{1.7}$$

Both $R_1$ and $R_2$ are the principal curvature radii. This term appears in the equation regardless of whether the layer's thickness is changed or not.

The constant $K_2$ for the twist deformation (figure 1.7) will disappear as long as the director is assumed to remain parallel to the layers normal.

$$\vec{n} \cdot \boldsymbol{\nabla} \times \vec{n} = 0 \tag{1.8}$$

This shows that twist deformation is forbidden in the smectic phase.

The third term in equation 1.5 always appears as long as there is a variation in smectic layers thickness. It is thus replaced by the dilation term described below. The term related to the Gaussian curvature is strictly zero if the smectic layers are topologically equivalent to the plane [24]. Finally, the only remaining contribution from the deformation of the nematic director in smectic phase is the splay term and is given by equation 1.9.

$$f_d = \frac{K_1}{2} \left( \frac{\partial^2 u(r)}{\partial x^2} + \frac{\partial^2 u(r)}{\partial y^2} \right)^2 \tag{1.9}$$

#### Contribution from the variation of the thickness of the layer and density of the smectic medium

Let's now look at the contribution from changing the smectic layer's thickness and density of the smectic medium. The general expression of this contribution to the distortion-free energy per unit volume is given in [24] as

$$f_e = \frac{A}{2}\theta^2 + C\theta\chi + \frac{B}{2}\chi^2 \tag{1.10}$$

where the parameter $\theta$ is the volume dilation and it comes from the fact that for a distorted material the density will vary from its of the non-distorted value [24]. It is defined as

$$\theta = \boldsymbol{\nabla} \cdot u(r) = -\frac{(\rho - \rho_o)}{\rho_o} \tag{1.11}$$

where $\rho$ is the density after deformation, $\rho_o$ is the density value without deformation.

The parameter $\chi$ is the smectic layer dilation or compression. It is defined as

$$\chi = \frac{\partial u(r)}{\partial z} = \frac{d_o - d}{d_o} \tag{1.12}$$

where $d_o$ is the value of the interlayer distance before deformation and $d$ is the actual value measured along the director (Z direction). This relation in equation 1.12 can be shown as follow We need to write this in terms of interlayer spacing. The smectic layers are region of maximum density [29] i.e $\cos\{q_o[\Phi(z)]\} = 1$ in equation 1.3. Let's consider two consecutive smectic layers. For the first one $\cos\{q_o[\Phi(z)]\} = \cos 2\pi n$ and the second one $\cos\{q_o[\Phi(z')]\} = \cos 2\pi(n+1)$.

We can now write two equations

$$\begin{cases} q_o[\Phi(z)] = 2\pi n \\ q_o[\Phi(z')] = 2\pi(n+1) \end{cases} \tag{1.13}$$

Using equation 1.4 $\Phi(z) = z + u(z)$ and $\Phi(z') = z + \Delta z + u(z + \Delta z)$

$$\begin{cases} q_o[z + u(z)] = 2\pi n \\ q_o[z + \Delta z + u(z + \Delta z)] = 2\pi(n+1) \end{cases} \tag{1.14}$$

If we take the difference between the corresponding sides of equation 1.13

$$\Delta z + [u(z + \Delta z) - u(z)] = \frac{2\pi}{q_o} \tag{1.15}$$

where $\Delta z$ is equal to the interlayer spacing $d'$. This equation is equivalent to write

$$\frac{\partial u}{\partial z} = (\frac{d_o}{d'} - 1) \tag{1.16}$$

Furthermore, all three constants $A$, $B$, and $C$ satisfy the condition of stability that is $A > 0$,$B > 0$, and $AB > C^2$ [24].

If the smectic sample is confined in a rigid and fully closed container, its volume will not be changed, making $\theta$ vanish. However, in our case, the samples are in the open air, so the volume can indeed freely change with the pressure inside the smectic samples remaining unchanged. The atmosphere exerts an upward pressure force on the sample. The pressure change for the sample can be quantified as

$$P - P_{atm} = -\frac{\partial \rho f}{\partial \theta} = -A\theta - C\chi = 0 \implies \theta = -\frac{C}{A}\chi \tag{1.17}$$

where

$$\rho f = f_d + f_e = \frac{K_1}{2}\left(\frac{\partial^2 u(r)}{\partial x^2} + \frac{\partial^2 u(r)}{\partial y^2}\right)^2 + \frac{A}{2}\theta^2 + C\theta\chi + \frac{B}{2}\chi^2 \tag{1.18}$$

Replacing the values of $\theta$ in the equation 1.10, it becomes

$$f_e = \frac{A}{2}(\frac{C}{A}\chi)^2 - C(\frac{C}{A}\chi^2) + \frac{B}{2}\chi^2 \tag{1.19}$$

This is equal to

$$f_e = \frac{1}{2}(B - \frac{C^2}{A})\chi^2 \tag{1.20}$$

In practice $A \gg C$ and $B$. Using this approximation in equation 1.20, we are able to show that the contribution from the variation of the layer's thickness and density of the smectic medium is given by just the compression or dilation of the smectic layers.

$$f_e = \frac{B}{2}(\frac{\partial u(r)}{\partial z})^2 \tag{1.21}$$

By adding equation 1.21 and 1.9, the total distortion-free energy per unit volume for smectic layers in equation 1.18 becomes 1.22

$$\rho f = \frac{B}{2}\left(\frac{\partial u(r)}{\partial z}\right)^2 + \frac{K_1}{2}\left(\frac{\partial^2 u(r)}{\partial x^2} + \frac{\partial^2 u(r)}{\partial y^2}\right)^2 \tag{1.22}$$

$B$ is the layer compression modulus and $K_1$ is the splay constant. These two constants are expressed in units of energy per unit volume and energy per unit length respectively. The square root of the ratio of $K_1$ to $B$ is defined as penetration length $\lambda$. This is a characteristic length of material, and it is of the order of magnitude of the layer spacing $d_o$. It measures the relative importance of the splay term versus the compressibility term.

$$\lambda = \sqrt{\frac{K_1}{B}} \tag{1.23}$$

The free energy can also be sometimes found written in terms of the phase $\Phi$ . It thus becomes

$$\Upsilon = \frac{B}{2}\left\{\int d^2x \left[\frac{(\nabla\Phi)^2 - 1}{2}\right]^2 + \lambda^2(\nabla^2 \cdot \Phi)^2\right\} \tag{1.24}$$

[30, 31, 32]

For such a purpose we use the fact :

$$\frac{(\nabla\Phi)^2 - 1}{2} = \frac{(\frac{\partial(z+u(z))}{\partial z})^2 - 1}{2} \iff \frac{(\nabla\Phi)^2 - 1}{2} =\approx \frac{\partial(u(z))}{\partial z} \tag{1.25}$$

Where the term with square of the derivative of the layer displacement is considered to be too small and is ignored. Using equation 4.40, it can easily be shown that

$$\nabla^2 u(z) = \nabla^2 \Phi(z) \tag{1.26}$$

The second term of 1.22 is $\nabla^2 u(r) - \frac{\partial^2 u(r)}{\partial z^2}$ . This last term is small compare to the first term of $\rho f$ and is negligible, allowing to write the second term of 1.22 as $\nabla^2 u(r)$. Following equation 1.26, the equation 1.22 can therefore be written in terms of this phase field $\Phi(r)$ as in equation 1.22.

### 1.1.5 Anchoring and surface energy

As we will see later on in this manuscript, the liquid crystal may be bounded between two fixed surfaces or deposited in the open air on a surface. For example, the thin film samples we studied during this thesis were created by confining the 8CB smectic A liquid crystal between a rubbed PVA substrate and air. Without surface or applied forces, the average orientation of liquid crystal molecules at equilibrium is arbitrary. However, when deposited on a surface, the molecules must either be firmly or loosely anchored to the bounding surface(s). The anchoring refers to the orientation or alignment of liquid crystal molecules on a surface or interface. It is said to be strong when it permanently fixes the molecular orientation; otherwise, it is weak. The energy required to rotate the director $\vec{n}$ of a liquid crystal from its preferred orientation at the surface to some other orientation is called anchoring energy. A complete description of the deformed liquid crystal must consider the interaction between the molecule and the surface, i.e., anchoring. Therefore the total distortion-free energy may have the surface term to consider the anchoring energy. This total energy becomes as

$$F_d^{'} = F_d + F_{surface} \tag{1.27}$$

For the case of strongly anchored molecules, when an external perturbation field is applied, the direction axis of the molecules at the surfaces will be fixed, and only the molecules in bulk will be deformed, so the surface energy term is considered constant. It has not to be included in the total energy. In contrast to this first case, when the molecules are loosely anchored in the presence of the perturbation, the director axis of the molecules in bulk and those at the surface will be deformed. Therefore the surface energy term has to be included in the total distortion-free energy [28].

Two terms form the surface energy per unit surface. The first one is the anchoring energy per unit surface $W$. This is an anisotropic part. The other part is the surface tension $\tau(\theta, \phi)$ where the $\theta_o$ is the favorable (so-called easy orientation) zenithal anchoring angle and $\phi_o$ is the favorable azimuthal anchoring angle [27, 33].

$$F_{surface}(\theta, \phi) = \tau(\theta_o, \phi_o) + W(\theta - \theta_o, \phi - \phi_o)$$

The anchoring energy can be purely polar when the $\theta = \theta_o$.

$$W = w_p \sin^2(\theta - \theta_o)$$

and purely azimuthal when $\phi = \phi_o$.

$$W = w_a \sin^2(\phi - \phi_o)$$

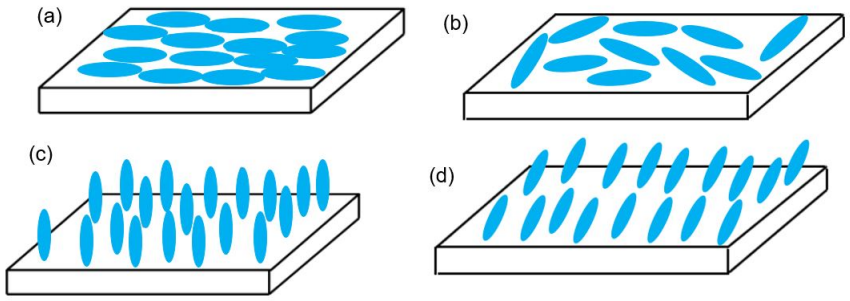


Figure 1.8: Schematic illustration of different types of anchoring conditions of molecules. (a) Uniform planar anchoring (b) Degenerate planar anchoring (c) Homeotropic anchoring (d) tilted anchoring. [24]

There are three types of anchoring as shown in figure 1.8: Planar ( can be uniform or degenerate), homeotropic, and tilted anchoring. When the director is parallel $\theta = 90^\circ$ to the surface, and all molecules are orientated in the same direction, the anchoring is called uniform planar anchoring (see figure 1.8(a)). Degenerate planar anchoring is when the molecules are randomly oriented parallel to the surface (see figure 1.8(b)). The anchoring is homeotropic if the molecular direction is perpendicular to the surface $\theta = 0^\circ$ (see figure 1.8(c)). The tilted anchoring is when the zenithal angle has a nonzero value less than $\theta = 90^\circ$ (see figure 1.8(d)).

In our study, the 8CB smectic A liquid crystal molecules will be confined between uniform planar and homeotropic anchoring. The former is produced by rubbing PVA substrate. So when 8CB molecules are deposited upon it, they are all oriented parallel to the substrate surface in a non-degenerate manner. The later anchoring is imposed by air.

## 1.2 Topological defects in smectic liquid crystal phase

The confinement of liquid crystal between interfaces or competing anchoring conditions and shearing techniques can distort it into topological defects. Using polarizing microscopy Georges Friedel has observed and described focal conics textures formed in smectic liquid crystal deposited between slide and cover slip [24]. The formation of a variety of topological defects is how the liquid crystal relaxes from breaking the symmetry of the smectic layers structures. Liquid crystal topological defects are associated with places where the liquid crystal order is no more defined. They can be linear such as dislocations and disclinations or 2D defects such as some 2D grain boundaries, between two regions of different molecular configurations. Due to their ubiquitous nature, the understanding of the physics associated with these topological defects is generally important. They indeed concern in various fields of research such as mathematics [34], cosmology [35]. The presence of topological defects is also vital in biological matter [36]. In soft condensed matter, in particular with liquid crystals, the anisotropy nature of mesogens molecules enriches the defects with tunable optical and morphology behavior which. This endows them with the ability to significantly alter the properties of the materials allowing to foster novel applications[37]. For instance, they can work as the matrix for particle assembly where they attract and trap nanoparticles like gold nanoparticles, fluorescent nanocrystals,

and semiconductor nanorods in their defects core. This stabilizes the liquid crystal-nanoparticles composite structure as a result of releasing the energy associated with defects cores [38] and thus allows to study new kinds of nanoparticle assemblies and their related optical properties. Other various applications such as optical imaging and motion control of bacteria can be possible by the use of some specific defect engineering. Wu et al. [37] have shown how smectic defects such as oily streaks can be manipulated by a combination of preprogramming of alignment condition. By deflecting, bending, and splaying they produce new types of defects. It is therefore vital to understand the structure of liquid crystal topological defects. There is ample literature on the theoretical study of topological defects in particular in smectic phase . However, the availability of comprehensive experimental data on their exact structure is still vital especially as nanoscale resolution and probably even more in smectic phase than in nematic phase.

The first type of topological defect in smectic liquid crystal is dislocation where the smectic order melts, $\psi = 0$. The second type of topological defect in smectic liquid crystal is disclination where the layer normals which are defined as $\frac{\nabla\Phi}{|\nabla\Phi|}$ are singular. [29]. In smectic there are also well known smectic textures called focal conic domains. They are defined around smectic topological defects. The two singular and conjugate lines, the ellipse and hyperbola, around which smectic layers are bent.

### 1.2.1 Disclination

Disclinations are singular lines in which rotational symmetry is broken. They are the most common defects in uniaxial nematic and smectic. Disclination lines in a smectic are where smectic layers intersect along a line as shown in figure 1.9. The smectic disclinations are characterized by a topological charge $Q_{df} \geq 1$ that is given by $Q_{df} = 1 - \frac{m}{2}$ where $m \geq 0$ is the integer number of layers that are attached to a generic point along the dislocation line [39]. A smectic disclination can have a maximum topological charge of $+1$ (as in figure 1.9(e)) [40].

In general, disclinations occur in pair of opposite or same signs which restore the long range order of the normal to layers. This pair is equivalent to a large charge dislocations (in figures 1.11(b) and 1.10(b)) of Burger vector equal to twice the number of layers between the two disclination defect cores [23]. The energy of the disclination defect is given by

$$E_{Disclination} = \frac{\pi}{2} K_1 \ln\left(\frac{bd_o}{2r_c}\right) + E_c \tag{1.28}$$

where $E_C$ is the energy of the disclination core where the smectic order decreases and the layer thickness is denoted by $d$.

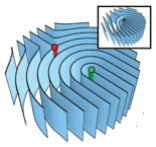

Figure 1.9: Smectic disclination points with different strength $Q$ which is defined as the number of time the vector field winds around the defect core in anticlockwise sense. For the red defect core, $m = 3$ and the $Q = -\frac{1}{2}$. For the green defect core, $m = 1$ and $Q = -\frac{1}{2}$ [29, 40, 41]

### 1.2.2 Dislocations

Dislocations are linear defects observed in smectic A material and crystals. They locally break the translational symmetry of the lamellar structure and involve local variations of layers thickness [29]. They are characterized by a Burger vector which has to be an integer multiple of the interlayer spacing $d$, where the integer is the number of all extra layers. Dislocations in the smectics play an important role in phase nucleation, layer reorientation, and dynamics [39]. There exists two main types of dislocation defects in smectic A liquid crystal materials: the edge dislocations and the screw dislocations.

### Screw dislocations

The first translation defects are screw dislocations (figure 1.10). Their Burger vector is parallel to the defect line. The energy of a screw dislocation is given by

$$E_{screw} = \frac{Bb^4}{128\pi^3 r_c^2} + \frac{K_1 b^4}{64\pi^3 r_c^4} + E_c \tag{1.29}$$

where $b$ is the Burger vector, $r_c$ is the core radius, $E_c$ is the core energy, $K_1$ is the bending constant. The screw dislocations can split into a $+\frac{1}{2}$ disclination pair [39]. The existence of giant screw dislocations has been demonstrated experimentally [42, 43]. However, experimental results on the exact structure of their core are still scarce.

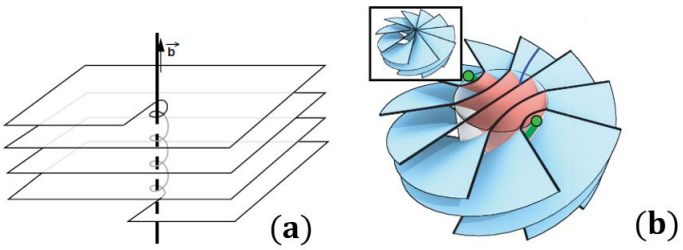


Figure 1.10: The screw dislocation in smectic materials. (a) small screw dislocation showing a Burger vector parallel to the defect line. Figure reprinted from [24]. (b) The giant screw dislocation formed by a pair of two dislocation lines (shown in green color) of topological charge $+\frac{1}{2}$. Figure reprinted from [39].

### Edge dislocations

Edge dislocations are other defects which break locally the translational symmetry of lamellar structure. They are shown in figure 1.11, the Burger vector $\vec{\mathbf{b}}$ is perpendicular to the defect line denoted by $\vec{\mathbf{t}}$ figure 1.11(a). They appear when one or more extra layers is/are added. The energy of the dislocation per unit length is

$$E_{edge} = \frac{\sqrt{K_1 B} b^2}{2r_c} + E_c \tag{1.30}$$

where $b$ is the Burger vector, $r_c$ is the core radius, $E_c$ is the core energy. Here by core, I mean the end of the broken layer(s)(see figure 1.11). The term in the square root is from to the competition between curvature energy and the elastic energy around the dislocation core (compression and dilation) [44]. They play a central role in explaining the plastic properties of the smectic A phase [45]. This smectic dislocations are not topologically protected and so the symmetry of smectic allows the dislocations of large enough Burger vectors to be decomposed into disclinations pair [29, 39]. This is the case of the edge dislocations of large Burger vector which can split into $+\frac{1}{2}/-\frac{1}{2}$ pair of disclination lines as shown in figure 1.11(b) [39]. The energy of such giant dislocation defect is given by equation 1.31

$$E_{giant} = \frac{\pi K_1}{2} \ln\left(\frac{b}{2r_c}\right) + E_c \tag{1.31}$$

where the $b$ is the Burger vector, $d$ is the layer thickness, $r_c$ is the core radius of the two disclinations and $E_c$ is their core energy [24, 37, 46] Despite of a substantial theoretical literature's, the detailed structure of elementary dislocations in real smectics remains largely elusive. Meyer et al [47] have reported the first experimental observation of elementary edge dislocations in smectic liquid crystals. The experimental characterizations of structure and defect core of elementary dislocations are scarce to date [24]. For instance, for smectic dislocation, only one Cryo-transmission electron microscopy (Cryo-TEM) observation of edge dislocations in smectic C* materials is available [48] and one polarized optical microscopy measurement for giant smectic rods [43].

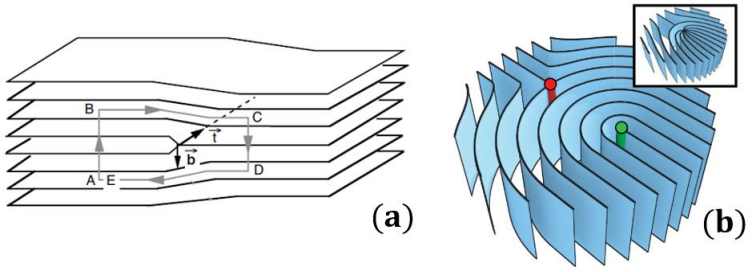


Figure 1.11: The dislocation in smectic materials. (a) small edge dislocation with a Burger vector defect line. [24]. (b) The giant edge dislocation in smectic with a core splits into a pair of disclination lines. These dislocations lines have a topological charge of $+\frac{1}{2}$ (green point) and $-\frac{1}{2}$(red point) respectively. Figure reprinted from [39].

### 1.2.3 Focal conics domain

The most common smectic textures associated with topological defects are focal conics domains (FCD). A FCD is characterized by two conjugate focal lines, the ellipse and hyperbola as shown in figure 1.12. The smectic layers rotate around the two lines, keeping constant their interlayers spacing parallel and having a common normals and curvature center along a same normal. They can be formed when the smectic A film is thick enough [24]. A 2D pattern of non-toroidal FCDs has been observed when

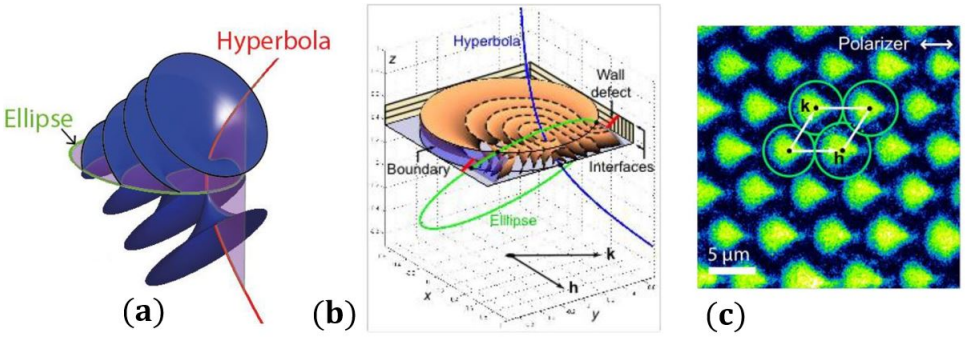


Figure 1.12: The focal conics domains. (a) The plane of that contains the ellipse is orthogonal to the plane that contain the hyperbola. [49] (b) Model of the 2d pattern non-toroidal FCDs (c) FCPEM image of a 2d pattern of non-toroidal FCDs [50].

the smectic-A 4-cyano-4'-n-octylbiphenyl (8CB) liquid crystal film of larger thickness deposited in air on different substrate such as molybdenite and mica crystals [51] and PVA and PI polymers [50]. Claire Meyer et al. have also worked on focal Conic Stacking in Smectic A Liquid Crystals. They reported two textures of topological defects, specifically the flower texture and the generation texture texture[52]. It was reported that when dislocations interact with focal conics domains, some imperfection on the FCD are produced as detailed in [53].

### 1.2.4 2D defect: Grain boundaries in smectics

Another feature that emerged from the frustrated smectic liquid crystal thin film is the grain boundary. These are are separating two domains of different orientations. They are characterized by a disorientation angle $\theta$ 1.13. Williams and Kléman [44] have considered an homeotropic sample or a perfect planar sample as shown in figure 1.13(a). If the sample is bent on its ends with a small disorientation angle $\theta \ll 1$, a curvature wall of layers will be formed in the between the two disoriented parts with an associated dilation of the layers without dislocations. This can be seen in figure 1.13(b). The curvature energy per unit surface is given by

$$E_c \approx \frac{2}{3}\sqrt{KB}\theta^3 \tag{1.32}$$

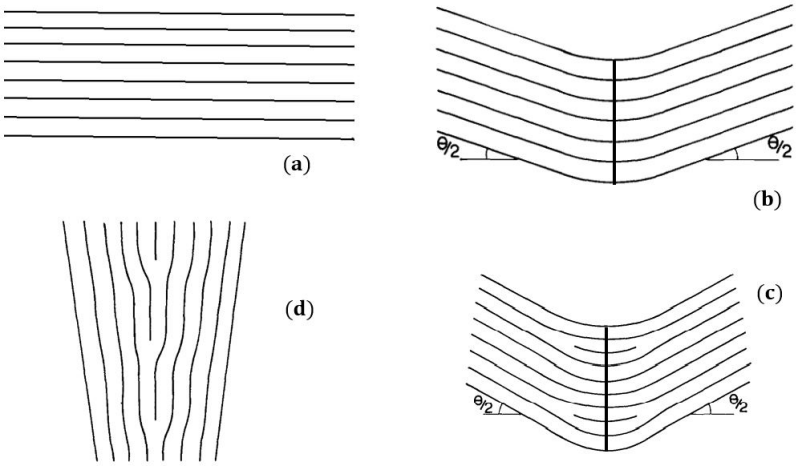


Figure 1.13: (a)The uniform planar sample (b) after applying a small disorientation angle, with no dislocation (c) curvature wall for larger disorientation angle. It has some dislocations. (d) when the disorientation is increasing further beyond $25^\circ$ the wall is full of dislocations only[44]

The energy of such a grain boundary has been more precisely calculated in [54]. When the disorientation angle increases, the stress increases and the system relax by adding extra layers which are associated with dislocation defects (see figure 1.13(c)). The produced curvature wall is called mixed curvature wall [24]. Its curvature energy is of the order

$$E_{comb} = \frac{E_{ed}}{d_o}\theta^2 \tag{1.33}$$

where $E_{ed}$ is the energy of the produced edge dislocation and $d_o$ layer thickness. This wall is expected to be experimentally obtained for $\theta$ between few degrees and $25^\circ$.

When the disorientation angle $\theta \approx \pi$, the curvature is made up only of dislocations as shown in figure 1.13(d). The energy of the curvature wall given is of the order of

$$E = \frac{E_{ed}}{b}(\pi - \theta) \tag{1.34}$$

When the samples exhibit planar anchoring with degenerate anchoring and the angle is much larger, the Grandjean walls, or focal domain walls appear as shown in figure 1.14. This only appears if the sample thickness is large enough [44]. When the film is thick enough (thicker than 1 $\mu m$) arrays of focal conics are formed as shown on figure1.14[44] and as discussed in section 1.3.3 below. However in my thesis I worked with thin films of thickness smaller than 300 nm. Topological defects and curvature wall were thus produced as described below and in the next chapters. Our film are confined between non-degenerate planar anchoring on the substrate and the homeotropic anchoring.

## 1.3 Study of the oily-streak in 8CB smectic A thin film

The smectic oily streaks are 1D patterns. They correspond to the structure adopted by smectic liquid crystal films deposited on a substrate which imposes a unidirectional planar anchoring whereas the liquid crystal molecules are imposed to be perpendicular to the air ( homeotropic anchoring) [38, 49, 55]. They have been found in many different liquid crystal system such as 8CB, other alkyl-cyanobiphenyls [56], alyloxy-cyanobyphenyls (8OCB)[57], and 9004 [58]. They have been obtained by depositing

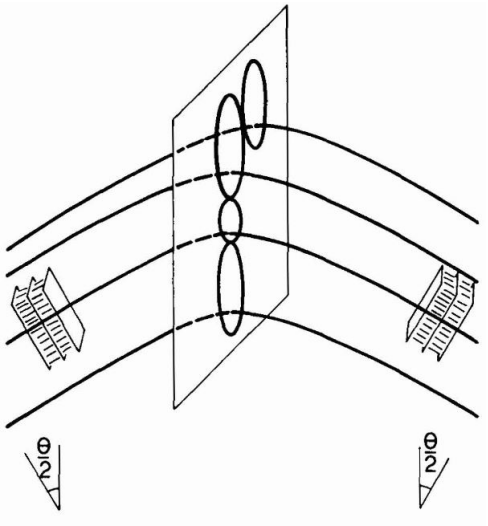


Figure 1.14: Tilt wall between two grains achieved by a system of confocal domains (Grandjean boundary) [44]

thin LC films in air on various substrates that impose unidirectional planar anchoring, such as molybdenite [55], mica [51, 59], the photoalignment agent sulfonic azo dye SD1 [37], rubbed polyimide (PI) [58], and the rubbed polyvinylalcohol (PVA) [38].

During my thesis, we have used rubbed PVA-coated glass slides as substrates. In this section I will start by introducing the sample preparation. Then, I will talk about the preliminary analysis which is based on the use of optical microscopy to not only determine the film thickness, the period of the pattern but also to ascertain the presence of the oily streaks or other structure known as larger streaks.I will then summarize the previous results that have been obtained concerning the structure of oily streaks such as how it evolves on different substrate, notably, the PVA, $MoS_2$ and muscovite mica. Right before concluding this chapter, I will talk about how this structure evolved as function film thickness.

### 1.3.1 sample preparation

The samples of the 8CB smectic A thin films that we have studied during my thesis were prepared by Professor Haifa Jeridi and two PhD students of Professor Emmanuelle Lacaze, notably Caterina Tosarelli and Lamya Essaoui. They have also done the preliminary analysis of these sample to ascertain the presence of oily streaks They also determined the film thickness. The first step in sample preparation was the preparation of the substrate. This consists of a scrupulous cleaning of the glass slide of surface 18 mm $\times$ 18 mm to ensure a good spreading of 8CB film upon substrate but also avoid dusts that may affect the anchoring of the molecules. Once the glass slide cleaning is finished, they deposit using spincoating a droplet (100 $\mu L$) of an aqueous solution of PVA (poly vinyl alcohol from Sigma Aldrich) (0.5 wt %, acceleration 400 $rpm\ s^{-1}$, speed 3000 $rpm$, during 30$s$) on the glass slides. The resulted PVA layer of thickness around 10 nm was firstly heated at the oven for 1 hour at 140°. Right after removing the PVA-coated glass slide from the oven, they rubbed the slides unidirectionally using the rubbing machine shown in figure 1.15. A great attention is taken during this rubbing in order to control the rubbing forces. This is a critical issue since, for strong forces (shorter distance between the PVA substrates and the rubbing roller of the rubbing machine), the oily streaks texture largely dominate the overall structure. By reducing the rubbing force, an other structure called Large stripes appear in majority. Recently H. Jeridi et al [60]. have proposed a schematized model of structure of the large stripes shown in figure 1.16(d). It may correspond to hemicylindrical superposition of smectic layers similarly to oily streaks with a similar structure at the edges of the hemicylinders (figure 1.16(b)), but its central part is larger than the one of oily streaks and the flat layers in this part may directly touch the substrate contrary to the oily streak structure. As a result larger widths of the hemicylinders are observed for large stripes with respect to oily streaks (1.16(a)). Detailed study is however necessary to obtain the precise structure of the large stripes and understand its relationship with the anchoring forces A moderate force produces a coexistence of the two structures.

The substrate/8CB film interface imposes a uniform unidirectional planar anchoring to the 8CB molecules deposited upon the substrate as shown in figure 1.8(a)). These 8CB liquid crystal films were deposited by spin-coating the droplets

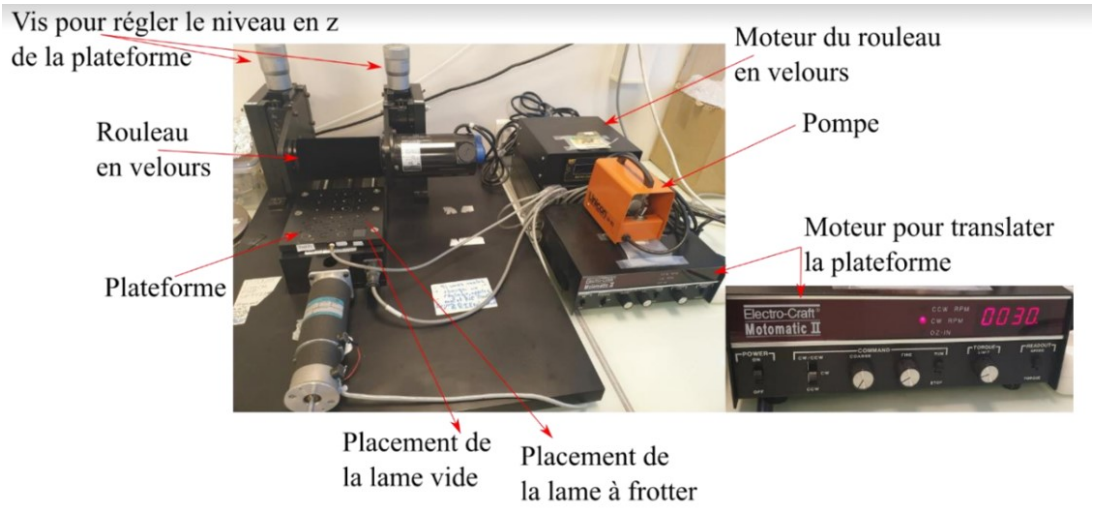


Figure 1.15: Rubbing machine

of 4-n-octyl-4'-cyanobiphenyl (8CB from Sigma-Aldrich), $(50\mu L, 0.2M)$ in toluene as solvent (speed 3000 $rpm$ during 30s, acceleration between 500 $rpm\ s^{-1}$ and 1000 $rpm\ s^{-1}$) on the rubbed PVA substrate. The air-8CB interface imposes an homeotropic anchoring on the 8CB molecules. Therefore the 8CB smectic A liquid crystal film is confined between the two antagonistic anchorings, the uniform unidirectional planar on the substrate/film interface and the homeotropic anchoring at the film/air interface. This induces a bending of the smectic layers into a periodic array of flatten hemicylinders which are parallel to the substrate and perpendicular to the anchoring direction as schematized in figure 1.16 (a) [55, 60]. In the next subsection, I will briefly talk about the optical microscopy analysis of the sample.

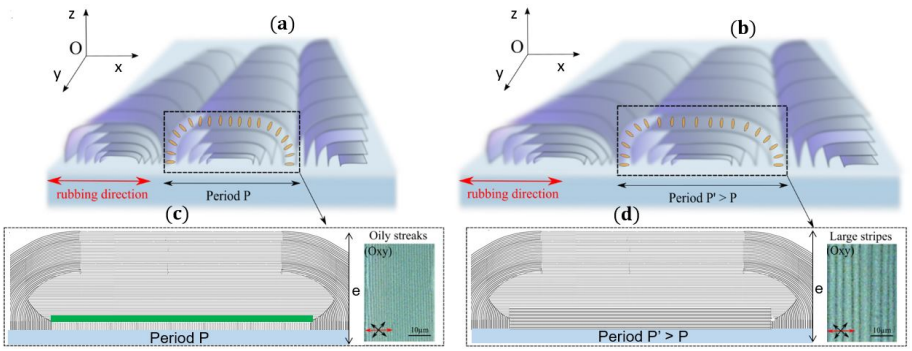


Figure 1.16: 3D schematized model of (a) oily streak and (b) large streak. Smectic layers are curved in flattened hemicylinders with the molecular orientation shown in yellow. The 2D cross-section view of (a) oily streaks (d) large stripes have the same expected structure in the edges of the hemicylinder but the central part of large streak is larger than that of the oily streaks. [60].

### 1.3.2 Polarized optical microscopy study

#### Birefringence

One of the quintessential properties of liquid crystal, in particular smectic phases is their birefringence property. This property makes the polarized optical microscopy most useful in the study of the liquid crystal structure. Let's briefly review what is the birefringence of the liquid crystal.

Birefringent materials have two different indices of refraction. The ordinary $n_o$ and extra-ordinary $n_e$ indices depend on the direction of the polarization of the light with respect to the director $\vec{n}$. The former is when the smectic director is perpendicular to the direction of light polarization and the latter is when the director is parallel to the light polarization. So birefringence $\Delta n$ is the difference between the two refraction indices.

$$\Delta n = n_e - n_o \tag{1.35}$$

Our smectic A sample were observed using an upright optical microscope (Leica DMRX). The light from either halogen lamp was impinged normally on our thin film placed between two polarizers like in the example shown in figure 1.17 for a nematic slab between two glass slides and two crossed polarizers.

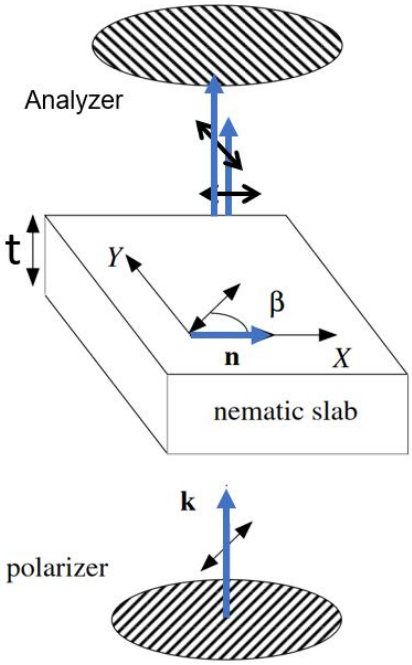


Figure 1.17: Propagation of light through a polarizer, a uniaxial slab, and analyzer. The image reused from the book:Soft matter Physics, an introduction, by Maurice Kleman and Oleg D.Lavrentovich, 2003 [27]

The polarizer between the lamp and the sample linearly polarizes the incident light. After passing through the 8CB thin film, the linearly polarized light splits into ordinary and extra-ordinary waves with mutually perpendicular polarizations and amplitudes $E_x = E_o \cos(\beta)$ and $E_y = E_o \sin(\beta)$, where $E_o$ is the amplitude of the incident light and $\beta$ is the angle between the direction of polarization of light and the local smectic director **n**. The two waves are out of phase with a phase difference of

$$\Delta\phi = \frac{2\pi t(n_e - n_o)}{\lambda_o}$$

where $t$ is the thickness of the liquid crystal sample, $\lambda_o$ is the wavelength of the incidence light.

If the liquid crystal director is planar and homogeneous, the light intensity passing through the thin film and the crossed polarizers is given by

$$I = I_o \sin^2(2\beta) \sin^2[\frac{\pi t(n_e - n_o)}{\lambda_o}]$$

This intensity expression is anyway qualitatively helpful for non homogeneously planar sample by taking an effective $n_e$ for studying the liquid crystal structure. In our optical microscope it is collected by a SONY CDD camera of resolution $1600 \times 1200$ pixels. We work in reflection mode between crossed polarizers. In the figure 1.18(b), we observe a periodic array of stripes Each stripe corresponds to a flattened hemicylinder parallel to the substrate and perpendicular to the unidirectional anchoring direction.

The dark parts of the stripes correspond to areas where $ne_{eff}$ is close to $n_o$ and I close to zero. It thus corresponds to the central part of the hemicylinders which is formed by a majority of molecules oriented parallel to the direction of light propagation. On the two edges of each hemicylinder there are rotating layers. When the stripes are orientated at $45°$ with respect to the polarizers, the intensity from this part of rotating layers is maximum and so it appears bright in the optical microscopy images, finally leading to stripes made of alternating dark and bright lines.

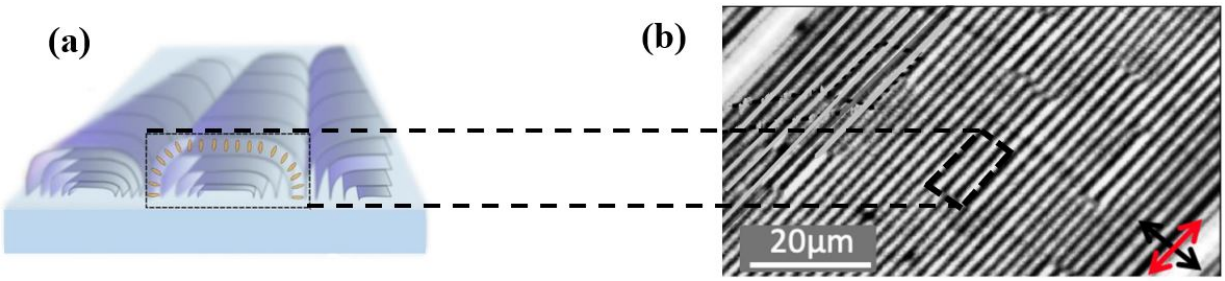


Figure 1.18: **(a)** Periodic array of the flattened hemicylinders in the 8CB film confined between unidirectional anchoring (on the $MoS_2$ single crystalline substrate) and the homeotropic anchoring on the film-air interfaces. In the highlighted part, the 8CB molecules are depicted in orange color. **(b)** Optical microscopy image between crossed polarizers of size $165\ \mu m \times 123 \mu m$ obtained on a sample of thickness $0.20\ \mu m$. [55, 60].

**Determination of the smectic film thickness and the period of oily steaks.**

The optical microscopy in reflection mode (with crossed polarizers) was used to observe the periodic array of oily streaks. The determination of the film thickness is done using the optical microscopy in reflection mode (with parallel polarizers). This gives pattern of colors as shown in figure 1.19. They come from the interference phenomenon between the light reflected from the two interfaces of the sample being observed under the microscope. The smectic film thickness is determined by using the measurement of the Newtons' tints shown in the appendix A. The film thickness $t$ is given by

$$t = \frac{\delta}{2n} \tag{1.36}$$

where $\delta$ is the path different between the reflected signals and $n$ is the average optical index and is given $n = \frac{n_e + 2n_o}{3}$. For the case of our 8CB smectic liquid crystal thin films, $n_o = 1.518$, $n_e = 1.673$ and $n = 1.57$.

The period of the streaks in an optical polarized image was determined for 8CB smectic A liquid crystal film deposited on different substrate.

### 1.3.3 Structural Evolution of the smectic stripe as function film thickness.

**Thin films**

The period is always greater than twice the film thickness. For PVA substrate, the slope is 1.5 and the offset 300 nm as shown in figure 1.19(inset) [38]. For $MoS_2$ the slope is 4.4 and the offset 500 nm. These results show that the structure of the oily streaks

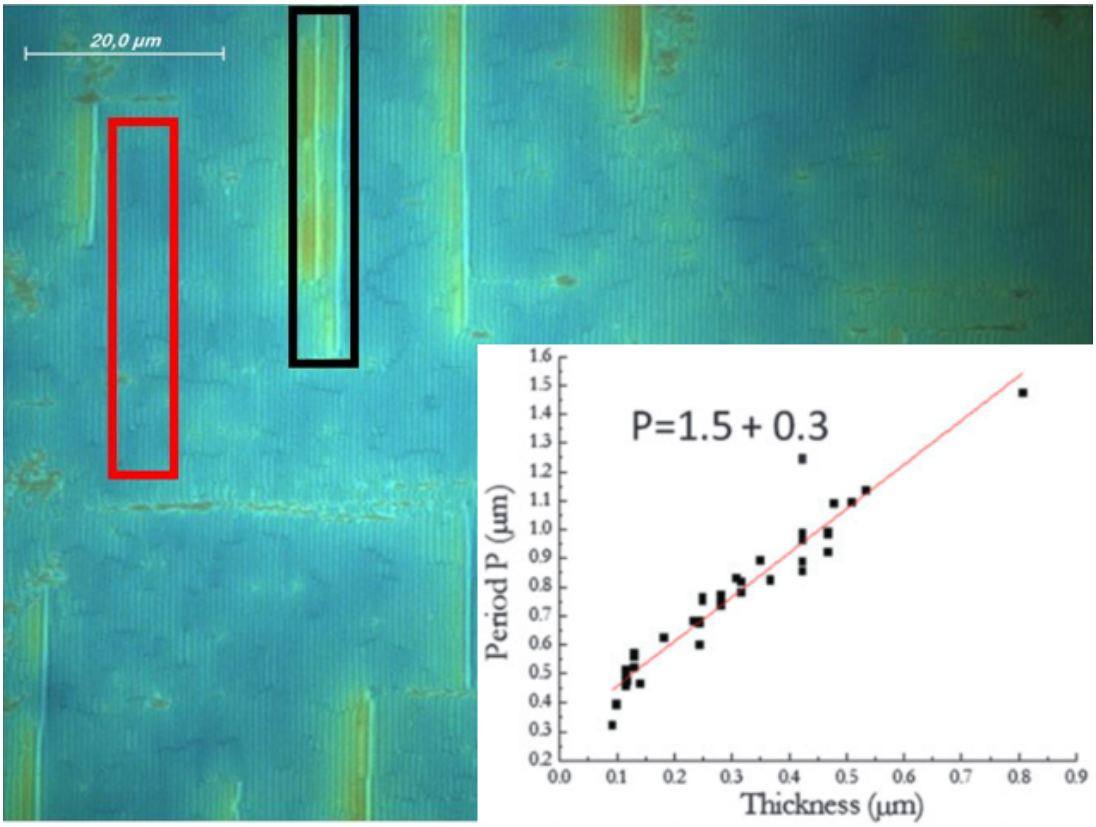


Figure 1.19: Image of optical microscopy in reflection mode between parallel polarizers of sample in average of 120 nm thick film. It has a large majority of oily streaks. The images was obtained from Lamya Essaoui. Inset graph: Stripe period as a function of film thickness. The red line is a linear fit [38].

can correspond to a perfect hemicylinder but,instead to flattened hemicylinders. This result is in contrast with the suggestion of Parodi [61] and Allet et al.[62]. They proposed a structure in which there was no central flat part, i.e., the two hemicylinder quarters were directly connected. Hence the stripes were formed by perfect hemicylinders and the area above the curvature wall between the neighboring perfect quarters of hemicylinder was either filled with nematic or kept unfilled. Allet, Kleman, and Vidal [62] have also proposed -$\frac{1}{2}$ disclination defect in this part. The instead observed flattened pattern is induced by the hybrid anchoring conditions where the surface energy tends to keep flat the smectic layers and thus favour the flat areas of the flattened hemicylinders.

The model schematized in figure 1.18(a), with flattened central part was found not only on $MoS_2$ single crystalline substrate for film thickness between 70 and 450nm, but it was also found when the 8CB film is deposited on the PVA substrate [38, 55, 63, 64]. The model of the internal structure of the 8CB film of 220nm thickness deposited on PVA was developed through a combination of ellipsometry, optical microscopy and X-RAY diffraction (I will come back on this in chapter 2). It is shown in figure 1.20 [38]. This model has three parts. The first part is formed by central layers that obeying the homeotropic anchoring. The second part is formed by two edges. Each is formed by rotating layers that are satisfying the hybrid anchoring. The third part is formed by perpendicular layers everywhere on the substrate obeying the uniform planar anchoring. This last part has a thickness of 30 nm of perpendicular layers.

Due to the strong anchoring that was on the PVA substrate, these perpendicular layers cover entirely [38]. As a result a 2D topological grain boundaries that separates the perpendicular layers from the central flat layers as shown in green color in fig. 1.20 is expected. It was shown that an hexagonal network of nanoparticles can be trapped in this 2D defect which also stabilized it energetically [60, 65]. This model has also rotating grain boundaries (shown in red in figure 1.20) separating the central flat

layers from the rotating smectic layers. In contrast to the PVA substrate, when the 8CB film is deposited on the $MoS_2$ single crystalline substrate, the central part is considerably larger as shown by the large slope of the curve of period as function of thickness. This would imply a very large and energetically expensive, grain boundary. So we expect this part to disappear and be replaced by possibly flat layers reaching directly the substrate. This suggests that the planar anchoring on this substrate is weak enough to be partially broken and allows formation of larger flat hemicylinders than the ones formed on PVA substrate [49].

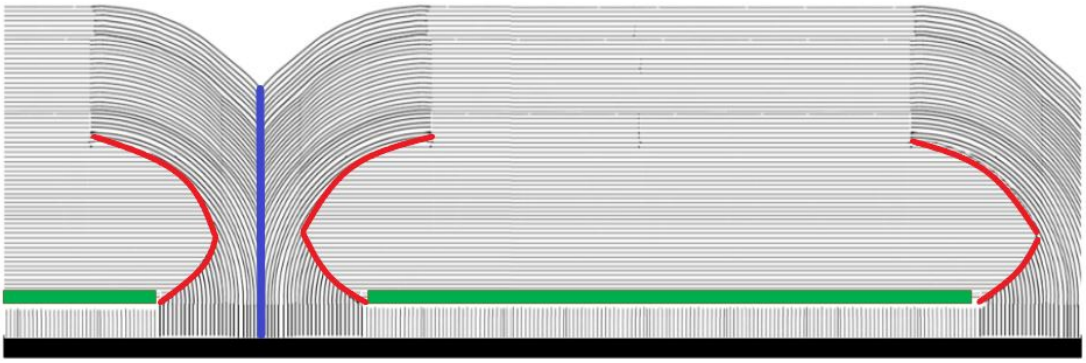

Figure 1.20: Schematized model of the internal structure of the oily streak for 8CB film of 220 nm [38]

Two neighboring hemicylinders are separated by a vertical curvature wall shown in blue in figure 1.20. The structure of this wall is still enigmatic. From top to down along this curvature wall, the bend distortion increases. A chain of dislocations can be expected along this wall [49]. However, Coursault Delphine [66] and other works such as Allet, Kleman, and Vidal [62] and [58] have suggested the possible existence of -$\frac{1}{2}$ disclination defect on the top of this wall near the air surface.

When the 8CB smectic film has been deposited in air on the muscovite mica, the model of flattened hemicylinders appears still valid since the scattered intensity resembled what was obtained for both PVA and MoS2 substrate [66] for similar thickness. As we will see in the chapter 2, this suggests a universality of the structure of the distorted 8CB thin films imposed by antagonistic anchoring.

### Thick films

For film thickness much larger than 300 nm, 8CB film of order of 1 µ m deposited on mica, a model completely different from those of both PVA and $MoS_2$ substrate was built issued from different X-RAY scattering result with respect to thin film. The model is shown in figure 1.21. It is centered on a virtual singularity, with some layers perpendicular to the substrate and two vertical grain boundaries separating two neighboring hemicylinders (vertical red line). The 2D central grain boundary (in green color 1.20) has disappeared for thicker film. The cylinders are bent around virtual disclinations (blue dots). This structure avoids almost all topological defects except at the junction between grain boundaries. This is only possible for thick films. For sufficiently small thickness the creation of a lot of topological defect takes place. [49].

For much larger 8CB film thickness such as 1.5 µ$m$, deposited on the muscovite mica, 1D pattern of oily streaks pattern transform into 2D patterns of non-toroidal focal conics as shown in figure 1.12 and 1.22. The smectic film thickness clearly appears as a crucial parameter for not only the appearance of the 1D pattern but even for the determination of the internal structure of the 1D patterns.

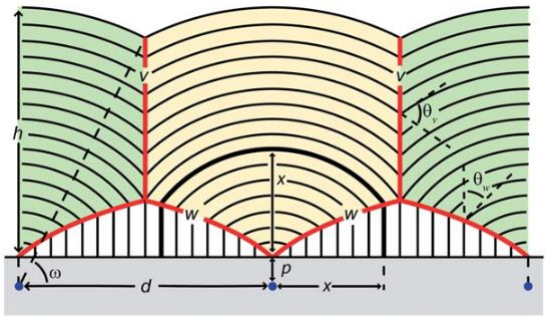


Figure 1.21: Schematized model of the internal structure of the oily streak for 8CB film of 1µm deposited on muscovite mica substrate. [59]

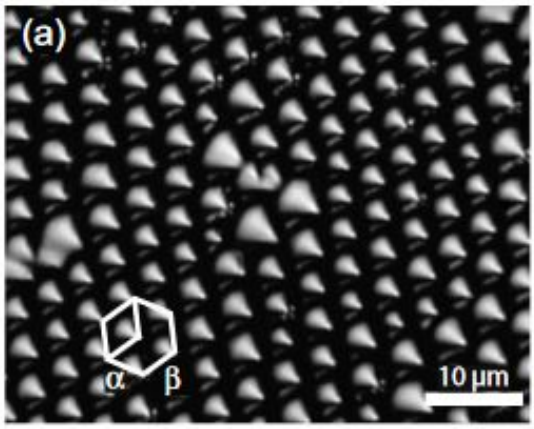


Figure 1.22: Bidimensional lattice of focal conics domains in a 8CB mica for a 8CB thickness of the order of 1.5 µ$m$. [51].

## 1.4 Conclusion and objectives

### 1.4.1 Conclusion

In this chapter I have introduced the smectic liquid crystal topological defects. We have seen that the confinement of the 8CB smectic A in antagonistic anchoring distorted its pristine configuration into a periodic array of stripes which can be either oily streaks or large stripes. We have focused on the previous studies on the evolution of these oily streaks as a function of both the film thickness and the nature of the substrate upon which the film is deposited. We have clearly seen that the exact internal structure of the oily streaks is still enigmatic with still pending questions at the origin of my PHD aimed at clarifying their exact structure and its evolution with the films thickness.

What is the exact structure of the central part of the hemicylinders and in particular of the 2D grain boundary area ? In the area between two neighboring hemicylinders, the bend distortion energy increases from top to bottom, this strongly suggests the appearance of topological defects along this curvature wall, however, this has not yet been studied. Are there other topological defects inside this oily streaks configuration? For example what is the exact structure of the part at the top of the curvature wall between the two neighboring hemicylinders? We have seen that the film thickness affects the periodic pattern of stripes. The thickness increases can fully modify the pattern ultimately leading to a transformation into focal conics domains. It would be interesting to study the effect of the film thickness of the intimate structure on the oily streaks.

My thesis aims at responding to all of these questions. The main goal was to reconstruct the intimate internal structure of

the oily streaks structure and to study the effect of the variation of the film thickness on the oily streaks structure. Topological defects are crucial in tailoring properties of liquid crystal materials and they can lead to various applications. Nanoparticles and microparticles can be efficiently be trapped in the defect core and therefore inherit their self assembling from this topological matrices. The emerged composite could be useful for metamaterial, sensor, or solar cell production [67, 68, 69, 70, 71]. The determination of the intimate structure of the oily streaks has become more interesting for theoreticians and experimental physicist. Xia et al. [67] have worked on the structural landscape in geometrically frustrated smectic. They have developed a free energy model suitable for finite element simulation. They have proposed a simulated structure of the oily streak reported in [38, 55, 63]. For these theoreticians, oily streaks consist in thin smectic films, thus appropriate for simulations, of distortions displaying cylindrical symmetry that allow to work mainly in 2-dimension which is an advantage. This latter advantage is also used in my study together with the induced periodic structure for an easier analysis of X-RAY diffraction. The unprecedented resolution that can be achieved is thus particularly interesting for simulation since it provides accurate comparison with experimental systems. Wu et al. [37] have also worked on this structure. They reported a flexible defect engineering based oily streaks. They have also shown that the distribution of the electric field can manipulate the width and the orientation of the oily streaks. These results evidence that many unprecedented application may be developed based on oily streaks. Recently, Missaoui et al. [72] have also reported a new way of distorting oily streaks. Understanding how to be able to modify the defects requires however, to understand them first in the simplest unidirectional situation.

All the above works highlight the interesting and indispensable work that has to be done to precisely understand the internal structure of the oily streak in smectic thin films. This would open gates to not only many liquid crystal-based technological applications but also fundamental applications towards a full understanding of these still complex smectic phases.

# Bibliography


[1] Gregory A DiLisi. *An Introduction to Liquid Crystals*. 2053-2571. Morgan & Claypool Publishers, 2019. ISBN: 978-1-64327-684-7. DOI: 10.1088/2053-2571/ab2a6f. URL: https://dx.doi.org/10.1088/2053-2571/ab2a6f (cit. on p. 16).

[2] Mr G Friedel. *The mesomorphic states of matter*. US Army Engineer Research and Development Laboratories, 1967 (cit. on p. 16).

[3] Michel Mitov. "Liquid-crystal science from 1888 to 1922: Building a revolution". In: *ChemPhysChem* 15.7 (Jan. 2014). Publisher: Wiley-VCH Verlag, pp. 1245–1250. DOI: 10.1002/cphc.201301064. URL: https://hal.archives-ouvertes.fr/hal-01764620 (visited on 06/26/2022) (cit. on p. 16).

[4] James L. Fergason and Glenn H. Brown. "Liquid crystals and living systems". en. In: *Journal of the American Oil Chemists' Society* 45.3 (Mar. 1968), p. 120. ISSN: 0003021X. DOI: 10.1007/BF02915335. URL: http://doi.wiley.com/10.1007/BF02915335 (visited on 07/06/2022) (cit. on p. 16).

[5] Christopher Viney. "Liquid crystalline phase behavior of proteins and polypeptides". In: *Protein-based materials*. Springer, 1997, pp. 281–311 (cit. on p. 16).

[6] Peter Palffy-Muhoray. "The diverse world of liquid crystals". en. In: *Physics Today* 60.9 (Sept. 2007), pp. 54–60. ISSN: 0031-9228, 1945-0699. DOI: 10.1063/1.2784685. URL: https://pubs.aip.org/physicstoday/article/60/9/54/395691/The-diverse-world-of-liquid (visited on 09/06/2023) (cit. on p. 16).

[7] Michel Mitov. "Cholesteric liquid crystals in living matter". In: *Soft Matter* 13.23 (2017). Publisher: The Royal Society of Chemistry, pp. 4176–4209. DOI: 10.1039/C7SM00384F. URL: http://dx.doi.org/10.1039/C7SM00384F (cit. on p. 16).

[8] O. Pelletier et al. "A Detailed Study of the Synthesis of Aqueous Vanadium Pentoxide Nematic Gels". In: *Langmuir* 16.12 (June 2000). Publisher: American Chemical Society, pp. 5295–5303. ISSN: 0743-7463. DOI: 10.1021/la9914155. URL: https://doi.org/10.1021/la9914155 (visited on 09/06/2023) (cit. on p. 16).

[9] P. Davidson et al. "A structural study of the lyotropic nematic phase of vanadium pentoxide gels". In: *J. Phys. II France* 5.10 (1995), pp. 1577–1596. DOI: 10.1051/jp2:1995200. URL: https://doi.org/10.1051/jp2:1995200 (cit. on p. 16).

[10] Patrick Davidson. "Mineral liquid crystals: Liquid-crystalline suspensions of mineral nanoparticles". In: *Handbook of liquid crystals*. Section: 3 tex.eprint: https://onlinelibrary.wiley.com/doi/pdf/10.1002/9783527671403.hlc090. John Wiley & Sons, Ltd, 2014, pp. 1–22. ISBN: 978-3-527-67140-3. DOI: https://doi.org/10.1002/9783527671403.hlc090. URL: https://onlinelibrary.wiley.com/doi/abs/10.1002/9783527671403.hlc090 (cit. on p. 16).

[11] O Pelletier et al. "A biaxial nematic gel phase in aqueous vanadium pentoxide suspensions". In: *The European Physical Journal B-Condensed Matter and Complex Systems* 12 (1999), pp. 541–546 (cit. on p. 16).

[12] P. Davidson et al. "A Structural Study of the Lyotropic Nematic Phase of Vanadium Pentoxide Gels". en. In: *Journal de Physique II* 5.10 (Oct. 1995), pp. 1577–1596. ISSN: 1155-4312, 1286-4870. DOI: 10.1051/jp2:1995200. URL: http://www.edpsciences.org/10.1051/jp2:1995200 (visited on 09/06/2023) (cit. on p. 16).

[13] P. Davidson, A. Garreau, and J. Livage. "Nematic colloidal suspensions of $V_2O_5$ in water—or Zocher phases revisited". en. In: *Liquid Crystals* 16.5 (May 1994), pp. 905–910. ISSN: 0267-8292, 1366-5855. DOI: 10.1080/02678299408027861. URL: http://www.tandfonline.com/doi/abs/10.1080/02678299408027861 (visited on 09/06/2023) (cit. on p. 16).

[14] Nobuo Donkai et al. “Lyotropic mesophase of imogolite: Molecular weight fractionation and polydispersity effect”. en. In: *Die Makromolekulare Chemie, Rapid Communications* 14.9 (1993), pp. 611–617. ISSN: 0173-2803. DOI: 10.1002/marc.1993.030140913. (Visited on 09/06/2023) (cit. on p. 16).

[15] Jean-Christophe P. Gabriel et al. “Swollen liquid-crystalline lamellar phase based on extended solid-like sheets”. en. In: *Nature* 413.6855 (Oct. 2001), pp. 504–508. ISSN: 0028-0836, 1476-4687. DOI: 10.1038/35097046. URL: https://www.nature.com/articles/35097046 (visited on 09/06/2023) (cit. on p. 16).

[16] Liang-shi Li et al. “Semiconductor Nanorod Liquid Crystals”. en. In: *Nano Letters* 2.6 (June 2002), pp. 557–560. ISSN: 1530-6984, 1530-6992. DOI: 10.1021/nl0255146. URL: https://pubs.acs.org/doi/10.1021/nl0255146 (visited on 07/06/2022) (cit. on p. 16).

[17] Patrick Davidson. “Mineral Liquid Crystals: Liquid-Crystalline Suspensions of Mineral Nanoparticles”. en. In: *Handbook of Liquid Crystals*. Ed. by John W Goodby et al. 1st ed. Wiley, Feb. 2014, pp. 1–22. ISBN: 978-3-527-32773-7 978-3-527-67140-3. DOI: 10.1002/9783527671403.hlc090. URL: https://onlinelibrary.wiley.com/doi/10.1002/9783527671403.hlc090 (visited on 09/06/2023) (cit. on p. 16).

[18] Patrick Davidson and Jean-Christophe P. Gabriel. “Mineral liquid crystals”. In: *Current Opinion in Colloid & Interface Science* 9.6 (2005), pp. 377–383. ISSN: 1359-0294. DOI: https://doi.org/10.1016/j.cocis.2004.12.001. URL: https://www.sciencedirect.com/science/article/pii/S1359029404001190 (cit. on p. 16).

[19] ZX Zhang and Jeroen S van Duijneveldt. “Isotropic-nematic phase transition of nonaqueous suspensions of natural clay rods”. In: *The Journal of chemical physics* 124.15 (2006) (cit. on p. 16).

[20] Patrick Oswald and Pawel Pieranski. *Nematic and cholesteric liquid crystals concepts and physical properties illustrated by experiments*. en. ISBN: 9780415321402 9780203023013 Place: Boca Raton, Fla. OCLC: 612290103. 2005 (cit. on pp. 16, 19).

[21] CR Safinya and WA Varady. “Calamitic liquid crystals-nematic and smectic mesophases”. In: *Liq. Cryst* 57 (1986), pp. 43–77 (cit. on p. 18).

[22] A.J. Leadbetter et al. “The structure of smectic A phases of compounds with cyano end groups”. en. In: *Journal de Physique* 40.4 (1979), pp. 375–380. (Visited on 05/12/2022) (cit. on p. 18).

[23] Pierre Gilles de Gennes. *The physics of liquid crystals*. eng. Oxford : Clarendon Press ; New York : Oxford University Press, 1993. ISBN: 978-0-19-852024-5 978-0-19-851785-6. URL: http://archive.org/details/physicsofliquidc0000genn_l4c2 (visited on 01/15/2023) (cit. on pp. 18, 19, 24).

[24] Patrick Oswald and Pawel Pieranski. *Smectic and Columnar Liquid Crystals: Concepts and Physical Properties Illustrated by Experiments*. Boca Raton: CRC Press, Dec. 2005. ISBN: 978-0-429-12555-3. DOI: 10.1201/9781420036343 (cit. on pp. 18, 20, 21, 23, 25–27).

[25] Wim H. De Jeu, Boris I. Ostrovskii, and Arcadi N. Shalaginov. “Structure and fluctuations of smectic membranes”. en. In: *Reviews of Modern Physics* 75.1 (Feb. 2003), pp. 181–235. ISSN: 0034-6861, 1539-0756. DOI: 10.1103/RevModPhys.75.181. URL: https://link.aps.org/doi/10.1103/RevModPhys.75.181 (visited on 07/26/2023) (cit. on pp. 18, 19).

[26] P. G. de Gennes. “An analogy between superconductors and smectics A”. en. In: *Solid State Communications* 10.9 (May 1972), pp. 753–756. ISSN: 0038-1098. DOI: 10.1016/0038-1098(72)90186-X. URL: https://www.sciencedirect.com/science/article/pii/003810987290186X (visited on 05/12/2022) (cit. on p. 19).

[27] Maurice Kleman and Oleg D. Lavrentovich, eds. *Soft Matter Physics: An Introduction*. en. New York, NY: Springer, 2003. ISBN: 978-0-387-95267-3 978-0-387-21759-8. DOI: 10.1007/b97416. URL: https://link.springer.com/10.1007/b97416 (visited on 05/16/2023) (cit. on pp. 19, 23, 30).

[28] Iam-Choon Khoo. *Liquid crystals*. John Wiley & Sons, 2022 (cit. on pp. 19, 22).

[29] Thomas Machon et al. "Aspects of Defect Topology in Smectic Liquid Crystals". en. In: *Communications in Mathematical Physics* 372.2 (Dec. 2019), pp. 525–542. ISSN: 0010-3616, 1432-0916. DOI: 10.1007/s00220-019-03366-y. URL: http://link.springer.com/10.1007/s00220-019-03366-y (visited on 04/17/2021) (cit. on pp. 21, 24, 25).

[30] R. D. Kamien et al. "Extrinsic Curvature, Geometric Optics, and Lamellar Order on Curved Substrates". In: *Physical Review E* 80.5 (Nov. 2009). arXiv:0908.4358 [cond-mat], p. 051703. ISSN: 1539-3755, 1550-2376. DOI: 10.1103/PhysRevE.80.051703. URL: http://arxiv.org/abs/0908.4358 (visited on 08/29/2023) (cit. on p. 22).

[31] Patricio Aviles and Yoshikazu Giga. "A mathematical problem related to the physical theory of liquid crystal configurations". In: *Miniconference on geometry/partial differential equations, 2*. Vol. 12. Australian National University, Mathematical Sciences Institute, Jan. 1987, pp. 1–17. (Visited on 11/06/2023) (cit. on p. 22).

[32] Christophe Blanc et al. *Helfrich-Hurault elastic instabilities driven by geometrical frustration*. Tech. rep. Publication Title: arXiv e-prints ADS Bibcode: 2021arXiv210914668B Type: article. Sept. 2021. DOI: 10.48550/arXiv.2109.14668. URL: https://ui.adsabs.harvard.edu/abs/2021arXiv210914668B (visited on 02/27/2023) (cit. on p. 22).

[33] Sandro Faetti. "Azimuthal anchoring energy of a nematic liquid crystal at a grooved interface". en. In: *Physical Review A* 36.1 (July 1987), pp. 408–410. ISSN: 0556-2791. DOI: 10.1103/PhysRevA.36.408. URL: https://link.aps.org/doi/10.1103/PhysRevA.36.408 (visited on 06/02/2023) (cit. on p. 23).

[34] J M Ball. "Mathematics and liquid crystals". en. In: (), p. 28 (cit. on p. 23).

[35] E. P. S. Shellard. "Topological defects in cosmology". In: *Current topics in astrofundamental physics: The early universe*. Ed. by N. Sánchez and A. Zichichi. Dordrecht: Springer Netherlands, 1995, pp. 129–177. ISBN: 978-94-011-0095-3. DOI: 10.1007/978-94-011-0095-3_4. URL: https://doi.org/10.1007/978-94-011-0095-3_4 (cit. on p. 23).

[36] Aleksandra Ardaševa and Amin Doostmohammadi. "Topological defects in biological matter". In: *Nature Reviews Physics* 4 (May 2022). DOI: 10.1038/s42254-022-00469-9 (cit. on p. 23).

[37] Sai-Bo Wu et al. "Smectic Defect Engineering Enabled by Programmable Photoalignment". en. In: *Advanced Optical Materials* 8.17 (2020), p. 2000593. ISSN: 2195-1071. DOI: 10.1002/adom.202000593. (Visited on 03/23/2022) (cit. on pp. 23–25, 28, 35).

[38] Delphine Coursault et al. "Self-organized arrays of dislocations in thin smectic liquid crystal films". en. In: *Soft Matter* 12.3 (2016), pp. 678–688. ISSN: 1744-683X, 1744-6848. DOI: 10.1039/C5SM02241J. URL: http://xlink.rsc.org/?DOI=C5SM02241J (visited on 01/17/2023) (cit. on pp. 24, 27, 28, 31–33, 35).

[39] Hillel Aharoni, Thomas Machon, and Randall D. Kamien. "Composite dislocations in smectic liquid crystals". In: *Physical review letters* 118.25 (2017). Publisher: APS, p. 257801 (cit. on pp. 24–26).

[40] V. Poénaru. "Some aspects of the theory of defects of ordered media and gauge fields related to foliations". In: *Communications in Mathematical Physics* 80.1 (Mar. 1981), pp. 127–136. ISSN: 1432-0916. DOI: 10.1007/BF01213598. URL: https://doi.org/10.1007/BF01213598 (cit. on p. 24).

[41] G. Foffano et al. "The dynamics of colloidal intrusions in liquid crystals: a simulation perspective". In: *Liquid Crystals Reviews* 2.1 (2014). Publisher: Taylor & Francis tex.eprint: https://doi.org/10.1080/21680396.2013.878672, pp. 1–27. DOI: 10.1080/21680396.2013.878672 (cit. on p. 24).

[42] C. E. Williams. “Helical disclination lines in smectics a”. en. In: *Philosophical Magazine* 32.2 (Aug. 1975), pp. 313–321. ISSN: 0031-8086. DOI: 10.1080/14786437508219956. URL: http://www.tandfonline.com/doi/abs/10.1080/14786437508219956 (visited on 09/16/2023) (cit. on p. 25).

[43] Andrii Repula and Eric Grelet. “Elementary Edge and Screw Dislocations Visualized at the Lattice Periodicity Level in the Smectic Phase of Colloidal Rods”. en. In: *Physical Review Letters* 121.9 (Aug. 2018), p. 097801. ISSN: 0031-9007, 1079-7114. DOI: 10.1103/PhysRevLett.121.097801. URL: https://link.aps.org/doi/10.1103/PhysRevLett.121.097801 (visited on 09/13/2023) (cit. on p. 25).

[44] C. Williams and M. Kléman. “DISLOCATIONS, GRAIN BOUNDARIES AND FOCAL CONICS IN SMECTICS A”. In: *Journal de Physique Colloques* 36.C1 (1975), pp. C1–315–C1–320. DOI: 10.1051/jphyscol:1975152. URL: https://hal.archives-ouvertes.fr/jpa-00216231 (visited on 07/27/2022) (cit. on pp. 25–28).

[45] Patrick Oswald. “Dynamics of Dislocations in Smectic A Liquid Crystals Doped with Nanoparticles”. en. In: *Crystals* 9.8 (Aug. 2019), p. 400. ISSN: 2073-4352. DOI: 10.3390/cryst9080400. URL: https://www.mdpi.com/2073-4352/9/8/400 (visited on 03/30/2021) (cit. on p. 25).

[46] Maurice Kléman and Oleg D. Lavrentovich. “Grain boundaries and the law of corresponding cones in smectics”. In: *The European Physical Journal E* 2.1 (2000). Publisher: Springer, pp. 47–57 (cit. on p. 25).

[47] R. B. Meyer, B. Stebler, and S. T. Lagerwall. “Observation of Edge Dislocations in Smectic Liquid Crystals”. In: *Phys. Rev. Lett.* 41 (20 Nov. 1978), pp. 1393–1395. DOI: 10.1103/PhysRevLett.41.1393. URL: https://link.aps.org/doi/10.1103/PhysRevLett.41.1393 (cit. on p. 25).

[48] C. Zhang et al. “Nanostructure of edge dislocations in a smectic-c* liquid crystal”. In: *Physical review letters* 115.8 (2015). Publisher: APS, p. 087801 (cit. on p. 25).

[49] Bruno Zappone and Emmanuelle Lacaze. “One-dimensional patterns and topological defects in smectic liquid crystal films”. en. In: *Liquid Crystals Reviews* (July 2022), pp. 1–18. ISSN: 2168-0396, 2168-0418. DOI: 10.1080/21680396.2022.2076748. URL: https://www.tandfonline.com/doi/full/10.1080/21680396.2022.2076748 (visited on 04/24/2023) (cit. on pp. 26, 27, 33).

[50] Bruno Zappone et al. “Periodic lattices of frustrated focal conic defect domains in smectic liquid crystal films”. en. In: *Soft Matter* 8.16 (2012), p. 4318. ISSN: 1744-683X, 1744-6848. DOI: 10.1039/c2sm07207f. URL: http://xlink.rsc.org/?DOI=c2sm07207f (visited on 04/06/2023) (cit. on p. 26).

[51] Bruno Zappone and Emmanuelle Lacaze. “Surface-frustrated periodic textures of smectic- A liquid crystals on crystalline surfaces”. en. In: *Physical Review E* 78.6 (Dec. 2008), p. 061704. ISSN: 1539-3755, 1550-2376. DOI: 10.1103/PhysRevE.78.061704. URL: https://link.aps.org/doi/10.1103/PhysRevE.78.061704 (visited on 01/10/2023) (cit. on pp. 26, 28, 34).

[52] Claire Meyer et al. “Focal Conic Stacking in Smectic A Liquid Crystals: Smectic Flower and Apollonius Tiling”. en. In: *Materials* 2.2 (Apr. 2009), pp. 499–513. ISSN: 1996-1944. DOI: 10.3390/ma2020499. URL: http://www.mdpi.com/1996-1944/2/2/499 (visited on 09/17/2023) (cit. on p. 26).

[53] M. Kleman, C. Meyer, and Yu. A. Nastishin. “Imperfections in focal conic domains: the role of dislocations”. In: *Philosophical Magazine* 86.28 (Oct. 2006). Publisher: Taylor & Francis, pp. 4439–4458. ISSN: 1478-6435. DOI: 10.1080/14786430600724496 (cit. on p. 26).

[54] C. Blanc and M. Kléman. “Curvature walls and focal conic domains in a lyotropic lamellar phase”. In: *The European Physical Journal B - Condensed Matter and Complex Systems* 10.1 (May 1999), pp. 53–60. ISSN: 1434-6036. DOI: 10.1007/s100510050829. URL: https://doi.org/10.1007/s100510050829 (cit. on p. 27).

[55] Jean-Philippe Michel et al. “Optical gratings formed in thin smectic films frustrated on a single crystalline substrate”. en. In: *Physical Review E* 70.1 (July 2004), p. 011709. ISSN: 1539-3755, 1550-2376. DOI: 10.1103/PhysRevE.70.011709. URL: https://link.aps.org/doi/10.1103/PhysRevE.70.011709 (visited on 10/20/2021) (cit. on pp. 27–29, 31, 32, 35).

[56] E. Lacaze et al. “Ordered interfaces for dual easy axes in liquid crystals”. In: *Soft Matter* 7.3 (2011). Publisher: The Royal Society of Chemistry, pp. 1078–1083. DOI: 10.1039/C0SM00727G. URL: http://dx.doi.org/10.1039/C0SM00727G (cit. on p. 27).

[57] Bruno Zappone et al. “Analogy between periodic patterns in thin smectic liquid crystal films and the intermediate state of superconductors”. In: *Proceedings of the National Academy of Sciences* 117.30 (2020), pp. 17643–17649 (cit. on p. 27).

[58] I. R. Nemitz et al. “Observations of a streak texture in the hybrid-aligned smectic-C phase”. en. In: *Soft Matter* 14.3 (Jan. 2018). Publisher: The Royal Society of Chemistry, pp. 460–469. ISSN: 1744-6848. DOI: 10.1039/C7SM02129A. URL: Self-Assembly%20of%20Nanostructures%E2%80%9D.%20In:%20Self-Assembly%20of%20Nanostructure (visited on 05/20/2021) (cit. on pp. 27, 28, 33).

[59] Bruno Zappone et al. “Self-ordered arrays of linear defects and virtual singularities in thin smectic-A films”. en. In: *Soft Matter* 7.3 (2011), pp. 1161–1167 (cit. on pp. 28, 34).

[60] Haifa Jeridi et al. “Unique orientation of 1D and 2D nanoparticle assemblies confined in smectic topological defects”. en. In: *Soft Matter* 18.25 (June 2022). Publisher: The Royal Society of Chemistry, pp. 4792–4802. ISSN: 1744-6848. DOI: 10.1039/D2SM00376G. URL: https://pubs.rsc.org/en/content/articlelanding/2022/sm/d2sm00376g (visited on 08/17/2022) (cit. on pp. 28, 29, 31, 32).

[61] O Parodi. “A possible magnetic transition in smectics A”. In: *Solid State Communications* 11.11 (1972), pp. 1503–1507. ISSN: 0038-1098. DOI: https://doi.org/10.1016/0038-1098(72)90509-1. URL: https://www.sciencedirect.com/science/article/pii/0038109872905091 (cit. on p. 32).

[62] C. Allet, M. Kleman, and P. Vidal. “Striped patterns in a thin droplet of a smectic C phase”. en. In: *Journal de Physique* 39.2 (1978), pp. 181–188. ISSN: 0302-0738. DOI: 10.1051/jphys:01978003902018100. URL: http://www.edpsciences.org/10.1051/jphys:01978003902018100 (visited on 04/26/2023) (cit. on pp. 32, 33).

[63] Jean-Philippe Michel et al. “Structure of smectic defect cores: X-ray study of 8CB liquid crystal ultrathin films”. In: *Physical review letters* 96.2 (2006). Publisher: APS, p. 027803 (cit. on pp. 32, 35).

[64] Emmanuelle Lacaze et al. “Planar anchoring and surface melting in the smectic- A phase”. en. In: *Physical Review E* 76.4 (Oct. 2007), p. 041702 (cit. on p. 32).

[65] “Composites cristaux liquides/nanoparticules, synergies entre matière molle et propriétés électroniques de nanoparticules”. PhD thesis (cit. on p. 32).

[66] Coursault Delphine. “Décoration de réseaux linéaires de défauts smectiques par des nanoparticules d’or.” PhD thesis. Paris: Université Pierre et Marie Curie, 2013 (cit. on p. 33).

[67] Jingmin Xia et al. “Structural Landscapes in Geometrically Frustrated Smectics”. In: *Physical Review Letters* 126.17 (Apr. 2021). Publisher: American Physical Society, p. 177801. DOI: 10.1103/PhysRevLett.126.177801. URL: https://link.aps.org/doi/10.1103/PhysRevLett.126.177801 (visited on 09/17/2023) (cit. on p. 35).

[68] Syou-P’heng Do et al. “Interactions Between Topological Defects and Nanoparticles”. English. In: *Frontiers in Physics* 7 (2020). Publisher: Frontiers. ISSN: 2296-424X. DOI: 10.3389/fphy.2019.00234. URL: https://www.frontiersin.org/articles/10.3389/fphy.2019.00234/full (visited on 05/13/2021) (cit. on p. 35).

[69] George Cordoyiannis et al. “Different modulated structures of topological defects stabilized by adaptive targeting nanoparticles”. In: *Soft Matter* 9.15 (2013). Publisher: The Royal Society of Chemistry, pp. 3956–3964. DOI: 10.1039/C3SM27644A. URL: http://dx.doi.org/10.1039/C3SM27644A (cit. on p. 35).

[70] Brigita Rožič et al. “Oriented Gold Nanorods and Gold Nanorod Chains within Smectic Liquid Crystal Topological Defects”. In: *ACS Nano* 11.7 (July 2017). Publisher: American Chemical Society, pp. 6728–6738. ISSN: 1936-0851. DOI: 10.1021/acsnano.7b01132. URL: https://doi.org/10.1021/acsnano.7b01132 (cit. on p. 35).

[71] Apiradee Honglawan et al. “Synergistic assembly of nanoparticles in smectic liquid crystals”. In: *Soft Matter* 11.37 (2015). Publisher: The Royal Society of Chemistry, pp. 7367–7375. DOI: 10.1039/C5SM01458A. URL: http://dx.doi.org/10.1039/C5SM01458A (cit. on p. 35).

[72] Amine Missaoui et al. “Energetics of topographically designed Smectic-A oily streaks”. In: *Soft Matter* 19.20 (2023). Publisher: The Royal Society of Chemistry, pp. 3733–3738. DOI: 10.1039/D3SM00306J. URL: http://dx.doi.org/10.1039/D3SM00306J (cit. on p. 35).

# Chapter 2

# X-ray diffraction of smectic liquid crystal

*Somewhere, something incredible is waiting to be known*

– Carl Sagan

## Contents



## Contents


2.1 Introduction . . . 45
2.2 X-ray diffraction from a 3D structure . . . 46
2.2.1 Scattered intensity from a single isolated atom . . . 46
2.2.2 Scattered intensity from an ensemble of atoms . . . 47
2.2.3 3D crystal . . . 48
2.3 Peierls-Landau instability . . . 53
2.4 X-ray scattering of perfectly oriented smectic A liquid crystal . . . 54
2.5 Finite-size Effects on the structure factor of the smectic A liquid crystal . . . 56
2.6 The X-ray scattering of distorted smectic A liquid crystal films . . . 57
2.6.1 Smectic ordering in a silica aerogel . . . 57

## 2.1 Introduction

My thesis was focused on the study of oily streaks using synchrotron X-ray scattering. Consequently this chapter is devoted to an overview of X-ray scattering studies that focused in particular on smectic A phase. I will give an review on studies in our group on the intimate structure of the oily streaks using X-ray scattering.

X-rays are high-energy electromagnetic waves which have a wavelength between $0.01 - 10$ nm and energy between 124 eV and 124 KeV. This X-ray radiation can be produced using X-ray tubes or synchrotron facilities. The later are designed to generate electromagnetic radiation from the far infrared to the hard X-ray regime as shown in figure 2.1 (b). The third-generation synchrotron light sources are capable of producing $10^{12}$ times higher brilliance than laboratory-based sources [1]. During my thesis, we conducted experiments using the X-ray beam from Soleil synchrotron, a third-generation synchrotron facility. The synchrotron facility is a particular type of cyclic particle accelerator. One of its main components is a ring-shaped vacuum-filled pipe surrounded by magnets (figure 2.1 (a)). Synchrotron radiation is produced when an electron accelerates, either by changing

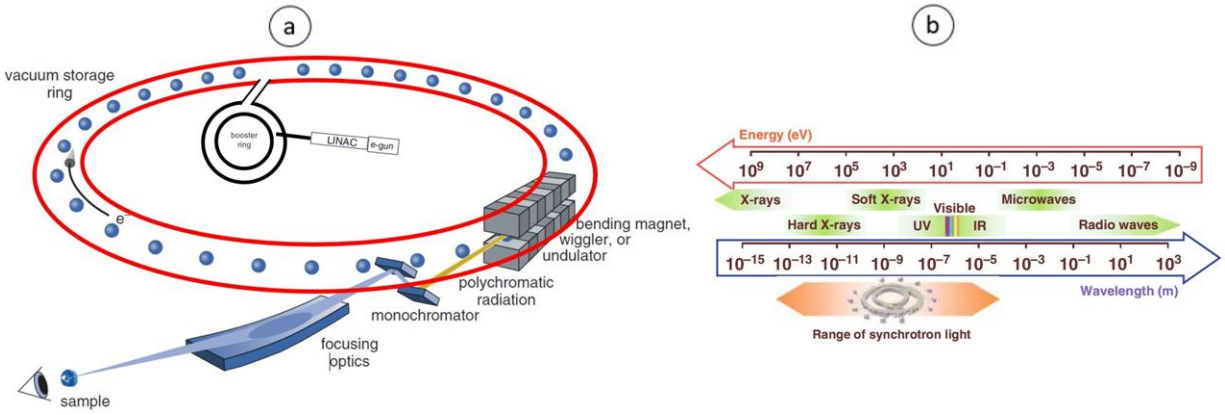


Figure 2.1: (a) A schematic of the most important components of a third-generation synchrotron. Electrons from a source (e.g. a heated filament in an electron gun) are accelerated in a linear accelerator (linac) into an evacuated booster ring (the black ring inside the storage ring), where they undergo further acceleration. Accelerated electrons in the evacuated storage ring emitting electromagnetic (synchrotron) radiation as their direction is changed by bending magnets, wigglers, or undulators [2]. (b) Synchrotron radiations range from the far infrared to the hard X-ray regime

the speed or direction of its motion using bend magnets to steer them in a closed path or special insertion magnet devices (wigglers or undulators) that keep an average straight trajectory [2].

At the beamline, tangential to the storage ring, the radiation is normally (but not always) monochromated and focused using X-ray optics onto a sample. The beamlines are designed for specific applications. For instance, we have used an X-ray beam of energy 18.4 keV and beam size of 300 $\mu m^2$ on the SIXS beamline which is dedicated to the structural characterization of surfaces, interfaces, as well as nano-objects in controlled environments by means of surface-sensitive X-ray scattering techniques, such as Grazing Incidence X-ray Diffraction (GIXD), X-ray Reflectivity (XRR), Grazing Incidence Small Angle X-ray Scattering (GISAXS) and Transmission Small Angle X-ray Scattering (TSAXS). We have used the GISAXS and TSAXS in an helium gas environment aimed at protecting the liquid crystal from X-ray damages.

The interaction of X-rays radiation with material depends on the X-ray's energy and the material's composition but poorly on its chemical properties since the photon energy is much higher than the chemical binding energy. These X-rays radiation can interact with material through transmission, absorption, and scattering. The latter can be inelastic such as Compton scattering. In this case, the scattered waves' wavelength differs from that of the incident waves. Such scattering is incoherent and cannot produce an interference phenomenon, so it contains information on the structure of the scattering material only at short scale. The X-ray scattering can also be elastic, i.e., the incident and scattered waves have the same wavelength. Elastically scattered beams are coherent with incident one and can produce interferences. Therefore they are helpful for the determination of the structure of the crystal or liquid crystal material [3]. Since liquid crystal materials, particularly smectic A materials, have crystalline properties; we will start in the section 2.2 of this chapter with X-ray diffraction of a 3D crystalline structures I will

then describe how it is related to a system of flat layers of smectic A liquid crystal film. In section 2.3, I will describe the Peierls-Landau instability and in the next two sections, I discussed its impact on X-ray diffraction of smectic A liquid crystals. In particular, I will describe different works that have been done on both the ideal smectic samples system (in section 2.4) and real smectic samples. Finally, in section 2.6, I will reviewed different examples of the X-ray scattering of distorted smectic A liquid crystal films focusing on the so-called oily streaks.

## 2.2 X-ray diffraction from a 3D structure

### 2.2.1 Scattered intensity from a single isolated atom

When X-rays irradiate a crystalline material, the oscillating electric field $\vec{E} = E_o e^{i(\nu t - \overrightarrow{k_i}.\overrightarrow{r})}$ acts on the charged particles such as atoms and molecules and leads them to oscillate at the same frequency $\nu$. These particles thus behave like small dipoles that radiate the scattered light. Waves emitted from different particles have amplitude and phase and can interfere constructively or destructively. These interferences lead to fringe patterns that contain information on the structure of the scattering material. For constructive interference, the path difference equals an integer multiple of the X-ray wavelength. In this subsection, we will start by looking at the scattered intensity from an isolated atom with many electrons, and then we shall generalize the expression of the scattered intensity.

The scattered light from an free electron interacting with the X-ray, has an electric field given by the Thomson approximation formula shown below

$$\overrightarrow{E_e} = \frac{e^2 \sin(\theta) e^{i(\nu t - \overrightarrow{k_D}.\overrightarrow{r})} E_o}{m_e c^2 r} \tag{2.1}$$

where $E_o$ is the amplitude of the incident electric field, $e$ is the charge of an electron, $m_e$ is the mass of an electron, $c$ is the speed of light and $\vec{k_D}$ is the scattered wave vector. $\theta$ is defined in figure 2.2. The use of the previous formula 2.1 for an atom which has an electron density distribution $\rho$, and an infinitesimal volume $dv$ positioned at $\overrightarrow{r}$ from the origin, scatters an electric field amplitude $dE_s$ (in equation 2.2) at any point $M$ at distance $\overrightarrow{R}$ from the origin as shown in figure 2.2 and $R = \overrightarrow{R}$. It is a standard approximation in X-ray scattering and leads to

$$dE_s = \frac{e^2 \sin(\theta) e^{i(\nu t - \overrightarrow{k_D}.\overrightarrow{R'})} E_o}{m_e c^2 R'} \rho(\vec{r}) dv e^{i(-\vec{k_i}.\vec{r})} \tag{2.2}$$

where $\overrightarrow{R'} = \overrightarrow{R} - \overrightarrow{r}$.

This infinitesimally small scattered amplitude can be written as

$$dE_s = \frac{e^2 \sin(\theta) e^{i(\nu t - \overrightarrow{k_D}.(\overrightarrow{R} - \overrightarrow{r}))} E_o}{m_e c^2 R'} \rho(\vec{r}) dv e^{i(-\vec{k_i}.\vec{r})}$$

$$\implies dE_s = \frac{e^2 \sin(\theta) e^{i(\nu t - \overrightarrow{k_D}.\overrightarrow{R})} E_o}{m_e c^2 R'} \rho(\vec{r}) dv e^{i(\vec{k_D}.\vec{r})} e^{i(-\vec{k_i}.\vec{r})}$$

$$\implies dE_s = \frac{e^2 \sin(\theta) e^{i(\nu t - \overrightarrow{k_D}.\overrightarrow{R})} E_o}{m_e c^2 R'} \rho(\vec{r}) e^{i(\vec{q}.\vec{r})} dv$$

with $\vec{q} = \vec{k_D} - \vec{k_i}$ and $r \ll R$. $\vec{K_i}$ is the incident wave vector. The total scattered amplitude from the single isolated atom can then be obtained by integrating over the whole region around point $M$ as follow

$$E_s = \frac{e^2 \sin(\theta) e^{i(\nu t - \overrightarrow{k_D}.\overrightarrow{R})} E_o}{m_e c^2 R} \int \rho(\vec{r}) e^{i(\vec{q}.\vec{r})} dv = E_e \times FT(\rho(\overrightarrow{r})) \text{ with } E_e \text{ the electric field due to an isolated electron.} \tag{2.3}$$

The total scattered amplitude is proportional to the Fourier transform of the spatial distribution of electrons, the electronic density, i.e., $FT(\rho(\overrightarrow{r}))$. It is known as the atomic scattering factor and is a measure of the scattering amplitude of a wave by an isolated atom. In the following we will call it $f_i$, where $i$ denotes the index of the $i^{th}$atom.

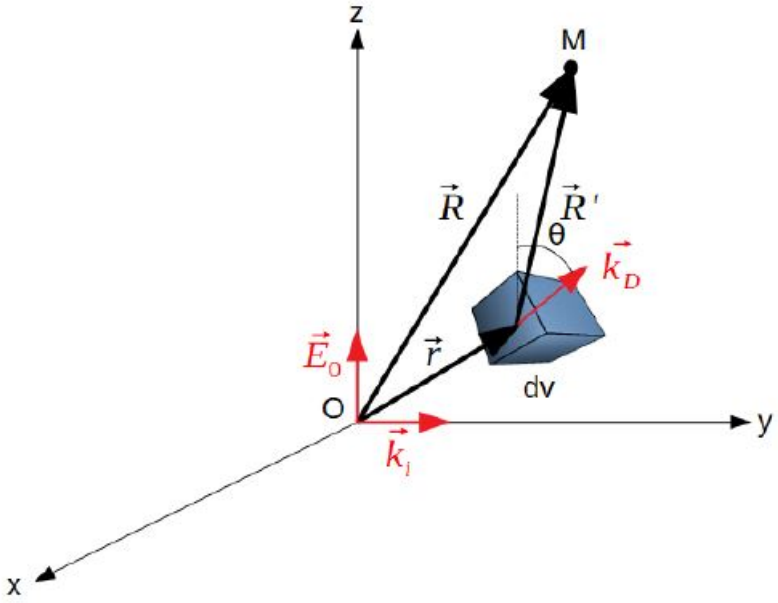


Figure 2.2: Schematized illustration of scattering from an infinitesimal volume $dv$. The electric field $dE_D$ is calculated on an arbitrary point $M$.

### 2.2.2 Scattered intensity from an ensemble of atoms

For a case of an ensemble of $N$ atoms positioned at $R_i, i = 1, \ldots, N$, let's assume that we work under the kinematic diffraction so that the absorption and multiple scattering are neglected. Let's use equation 2.3 to calculate the total intensity scattered by the arbitrary ensemble of atoms. The total amplitude scattered by the ensemble of atoms is given by

$$A(\vec{q}) = \sum_{i=1}^{N} E_e \int \rho_i(\vec{r}) e^{i(\vec{q}\cdot\vec{r_i})} dv \tag{2.4}$$

It is equal to

$$E_e \sum_{i=1}^{N} FT(\rho_i(\vec{r})) \tag{2.5}$$

The total scattered intensity is

$$I_s = E_e.E_e^* \left( \sum_{i=1}^{N} FT(\rho_i(\vec{r})) \right) \left( \sum_{i=1}^{N} FT(\rho_i(\vec{r})) \right)^* \tag{2.6}$$

The Fourier transform of a sum of functions is equal to the sum of Fourier transform of individual functions. Hence we can write 2.6 as

$$I_s = |E_e|^2 \left( FT(\sum_{i=1}^{N}(\rho_i(\vec{r}))) \right) \left( FT(\sum_{i=1}^{N}(\rho_i(\vec{r}))) \right)^* \tag{2.7}$$

This can be written as

$$I_s = |E_e|^2.FT[\rho^{'}(\vec{r})]FT[\rho^{'}(\vec{r})]^*$$

The equation 2.4 becomes

$$I_s = |E_e|^2 \cdot FT[G(\vec{r})] \tag{2.8}$$

where $G(\vec{r}) = \rho^{'}(\vec{r}) \circledast \rho^{'}(\vec{r})^*$ is a pair-correlation function. The structure factor $S_{Bragg}(\vec{q})$ is defined as a normalized intensity [4, 5, 6]. The normalization factor for an ensemble of atom is the square of the total amplitude scattered by all electron. For an ensemble of identical atoms, $G(\vec{r}) = N^2 \rho_i(\vec{r}) \circledast \rho_i(\vec{r})^*$ and the structure factor is given by

$$S_{Bragg}(\vec{q}) = \frac{I_s}{|NE_e|^2} = FT[G(\vec{r})] \tag{2.9}$$

The structure factor is the Fourier transform of a pair-correlation function $G(\vec{r})$ [7, 8].

$$S_{Bragg}(\vec{q}) = \int G(\vec{r}) e^{i\vec{q}.\vec{r}} d\vec{r} \tag{2.10}$$

### 2.2.3 3D crystal

The intensity of the scattering peaks is determined by the arrangement of atoms in the entire crystal. Here the magnitude of the transferred wave vector is also known as the scattering vector and is given by $\vec{q} = \vec{k_D} - \vec{k_i}$ as defined above. Consider a 3D crystal formed by periodic 3D array of layers with finite number of scatters in each layer. For example, these scatterers may be atoms. Positions of atoms in a crystal are defined by considering that they form layers with periodic structure and long-range translational symmetry. These position are given by

$$\begin{gathered} \vec{r_l} = \vec{R} + \vec{r} \\ \begin{cases} \vec{R} = p\vec{l} + t\vec{j} + w\vec{k} \\ \vec{r} = x_i\vec{l} + y_i\vec{j} + z_i\vec{k} \end{cases} \end{gathered} \tag{2.11}$$

$R$ is a lattice vector, $r_l$ is the position of an atom in the initial unit cell. The scattering amplitude from crystalline materials composed of atoms can be written in general as [9, 10, 11]

$$A^{crystal}(\vec{q}) = \sum_{l}^{AllAtoms} f_l(\vec{q}) e^{i\vec{q}.\vec{r_l}}$$

$$A^{crystal}(\vec{q}) = \sum_{\vec{R}+\vec{r}}^{Allatoms} f_m(\vec{q}) e^{i\vec{q}.(\vec{R}+\vec{r})}$$

$$A^{crystal}(\vec{q}) = \overbrace{\sum_{n}^{}}^{Lattice} e^{i\vec{q}\vec{R}} \overbrace{\sum_{m}^{}}^{Unitcell} f_m(\vec{q}) e^{i\vec{q}\vec{r}} \tag{2.12}$$

The equation 2.12 becomes

$$A^{crystal}(\vec{q}) = F \overbrace{\sum_{n}^{}}^{Lattice} e^{i\vec{q}\vec{R}} \tag{2.13}$$

where $F = \overbrace{\sum_{m}^{}}^{Unitcell} f_m(\vec{q}) e^{i\vec{q}\vec{r}}$ is the unit cell form factor. and $f_m$ is the atomic form factor. Using equation 2.13 we can calculate the total scattered amplitude from this 3D crystal.

$$A^{crystal}(\vec{q}) = F \sum_{n,t,w} e^{i\vec{q}\vec{R}} \tag{2.14}$$

$$A^{crystal}(\vec{q}) = F\sum^{N} e^{ip\vec{q}\vec{l}}\sum^{T} e^{i\vec{q}t\vec{j}}\sum^{W} e^{i\vec{q}w\vec{k}} = A_N A_T A_W \tag{2.15}$$

Let's start in the direction $\vec{l}$. Let us take the position $x_o$ as the origin of the space, and other scatters are positioned at $d$, $2d$, $3d$, $4d$, ...,$Nd$ where $d$ is the interlayer period in $l$ direction. In other words $p = xo + nd$

$$A_N = F\sum^{N} e^{iq(x_O+nd)} = F\Bigg[e^{iqx_O} + e^{iq(x_O+d)} + e^{iq(x_O+2d)} + e^{iq(x_O+3d)} + e^{iq(x_O+4d)} + e^{iq(x_O+5d)} + e^{iq(x_O+6d)} + \cdots + e^{iq((x_O+(N-1)d)}\Bigg] \tag{2.16}$$

$N$ is the number of layers, $q$ is the projection of the wave vector transfer along $\vec{l}$,

$$A_N = F\sum^{N} e^{iq(x_O+md)} = Fe^{iqx_O}\Bigg[1 + e^{iq(d)} + e^{iq(2d)} + e^{iq(3d)} + e^{iq(4d)} + e^{iq(5d)} + e^{iq(6d)} + \cdots + e^{iq(N-1)d}\Bigg] \tag{2.17}$$

let's define $b = e^{iqd}$, then the equation 2.17 becomes

$$A_N = Fe^{iqx_O}\Big(1 + b + b^2 + ... + b^{N-1}\Big)$$

$$A_N - bA_N = Fe^{iqx_O}\Big(1 - b^N\Big) \iff A(1-b) = Fe^{iqx_O}\Big(1 - b^N\Big)$$

$$A_N = Fe^{iqx_O}\Big(\frac{1-b^N}{1-b}\Big) = Fe^{iqx_O}\Big(\frac{1-(e^{iqd})^N}{1-e^{iqd}}\Big)$$

$$A_N = Fe^{iqx_O}\Big[\frac{e^{\frac{iqd(N-1)}{2}}(e^{-\frac{iqdN}{2}} - e^{\frac{iqdN}{2}})}{(e^{-\frac{iqd}{2}} - e^{\frac{iqd}{2}})}\Big] \tag{2.18}$$

$$A_N = F\exp\Bigg\{\frac{iq\Big(2x_o + (N-1)d\Big)}{2}\Bigg\}\frac{\sin(\frac{qdN}{2})}{\sin(\frac{qd}{2})}$$

$I = A_N A_N^*$ as results,

$$I = FF^*\frac{\sin^2(\frac{qdN}{2})}{\sin^2(\frac{qd}{2})} \tag{2.19}$$

where $FF^* = \mid F \mid^2 = F^2$

$$\implies I = F^2\frac{\sin^2(\frac{qdN}{2})}{\sin^2(\frac{qd}{2})} \tag{2.20}$$

The structure factor $S_{Bragg}(\vec{q})$ is defined as a normalized intensity [4, 5, 6]. The normalization factor for many atoms system such as this 3D crystal is $\frac{1}{\sum_{i=1}^{N}(F_i^2)} = \frac{1}{NF^2}$ with $F$ is the unit cell form factor. So,

$$S_{Bragg}(\vec{q}) = \frac{1}{N}\frac{\sin^2(\frac{qdN}{2})}{\sin^2(\frac{qd}{2})} \tag{2.21}$$

We eventually arrive at the expression of the total scattered intensity as a function of both the form factor and the structure factor as

$$I = NF^2 S_{Bragg}(\vec{q}) \tag{2.22}$$

The structure factor defines the so-called Bragg peaks which present a Gaussian form as shown in figure 2.3. Let's look at the

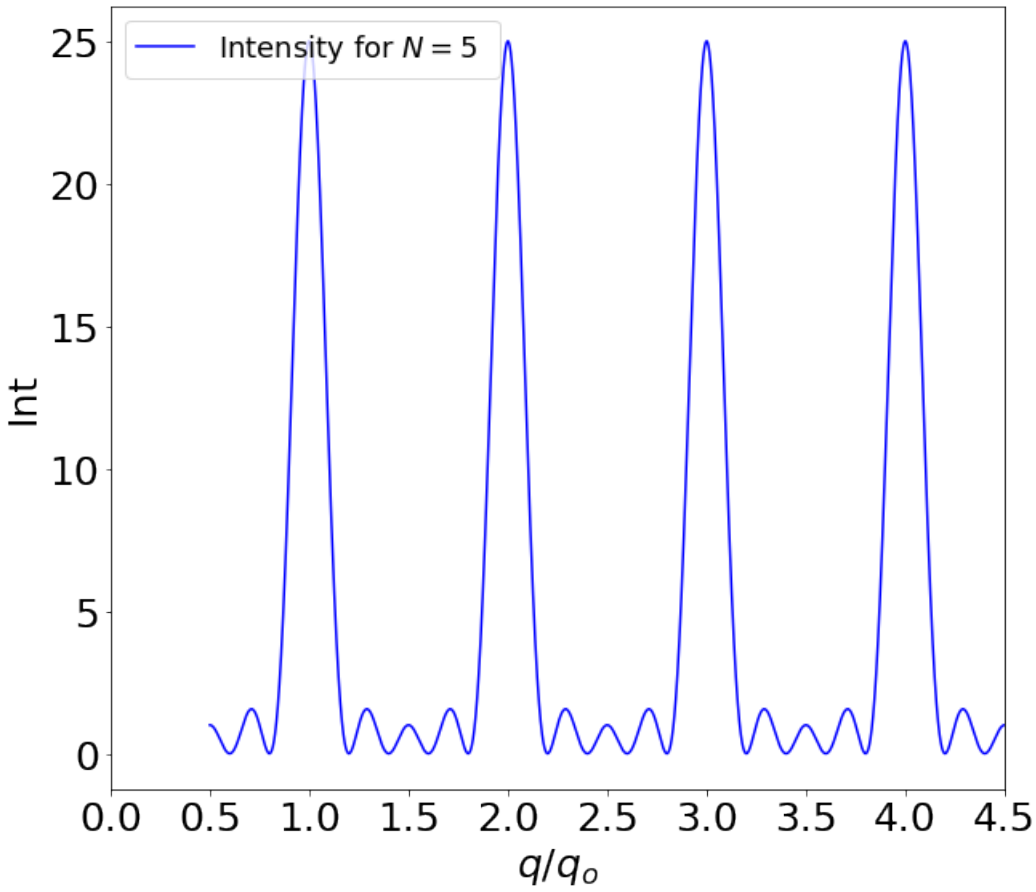


Figure 2.3: The calculated of intensity as function the magnitude wave vector transfer $q$ with $N = 5$.

Bragg position $q_{max}$ of the maximum intensity using equation 2.22. The maximum intensity is when this quantity is an even multiple of $\pi$, i.e., $\frac{q_{max}d}{2} = k\pi$ where $k = 1, 2, 3, ...$ and $d = \frac{2\pi}{q_m}$. $q_m$ is the Bragg wave-vector transfer. These values give $\sin\frac{q_{max}d}{2} = 0$. Hence the position of the maximum intensity can be obtained using

$$q_{max} = kq_m \tag{2.23}$$

The equation 2.21 gives an indeterminate case as $q$ approach the $q_{max}$. After applying twice the L'Hôpital's rule on it we obtained $S_{Bragg}(\vec{q}) = N$. Using this value in the equation 2.22, we obtain a maximum intensity $I_{max} = N^2F^2$ at positions $q_{max} = kq_m$.

The intensity peak gets as much as stronger and narrower as the number $N$ of the scattering center increases.

Our next step is to find a relationship between the number of the diffracting smectic layers and the width of the peak of diffracted intensity of Equation 2.22.

Let's now introduce a new parameter in this equation $x = k\pi - \frac{qd}{2}$ in the equation 2.36 and it becomes equation 2.24 to be used to calculate the relationship between the number of scattering layers and the Full Width at Half Maximum (FWHM).

$$I = NF^2\left(\frac{\sin N(k\pi - x)}{\sin(k\pi - x)}\right)^2 = NF^2\left(\frac{\sin Nx}{\sin x}\right)^2 \tag{2.24}$$

The intensity becomes maximum when $x \to 0$ i.e $\frac{qd}{2} \to k\pi$ which is gives the position of maximum intensity $q_{max} = kq_m$. The Mac-Lauren's expansion of sinus function up to the second term is

$$\sin x = (x) - \frac{(x)^3}{3!} + \frac{(x)^5}{5!} - ...$$

Other terms are neglected since they are too small when $x \to 0$. We can use this expansion in equation 2.24 to get the width of the peak of intensity and its relationship with the number of diffracting layers. So

$$I = F^2\left(\frac{Nx - \frac{(Nx))^3}{6}}{x - \frac{(x)^3}{6}}\right)^2 \iff I = F^2N^2\left(\frac{1 - \frac{(Nx)^2}{6}}{1 - \frac{(x)^2}{6}}\right)^2$$

Expanding both parts of the fraction, we neglect the term to the power 4 since they are much smaller as $x \to 0$. We get this equation

$$I(x) = F^2N^2\left(\frac{1 - \frac{(xN)^2}{3}}{1 - \frac{x^2}{3}}\right) \tag{2.25}$$

From this equation 2.25, we can write the intensity at Full Width Half Maximum (FWHM) as

$$\begin{aligned}
F^2N^2\left(\frac{1 - \frac{(xN)^2}{3}}{1 - \frac{x^2}{3}}\right) &= F^2\frac{N^2}{2} \\
\implies \left(1 - \frac{(xN)^2}{3}\right) &= \frac{1}{2}\left(1 - \frac{x^2}{3}\right) \\
2 - \frac{2(xN)^2}{3} &= 1 - \frac{x^2}{3} \\
\implies 1 &= \frac{x^2}{3}(-1 + 2N^2) \\
1 &= \frac{x^2}{3}(2N^2) \\
x &= \sqrt{\frac{3}{2}\frac{1}{N}}
\end{aligned}$$

Since $x = k\pi - \frac{qd}{2}$ then $\frac{qd}{2} = k\pi \pm \sqrt{\frac{3}{2}\frac{1}{N}}$, these two values are around the position of the maximum intensity on the Gaussian Peak. Hence full width at half maximum can be obtained

$$\Delta q = \frac{\sqrt{6}q_m}{\pi N}$$

and the number of diffracting layers be given by

$$N = \frac{\sqrt{6}}{\pi}\frac{q_m}{\Delta q} \tag{2.26}$$

Let's consider our Gaussian function

$$G(x) = Ae^{(\frac{x-pos}{\sigma_q})^2} \tag{2.27}$$

Where the standard parameter $\sigma_q = \sigma'\sqrt{2}$ is related to the full width at half maximum as

$$FWHM = 2\sigma'\sqrt{2\ln 2} \iff FWHM = 2\sigma_q\sqrt{\ln 2} \tag{2.28}$$

Experimental determination of the Gaussian Peak of intensity, leads to the Full width at Half maximum which is related to the fitting parameter for $\sigma_q$ finally giving:

$$\Delta q = 2\sigma_q\sqrt{\ln 2} \tag{2.29}$$

This gives us finally

$$N = \frac{\sqrt{6}}{4\pi}\frac{q_m}{\sigma\sqrt{\ln 2}} \tag{2.30}$$

### Integrated Intensity

Since the Bragg peaks of intensity as a function of the $q$ in figure 2.3 have a Gaussian form, we can use the Gaussian integral to calculate the integrated intensity. The Bragg intensity in the above peak is given

$$I(q) = I_{max}e^{-(\frac{q-q_m}{\sigma_q})^2} \tag{2.31}$$

The integrated intensity is given by

$$I_{integ}(q) = I_{max}\int_{-\infty}^{+\infty} e^{-(\frac{q-q_m}{\sigma_q})^2}dq \tag{2.32}$$

let's denote $x = \frac{q-q_m}{\sigma_q}$, so this equation 2.32 can be written as

$$I_{integ}(q) = I_{max}\sigma q\int_{-\infty}^{+\infty} e^{-x^2}dx \tag{2.33}$$

Using the famous Gaussian integral, we obtain the integrated intensity as

$$I_{integ}(q) = I_{max}\sigma_q\sqrt{\pi} \tag{2.34}$$

we have seen in the equation 2.29 that the full width at half maximum is related to the $\sigma_q$ by $\Delta q = 2\sigma_q\sqrt{\ln 2}$ and so the integrated intensity of a Bragg peak is given

$$I_{integ}(q) = I_{max}\Delta q(\frac{\sqrt{\pi\ln 2}}{2\ln 2}) \tag{2.35}$$

The integrated intensity is thus proportional to the product of the maximum intensity with $\Delta q$. Since the maximum intensity is proportional to the $N^2$. and the $\Delta q$ is proportional to $\frac{1}{N}$ (equation 2.26), hence the integrated intensity is proportional to the $N$.

Now that we finish the calculation in one direction $\vec{l}$, the remaining directions in the equation 2.15 give the same results. So we can write the total scattered intensity in 3D as follows

$$I \propto \left(\frac{\sin^2(\frac{qdN}{2})}{\sin^2(\frac{qd}{2})}\right)\left(\frac{\sin^2(\frac{qvM}{2})}{\sin^2(\frac{qv}{2})}\right)\left(\frac{\sin^2(\frac{qwT}{2})}{\sin^2(\frac{qw}{2})}\right) \tag{2.36}$$

where $d$, $v$, and $w$ are the period in each direction and $N$, $M$, and $T$ are the total number of layers in each direction. The maximum intensity in each direction is proportional to $N^2$, $M^2$, and $T^2$ and the full width at half maximum of the peak follow the equation 2.26. The integrated intensity for a $3D$ crystal is thus proportional the $N$, $M$, and $T$ respectively in the 3 directions.

### Smectic liquid crystal materials

The smectic liquid crystal material has a 1D quasi-long range translational order. Inside each smectic layer the molecules do not have crystalline order. So all the above calculations for a 1D system correspond to a perfectly oriented smectic A liquid crystal system. In this case, the equation 2.22 corresponds to the intensity scattered by $N$ perfectly flat smectic layers. $F$ is the form factor of an entire smectic later, where the surface of the smectic layer is taken into account in $F$.The $S_{Bragg}(\vec{q})$ corresponds to the smectic structure factor. In the following section, we will use the definition of smectic structure factor given in equation 2.10. The number of scattering smectic layers $N$ is expected to be related to the FWHM of the peak of the scattered intensity by equation 2.26 where $q_m = \frac{2\pi}{d}$ with $d$ the smectic A interlayer distance. The integrated Bragg intensity of $N$ perfectly periodic flat smectic layers is proportional to $N$. Would this relationship between the number of scattering smectic layers and the integrated Bragg intensity or the full width at half maximum be still the same for our system which is made of rotating smectic layers ? The answer to this question would help in the rest chapters of this manuscript because it will help us to reconstruct the internal structure of the oily streaks in chapter 4 sections 4.7 and 4.9. Each oily streak can be considered as in 3D where the third orientation doesn't change. In next section, I will review various works that have been performed on both ideal and real smectic A material.

## 2.3 Peierls-Landau instability

3D solid crystals exhibit 3D long-range translational order and present layer fluctuations of amplitude smaller than the lattice spacing. When the dimensionality decreases, these thermal fluctuations become strong and eventually destroy the long-range translational order in either one or two dimensional systems As a result the bodies with one or two dimensional periodic density cannot exist [12]. Hence, the smectic A phase should not exist since its long-range translational order is destroyed by the thermal fluctuation modes related to bending and compression of the layers (Fig. 1.6). This result is known as Landau-Peierls instability. In this section, we will review the Landau-Peierls instability that has been described for smectic A. In the next section we will see its implication on the X-ray scattering of the smectic liquid crystal.

Using equation 1.22 of Chapter 1, we can write the total distortion energy[8, 13, 14, 15].

$$\Upsilon = \int dr^3 \left\{ \frac{B}{2} \left[ \frac{\partial u(r)}{\partial z} \right]^2 + \frac{K_1}{2} \left[ \frac{\partial^2 u(r)}{\partial x^2} + \frac{\partial^2 u(r)}{\partial y^2} \right]^2 \right\} \tag{2.37}$$

The integration in equation 2.37 is carried out over the volume of the system. It can be written in Fourier space as a sum of contributions from fluctuations with different wave vectors in Fig. 1.6. To do this, let's denote $FT(\Upsilon) = \tilde{\Upsilon}_q$

$$\tilde{\Upsilon}_q = \frac{1}{2(2\pi)^3} \int dq^3 \left\{ \frac{B}{2} \left[ \frac{\partial (u(q) e^{i\vec{r}\vec{q}})}{\partial z} \right]^2 + \frac{K_1}{2} \left[ \frac{\partial^2 (u(q) e^{i\vec{r}\vec{q}})}{\partial x^2} + \frac{\partial^2 (u(q) e^{i\vec{r}\vec{q}})}{\partial y^2} \right]^2 \right\} \tag{2.38}$$

Using the quantity $\vec{r}\vec{q} = (zq_z + q_\perp(x+y))$ the equation 2.38 becomes

$$\tilde{\Upsilon}_q = \frac{1}{2(2\pi)^3} \int dq^3 \left\{ \frac{B}{2} \left[ \frac{\partial (u(q) e^{i(zq_z + q_\perp(x+y))})}{\partial z} \right]^2 + \frac{K_1}{2} \left[ \frac{\partial^2 (u(q) e^{i(zq_z + q_\perp(x+y))})}{\partial x^2} + \frac{\partial^2 (u(q) e^{i(zq_z + q_\perp(x+y))})}{\partial y^2} \right]^2 \right\} \tag{2.39}$$

After the derivation, the equation 2.39 becomes

$$\tilde{\Upsilon}_q = \frac{1}{2(2\pi)^3} \int dq^3 \left[ Bq_z^2 + Kq_\perp^4 \right] \mid u(\mathbf{q}) \mid^2 \tag{2.40}$$

Using the theorem of energy equipartition [13], we get the mean-square fluctuation to be in real space

$$\langle u(r)^2 \rangle = \frac{k_B T}{(2\pi)^3} \int \frac{d^3 q}{Bq_Z^2 + Kq_\perp^4} \tag{2.41}$$

Fluctuation modes with wavelengths larger than the sample size $L$ normal to the layers (film thickness) and $W$ in the plane of the layers are not possible. Also modes with wavelengths shorter than layers spacing $d$ or the lateral molecular spacing $a_o$ is

not allowed [8]. So the integration boundaries are $\frac{2\pi}{W} \leq q_\perp \leq \frac{2\pi}{a_o}$ and $\frac{2\pi}{L} \leq q_z \leq q_m = \frac{2\pi}{d}$. As $W \gg L$ and $a_o < d$ then $W \to \infty$ and $a_o \to 0$

$$\langle u(r)^2 \rangle = \frac{k_B T}{4\pi^2} \int_0^\infty \int_{L^{-1}}^{q_m} dq_z dq_\perp \frac{q_\perp}{B q_Z^2 + K q_\perp^4} \simeq \frac{k_B T}{8\pi\sqrt{KB}} \ln\left(\frac{L}{p}\right) \tag{2.42}$$

When $L$ goes to infinity, we can see the logarithmic divergence of the mean-squared fluctuations, a result known as Landau-Peierls instability in the limit of $|\psi_o| = 1$ [13]. This divergence of the real-space positional fluctuation leads to the replacement of the Bragg peaks by power-law singularities as we will see below. In the following part of this chapter, I will show the effect of this instability on both idealistic and realistic smectic A systems.

## 2.4 X-ray scattering of perfectly oriented smectic A liquid crystal

To write this part many sources were available. Among them, is the work of Leon Gunther et al. [16] and the other one is the work of Kaganer et al [17]. Both of them are on the X-ray scattering of the smectic liquid crystal.

Let's $S_{Caille}(\vec{q})$ be the static structure factor of a perfectly oriented infinitely large smectic A sample, where $\vec{q} = \vec{K}_i - \vec{K}_s$ is the wave-vector transfer, $K_i$ and $Ks$ are the incident and scattered waves respectively. We have seen that the static structure factor is given by

$$S_{Caille}(\vec{q}) = \int G(\vec{r}) e^{i\vec{q}.\vec{r}} d\vec{r} \tag{2.43}$$

where $G(\vec{r})$ is the smectic pair-correlation function.

In chapter 1 we have seen that the smectic A system is periodic in direction $z$, this allows to develop the density $\rho$ as shown in equation 2.44. For this development we can use the density described in chapter 1 in equation 4.38.

$$\rho(r) = \rho_o + \rho_1 \cos\Big\{q_m \Big[r + u(r)\Big]\Big\} \tag{2.44}$$

Since the smectic layers are fluctuating in z-direction then

$$\Big\langle \rho(r)\rho(0) \Big\rangle - \Big\langle \rho_1^2 \Big\rangle \approx \Big\langle \exp\Big(iq_m \cdot (u(r) - u(0))\Big)\Big\rangle \text{[8, 13, 14]}$$

where $G(\vec{r}) = \Big\langle \exp\Big(iq_m \cdot (u(r) - u(0))\Big)\Big\rangle$ is the displacement-displacement correlation function. In the harmonic approximation this correlation function becomes

$$G(\vec{r}) =< e^{-\frac{1}{2} q_m^2 [u(r) - u(0)]^2} >$$

Where the reciprocal-lattice vector for a smectic domain is $q_m = m(\frac{2\pi}{p})$, $m$ is in integer as defined previously. For the case of perfect crystal materials which have true long-range order $r \to \infty$, then $G(\vec{r})$tends to a constant value. However, as consequence of the Landau-Peierls instability, the liquid crystal materials exhibit exhibit the quasi-long-range order as we have seen in the previous section. The function $G(\vec{r})$ describes the algebraic decay typical for the layer structure of a smectic liquid crystal [7]. This correlation function has been calculated to be [13, 14, 16, 17]

$$G(\vec{r}) = G(\varrho, z) \approx (\frac{2p}{\varrho})^{2\eta} e^{-2\eta\gamma} e^{-\eta E_1(\frac{\varrho^2}{4\lambda z})} \tag{2.45}$$

where $r = z^2 + \varrho^2$ is the position of the layer and $\varrho^2 = x^2 + y^2$. After using the asymptotic expression for the exponential integral [16], the equation 2.45 was written as

$$G(\varrho, z) = \begin{cases} (\frac{d^2}{\lambda z})^\eta e^{(-\eta\gamma)} \propto z^{-\eta}, \varrho \ll \sqrt{(\lambda z)} \\ (\frac{2d}{\varrho})^{2\eta} e^{(-2\eta\gamma)} \propto (\varrho)^{-2\eta}, \varrho \gg \sqrt{\lambda z} \end{cases} \tag{2.46}$$

where $\gamma = 0.5772$ is the Euler's constant, $E_1$ is the exponential integral function. The power-law exponential $\eta$ is given by

$$\eta = (\frac{2\pi m}{d})^2 \frac{k_B T}{8\pi\sqrt{BK}}$$

where $(m = 1, 2, ...$

This exponent is determined by how close $1 - \frac{T}{T_C}$ is to 0 i.e how close the temperature $T$ is close to the phase transition temperature $T_c$. The results of substituting the algebraic decay of the positional correlations in the smectic layers given by equation 2.46 in the equation 2.43 are the power-law singularities (equations 2.47 and 2.48) that replace the smectic Bragg peaks [13, 16, 17].

For longitudinal scan, when $q_\perp = 0$, the structure factor is given by the equation

$$S_{Caille}(q_\perp = 0, q_z) \propto (q_z - q_m)^{-2+\eta} \tag{2.47}$$

We note $Q = q_z - q_m$ is the deviation of the reciprocal-lattice vector $q_m$, from the Bragg wave-vector transfer $q_m$ in the direction parallel to the layer normal. For transverse scan, when $Q = 0$, the structure factor is given by the equation

$$S_{Caille}(q_\perp, q_z = q_m) \propto q_\perp^{-4+2\eta} \tag{2.48}$$

These results are only valid if fluctuations in the layer displacement are smaller than $d$, the interlayer spacing [17]. Otherwise the correlation function $G(r)$ will vanish and hence no structure factor peak would be obtained. We have seen that the phase of the smectic order parameter is related to the layer displacement is proportional $q_m u(\vec{r})$. Thermal fluctuations in the phase of the order parameter in smectic A liquid crystal sample can be inferred from the mean-square fluctuation $\langle |u(r)|^2 \rangle$ of the smectic layers in equation 2.42. They lead to the destruction of the true 1-dimensional long range transitional order in smectic sample. The consequence is the replacement of the Structure factor of $\delta(\vec{q})$ function-type Bragg peaks obtained for a system of long-range positional order of of 3-D crystals, by power-law singularities given in equations 2.47 and 2.48. These two equations were first calculated by $Caille^{'}$ for a perfectly oriented smectic liquid crystal in the harmonic approximation. Als-Nielsen et al. [14, 18] was the first to observe experimentally these intensity distributions of X-ray scattering in form of algebraïc decay of the smectic liquid crystal translational order in the limit of an ideal infinitely large sample of the octyloxy-cyanobiphenyl (8OCB) in smectic A phase.

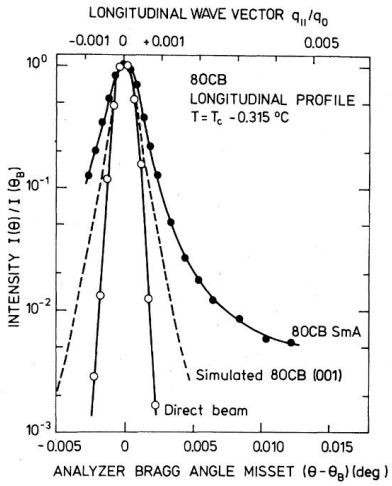


Figure 2.4: Simulated true Bragg peak (dashed line) and experimentally measured (solid circle) line profile of intensity from $1.5mm$ thick 8 OCB in smectic A liquid crystal phase [14] .

They have used a high-resolution X-ray diffraction study of the density wave to prove that the X-ray scattering near $q_m = \frac{2m\pi}{d}$ in the smectic A phase of the (8OCB) can be described by equations 2.47 and 2.48, the consequence of Landau-Peierls instability.

The result are shown in figure 2.4. This figure is showing the direct beam (open circle), the simulated true Bragg peak profile of the 8OCB (dashed line) and the experimentally measured profile of diffuse scattering of the (8OCB) (closed circle).

This measured smectic-A 8OCB liquid crystal diffuse scattering intensity is significantly different from the simulated true Bragg peak and indeed consistent with the predicted power-law singularity form shown in equation 2.47. This result confirms that the smectic A phase has not long-range order but a quasi-long range order.

Kaganer, Petrov, and Samoylova [7] have expanded this theory of X-ray scattering in smectic liquid crystals from ideal to real systems where they have even considered several factors that contribute to the X-ray diffraction line profile in smectic-A liquid crystal such as finite size effect [17]. I will describe the finite size effects in the next section.

## 2.5 Finite-size Effects on the structure factor of the smectic A liquid crystal

So far, we have looked at the calculation on the infinite system as in a case where the X-ray beam impinged on the whole endless sample. However, in practice, our samples have a finite size and the X-ray beam may cover an entire sample or part of it. This finite size refers to an actual size of entire sample or size of domains in it [17]. Gunther, Imry, and Lajzerowics [16] have investigated the effect of finite size on the X-ray intensity scattered by a smectic A liquid crystal sample of finite size. They have found that it is formed by the thermal diffuse scattering given by equations 2.47 and 2.48 in addition with true albeit weak Bragg peak. The later comes into existence because this limitation of the sample size to a finite value or subject to an a external field results in a strong coupling between layers.

The correlation function in equation 2.45 is replaced by an other function $G'(R) = G(R).F_s(R)$ where $F_s(R)$ is the finite smectic structure factor. The structure factor of the smectic finite sample was written in real space as the convolution of the scattering intensity of an infinite sample $S_{kaganer}(\vec{q})$ with the lattice sum for function $F_s(R)$ [17].

$$S_{kaganer}(\vec{q}) \propto \int dRG(R)F_s(R)\exp\{(i\vec{q}R)\} \tag{2.49}$$

For a wave vector in the vicinity of the reciprocal lattice vector $q_m$, the Fourier transform of the finite sample structure factor function $F_s(R)$ is

$$F_s(q_m + Q) = \upsilon^{-2}|s(Q)|^2, \text{where}, |s(Q)|^2 = \prod_{i=1}^{3}\left(\frac{\sin^2(\frac{Q_i L_i}{2})}{\sin^2(\frac{Q_i d}{2})}\right) \tag{2.50}$$

where $Q = q_z - q_m$ and $\upsilon$ is the volume per molecule. $s(Q)$ is the domain-shape function which is the Bragg Peak that we have seen in section 2.2.3. The $L_i = N_i d$ is the domain size in the $i$ direction i.e it can be either x or y or z direction and $N_i$ is the number of smectic layers in either of the directions . For a domain of finite dimension $L = Nd$, the width of Bragg peak is $\Delta Q_i \simeq N^{-1}$ and it is accompanied by tails that are decreasing proportional to $(Q_i)^{-2}$ [17]. They have considered the dimension $L_z$ in the direction normal to the sample and $L' \cong L_x, L_y$ is domain size in the plane of layers. For the case $q_\perp = 0$ and $Q \neq 0$ using the integration over $\varrho$ and then $z$ in the two corresponding parts as shown in the equation 2.47, the result of the X-ray scattering can be written as

$$S_{kaganer}(\vec{q}) \propto D\frac{\lambda^{1-\eta}}{(q_z - q_m)^{-2+\eta}} + F_s(q_m + Q)(L^{'})^{2-2\eta} \tag{2.51}$$

This equation 2.51 displays a Bragg peak of the finite domain or the whole finite sample (second term ) associated with $\Delta Q \propto L_z^{-1}$. The algebraic decay in the first term is associated with tails. $D$ is a numerical constant.

Stamatoff et al. [19] have also observed the lineshape of the first-order diffraction Bragg peak from COB with subtle deviation from the true long-range order (figure 2.5). They observed a peak which had a relatively large tail associated with the strong thermal fluctuation and obeying the power law singularities that we have seen above.

A.N.Zisman et al. [20] have also studied this effect of finite size on 8CB in the smectic A liquid crystal phase. They have carried out an X-ray study in which, in contrast to Caill$e^{'}$ calculation, the fluctuations in the amplitude of the order parameter $|\psi|$ of the smectic A phase was taken into account. In their study, they also considered that the bounded nature of the homogeneous blocks can alter the line shape. They have used the result that we have just seen above on a system with finite-size; for small size blocks, the $\delta-$ function can be replaced by $I(\vec{q}) \sim (sin^2(qL))/q^2$. So, for such a sample the scattered intensity would be expressed in terms of both the latter function and an algebraic decay function just as equation 2.51 .

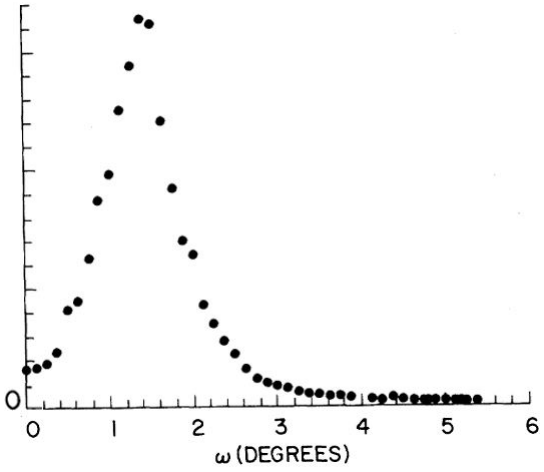


Figure 2.5: Line profile of first-order diffraction intensity from a $1mm$ thick rectangular COB in smectic A liquid crystal phase [19].

The results in this section are showing that for finite size smectic domains or samples, the scattered intensity is formed by the addition of the Bragg peak and the tails. These tails are governed by the power-law exponent parameter $\eta$ which is temperature dependent. The samples that we have used in this thesis are also of finite size and confined between the PVA substrate and air with particularly small thickness. We have worked at room temperature such that the $\eta$ is sufficiently small that the tail can be too small to be ignored. In this case the effects of the Peierls–Landau instability have not displaced the Bragg peaks and we can easily measure these peaks. Moreover, we are interested only in the Bragg peaks (and their widths) which contain information on the structure of our 8CB films. In our experimental data the tails were not only small but also overlapped with the background noise. Therefore, we have filtered them out together with the background noise and we have measured and analyzed only the Bragg's peaks.

## 2.6 The X-ray scattering of distorted smectic A liquid crystal films

### 2.6.1 Smectic ordering in a silica aerogel

Silica gel is a highly porous, noncrystalline type of silicon dioxide (silica) made of nanometer-sized gaps and pores. The 8CB molecules have been confined inside these pores. The confinement of the smectic A liquid crystal film strongly affects its layers ordering [21]. Clark et al. [22] have used X-ray scattering to study the effect on smectic ordering in 8CB incorporated into the pores of a silica aerogel. The pore size was 200Å. They found that the diffraction peaks of the 8CB in the aerogel are broader than those of pure 8CB. The broadening of the peaks in Fig 2.6 shows that long range translational order is replaced by short order as temperature increases. Only smectic short-range order was observed [22, 23, 24]. The aerogel-8CB system contains distribution of finite size domains and so as we discussed in section 2.5 for finite size effect, the curves of intensity in this figure 2.6 were formed by Bragg peak for the $8CB$ smectic A which is accompanied by algebraic decay (background aerogel). The shape of the scattering of this background aerogel can be seen between $1.2\ nm^{-1} < q < 3.0\ nm^{-1}$ at the lowest temperature where there is no smectic peak. This background was fitted by a sum of a power-law plus the background constant $Bq^{-k} + C$ where the $k$ value was fixed at 3.68.

The Bragg peaks for smectic were best fitted by a Lorentzian peak $I(q) \equiv A\{R(q) \circledast \left[1 + (q - q_m)^2\xi^2\right]^{-1}\}$ and the parameters $A, B, C, \xi$ and $q_m = \frac{2\pi}{d}$ were adjustable with the results in figure 2.6 a They found that the 8CB smectic-A layering peak centered at $q_m = 1.98\ nm^{-1}$ was gradually narrowing as temperature decrease and eventually disappeared at $0°C$ being replaced at temperature $-4°C$ by crystalline peaks in range $4.8\ nm^{-1} < q < 14.0\ nm^{-1}$. As temperature increases the thermal fluctuations increases and washed out the long range translational order. It was replaced by the short range order in smectic A. When the temperature increases further, these fluctuations continue to eventually destroy completely the short range

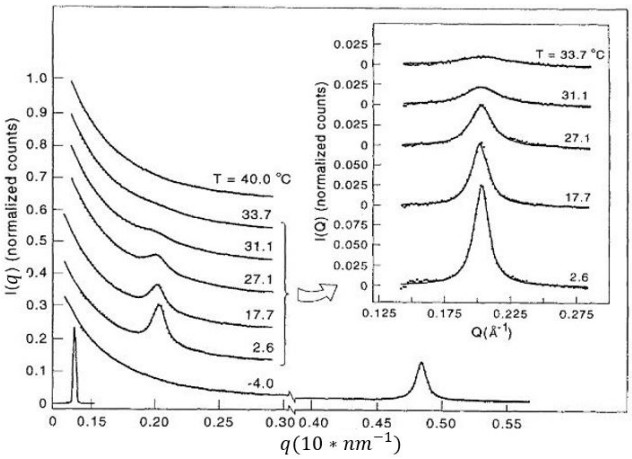


Figure 2.6: Measured X-ray integrated scattered intensity as function of temperature where the $S_{Bragg}(\vec{q})$ is the X-ray structure factor of the aerogel-8CB system. It is from $0.36\frac{g}{cm^3}$ silica aerogel-8CB composite [22].

order. This can be seen in the inset of figure 2.6 where the smectic A peak gradually transforms from narrow and high intensity to the much broader and nearly null intensity peak. This shows that beyond the A-N phase transition temperature the smectic peak completely disappear. There are numerous X-ray scattering study of the confinement of the 8CB systems in aerogel, where similar results were found [22, 23, 24, 25, 26].

### 2.6.2 Review on the construction of the oily-streak model

The confinement of smectic liquid crystal materials is a good candidate to produce and study the topological defects [27]. In the literature described above, there is no work on X-ray diffraction aimed at studying the internal structure of the topological defects that arise as a way to relax from such confinement. The group of Dr. Emmanuelle Lacaze has been working to fill this gap for nearly two decades [28]. For such a purpose, the 8CB molecules have been deposited on different substrates such as molybdenum disulfide ($MoS_2$), mica, and Polyvinyl Alcohol(PVA), all these substrates imposing a planar unidirectional anchoring.

The structure induced by competing boundary conditions (planar unidirectional and homeotropic) has been described in chapter 1. It has been studied using a combination of different but complementary experimental techniques such as polarized optical microscopy, ellipsometry, Atomic force microscopy, and X-ray diffraction. The latter technique is used because of the periodic layered structure of 8CB in the smectic A phase. The group of E. Lacaze used Grazing incident small angle X-ray Scattering (GISAXS) and Transmission Small Angle X-ray Scattering (TSAXS). In this section I will describe the X-ray diffraction results from these studies.

Michel et al. [29] have demonstrated that the oily streaks are formed by flattened hemicylinders. Two cylinder quarters at the edges are formed by smectic layers rotating around the hemicylinder's axis. They are joined by a set of horizontal smectic layers (figure 1.20 , in section 1.3 , chapter 1). To study the internal structure of the oily streaks, they hypothesized that , the normalized scattered Bragg intensity for the wave-vector transfer $\vec{q}$ oriented at an angle $\alpha$ from the substrate was directly proportional to the number of smectic layers whose normal is parallel to $\vec{q}$ (figure 2.7b). For $\alpha = 0^\circ$ the layers are perpendicular to the substrate and for $\alpha = 90^\circ$ they are parallel to the substrate.

#### 8CB deposited on the molybdenite in the air

When the 8CB film was adsorbed on molybdenite ($MoS_2$), the observed scattered intensity is shown in figure 2.7a. It was scattered from a smectic film of thickness 450 nm. The continuous intensity profile, almost constant from $\alpha = 10^\circ$ to $\alpha = 80^\circ$, corresponds to the smectic layers rotating in the two edges of the hemicylinder model shown in figure 2.7b. The intensity in the inset corresponds to $\alpha = 90^\circ$, in other words to the central flat layers. These results are consistent with the model of smectic layers superimposed into flattened hemicylinders with edges made of cylinder quarters and the existence of a large volume of

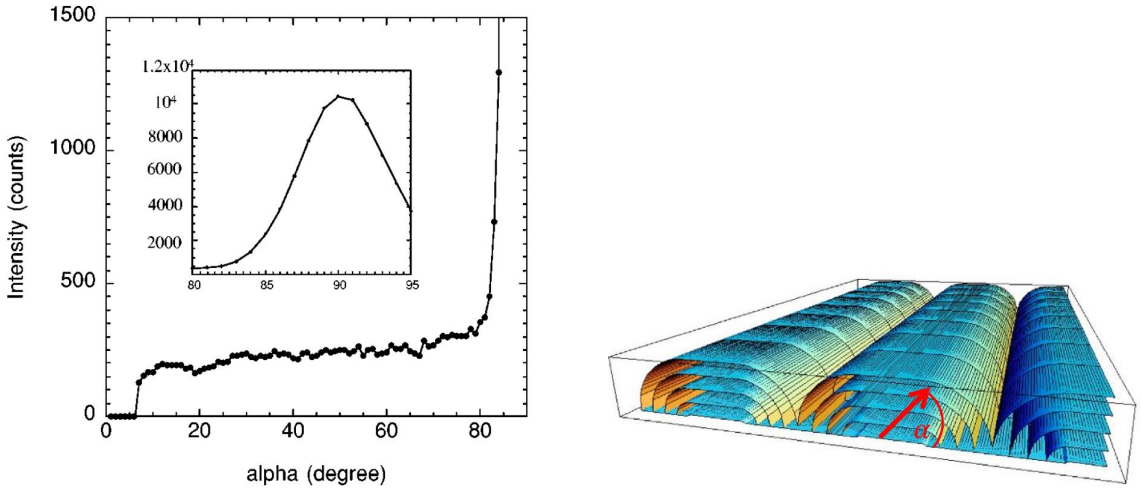


(a) (b)

Figure 2.7: **(a)**. X-ray scattering intensity for a sample of thickness 450 nm measured by continuously rotating the wave vector transfer q between $\alpha = 0°$ to $\alpha = 80°$.The inset corresponds to a zoom on the intensity values around $\alpha = 90°$. **(b)** The hemicylinder mode that agrees with this measured intensity.

smectic layers which contain molecules in the homeotropic geometry (flat smectic layers) the central part of the hemicylinder (See chapter 1, section 1.3). When $\alpha$ is smaller than $7°$ , the incident beam tilt angle becomes smaller than $\theta_{8CB} = 0.17°$ the critical angle and the beam penetration becomes negligible. This explains the null intensity between $\alpha = 0°$ and $\alpha = 7°$.

### 8CB deposited on the PVA (polyVinyl Alcohol) substrate in the air

Delphine Coursault et al [30] have studied the structure of the oily streaks on rubbed PVA using X-ray diffraction. They used 8CB film deposited on rubbed-PVA coated glass slide. In chapter 1 we have seen that this substrate imposes a strong uniform unidirectional planar anchoring on the 8CB molecules deposited upon it in contrast with the 8CB/air interface, it imposes an homeotropic anchoring. They used grazing incidence set-up (incident angle of $0.2°$) with an X-ray beam of 18 $keV$ and beam size of $300 \times 300$ $mm^2$. They observed on an XPAD detector a scattering ring (figure 2.8) It shows that, for each $\alpha$ value in the ring, a non-zero intensity is measured in agreement with a continuous rotation of the smectic layers around the axis of the hemicylinder at the edges of the flattened hemicylinders.

In figure 2.8b, we see the intensity evolution for a thickness $e = 100$ nm as a function of $\alpha$ extracted from combination of both the GISAXS scattering ring shown on figure 2.8a and the TSAXS data. In figure 4.4b we have TSAXS data for $e = 230$ nm, where $\alpha = 0°$ corresponds to perpendicular layers.

For the thickness 100 $nm$, a decrease of intensity is observed from $\alpha = 5$ to $\alpha = 80°$.

Using this observed decrease of intensity the group of E.Lacaze has built a model for the internal structure of the oily streaks (shown in figure 2.9a). The model is based on the following hypotheses [30]:

1. The measured intensity is approximated to the integrated intensity and is thus proportional to the number $N(\alpha)$ of smectic layers which have normals oriented at $\alpha$ in agreement with the calculation described in section 2.2.3.
2. The junction between the hemicylinders is made of a curvature wall characterized by an angle $\omega$ which is an angle between the substrate and the line drawn from curvature center to the top of the curvature wall (figure 2.9).

With these hypotheses, the profile $r(\alpha)$ of the rotating grain boundary that joins the rotating smectic layers and the central flat smectic layers close to the curvature center (in red on figure 2.9) has thus been calculated using $n * d$ extracted from the measurement of a film of thickness 100 $nm$ (shown on Figure 2.8b).

The rotating grain boundary shown in side view (red color) in figure 2.9 was described as a half tube with a quasi-elliptical profile of minor axis and semimajor axis of 140 nm and 110 nm (figure 2.10a) respectively. These values are close to the ones

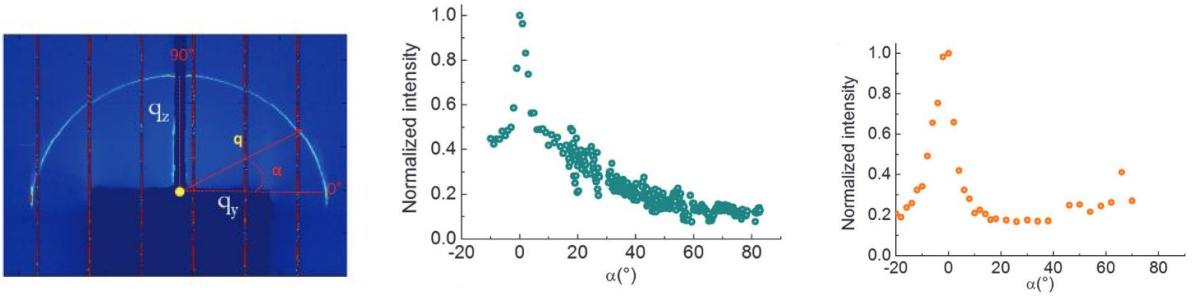


(a) (b) (c)

Figure 2.8: (a) The scattering ring observed on 2D XPAD detector using GISAXS (b) Normalized integrated intensity for the 8CB film of 100 nm thickness, obtained by combining the GISAXS and TSAXS signals (c) Normalized integrated intensity for an 8CB film of 230 nm thickness obtained in the TSAXS configuration [30].

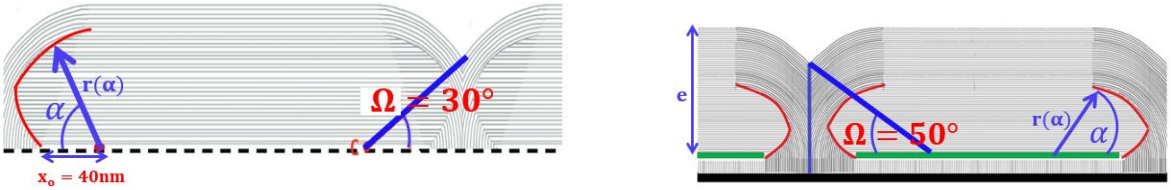


(a) (b)

Figure 2.9: The hemicylinder model for the oily-streak in the 8CB deposited on the rubbed PVA on film of (a) 100 nm thickness (b) 230nm thickness [30].

previously extracted from measurements performed on $MoS_2$ substrates (figure 2.10b) [31]. The lower part of this profile is expected to be dislocation-free. The profile of dislocation-free grain boundary can indeed be calculated [30, 32] and it fitted well with the basis of the extracted profile of the rotating grain boundary (green in figure 2.10a). The curvature wall angle $\Omega$ was found to be $30^\circ$ for the 100 nm thick film and $50^\circ$ for the 230 $nm$ thick film sample.

This suggests also that the dislocations populate only the top of the rotating grain boundary with 3 suggested dislocations of different Burger vectors.

However, the exact number of dislocations on this upper part and where exactly they are located are still bewildering facts.

Two topological defects have been evidenced: the dislocation defects on the upper part of the rotating grain boundary and the 2D topological grain boundary. This latter one has been evidenced for thick sample (in green color in figure 2.9b). It is separating the perpendicular layers on the substrate and the central flat layers. For the 100 nm thick film, the model (figure 2.9a) is associated with a large area in the center of the flattened hemicylinders of unfavorable anchoring where the central layers are directly deposited on the substrate.

### 8CB deposited on the muscovite mica crystalline substrate

Another X-ray ray scattering study of confined smectic A liquid crystals was done by Zappone et al. [32] in order to analyze the structural evolution when thickness increases. 8CB smectic A film of thickness 1µm was deposited in the air on a muscovite mica crystalline substrate. The X-ray scattering intensity obtained for a thicker film (figure 2.11) was completely different from what was obtained for thin films of 8CB deposited on PVA or molybdenite substrate. A completely new model has thus been proposed to explain these experimental results as discussed in chapter 1, section 1.3.3.

During the thesis of Delphine Coursault [33], it was found that for thin film, the intensity as a function of layer orientation $\alpha$ was similar to that of $MoS_2$ as shown in figure 2.12. In this figure, we compare the intensity profiles obtained on both

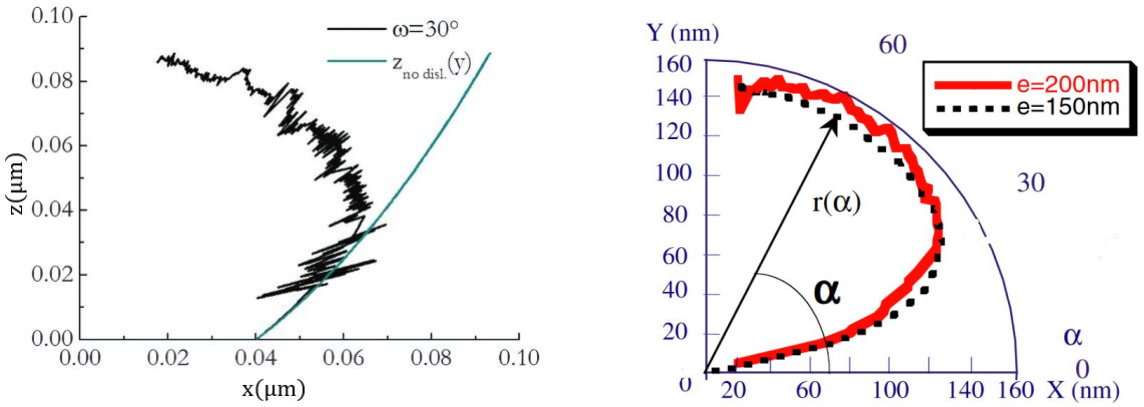


(a) (b)

Figure 2.10: (a) The profile of rotating grain boundary extracted from experimental data (in black color) and for the oily-streak in the 8CB film of 100 nm thickness deposited on the rubbed PVA substrate (with a calculated grain boundary without dislocation in green) (b) Profile of the rotating grain boundary from data obtained for 8CB films of different thicknesses deposited on $MoS_2$ substrate [30, 31].

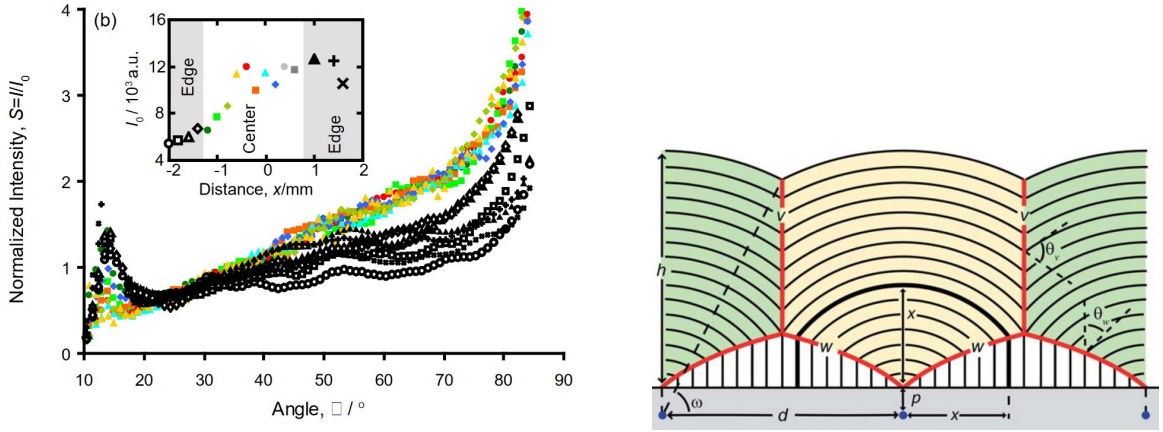


(a) (b)

Figure 2.11: The X-ray diffraction intensity from smectic A 8CB thicker film deposited on mica (thickness around $1\mu m$ (a) The model of the internal structure of the oily streaks observed with mica (b) [32].

muscovite mica and $MoS_2$ for thin films and those obtained on PVA substrate. We can see that the scattered intensity from these thin smectic films are nearly the same. This shows that the thin film structure, at least for the rotating layers, may not strongly depend on the substrate nature. The structure mostly depends on the thickness. For large thicknesses topological defects mostly disappear. they are present only for thin enough films. We have thus decided to concentrate on the films with topological defects and also to study how the defects themselves vary as a function of thickness.

### 2.6.3 Chevron structure evidenced using X-ray diffraction in thick films

Takanishi et al. [34] have reported a chevron structure in 8CB smectic A which was caused by temperature. They have used an X-ray diffraction study of a confined smectic A liquid crystal sample to study its structure. They confined the 8CB between

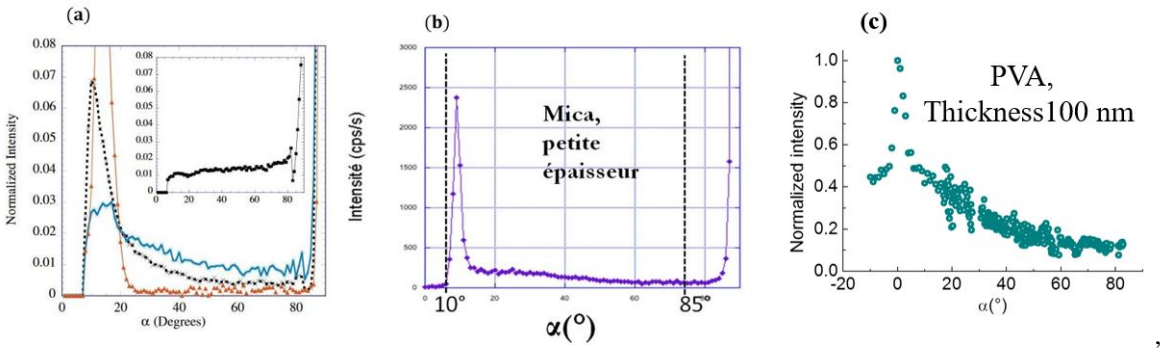


Figure 2.12: X-ray scattering intensity as a function of the orientation $\alpha$ of the wave vector transfer $\vec{q}$ with respect to the substrate for 8CB thin thickness [$e = 70$, 150, and 200 nm (full red triangles, black crosses, and open blue circles, respectively)] deposited on (a) $MoS_2$ [31] (b) muscovite mica thickness not precisely known) [33]. (c) Rubbed PVA

two rubbed polyvinyl alcohol (PVA) coated glasses. The two plates were rubbed in an anti-parallel direction imposing a planar alignment of the 8CB deposited on them [35]. The sample cell was $25\mu m$. These experiments were done by heating and cooling processes (figure 2.13 ). In the cooling process, a single diffraction peak was observed at tilt angle $0^\circ$ near the

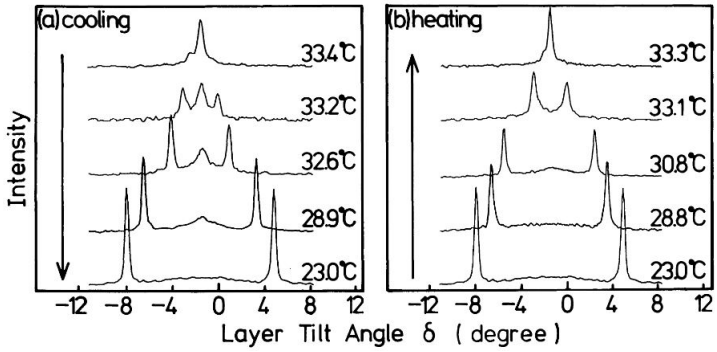


Figure 2.13: X-ray scattering of 8CB smectic A sample of 25 µm thickness. The tilt angle is the angle between the glass-plate normal and a layer direction [34].

smectic/nematic phase transition temperature. This peak was attributed to the bookshelf structure with layers perpendicular to the glass plates ( figure 2.14 ). As the temperature decreases, the single peak splits into three peaks; one central and two lateral peaks. They inferred from this result that there was a gradual bend of the bookshelf structure that was observed very close to the smectic/nematic phase transition temperature. This bending eventually led to formation of a chevron structure which they associated with the lateral diffraction peaks as shown in figure 2.13. They concluded that the chevron resulted from the thermal contraction of smectic layers reducing their thickness in the bulk part away from the surface. This chevron structure is more favorable than the bookshelf structure with dislocations defects near the bounding surface [36, 37, 38].

In our study of smectic thin film using X-ray diffraction we have also evidenced the chevron structure, which was not caused by temperature variation but by mechanical strain. We will describe this results in chapter 4.

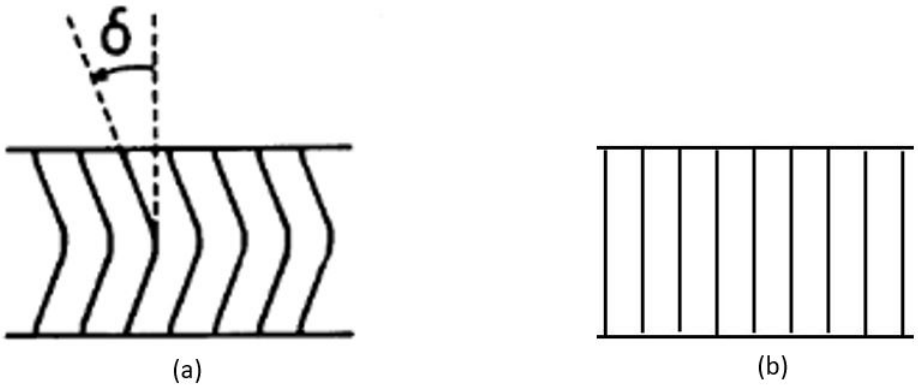


Figure 2.14: (a) Chevron structure scheme in homogeneously aligned 8CB Smectic sample. The tilt angle is between the direction of the layers and the normal to the bounding plate (b) non-deformed Bookshelf structure in smectic A where the molecules are perpendicular to the layers. The layers are normal to the bounding plates that induce planar anchoring.

## 2.7 Conclusion

Various factors contribute to the lineshape peak of the scattered intensity for a smectic A liquid crystal sample. Notably, the finite-size effects cover or destroy the Landau-Peierls instability effect that comes from the thermal fluctuation. These factors mask the algebraic decay of the displacement correlation between the layers. The long tails associated with the power-law decay become insignificant in the case of a finite-size sample, so they can be neglected. We will use the usual features of periodic compounds that have been calculated in the first sections of this chapter. The Landau-Peierls instability effects do not displaced the Bragg peak and so the observed peak are centered on the Bragg position. We will be interested in the following chapters on this Bragg peak.

Concerning X-ray diffraction of smectic 8CB distorted by antagonistic anchorings with thicknesses not larger than 1µm, analysis using Bragg condition has been considered already in the past. As shown in the first sections of this chapter is vital that the Bragg condition is satisfied we want to extract the structural information on the 8CB films using the scattered Bragg intensity expected to be proportional to $N^2$ but it has been shown to be possible by the past measurements. This makes the 8CB smectic film a laboratory for the understanding of the topological defects intimate structure which is still scarce despite of currently existing literature on them. Moreover, interesting results had already been obtained but they necessitate that the efforts may be continued since some questions are still pending (see conclusion of chapter 1). For instance in the oily streaks of smectic 4-n-octyl-4'-cyanobiphenyl (8CB), 1D defects lead to NP chain formation whereas 2D topological grain boundary leads to the formation of 2D hexagonal networks of gold nanospheres [39, 40, 41]. The precise understanding of this nanoparticles confinement in the defect cores requires a precise understanding of the intimate structure of the topological defects in smectic A system. The calculation presented at the start of this chapter highlights that specific effort be devoted for ensuring that the Bragg's condition is satisfied; in chapter 3 of this manuscript we have described an unprecedented determination of this condition. All the above studies of confinement of the 8CB smectic A liquid crystal between air and crystalline substrate show that for the study of these 1D patterns, the so-called oily-streaks [28]. X-ray diffraction is a powerful tool. In particular, it may allow to study how topological defects appear when the thickness is small enough. Most of the previous studies are based on the hypothesis that the number of diffracting smectic layers is directly proportional to the scattered intensity. The relationship between this scattered intensity and the number of diffracting smectic layers or scatters in the 8CB thin film must thus be established, not only for flat smectic layers like in the calculations of this chapter but also for rotating layers. Moreover, studies however, the integrated intensity has not been determined with a high precision. We have seen in this last chapter 2 what are the necessary ingredient to determined precisely the integrated intensity. Firstly, it is the $\Delta q$ parameter which is associated with the domain size; in our case, it is connected with the number of diffracting smectic layers in one hemicylinder. Secondly, it is the domain mosaicity. Since the rubbing of the PVA crystalline substrate induces azimuthal misorientation of the hemicylinders it is vital to consider the mosaicity effect on the intensity. It also appears that the validity of Bragg conditions must be scrutinized

to allow for a safe use of the integrated intensity.

In the next chapters of my manuscript, I will thus show how a more precise analysis of the X-ray data can be used to ascertain in more detail the intimate system of the oily streak with nanoscale resolution. All these features led us to fully reconsider the analysis of the X-ray data which will be the subject of the next chapter, the chapter 3. The idea was also to obtain the largest possible amount of experimental results to build the safest model as possible for the oily streaks intimated structure (presented in chapters 4 and 5 that even include revisiting the structure of the central flat layers).

# Bibliography


[1] Amardeep Bharti and Navdeep Goyal. "Fundamental of synchrotron radiations". In: *Synchrotron radiation*. Ed. by Daisy Joseph. Section: 2. Rijeka: IntechOpen, 2019. DOI: 10.5772/intechopen.82202. URL: https://doi.org/10.5772/intechopen.82202 (cit. on p. 45).

[2] Willmott Philip and Philip Willmott. "An introduction to synchrotron radiation : techniques and applications / Philip Willmott". eng. In: *An introduction to synchrotron radiation : techniques and applications*. 2nd edition. Chichester, UK: Wiley, 2019. ISBN: 978-1-119-28039-2 (cit. on p. 45).

[3] Heimo Schnablegger and Yashveer Singh. "Getting acquainted with the principles 4th edition". en. In: () (cit. on p. 45).

[4] Takeshi Egami and Simon J. L.. Billinge. *Underneath the Bragg peaks : structural analysis of complex materials*. eng. 2nd edition. Pergamon materials series. Amsterdam: Elsevier, 2012. ISBN: 978-0-08-097133-9 0-08-097133-4 (cit. on pp. 48, 50).

[5] Dingning Li and Kai Zhang. "Unifying the concepts of scattering and structure factor in ordered and disordered samples". en. In: *Journal of Applied Crystallography* 54.2 (Apr. 2021), pp. 644–660. ISSN: 1600-5767. DOI: 10.1107/S1600576721001965. URL: https://scripts.iucr.org/cgi-bin/paper?S1600576721001965 (visited on 06/28/2023) (cit. on pp. 48, 50).

[6] Maurice Kleman and Oleg D. Lavrentovich, eds. *Soft Matter Physics: An Introduction*. en. New York, NY: Springer, 2003. ISBN: 978-0-387-95267-3 978-0-387-21759-8. DOI: 10.1007/b97416. URL: https://link.springer.com/10.1007/b97416 (visited on 05/16/2023) (cit. on pp. 48, 50).

[7] Vladimir M. Kaganer, Ilia Petrov, and Liubov Samoylova. "X-ray diffraction from strongly bent crystals and spectroscopy of X-ray free-electron laser pulses". en. In: *Acta Crystallographica Section A Foundations and Advances* 76.1 (Jan. 2020), pp. 55–69. ISSN: 2053-2733. DOI: 10.1107/S2053273319014347. URL: https://scripts.iucr.org/cgi-bin/paper?S2053273319014347 (visited on 08/21/2022) (cit. on pp. 48, 54, 56).

[8] Wim H. De Jeu, Boris I. Ostrovskii, and Arcadi N. Shalaginov. "Structure and fluctuations of smectic membranes". en. In: *Reviews of Modern Physics* 75.1 (Feb. 2003), pp. 181–235. ISSN: 0034-6861, 1539-0756. DOI: 10.1103/RevModPhys.75.181. URL: https://link.aps.org/doi/10.1103/RevModPhys.75.181 (visited on 07/26/2023) (cit. on pp. 48, 53, 54).

[9] "Kinematical scattering II: crystalline order". In: *Elements of modern X-ray physics*. Section: 5 tex.eprint: https://onlinelibrary.wiley.com/doi/pdf/10.1002/9781119998365.ch5. John Wiley & Sons, Ltd, 2011, pp. 147–205. ISBN: 978-1-119-99836-5. DOI: https://doi.org/10.1002/9781119998365.ch5. URL: https://onlinelibrary.wiley.com/doi/abs/10.1002/9781119998365.ch5 (cit. on p. 48).

[10] "X-rays and their interaction with matter". In: *Elements of modern X-ray physics*. Section: 1 tex.eprint: https://onlinelibrary.wiley.com/doi/pdf/10.1002/9781119998365.ch1. John Wiley & Sons, Ltd, 2011, pp. 1–28. ISBN: 978-1-119-99836-5. DOI: https://doi.org/10.1002/9781119998365.ch1. URL: https://onlinelibrary.wiley.com/doi/abs/10.1002/9781119998365.ch1 (cit. on p. 48).

[11] "Kinematical scattering I: non-crystalline materials". In: *Elements of modern X-ray physics*. Section: 4 tex.eprint: https://onlinelibrary.wiley.com/doi/pdf/10.1002/9781119998365.ch4. John Wiley & Sons, Ltd, 2011, pp. 113–146. ISBN: 978-1-119-99836-5. DOI: https://doi.org/10.1002/9781119998365.ch4. URL: https://onlinelibrary.wiley.com/doi/abs/10.1002/9781119998365.ch4 (cit. on p. 48).

[12] R. E. Peierls. In: *Helv. Phys. Acta* 7 (Suppl. II).81 (1934) (cit. on p. 53).

[13] Pierre Gilles de Gennes. *The physics of liquid crystals*. eng. Oxford : Clarendon Press ; New York : Oxford University Press, 1993. ISBN: 978-0-19-852024-5 978-0-19-851785-6. URL: http://archive.org/details/physicsofliquidc0000genn_l4c2 (visited on 01/15/2023) (cit. on pp. 53–55).

[14] J. Als-Nielsen et al. "Observation of algebraic decay of positional order in a smectic liquid crystal". en. In: *Physical Review B* 22.1 (July 1980), pp. 312–320. ISSN: 0163-1829. DOI: 10.1103/PhysRevB.22.312. URL: https://link.aps.org/doi/10.1103/PhysRevB.22.312 (visited on 06/15/2022) (cit. on pp. 53–55).

[15] Norman H March and Mario P Tosi. *Polymers, liquid crystals, and low-dimensional solids*. Springer Science & Business Media, 2012 (cit. on p. 53).

[16] Leon Gunther, Yoseph Imry, and Joseph Lajzerowicz. "X-ray scattering in smectic- A liquid crystals". en. In: *Physical Review A* 22.4 (Oct. 1980), pp. 1733–1740. ISSN: 0556-2791. DOI: 10.1103/PhysRevA.22.1733. URL: https://link.aps.org/doi/10.1103/PhysRevA.22.1733 (visited on 12/30/2022) (cit. on pp. 54–56).

[17] Vladimir M. Kaganer, Boris I. Ostrovskii, and Wim H. de Jeu. "X-ray scattering in smectic liquid crystals: From ideal- to real-structure effects". en. In: *Physical Review A* 44.12 (Dec. 1991), pp. 8158–8166. ISSN: 1050-2947, 1094-1622. DOI: 10.1103/PhysRevA.44.8158. URL: https://link.aps.org/doi/10.1103/PhysRevA.44.8158 (visited on 01/05/2023) (cit. on pp. 54–56).

[18] J. Als-Nielsen et al. "Experimental Observation of Anomalous Ordering in a Landau-Peierls System". en. In: *Physical Review Letters* 39.26 (Dec. 1977), pp. 1668–1671. ISSN: 0031-9007. DOI: 10.1103/PhysRevLett.39.1668. URL: https://link.aps.org/doi/10.1103/PhysRevLett.39.1668 (visited on 01/05/2023) (cit. on p. 55).

[19] J. Stamatoff et al. "X-Ray Diffraction Intensities of a Smectic- A Liquid Crystal". en. In: *Physical Review Letters* 44.23 (June 1980), pp. 1509–1512. ISSN: 0031-9007. DOI: 10.1103/PhysRevLett.44.1509. URL: https://link.aps.org/doi/10.1103/PhysRevLett.44.1509 (visited on 01/05/2023) (cit. on pp. 56, 57).

[20] AN ZISMAN et al. "X-ray scattering in the smectic A phase of the liquid crystal octylcyanobiphenyl (8CB)". In: *Jetp Letters* 45 (Feb. 1987), pp. 238–242 (cit. on p. 56).

[21] G. S. Iannacchione et al. "Calorimetric and small angle x-ray scattering study of phase transitions in octylcyanobiphenyl-aerosil dispersions". en. In: *Physical Review E* 58.5 (Nov. 1998), pp. 5966–5981. ISSN: 1063-651X, 1095-3787. DOI: 10.1103/PhysRevE.58.5966. URL: https://link.aps.org/doi/10.1103/PhysRevE.58.5966 (visited on 01/04/2023) (cit. on p. 57).

[22] Noel A. Clark et al. "X-ray scattering study of smectic ordering in a silica aerogel". en. In: *Physical Review Letters* 71.21 (Nov. 1993), pp. 3505–3508. ISSN: 0031-9007. DOI: 10.1103/PhysRevLett.71.3505. URL: https://link.aps.org/doi/10.1103/PhysRevLett.71.3505 (visited on 01/05/2023) (cit. on pp. 57, 58).

[23] S. Park et al. "Hydrogen-bonded silica gels dispersed in a smectic liquid crystal: A random field XY system". en. In: *Physical Review E* 65.5 (May 2002), p. 050703. ISSN: 1063-651X, 1095-3787. DOI: 10.1103/PhysRevE.65.050703. URL: https://link.aps.org/doi/10.1103/PhysRevE.65.050703 (visited on 12/16/2022) (cit. on pp. 57, 58).

[24] R. L. Leheny et al. "Smectic ordering in liquid-crystal–aerosil dispersions. I. X-ray scattering". en. In: *Physical Review E* 67.1 (Jan. 2003), p. 011708. ISSN: 1063-651X, 1095-3787. DOI: 10.1103/PhysRevE.67.011708. URL: https://link.aps.org/doi/10.1103/PhysRevE.67.011708 (visited on 12/14/2022) (cit. on pp. 57, 58).

[25] Samo Kralj et al. “Presmectic wetting and supercritical-like phase behavior of octylcyanobiphenyl liquid crystal confined to controlled-pore glass matrices”. en. In: *The Journal of Chemical Physics* 127.15 (Oct. 2007), p. 154905. ISSN: 0021-9606, 1089-7690. DOI: 10.1063/1.2795716. URL: http://aip.scitation.org/doi/10.1063/1.2795716 (visited on 12/14/2022) (cit. on p. 58).

[26] Apparao Gudimalla, Sabu Thomas, and Aleksander Zidanšek. “Phase behaviour of n-CB liquid crystals confined to controlled pore glasses”. en. In: *Journal of Molecular Structure* 1235 (July 2021), p. 130217. ISSN: 0022-2860. DOI: 10.1016/j.molstruc.2021.130217. URL: https://www.sciencedirect.com/science/article/pii/S0022286021003483 (visited on 03/24/2022) (cit. on p. 58).

[27] C. Blanc and M. Kleman. “The confinement of smectics with a strong anchoring”. en. In: *The European Physical Journal E* 4.2 (Jan. 2001), pp. 241–251. ISSN: 1292-8941. DOI: 10.1007/s101890170134. URL: https://doi.org/10.1007/s101890170134 (visited on 01/27/2022) (cit. on p. 58).

[28] Bruno Zappone and Emmanuelle Lacaze. “One-dimensional patterns and topological defects in smectic liquid crystal films”. en. In: *Liquid Crystals Reviews* (July 2022), pp. 1–18. ISSN: 2168-0396, 2168-0418. DOI: 10.1080/21680396.2022.2076748. URL: https://www.tandfonline.com/doi/full/10.1080/21680396.2022.2076748 (visited on 04/24/2023) (cit. on pp. 58, 63).

[29] Jean-Philippe Michel et al. “Optical gratings formed in thin smectic films frustrated on a single crystalline substrate”. en. In: *Physical Review E* 70.1 (July 2004), p. 011709. ISSN: 1539-3755, 1550-2376. DOI: 10.1103/PhysRevE.70.011709. URL: https://link.aps.org/doi/10.1103/PhysRevE.70.011709 (visited on 10/20/2021) (cit. on p. 58).

[30] Delphine Coursault et al. “Self-organized arrays of dislocations in thin smectic liquid crystal films”. en. In: *Soft Matter* 12.3 (2016), pp. 678–688. ISSN: 1744-683X, 1744-6848. DOI: 10.1039/C5SM02241J. URL: http://xlink.rsc.org/?DOI=C5SM02241J (visited on 01/17/2023) (cit. on pp. 59–61).

[31] Jean-Philippe Michel et al. “Structure of smectic defect cores: X-ray study of 8CB liquid crystal ultrathin films”. In: *Physical review letters* 96.2 (2006). Publisher: APS, p. 027803 (cit. on pp. 60–62).

[32] Bruno Zappone et al. “Self-ordered arrays of linear defects and virtual singularities in thin smectic-A films”. en. In: *Soft Matter* 7.3 (2011), pp. 1161–1167 (cit. on pp. 60, 61).

[33] Coursault Delphine. “Décoration de réseaux linéaires de défauts smectiques par des nanoparticules d’or.” PhD thesis. Paris: Université Pierre et Marie Curie, 2013 (cit. on pp. 60, 62).

[34] Yoichi Takanishi et al. “Chevron Layer Structure in the Smectic A Phase of 8CB”. In: *Japanese Journal of Applied Physics* 28.3A (Mar. 1989), p. L487. ISSN: 0021-4922, 1347-4065. DOI: 10.1143/JJAP.28.L487. URL: https://iopscience.iop.org/article/10.1143/JJAP.28.L487 (visited on 01/09/2023) (cit. on pp. 61, 62).

[35] Iam-Choon Khoo. *Liquid crystals*. 2nd ed. Wiley series in pure and applied optics. Hoboken, N.J: Wiley-Interscience, 2007. ISBN: 978-0-471-75153-3 (cit. on p. 62).

[36] Lei Z. Cheng and Daniel Phillips. “An Analysis of Chevrons in Thin Liquid Crystal Cells”. In: *SIAM Journal on Applied Mathematics* 75.1 (2015). Publisher: Society for Industrial and Applied Mathematics, pp. 164–188. ISSN: 0036-1399. URL: https://www.jstor.org/stable/24511442 (visited on 04/25/2023) (cit. on p. 62).

[37] S. Kralj and T. J. Sluckin. “Landau–de Gennes theory of the chevron structure in a smectic- *A* liquid crystal”. en. In: *Physical Review E* 50.4 (Oct. 1994), pp. 2940–2951. ISSN: 1063-651X, 1095-3787. DOI: 10.1103/PhysRevE.50.2940. URL: https://link.aps.org/doi/10.1103/PhysRevE.50.2940 (visited on 06/30/2023) (cit. on p. 62).

[38] N. Vaupotič et al. “Landau–de Gennes theory of the chevron structure in a smectic liquid crystal”. en. In: *Physical Review E* 54.4 (Oct. 1996), pp. 3783–3792. ISSN: 1063-651X, 1095-3787. DOI: 10.1103/PhysRevE.54.3783. URL: https://link.aps.org/doi/10.1103/PhysRevE.54.3783 (visited on 06/30/2023) (cit. on p. 62).

[39] Syou P’heng Do et al. “From Chains to Monolayers : Nanoparticle Assembly Driven by Smectic Topological Defects”. In: *Nano Letters* (Jan. 2020). Publisher: American Chemical Society. DOI: 10.1021/acs.nanolett.9b04347. URL: https://hal.archives-ouvertes.fr/hal-02450544 (visited on 10/03/2021) (cit. on p. 63).

[40] Haifa Jeridi et al. “Unique orientation of 1D and 2D nanoparticle assemblies confined in smectic topological defects”. en. In: *Soft Matter* 18.25 (June 2022). Publisher: The Royal Society of Chemistry, pp. 4792–4802. ISSN: 1744-6848. DOI: 10.1039/D2SM00376G. URL: https://pubs.rsc.org/en/content/articlelanding/2022/sm/d2sm00376g (visited on 08/17/2022) (cit. on p. 63).

[41] Delphine Coursault et al. “Tailoring anisotropic interactions between soft nanospheres using dense arrays of smectic liquid crystal edge dislocations”. In: *ACS nano* 9.12 (2015). Publisher: ACS Publications, pp. 11678–11689 (cit. on p. 63).

# CHAPTER 3

# EXPERIMENTAL TECHNIQUE AND DATA ANALYSIS

*"If I have seen further than others, it is by standing upon the shoulders of giants." –*

– Isaac Newton

## Contents

## 3.1 Introduction

The confinement of the 4-n-octyl-4'-cyanobiphenyl (8CB) smectic A thin film between two antagonistic anchoring distorts it into two kinds of arrays of linear defect structures, the so-called oily streaks and large streaks structures. These structures can be monitored by the anchoring strength. The oily streaks structure has been studied in the past [1, 2, 3, 4] but several questions are still pending as discussed in chapters 1 and 2 of this manuscript. It is made of smectic layers superimposed in flattened hemicylinders as described in chapter 1 and in chapter 2 with an emphasis on the X-ray diffraction results. Topological defects in this structure were found to effectively act as traps for nanoparticles being able to transfer their geometry to nanoparticles organization and therefore to work as a template for their self-assembling [5, 6]. Recently, the internal structure of the so-called large streaks has been suggested [7].

We aim to accurately determine the models of the internal structure of oily with high precision. This would not only help to study the intimate structure of liquid crystal topological defects, all this being still elusive but also in a second step, it would help to understand and control the self-assembling processes of nanoparticles inside the core of the topological defects. For such a purpose, during my Ph.D. thesis, I have developed a new way of analyzing our experimental X-ray data that I will present in this chapter. We have developed particularly an unprecedented methodology of ascertaining the satisfaction of the Bragg condition for particular orientation $\alpha$ of rotating smectic layers inside the hemicylinder.

### 3.1.1 Experimental set up

We have carried out two X-ray scattering measurements at the SIXS beamline on the SOLEIL Synchrotron facility in collaboration between the team of Professor Emmanuelle Lacaze, Bernard Croset, Haifa Jeridi, Michel Goldmann (INSP), the colleagues of SIXS beamline (Alina Vlad , Yves Garreau and Alessandro Coati), David Baboneau and Doru Constantin. We collected huge amount of data that I have been analyzing throughout this thesis. The experiment set-up is shown in figure 3.1. We have used an X-ray beam of 300 $\mu m \times$ 300 $\mu m$ and a photo-energy fixed at 18.44 KeV. The X-ray beam exiting from the vacuum tube is impinged on a sample of 18 mm $\times$ 18 mm. The Sample-Detector distance was 1.7 m for an Eiger detector. This detector is a single-photon counting X-ray pixel detector made of $(1065, 1030)$ pixels, i.e 1065 lines and 1030 columns. The size of a pixel is $75 \times 75$ $\mu m^2$, this corresponds to a $q$ pixel size of $0.004\ nm^{-1} \times 0.004\ nm^{-1}$. The sample is fastened to a copper component and covered by a Kapton cone connected to a helium bottle (see figure 3.1 ) to allow the sample to be kept under a helium atmosphere and hence prevent the liquid crystal from being deteriorated while the sample holder remains transparent to the X-ray beam during the measurements.

We have used Grazing Incident Small Angle X-ray Scattering (GISAXS ) (figure 3.2a) and Transmission Small Angle X-ray Scattering (TSAXS ) (figure 3.2b). We have studied samples of 8CB smectic A liquid crystal thin films of different thicknesses. The experimental setups of these two configurations was first used during the thesis of Delphine Coursault [8] and of M. Syou-p'heng DO [9], the former students of Professor Emmanuelle Lacaze.

Using the TSAXS configuration, the intensity scattered by the perpendicular layers close to the substrate (see chapter 2 section 2.6.2) was measured by rotating the sample through $90^\circ$ to make it perpendicular to the X-ray beam and hence probe an area of size 300 $\mu m \times$ 300 $\mu m$ [1]. Using the GISAXS configuration shown in figure 3.2a, we have measured the intensity scattered by all the rotating smectic layers in the two edges of the hemicylinder together with the intensity of scattered by the smectic layers in the central part of the hemicylinder. The sample surface being almost parallel to X-ray beam, we probe an area of size 300 $\mu m \times 18\ mm$. For each sample, a 2D optical map ($z_{mc}$, $y_{mc}$ on the surface) was drawn. For this purpose the surface of the sample has been divided into squares of size 100 $\mu m$ per 100 $\mu m$ where the thickness has been identified using the colors by optical Microscopy. The $z_{mc}$ was parallel to the direction of the stripes and $y_{mc}$ was perpendicular to the $z_{mc}$. The borders of the sample have been precisely identified by X-ray in transmission, allowing to precisely combine X-ray measurements with optical maps to determine the thickness of each zone.

For instance, in the sample that we will analyze in this chapter 3 and in the chapter 4, in the TSAXS configuration, we have measured two $y_{mc}$ zones: $y_{mc} = -2$ and $y_{mc} = 0$. For each of these zones, we have measured 4 $z_{mc}$ zones, notably $-4$, $-1$, 1 and 0. For the $y_{mc} = -2$, the thicknesses are respectively 200 nm, 192 nm, 182 nm and 182 nm whereas for the $y_{mc} = 0$, the thicknesses are respectively 185 nm, 192 nm, 198 nm and 192 nm. In GISAXS configuration, different zone were also measured, notably $-4$, $-1$, 1 and 0 and their thicknesses are respectively 180 nm, 200 nm, 200 nm and 210 nm. It appears that generally the thickness is mostly homogeneous along the stripes but less homogeneous perpendicular to the stripes. This allows to define properly the thickness in both TSAXS and GISAXS set-up, with an uncertainty around 30 $nm$. The effective domination of oily streaks with respect to large stripes has also been identified.

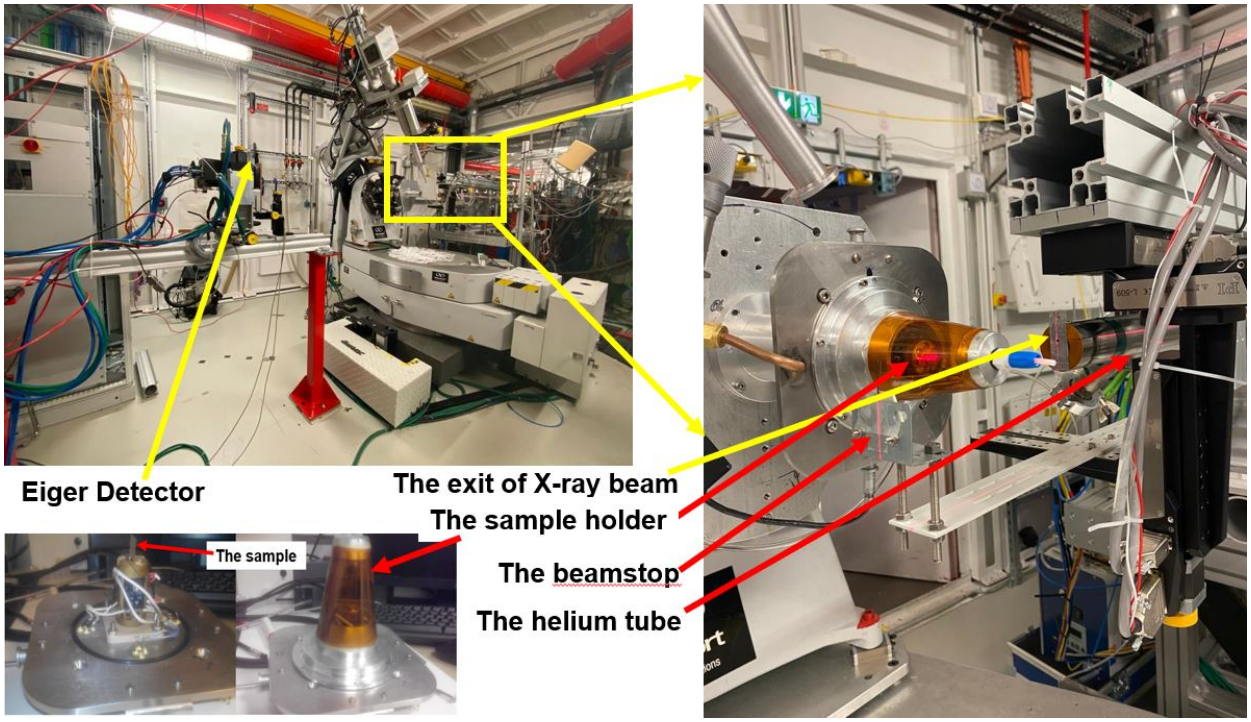


Figure 3.1: The experimental setup at SIXS beam line of Soleil synchrotron facilities.

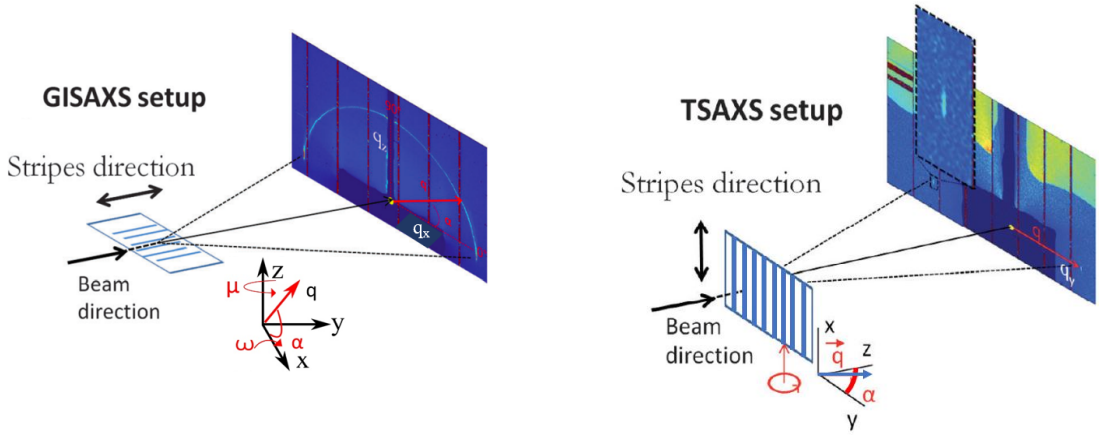


(a) (b)

Figure 3.2: Grazing incident Small Angle X-ray Scattering set up and the diffraction image (a)Transmission Small Angle X-ray Scattering set up and the signal (the comma in the zoomed part) scattered from the perpendicular layer (b).

In the GISAXS step, we have used seven different incident angles $\omega$: $0.1°, 0.15°, 0.2°, 0.25°, 0.3°, 0.5°, 0.6°$. For each measurement, a scattering ring (see figure 3.7) centered on the direct beam position is observed on the 2D detector (see figure 3.2a). This ring depicts the rotation of the smectic layers whose normal is parallel to the wave-vector transfer $q_{\vec{film}}$ which is

rotating around the axis of the hemicylinder through an angle $\alpha_{film}$ with respect to the substrate. The ring is formed by the intensity scattered by such layers.

The measurements were systematically done with a detector placed in a position that was preventing the direct X-ray beam to reach the detector since it could damage it. In addition a hidden zone was present in the middle of the detector (the pink ribbon visible in figure 3.3). The effect of this was that the signals scattered by smectic layers in the central part of the hemicylinder were hindered on the detector (figure 3.3 (a)), the purple thick line passing through the central part of the scattering ring. These hidden data are crucial to get the complete structure of the hemicylinder and its understanding. To get this data we have shifted the detector as shown in figure 3.3(b) which is showing a ring formed by the signal scattered by both the smectic layers in the central part of the hemicylinder (they are highlighted in the black box) and the rotating smectic layers in the rest part of the ring. Almost systematically we have measured the two positions of the detector.

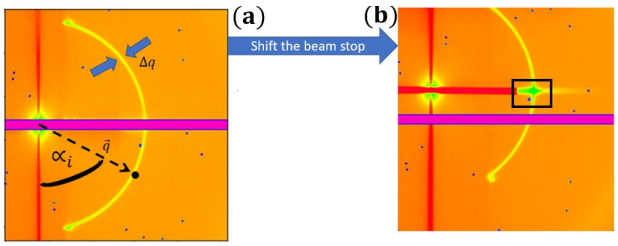


Figure 3.3: Images from Eiger detector (a) before (b) after shifting the detector in order to visualize the signal scattered from the central part of the hemicylinder. The part highlighted in black is the central part of the hemicylinder.In red the position of the beam-stop that hides the direct beam is visible.

We have used two different but complementary techniques to measure the scattering of the smectic layers. The first one was to keep the rotation angle $\mu = 0$ (this $\mu$ is an angle of rotation of the sample around the axis-z perpendicular to the substrate see figure 3.2a) and to change only the incidence angle $\omega$ while keeping the detector and the direct beam fixed. This is the technique that had been used before this thesis. The second technique, which is a new one, consists in rotating the sample through the angle $\mu$ around the z-axis that is perpendicular to the substrate and keeping fixed the incident angle $\omega$. In the next coming sections of this chapter I will detail the extraction and treatment of data from a pure liquid crystal sample on a specific measured zone of 180 $nm$, $z_{mc} = -4$.

## 3.2 Data treatment technique and analysis for measurement at $\mu = 0$

### 3.2.1 Extraction of the data from perpendicular layers

In figure 3.2b, we showed the setup of the experimental Transmission Small Angle X-ray scattering configuration where the X-ray beam is perpendicular to the substrate and to the hemicylinders (the stripes which are visible by Optical Microscopy and are parallel to the $x$ direction ). The intensity scattered on the 2D detector is shown in figure 3.4. Two scattered spots are detected ( in the zoomed parts) in form of an arc. When the motor $\mu$ is at $\mu = 0°$, the two spots correspond to the signals scattered by perpendicular layers. In TSAXS configuration, when $\mu$ is varied, the spots correspond to the scattering of the smectic layers oriented at $\alpha = \mu$. For each $\mu$, we have fitted the detector image with a 2D Gaussian function written in polar coordinates. The results were the maximum intensity, the radial position $q$, $\Delta q$ and the mosaicity as a function of motor $\mu$, in other words in its configuration as a function of $\alpha$. The results are shown in figure 3.5a and figure 3.5b for the intensity and for $q$ respectively. These results will be discussed in chapter 4.

### 3.2.2 Extraction of Data from rotating smectic layers

To extract the data diffracted by the smectic layers for each $\alpha$ along the whole diffraction ring, we have developed a Python code that allowed us to process the raw data from the experiment in HDF5 format. In the following I will start with the data obtained for different incident angles $\omega$ with the sample fixed at $\mu = 0°$. I will then explain the extraction of the data obtained by varying $\mu$ for fixed incident angle $\omega$. This latter technique will be hereinafter referred to as $\mu_{scan}$.

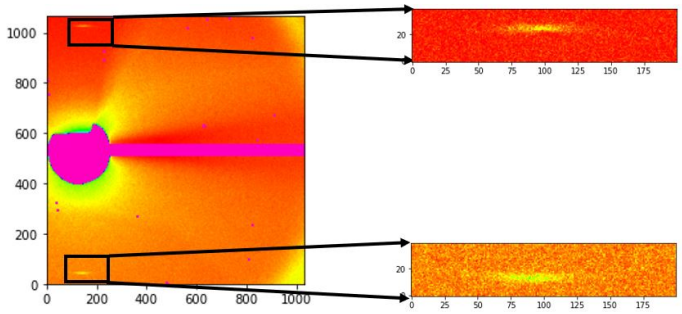

Figure 3.4: The image showing the intensity scattered by the perpendicular layers. It is obtained from TSAXS set-up with a 8CB zone of thickness $185\ nm$.

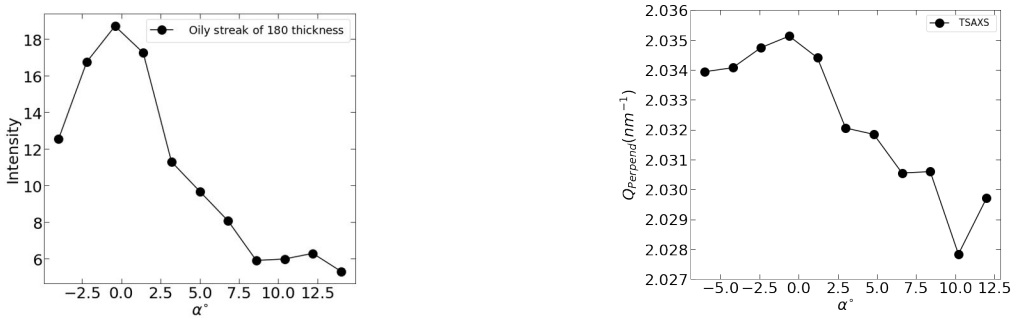


(a) (b)

Figure 3.5: The maximum intensity scattered from perpendicular layers (a) The position of the maximum intensity from perpendicular layers (b).

Figure 3.7 is showing the diffraction rings for all incident angle $\omega$ values obtained for $\mu = 0$ at the position $z_{mc} = -4$ corresponding to an average thickness $e = 180$ nm. With a close look, we can see that the range of angular position of the ring which is visible is becoming smaller as the incident $\omega$ is increasing. This is the effect of the horizon which is due to refraction and will be explained in section 3.2.4 of this chapter.

The process of data extraction was as follow: For each line $Z$, we have drawn the intensity curve as a function of the column pixels denoted as $Y$ (see figure 3.6 ). We have then defined the background noise of this intensity and fitted it with an affine function to ensure that the background noise and the tails that we have discussed in chapter 2 are well defined and then removed. After removing these background from the raw intensity, the remaining intensity was fitted with a Gaussian function. The results of this fitting process are the maximum intensity, the position $Y$ of this maximum intensity in pixel unit and the width ($\Delta Y$). These data were drawn as a function of the line $Z$.

This process was also done using column fitting of the scattering ring. The results of this fitting process are the maximum intensity, the position $Z$ of this maximum intensity in pixel unit and the width ($\Delta Z$). The results from the column fitting were correct for only small $\alpha$ angle since the column was tangent to the scattering at large $\alpha$ whereas those from the line fitting were correct only at larger $\alpha$, since line was tangent to the scattering ring at small $\alpha$. We needed to get the radial values of both the width and the position of the maximum intensity. This radial position is the magnitude of the wave vector transfer $q$. The radial width of the scattering is $\Delta q$. The two parameters are shown in figure 3.3(a). To obtain them we have applied a correction in the two fitting processes. The radial width was $\Delta q = \sin(\alpha)\Delta Y$ for the line fitting and $\Delta q = \cos(\alpha)\Delta Z$ for the column fitting. These radial width values from the two fitting process were found to be the same and correct for all orientations $\alpha$ along the scattering ring which is also shown in figure 3.3(a) and will be discussed in section 3.3.5. In the following part of this manuscript we have used the results from the line fitting. The evolution of these full width at half maximum (FWHM) will be discussed in section 3.3.5 and the calculation and discussion of the radial position $q$ will be discussed in section 3.2.4.

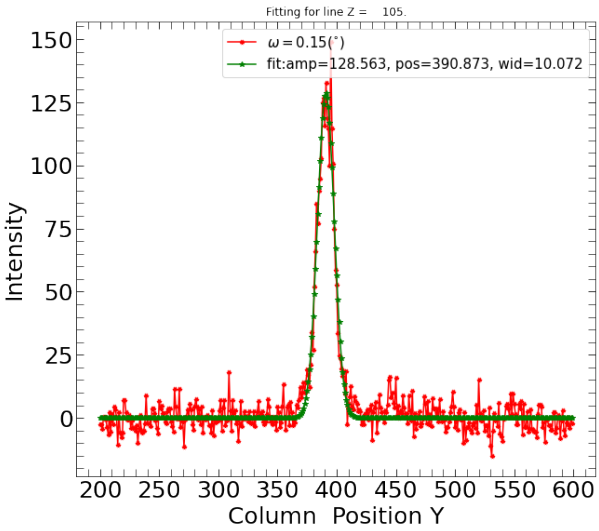


Figure 3.6: Fitting of intensity at line Z = 105 pixels along the scattering ring

All the data we extracted from this scattering ring need to be plotted as a function of the orientation $\alpha$, which is the polar coordinate. The first task that we had was the determination of the center of the polar coordinates. This center is the position of the direct beam. In the next section I will describe how this position was determined.

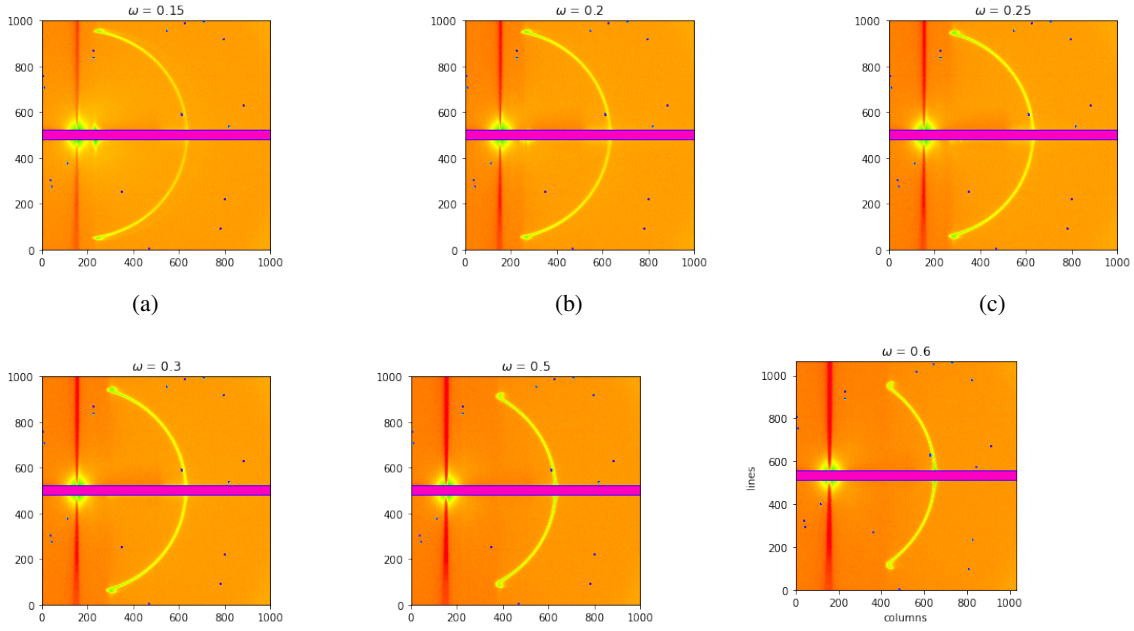


(a) (b) (c)

(d) (e) (f)

Figure 3.7: Evolution of the diffraction ring as a function angle of incidence

### 3.2.3 Determination of the Direct beam position

Let's consider an incident X-ray beam impinged on the air-liquid crystal interface with the incident angle angle $\omega_i$. This beam is refracted at an angle $\omega_{ri}^{'}$ (see figure 3.8 (a)). The Snell–Descartes law of refraction at this interface is $n_i \cos\omega_i = n_{8CB} \cos\omega_{ri}^{'}$, where $n_i = 1$ and $n_{8CB}$ are respectively the refractive indices for air and the smectic liquid crystal which is in our case, 8CB. The critical angle of external reflection of the film can then be obtained from $n_{8CB} = \cos\omega_c$. The refractive index of the 8CB $n_{8CB} = 1 - \delta_{8CB}$ with $\delta_{8CB} = 8.57 \times 10^{-7}$ is the dispersion constant for 8CB. This critical angle is $\omega_c = 0.075°$.

Using the value of the refraction index of the 8CB liquid Crystal in the Snell's law, we get

$$\cos\omega_i = \cos\omega_c \cos\omega_{ri}^{'} \tag{3.1}$$

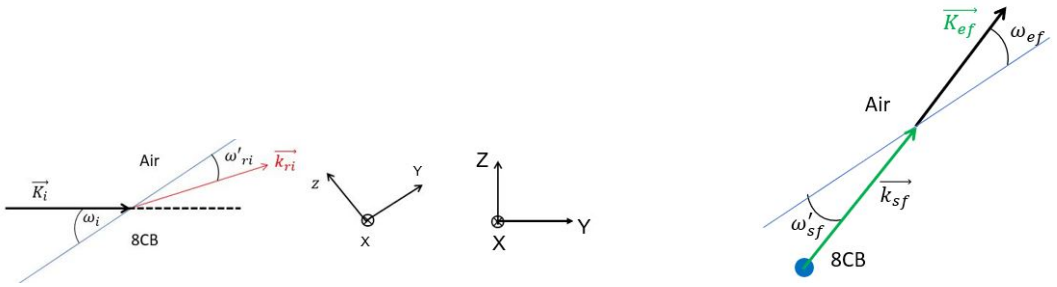


(a) (b)

Figure 3.8: (a) Refraction of the beam impinging on the 8CB film. The sample coordinate system is $(x, y, z)$ and the detector coordinate system is $(X, Y, Z)$ (b) Refraction of the scattered beam on the 8CB-air interface. This figure is in sample frame where the blue line is depicting the sample surface. The blue point is depicting the 8CB film that is diffracting the X-ray beam.

Considering that all the omega angles are small we can use $\cos\omega \approx 1 - \frac{\omega^2}{2}$ and hence, we can easily obtain

$$\omega_i^2 = \omega_{ri}^{'2} + \omega_c^2 \iff \omega_{ri}^{'} = \sqrt{\omega_i^2 - \omega_c^2} \tag{3.2}$$

We can now get the deviation angle of the direct beam due to refraction at the air-liquid crystal interface as

$$\Delta\omega = \omega_i - \omega_{ri}^{'} \iff \Delta\omega = \omega_i - \omega_i\sqrt{1 - \frac{\omega_c^2}{\omega_i^2}} \tag{3.3}$$

Using the distance $D$ between the sample and the detector ($D = 1.7$ m), we can get the relationship between $\Delta\omega$ and the spatial refraction of the direct beam $\Delta Z$ measured in the detector to be

$$\tan\Delta\omega = \frac{\Delta Z}{D} \iff \Delta\omega = \frac{\Delta Z}{D}$$

which is eventually

$$\Delta Z(\omega_i) = D \times \omega_i(1 - \sqrt{1 - \frac{\omega_c^2}{\omega_i^2}}) \tag{3.4}$$

Each ring presented on figure 3.7 has been fitted by a circle. This allowed to extract the ring center $Z$ position (green spots on figure 3.9) and to draw their evolution when omega varies. The comparison between the green spots and the red ones corresponding to the theoretical curve of equation 3.4 confirms that the centers of the rings correspond to the direct beam position, eventually refracted by the liquid crystal surface if the incident angle is small. We have therefore made a python code to calculate the direct beam position. In this code we have first combined all the ring positions $Y$ of maximum intensity of all

$\omega$ angles in one common array, all the $Z$ positions in another common array. The $Z$ position of the center of the ring would be given by

$$Z = Z_c + \Delta Z(\omega_i) + \sqrt{r^2 - (Y - Y_c)^2} \tag{3.5}$$

where $(Z_c, Y_c)$ is the direct beam position. We have thus used all positions of all rings, combined together and fitted by both the equation 3.4 and 3.5 to extract the best fit values of the direct beam position. They will be considered in the following of my manuscript as the direct beam coordinates.

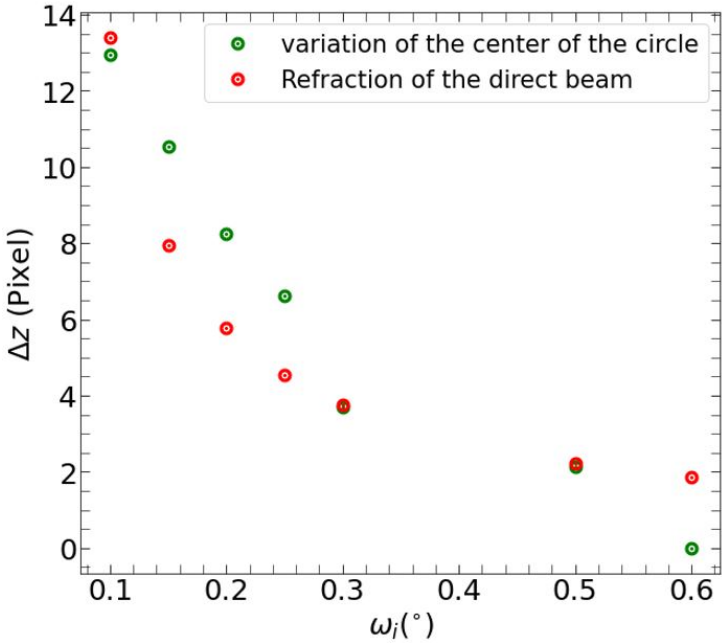


Figure 3.9: The comparison between the variation of the center of the ring and the shift of the direct beam due to its refraction on the air-film interface. The solid red circle is showing the shift of the direct beam for all values of the incident angle $\omega_i$.

### 3.2.4 Calculation of the correction of the refraction effects on the diffracted beam from the 8CB film

#### Refraction correction for the $q$ values

In section 3.2.3 we have introduced the extraction of the radial position $q$ of the maximum intensities.The radius of the scattering is given in $(nm^{-1})$ by

$$q = (\sqrt{(Z - Z_c)^2 + (Y - Y_c)^2})(\frac{2\pi sp}{D\lambda}) \tag{3.6}$$

where $sp$ is the size of a pixel on the detector. $D$ is the sample-detector distance and $\lambda$ is the wavelength of the X-ray beam that we have used. The orientation $\alpha$ along the scattering ring is given by

$$\alpha = \arctan\left(\frac{(Z - Zc)}{(Y - Yc)}\right) \tag{3.7}$$

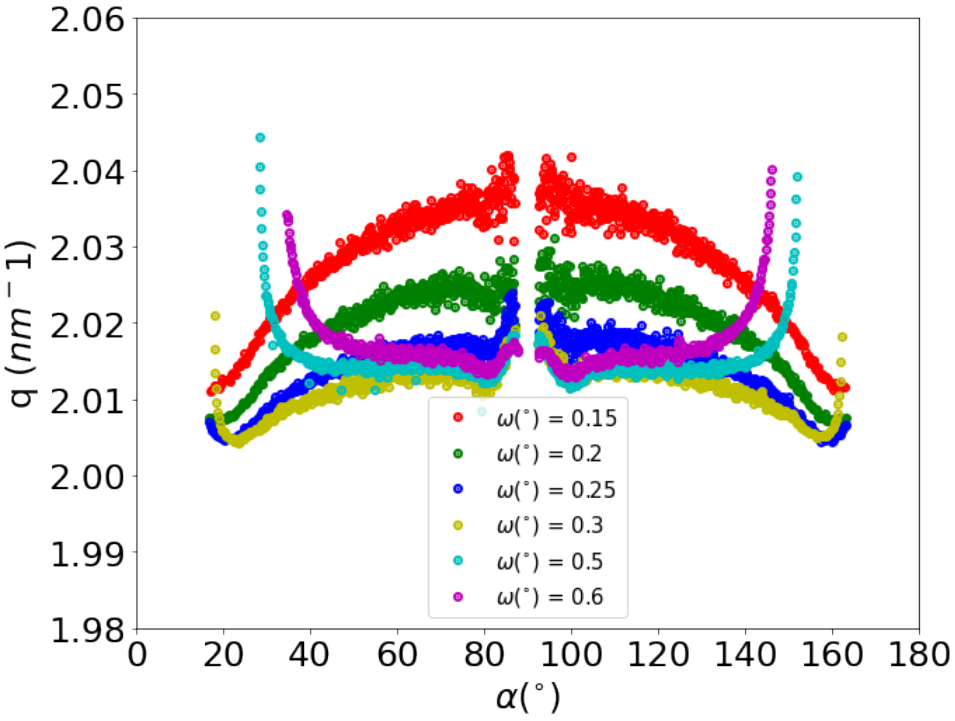


Figure 3.10: The wave vector transfer on the detector for the different omega values shown in different colors.

This equation 3.6 gives the values for $q$ measured on the detector and they are plotted in figure 3.10.

However, when an X-ray beam is impinged onto an 8CB thin film, it is refracted on the air-8CB interface (figure 3.8a). The refracted beam is diffracted by the molecules inside the film (the green beam in figure 3.8b) . This diffracted beam is also refracted as it exits the 8CB-air interface and hence, the signals we see on the detector are the refracted-diffracted beam. Therefore, we need the exact values of the wave vector transfer inside the $8CB$ film i.e the value corrected from the refraction on both the incident and exiting beam. This is the aim of this section.

We know that the magnitude of the wave vector transfer in air $K_o = \frac{2\pi}{\lambda}$, where $\lambda$ is the wavelength of the X-ray beam being used. We also know the refractive index of the 8CB $n_{8CB} = 1 - \delta_{8CB}$ where $\delta_{8CB} = 8.57 \times 10^{-7}$ which is the dispersion constant for 8CB. There are two laws of optics that relate the wave vector in air $\overrightarrow{K}$ to the wave vector in the 8CB film $\overrightarrow{k}$. The first one is that the parallel components of the wave vector are conserved i.e $\overrightarrow{K}_{\parallel} = \overrightarrow{k}_{\parallel}$. The second law is $k_o = nK_o$ where the $k_o$ and $K_o$ are the magnitudes of the wave vector in the 8CB film and air respectively.

In figure 3.8a, we considered (x,y,z) the sample orthogonal coordinate system where $x$ and $y$ are parallel to the sample surface plane with $z$ being the normal to this surface. We also consider (X,Y,Z) as the detector orthogonal coordinate system such that $Y$ is parallel to the direct beam. Both $X$ and $Y$ form a plane which is parallel to the surface and perpendicular to the detector. The vertical $Z$ is parallel to the detector. We take the position of the direct beam without refraction as the origin of the two coordinate systems. If the beam impinges onto the sample through an angle $\omega_i$, which is done by rotating the sample around $X - axis$ , we will need to do a transformation of the coordinates from detector frame to the sample frame.

Let's start our calculation working in the sample coordinate system. Using the above two laws of the optics on the 3.8, we can easily get the Snell's law of refraction as follow:

$$\begin{cases} \cos\omega_i = n_{8CB}\cos\omega_{ri}^{'} & \text{(3.8a)} \\ \cos\omega_{ef} = n_{8CB}\cos\omega_{sf}^{'} & \text{(3.8b)} \end{cases}$$

Knowing the refractive index of the 8CB film we can found that the critical angle is $\omega_c = 0.075°$. Since we want to find the wave vector transfer inside the 8CB film, we start by the known law of diffraction in the film that the wave-vector transfer $q_{film}$

(see figure 3.8) is given by

$$\overrightarrow{q_{film}} = -\overrightarrow{k_{ri}} + \overrightarrow{k_{sf}} \tag{3.9}$$

and its component in z-direction is given by $qz_{film} = -k_{riz} + k_{sfz}$ The equation 3.9 can be written as

$$qz_{film} = k_o(\sqrt{1 - \cos^2(\omega'_{ri})} + \sqrt{1 - \cos^2(\omega'_{sf})}) \tag{3.10}$$

This equation can be written as

$$qz_{film} = K_o(\sqrt{n^2_{8CB} - \cos^2(\omega_i)} + \sqrt{n^2_{8CB} - \cos^2(\omega_{ef})}) \tag{3.11}$$

Similarly to Babonneau et al. [10] this equation can be rewritten as

$$qz_{film} = \sqrt{-K^2_{cz} + K^2_{iz}} + \sqrt{-K^2_{cz} + K^2_{efz}} \tag{3.12}$$

Where the critical wave vector transfer $K_c = q_c$ is given by $\frac{2\pi}{\lambda}\sin\omega_c$ [11].

We need to use the value of the refracted-diffracted beam $K_{efz}$ in the equation 3.12 to get an expression that is in function of all known parameters. The wave-vector transfer $q$ on the detector is usually found in the literature as

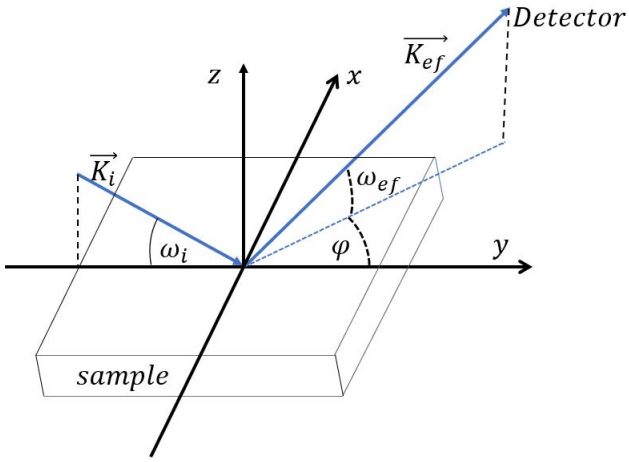


Figure 3.11: Grazing-incident in reflection geometry

$$\begin{cases} \overrightarrow{K_{ef}} = \overrightarrow{q} + \overrightarrow{K}_i & \text{(3.13a)} \\ \implies K_{efz} = qz - K\sin(\omega_i) & \text{(3.13b)} \end{cases}$$

Using equation 3.13 and 3.11 we can express it in a similar way as in literature[11, 12, 13, 14].

$$qz_{film} = \sqrt{-(K_o\sin\omega_c)^2 + (K_o\sin\omega_i)^2} + \sqrt{-(K_o\sin\omega_c)^2 + (qz - K_o\sin\omega_i)^2}$$

However, in our case, we want to relate $qz_{film}$ inside the film with the real values of the exiting refracted-diffracted beam in the sample frame. This can be achieved by a coordinates transformation from detector frame to the sample frame as follow:

$$\begin{pmatrix} K_{efx} \\ K_{efy} \\ K_{efz} \end{pmatrix} = \begin{pmatrix} 1 & 0 & 0 \\ 0 & \cos\omega_i & \sin\omega_i \\ 0 & -\sin\omega_i & \cos\omega_i \end{pmatrix} \begin{pmatrix} K_{efX} \\ K_{efY} \\ K_{efZ} \end{pmatrix} = \begin{pmatrix} K_{efX} \\ \cos\omega_i K_{efY} + K_{efZ}\sin\omega_i \\ -\sin\omega_i K_{efY} + K_{efZ}\cos\omega_i \end{pmatrix} \tag{3.14}$$

We thus obtain:

$$qz_{film} = \sqrt{-(K_o \sin\omega_c)^2 + (K_o \sin\omega_i)^2} + \sqrt{-(K_o \sin\omega_c)^2 + (-\sin\omega_i K_{efY} + K_{efZ}\cos\omega_i)^2} \tag{3.15}$$

We can write the coordinate of the refracted-diffracted beam in the detector in the polar coordinates as

$$\begin{cases} K_{efX} = q\cos\alpha \\ K_{efY} = \sqrt{K_o^2 - K_{efX}^2 - K_{efZ}^2} \\ K_{efZ} = q\sin\alpha \end{cases} \tag{3.16}$$

where $q$ and $\alpha$ are the measured parameters that are obtained from the 2D detector analysis and we get the following equation

$$qz_{film} = \sqrt{-(K_o \sin\omega_c)^2 + (K_o \sin\omega_i)^2} + \sqrt{(-\sin\omega_i \sqrt{K_o^2 - q^2} + (q\sin\alpha)\cos\omega_i)^2 - K_{cz}^2} \tag{3.17}$$

The exact value of the wave vector in the sample right before the refraction on the 8CB-air interface is

$$q_{film} = \sqrt{qz_{film}^2 + qx_{film}^2} \tag{3.18}$$

where $qx_{film} = K_{efX}$ i.e $q_{film}\cos(\alpha_{film}) = q\cos(\alpha)$ and

$$q = (\sqrt{(Z - Z_c)^2 + (Y - Y_c)^2}) * (\frac{2\pi * sp}{D\lambda})$$

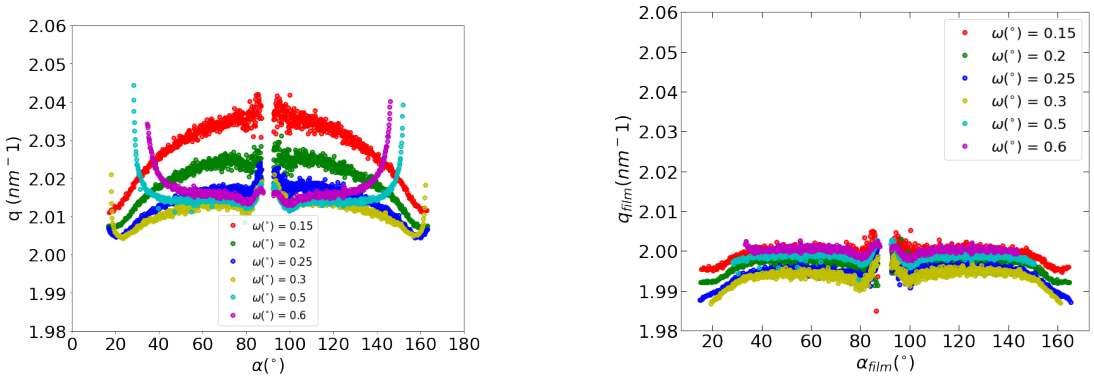


(a) (b)

Figure 3.12: (a) The raw value of the wave vector transfer on the detector (b) The wave vector transfer inside the 8CB film.

This $qx_{film}$ expression gives $\alpha_{film}$ as

$$\alpha_{film} = \arccos(\frac{q\cos(\alpha)}{q_{film}}) \tag{3.19}$$

$\alpha_{film}$ is the orientation of the wave vector transfer inside the film and we found that its difference from the orientation $\alpha$ of the wave vector transfer on the detector is negligible. From now on, we will be using the determination of $\alpha$. Figure 3.12 is showing the comparison between the raw values of the wave vector transfer $q$ on the detector (the refraction effect are not corrected) and the corrected values $q_{film}$ inside the sample which is plotted as a function of $\alpha_{film}$ whereas $q$ is plotted as a function of $\alpha$. The corrected $q_{film}$ values appear to have lost the border effects related to refraction. All $q$ curves for different incident angle $\omega$ values are very similar and almost superimposed in agreement with $q$ values almost independent of the incident angles. Once normalized all $q_{film}$ for different $\omega$ perfectly superimpose as shown by figure 3.13. In the following we will use these

superimposed curves to discuss the $q_{film}$ evolution when alpha varies in chapter 4. We are now able to get the exact values of $qz_{film}$ and hence the exact values of the interlayer layer spacing. These $q_{film}$ values will be used to reconstruct the intimate structure of the hemicylinder in chapter 4. $d$ will be written as $\frac{2\pi}{q}$ in the following. We can already observe how well defined are the $q$ curves once corrected. The variation with alpha are clearly visible whereas they are very small, of around 3 pixels in overall.

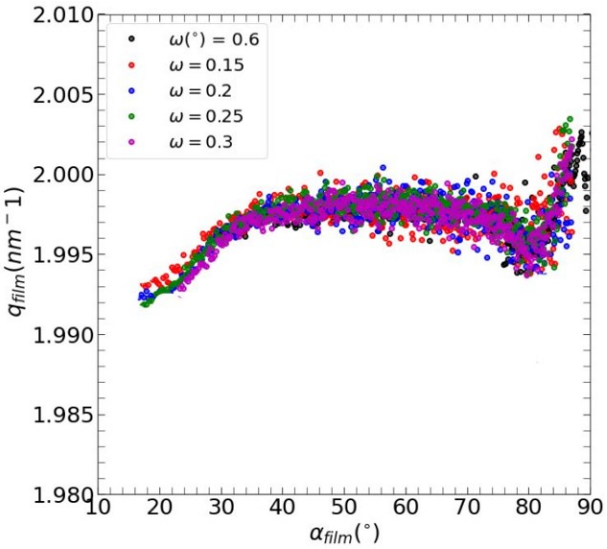


Figure 3.13: Evolution of normalized $q_{film}$ values as a function of $\alpha$

### Determination of the horizon

Let's take from equation 3.17 the part in the second square root and let's write it in details as follow

$$\left(\sqrt{(-\sin\omega_i\sqrt{1-(\frac{q}{K_o})^2}+\frac{1}{K_o}(q\sin\alpha\cos\omega_i))^2-\sin^2\omega_c}\right) \tag{3.20}$$

After replacing it the above equation 3.17 and neglecting all term with $K_o^2$ we get

$$qz_{film}\approx K_o\left(\sqrt{\sin^2\omega_i-\sin^2\omega_c}+\sqrt{(-\sin\omega_i+\frac{1}{K_o}(q\sin\alpha\cos\omega_i))^2-\sin^2\omega_c}\right) \tag{3.21}$$

where $K_o=\frac{2\pi}{\lambda}$ and $q=\frac{2\pi}{d}$, $d$ the inter-layers distance for the $8CB$ smectic A liquid crystal thin film, $\lambda=0.067nm$ The part inside the square root corresponds to the exiting beam. It has to be positive and zero at the horizon. We can thus write

$$\begin{cases}(-\sin\omega_i+\frac{1}{K_o}(q\sin\alpha\cos\omega_i))^2-\sin^2\omega_c\geq 0\\ \frac{1}{K_o}(q\sin\alpha\cos\omega_i)\geq\sin\omega_i+\sin\omega_c\end{cases} \tag{3.22}$$

Since the incident $\omega_i$ is small we can write $\frac{1}{K_o}(q\sin\alpha)\geq\omega_i+\omega_c$, an expression which gives the critical angle of orientation of the wave vector $\alpha_c$ below which no exiting beam can be seen on the detector since this beam is below the horizon

$$\alpha\geq\arcsin\left\{(\frac{d}{\lambda}(\omega_i+\omega_c))\right\}(\frac{180}{\pi}) \tag{3.23}$$

$$\alpha_c=\arcsin\left\{(\frac{d}{\lambda}(\omega_i+\omega_c))\right\}(\frac{180}{\pi}) \tag{3.24}$$

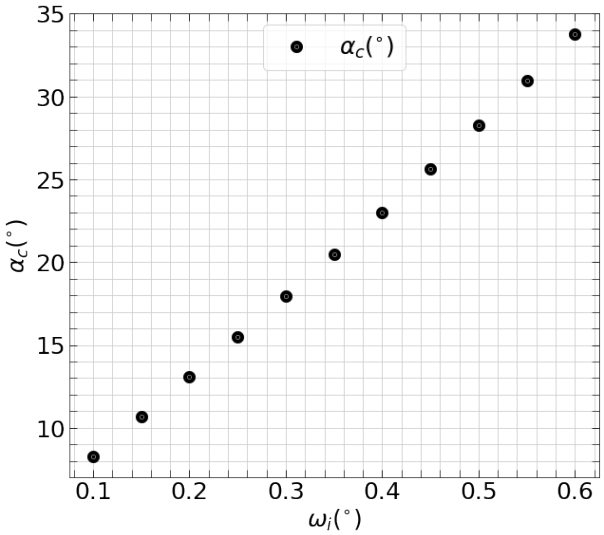


Figure 3.14: Evolution of the critical orientation $\alpha$ as a function of the incident angle $\omega$.

Using equation 3.24, we have plotted the figure 3.14. From this figure we can see that as the incident $\omega_i$ increases the critical angle $\alpha_c$ increases also. This explains the reason why in figure 3.7, as the incident angle increases, the scattering ring is becoming smaller since the horizon is also increasing. For small incident $\omega_i$ the critical alpha is much smaller and as a result, the scattering ring is larger, with scattering data on a broad range At large $\omega_i$ for example $0.6^\circ$, the scattering ring has become much smaller as it can be seen in figure 3.7 and we miss a number of $\alpha$ values.

### 3.2.5 Comparison of the experimental wave vector transfer $q$ values from different measurement techniques

Up to now we have seen three different but complementary techniques to measure the intensity scattered by the smectic layers inside the hemicylinders. The first one is associated with the TSAXS set-up, allowing to measure the scattered signals from the perpendicular layers on the substrate and its variation when $\alpha$ increases but on a small rang of $\alpha$ values. The second one is the one using the measurement of intensity scattered by rotating smectic layers in the edges of the hemicylinders. We see on figure 3.7 that the signal from the huge stack of central layers is hidden by a dead area in the detector. The corresponding position of the detector is called $eix = 0$. The third one is aimed at measuring the signal scattered by the central layers at $\alpha^\circ = 90^\circ$. It is done with the detector displaced (we name the corresponding position of the detector, $eix = -10$). For the 180 $nm$ thick sample, we have extracted the curves of wave vector transfer of magnitude $q$ as a function of orientation $\alpha$. The comparison of the $q$ values from these three techniques is shown in figure 3.15. Different values of $q$ are observed. The last two techniques gave values which have similar variation as a function of $\alpha$, however the $eix = -10$ data have an offset $0.019\ nm^{-1}$ with respect to those of $eix = 0$. If this offset is removed then the two values will almost perfectly superimpose. The TSAXS values are much larger than those from both $eix = 0$ and $eix = -10$ .The fact that $eix = 0$ and $eix = -10$ $q$ values have the same variation as a function of $\alpha$ assures us that the $\alpha$ variation is true. The reason why the displacement of the detector ( in TSAXS measurements, it is a $90^\circ$ rotation of the sample) induced offsets in the $q$ values, whereas the direct beam does not vary is not clear. It tells us that we are only able to measure very precisely relative values but not so precisely absolute values of q. In other words we have an uncertainty in the measurement of absolute q values. Based on figure 3.15 we can estimate the average absolute $q$value to to be $2.01\ nm^{-1} \pm 0.02\ nm^{-1}$. The bulk value of the wave vector transfer in literature is $1.99\ nm^{-1}$ [15, 16]. If the calculated value is compared with the experimental values then it seems that the value that we measure is consistent with the one of the literature if the uncertainty is taken into account. the one form the literature, even taking into account the previously discussed uncertainty.

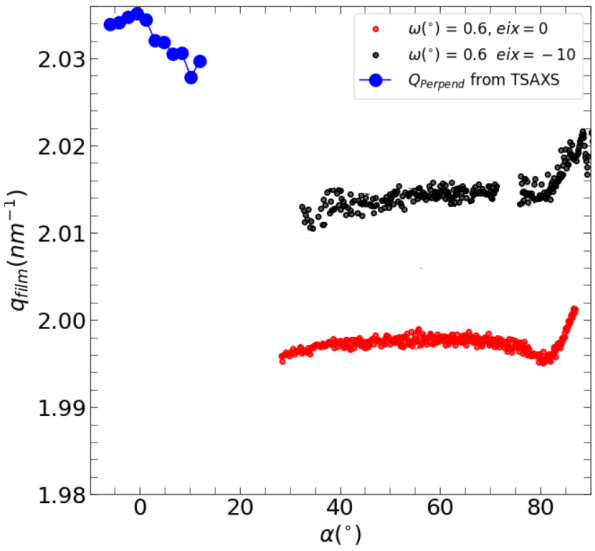


Figure 3.15: Comparison of the $q_{film}$ values measured using different techniques. Blue is for the TSAXS measurement. Red is for the GISAXS with the detector at position eix = 0. Black is the GISAXS with the detector at position eix = -10

### 3.2.6 Extraction of maximum intensity from the scattering ring

**Maximum intensity from measurement at $\mu = 0$**

The evolution of the scattered intensities obtained after the line fitting for different incident angle $\omega$ at $\mu = 0$ are shown in figure 3.16 (where the detector was not shifted) and 3.17 (with the detector shifted). In figure 3.16(a) we see that non-normalized intensities are not superimposed. We hypothesised that since these intensities obtained for different $\omega$ values were scattered from the same 8CB thin film they should be similar. We have performed a normalization of these curves of intensities. This normalization consists in determination of a factor that could superimpose all these curves. The normalized intensities are shown in the figure 3.16(b) (for the data collected without shifting the detector) and 3.17(b) (with the detector shifted). From all these figures, we can see that even the normalized curved from different $\omega$ values, are not all superimposed, for instance the intensity curves of the $\omega = 0.6°$ and $\omega = 0.5°$ are not at all the same at large alpha. We will come back on them latter in section 3.3

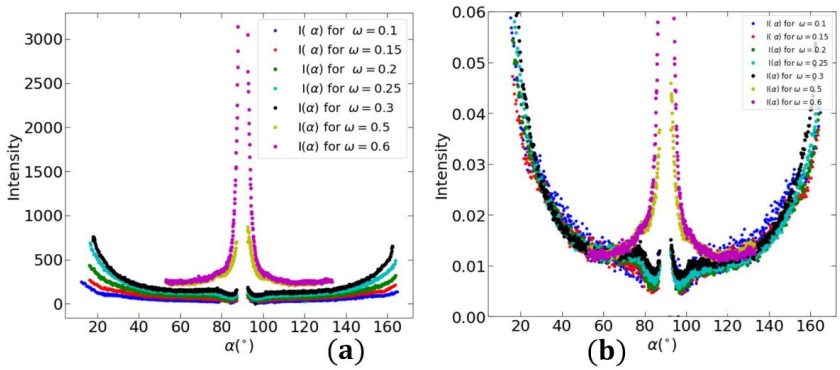


Figure 3.16: The evolution of (a) unnormalized intensities and normalized intensities (b) for all incident $\omega$ angles at $\mu = 0$.

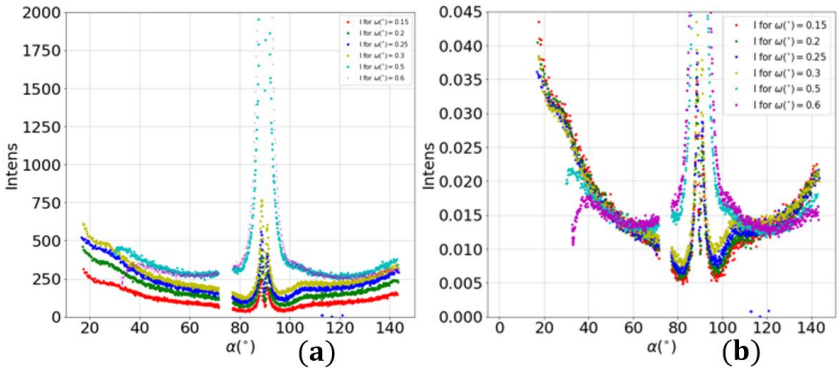


Figure 3.17: The non-normalized intensities (a) and normalized intensities (b) extracted with detector shifted to allow the signal from the central part of hemicylinder to reach on the detector.

### Maximum intensity from measurements with $\mu_{scan}$

To ensure that the Bragg condition is satisfied by the scattering smectic layers inside the hemicylinders, we had to systematically rotate our sample around the two axes: the Z-axis (vertical axis) through angle $\mu$ (we name the measurement procedure $\mu_{scan}$) and then rotation around the X-axis through angle $\omega$. Note that during the experiment the beam is fixed, so the variation of both $\mu$ and $\omega$ angles is done by rotating the sample rather than the X-ray beam. The $\mu_{scan}$ were performed between $-14^{\circ}$ and $14^{\circ}$ using a step of $0.09^{\circ}$ and counting time of 1 second. The counting for a very short time required a contrast enhancement. This was done in two steps. Firstly, we defined the position of the scattering ring as the position of maximum intensities along the ring that we have obtained from the extraction of data of the $\mu = 0$. Secondly, for a given $\alpha$ value, we have averaged the intensity measurements over 5 $\mu$ angles. This was possible because the scattering ring images were not shifted or rotated from one another, i.e.,they were in the same position on the detector for all $\mu$ values.

For all $\alpha$ values, this lead to curves of maximum intensity as function of $\mu$ as shown in the figure 3.18 for $\alpha = 75^{\circ}$ and $\omega = 0.6^{\circ}$. These curves were all fitted by a Gaussian function. As a result, the maximum intensity , its position ($\mu_{max}$), and full width at half maximum (FWHM) $\Delta\mu$ of the Gaussian peak for each $\alpha$ values were plotted as a function of angle $\alpha$. The curves of evolution of maximum intensities as a function of $\alpha$ are shown in 3.19. The normalization of these curves leads to well superimposed curves when $\omega$ varies contrary to the their corresponding curves for $\mu = 0^{\circ}$ shown in figures 3.16(b) and 3.17(b). The evolution of the position of the maximum intensities $\mu_{max}$ will be discussed in section 3.3.2. The evolution of the FWHM ($\Delta\mu$) will be discussed in section 3.3.3.

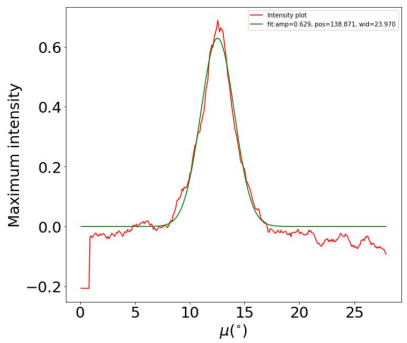


Figure 3.18: Maximum intensity extracted for alpha $75^{\circ}$


(a) (b)

Figure 3.19: The evolution as a function of $\alpha$ for different incident angles (a) unnormalized maximum intensities and (b) normalized intensities. They all come from the $\mu_{scan}$.

## 3.3 Determination of Bragg condition

We have seen that a confined 8CB smectic liquid crystal film is distorted into array of periodic stripes. Each of them is a flattened hemicylinder formed by various topological defects. The necessity of a more precise understanding of the hemicylinder internal structure is inevitable and requires the ascertainment of the Bragg condition to build in return a fully accurate model of the distorted smectic layers.

The scattering rings shown in figure 3.7 depict the intensity scattered by smectic layers whose normal is parallel to the wave vector transfer $\vec{q}$ that is oriented at angle $\alpha$. In this section we will see that not every scattering ring at whatever incident angle $\omega$ satisfies the Bragg condition.

Moreover, during the experimental measurement, we have met with a difficulty of measuring non-perfect oriented sample with respect to the incoming beam. In other words, despite an initial as much accurate as possible procedure of orienting the sample with respect to the X-ray beam, we have finally not measured samples of stripes perfectly parallel to the X-ray beam. As a result, we sometime observed asymmetric scattering rings. In this section we will also present the technique we have developed to solve this issue of misorientation.

### 3.3.1 The theoretical position $\mu_{Bragg}$ of Bragg intensity

We have developed two complementary procedures to determine the Bragg's condition for the smectic layers inside the hemicylinder. The first one is theoretical and the second one is experimental. I will first describe the theoretical procedure. The experimental procedure consists in measuring $\mu_{max}$ as described earlier. A theoretical $\mu_{Bragg}$ Bragg's formula has been developed, using the two rotation matrices named $R_x$ and $R_z$. The values of $\mu_{Bragg}$ are the theoretical position of the Bragg intensity for a fixed incident $\omega$. The matrix $R_x$ corresponds to the $\omega$-rotation around the X-axis which is perpendicular to both the direction of the sample stripes and Z-axis. The matrix $R_Z$ corresponds to the $\mu_{scan}$ around the Z-axis ( see Figure 3.2a ).

The final resultant rotation matrix has been found taking into account the correct rotation order during the experiment at Soleil Synchrotron.

$$R_x \times R_z = \begin{pmatrix} 1 & 0 & 0 \\ 0 & \cos\omega & -\sin\omega \\ 0 & \sin\omega & \cos\omega \end{pmatrix} \begin{pmatrix} \cos\mu & -\sin\mu & 0 \\ \sin\mu & cos\mu & 0 \\ 0 & 0 & 1 \end{pmatrix}$$

$$\begin{pmatrix} \overrightarrow{e_x} \\ \overrightarrow{e_y} \\ \overrightarrow{e_z} \end{pmatrix} = \begin{pmatrix} \cos\mu & -\sin\mu & 0 \\ -\cos\omega\sin\mu & \cos\omega\cos\mu & -\sin\omega \\ \sin\omega\sin\mu & \cos\mu\sin\omega & \cos\omega \end{pmatrix} \begin{pmatrix} \overrightarrow{e_X} \\ \overrightarrow{e_Y} \\ \overrightarrow{e_Z} \end{pmatrix}$$

We have assumed that we are in Bragg condition. The reciprocal vector associated with the rotating layers whose normal is orientated at angle $\alpha_{film}$ from the substrate is denoted by $q_{film}$.

$$\overrightarrow{q}_{film} = q_{film}\left[\cos(\alpha_{film})\overrightarrow{e_x} + 0\overrightarrow{e_y} + \sin(\alpha_{film})\overrightarrow{e_z}\right]$$

where $\overrightarrow{e_x}$, $\overrightarrow{e_y}$, and $\overrightarrow{e_z}$ are the unit vectors in the sample reference frame and $\overrightarrow{e_X}$, $\overrightarrow{e_Y}$, and $\overrightarrow{e_Z}$ are the unit vectors in the detector reference frame (see Figure 3.8). The Bragg diffraction is obtained when the scattering wave vector or the momentum wave vector transfer $\vec{q}$ is the reciprocal lattice vector $\overrightarrow{q}_{film}$ with $qx_{film} = q\sin\alpha$ and $qz_{film} = q\cos\alpha$. So the reciprocal wave vector has to equate the wave vector transfer $\vec{q} = \vec{k_{ef}} - \vec{k_i}$, where $\vec{k_i} = (0\overrightarrow{e_X} + k\overrightarrow{e_Y} + 0\overrightarrow{e_Z})$, since the incoming beam is parallel to the Y-axis. However, prior to this step, we have to first write the reciprocal wave vector transfer in terms of the unit vectors of the detector frame.

$$\overrightarrow{q}_{film} = q_{film}\begin{pmatrix}\cos\mu & -\cos\omega\sin\mu & \sin\omega\sin\mu\\ -\sin\mu & \cos\omega\cos\mu & \cos\mu\sin\omega\\ 0 & -\sin\omega & \cos\omega\end{pmatrix}\begin{pmatrix}\cos\alpha\\ 0\\ \sin\alpha\end{pmatrix}$$

$$\overrightarrow{q}_{film} = q_{film}\left[(\cos\mu\cos\alpha + \sin\omega\sin\mu\sin\alpha)e_X + (-\sin\mu\cos\alpha + \cos\mu\sin\omega\sin\alpha)e_Y + (\cos\omega\sin\alpha)e_Z\right]$$

As we have said before, for the diffraction to be obtained or the Bragg condition to be satisfied, the momentum wave vector transfer has to be equal to the reciprocal lattice vector. That is $\overrightarrow{q}_{film} = \vec{q} \Longleftrightarrow \overrightarrow{q}_{film} + \vec{k_i} = \vec{k_f}$

Considering that we have elastic scattering, we can get $|\vec{k_f}| = |\vec{k_i}| = k$ and $|\overrightarrow{q}_{film} + \vec{k_i}| = k$ and write

$$\overrightarrow{q}_{film} + \vec{k_i} = q_{film}\left[(\cos\mu\cos\alpha + \sin\omega\sin\mu\sin\alpha)\overrightarrow{e_X} + (-\sin\mu\cos\alpha + \cos\mu\sin\omega\sin\alpha + \frac{k}{q_{film}})\overrightarrow{e_Y} + (\cos\omega\sin\alpha)\overrightarrow{e_Z}\right]$$

Using the relation $|\overrightarrow{q}_{film} + \vec{k_i}|^2 = k^2$ we can get the following equation

$$q_{film} + 2k\sin\alpha\sin\omega\cos\mu + 2k\cos\alpha\sin\mu = 0$$

where $q_{film} = q$. From this equation We get

$$\mu_{Bragg} = \arcsin\left(\frac{(\frac{q}{\kappa})\cos\alpha \pm (\sin\alpha\sin\omega)\sqrt{(\cos\alpha)^2 + (\sin\alpha\sin\omega)^2 - (\frac{q}{\kappa})^2}}{(\cos\alpha)^2 + (\sin\alpha\sin\omega)^2}\right) \tag{3.25}$$

, where $\kappa = 2k$ or $\kappa = \frac{4\pi}{\lambda}$ and $q = \frac{2\pi}{d}$, $d$ is the interlayer distance, $\lambda$ is the wavelength of the X-ray beam we have used and $\alpha$ is the orientation of the normal of the smectic layers.The equation 3.25 has a positive and a negative solutions. I will discuss which solution to choose in the next subsection 3.3.2.

### 3.3.2 The experimental position, of Bragg intensity

#### Comparison of the calculated Bragg $\mu_{Bragg}$ angles with the experimental $\mu_{max}$

We have then plotted the experimental value of the position of the maximum intensity $\mu_{max}$ and the theoretical values $\mu_{Bragg}$ in figure 3.20a. It is showing an almost perfect superimposition of the theoretical $\mu$-Bragg values (shown in green and blue) obtained using equation 3.25, with the experimental $\mu$-max values (shown in red color) for incident angle $\omega = 0.25$. Similar agreements were obtained also for other incident angles $\omega$. The equation 3.25 is formed by two solutions, a positive and negative solutions. Each of them is correct for only a particular $\alpha$ range. The positive solution (in blue) is superimposed with the experimental values from $\alpha = 0^\circ$ to $\alpha = 89.4^\circ$ and the negative solution (in green) is superimposed with the experimental values from $\alpha = 90.6^\circ$ to $\alpha = 180^\circ$. This superimposition evidences that all our experimental $\mu_{max}$ rotation values are the $\mu$-Bragg angles, and their corresponding normalized intensities in 3.19b are Bragg intensities. This result evidences the reason why the normalization in figures 3.16 and 3.17 was not superimposing the intensities for all $\alpha$ values. The regions where the superimposition was not possible correspond to the regions where the data were not in Bragg condition. In contrast the intensities shown on figure 3.19 that correspond to $I_{max}$ are Bragg intensities and superimpose.

We have used the famous formulae of Bragg condition $2d\sin(\omega) = \lambda$ to calculate the incident Bragg angle for the 8CB smectic liquid crystal sample. We have two main parameters to get the value of $\omega_{Bragg}$. Notably the wavelength of the X-ray beam of energy 18.44 KeV that we have used and the interlayer distance $d = 3.16\ nm^{-1}$ for 8CB smectic liquid crystal as it was demonstrated by Leadbetter et al. [15]. Using these parameters we have obtained $\omega_{Bragg} = 0.6^\circ$.

On figure 3.20, we observe that if $\omega$ is strictly smaller than $0.6^\circ$, $\mu_{Bragg}$ varies from $-0.6^\circ$ to $-90^\circ$, then from $+90^\circ$ to $0.6^\circ$. However, if $\omega = \omega_{Bragg} = 0.6^\circ$ (green curve on figure 3.19b), $\mu_{Bragg}$ only varies from $-0.6^\circ$ to $+0.6^\circ$.

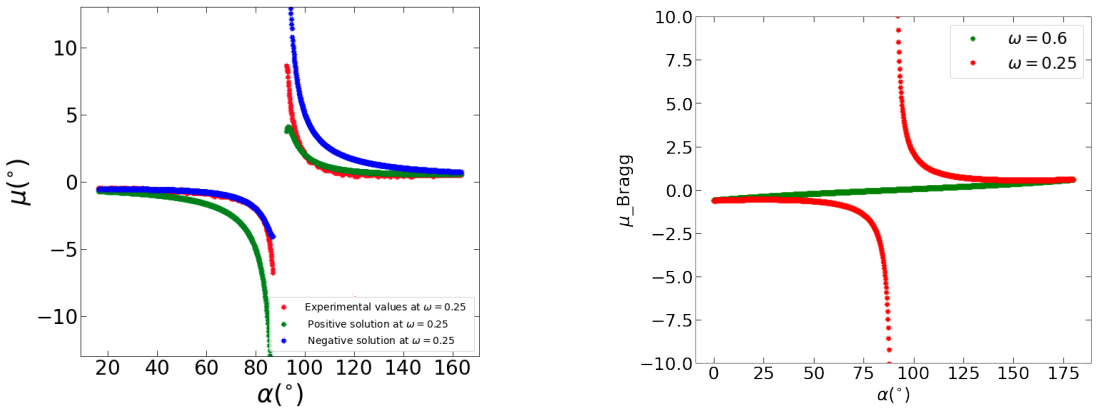


(a) (b)

Figure 3.20: Comparison of the evolution of the theoretical $\mu_{Bragg}$ and the position of the maximum intensities along the circle of $\omega = 0.25°$ as a function of $\alpha$ (a) and the evolution of the evolution of the $\mu_{Bragg}$ curves when omega increases from $0.25°$ to $0.6°$. (b)

### 3.3.3 Evolution of the width $\Delta\mu$ of the diffraction ring from $\mu_{scan}$ measurement

During the sample preparation, we rubbed the 8CB thin film deposited on the PVA substrate to impose the uniform planar anchoring (see chapter 1). The rubbing induces undulations along the hemicylinders in the direction of the stripes that can be considered as equivalent to a mosaicity in X-ray data. This hemicylinder mosaicity was measured using the $\mu_{scans}$ measurement. It is associated with the $\Delta\mu$ , the full width at half maximum of the Bragg peak of intensity obtained during the $\mu_{scans}$. In figure 3.21, we can see that $\Delta\mu$ is almost constant between $3°$ and $3.5°$ for all orientation $\alpha$. The variations that seem to occur for $80°$ are due to the fact that $\mu_{scan}$ are performed between $-14°$ and $+14°$ only, above $80°$ measurement they are not in strictly correct. The fact that this $\Delta\mu$ is independent of the $\alpha$ is compatible with the fact that we can attribute the $\Delta\mu$ to the undulation of the stripes. This is what is expected for a $\Delta\mu$ related to a non-perfect rubbing.

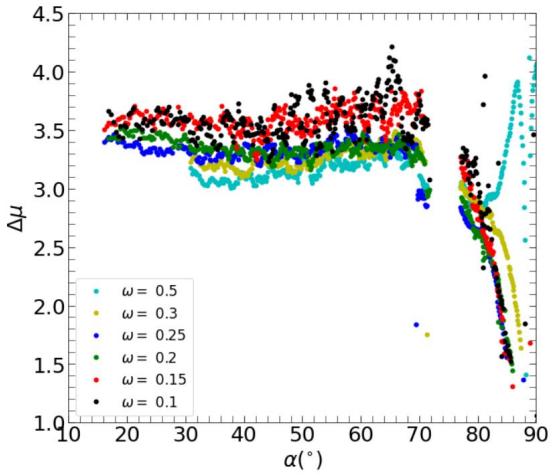


Figure 3.21: Evolution of $\Delta\mu$ as a function of $\alpha$ issued from the $\mu_{scan}$ measurement when the Eiger detector is on position $-10$ (as a result the beamstop hides the values between $\alpha = 68°$ and $\alpha = 75°$)

### 3.3.4 Bragg intensity

$\mu_{scans}$ obtained for each alpha values finally allowed to draw the Bragg intensity as a function of alpha (figure 3.19). However, isn't it possible to also draw Bragg intensity curves using the data obtained at $\mu = 0°$ ?. In figure 3.20b, it can been seen that for small $\alpha$ values of both $\omega = 0.25°$ and $\omega = 0.6°$, $\mu_{Bragg} = -0.6°$ ( this result is true for all $\omega$ between $0.1°$ and $0.6°$). Let's consider the Gaussian Bragg peak of intensity drawn as a function of $\mu$ shown in figure 3.18. It is characterized by a FWHM width $\Delta\mu$ around $3.5°$ on average. This width is shown in figure 3.21. It almost doesn't varies until $\alpha = 80°$, remaining between $3°$ and $3.5°$. Due to this large value of $\Delta\mu$, the intensity at $\mu = 0$ is close to the Bragg intensity until $\alpha = 70°$, since $\mu = 0°$ is close enough to $\mu = -0.6°$. Figure 3.20a indeed shows that it is only around $\alpha = 70°$ that $mu_{Bragg}$ becomes significantly different from $-0.6°$. This is indeed shown in figure 3.22, where the intensity at $\mu = 0$ (3.22(b)) is compared to the Bragg intensity (3.22(a)). For the case of intensity at $\mu = 0$, for most of $\omega$ values, the superimposition after normalization is perfect until $\alpha$ around $70°$. The Bragg condition is not satisfied between $\alpha$ around $70°$ and $90°$ for small incident $\omega$ values and this is why in this interval the superimposition is not possible. On the other hand, if $\omega = 0.6°$, the green curve of figure 3.20b shows that $\mu_{Bragg}$ only varies from $= -0.6°$ to $= +0.6°$. In other words if $\omega = 0.6°$, measurements performed at $\mu = 0°$ will always be in Bragg condition. Indeed on figure 3.21b the intensity at $\mu = 0°$ and $\omega = 0.6°$ are identical to the Bragg intensities of figure 3.22(a).

To get a full evolution of the Bragg intensity for all $\alpha$ for the measurement at $\mu = 0$, we consequently can combine the values at small $\alpha \leq 45°$ from small $\omega < 0.6°$ with the values at larger $\alpha \geq 45°$ from $\omega = 0.6°$. In such a case, the curve of intensity as a function of $\alpha$ obtained from $\mu = 0°$ data appear to be equivalent to Bragg intensities obtained from the $\mu_{scan}$.

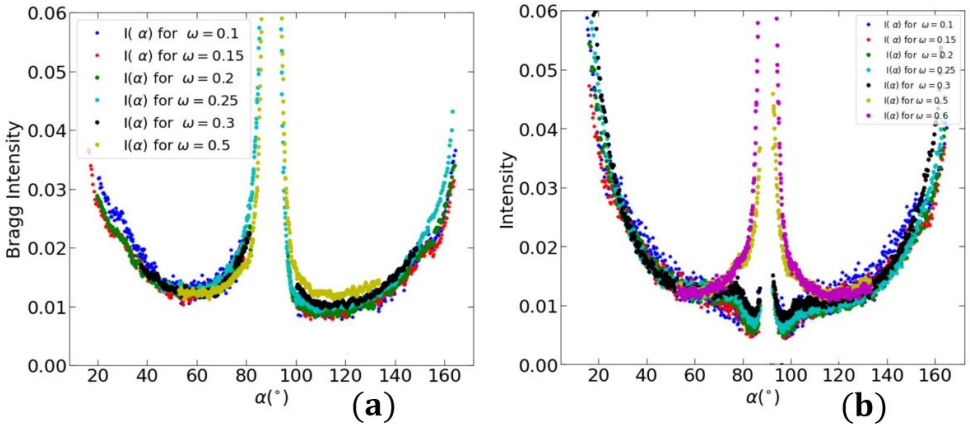


Figure 3.22: Comparison of profiles of Bragg Intensities issued for $\mu_{Bragg}$ (a) and maximum intensity issued from $\mu = 0$ measurement (b) at different incident angles $\omega$

Another way to get full evolution of the Bragg intensity was to perform a correction to the curves of maximum intensity obtained at $\mu = 0$. This correction is given by the equation 3.26 where the $I_{max}$ is the maximum intensity extracted from the scattering ring, the $\mu_{Bragg}$ are the position of Bragg intensities as described in section 3.3.2 whereas the $\Delta\mu$ has been described in section 3.3.5. This correction assumes simply that the curves of intensity as a function $\mu$ can be assumed to be a Gaussian peak of maximum intensity, $\mu = \mu_{Bragg}$. For the correction we consequently have to consider the difference between $\mu = 0°$ and $\mu = \mu_{Bragg}$ and its implication in the variation of the scattered intensity.

$$I_{Bragg} = I_{max} e^{(\frac{\mu_{Bragg}}{\Delta\mu})^2} \tag{3.26}$$

In figure 3.23, we have compared the maximum intensities from $\mu = 0$ (red color), their corresponding calculated Bragg intensities (blue) and the Experimental Bragg intensities (black) obtained with the $\mu_{scan}$. In this figure, I show that we were able to solve the issue at large $\alpha$ values.

During $\mu_{scan}$, we have measured for a given omega, 310 $\mu$ angles between $\mu = -14°$ and $\mu = 14°$. This implies that we do not have data in the range $-90° \leq \mu \leq -14°$ and $14° \leq \mu \leq 90°$. The evolution of $\mu$ angle as a function of $\alpha$ showed us

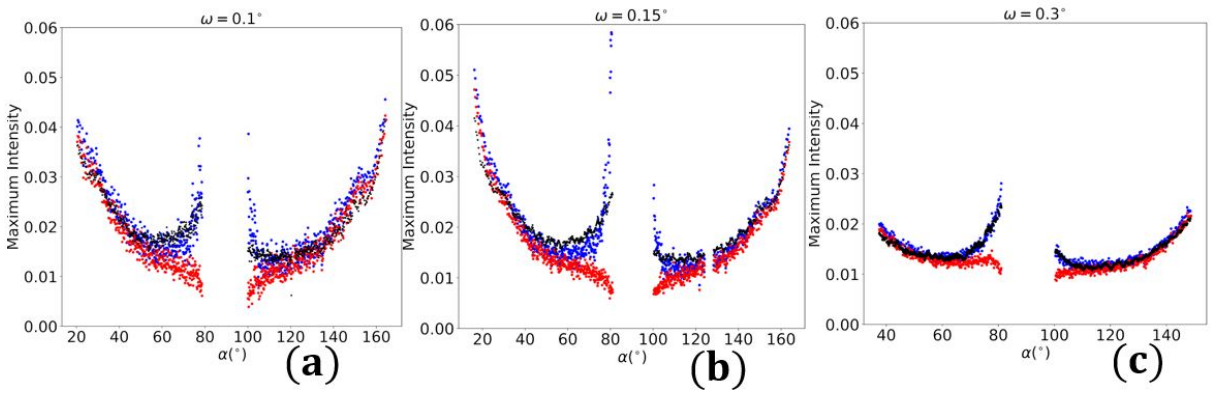


Figure 3.23: Thin film of 180 nm: Comparison of the maximum intensities collected at $\mu = 0°$ (red) with Bragg intensities (blue) calculated using equation 3.26, experimental Bragg intensities collected at $\mu_{scan}$ (Black) and for different diffraction incident angles $\omega$: (a) $\omega = 0.1°$, (b) $\omega = 0.15°$, (c) $\omega = 0.3°$.

that we can only measure up to $88°$ i.e. there is no data between $\alpha = 88°$ and $\alpha = 92°$ with the $\mu_{scan}$. For these measurements at very large $\alpha$, we used the detector displaced at position $-10$. The resulting scattering ring are shown in figure 3.3. Figure 3.17 is showing the data extracted from such a ring at $\mu = 0$.

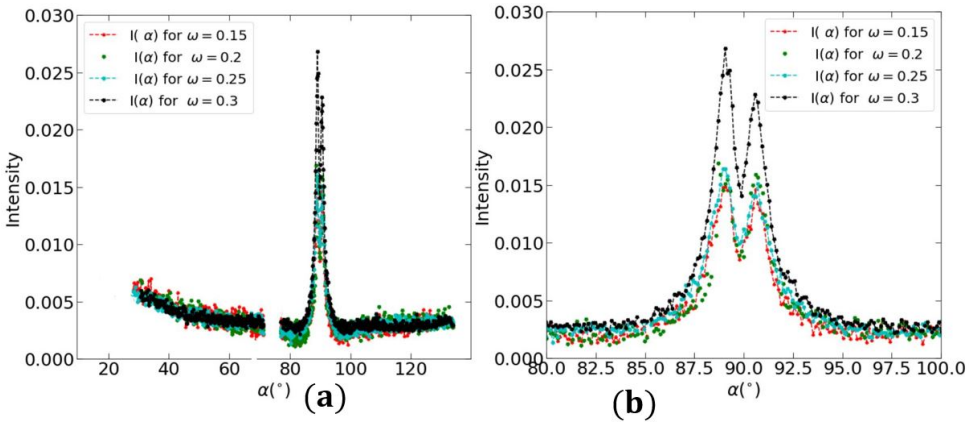


Figure 3.24: The Bragg intensity extracted at $\mu_{scan}$ with the detector shifted to allow the signal from the central part of the hemicylinder to reach on the detector (b) zoomed part showing the intensity from the central part of the hemicylinder.

As explained previously we have combined the data at small omega with data at $\omega = 0.6°$ to get the Bragg intensity complete at all $\alpha$ values. These results are shown in figure 3.24. They are crucial to obtain data at the upper part of the scattering ring (in figure 3.3(b) ) associated with the layers in the central part of the hemicylinder. The above results imply that the $\mu_{scan}$ measurements are not strictly necessary anymore to obtain the Bragg intensities for all alpha values.

### 3.3.5 Evolution of the width $\Delta$q of the diffraction ring

During the measurement at $\mu = 0$, we have seen that the intensity scattered from the smectic film is observed on the detector as a ring. For a given line $i$ on the image, the intensity extracted is a Gaussian peak and we fitted it using a Gaussian function as we have discussed before. The real width of the scattering ring is given by a radial width calculated from the full width at half

maximum of the Gaussian peak as discussed in section 3.2.2. Figure 3.25a exhibits curves of $\Delta q$ as a function of $\alpha$ for different $\omega$ i.e $\Delta q(\alpha, \omega)$.These values depend on the value of the $\omega$ and whether or not, the Bragg condition is satisfied. It is satisfied for all small $\alpha$ less or equal to $70^\circ$ for small $\omega$ whereas it is satisfied for all $\alpha$ values for $\omega = 0.6$. As we have seen for the intensity extracted from scattering obtained at $\mu = 0$, the value at large $\alpha$ value, do not correspond to the Bragg condition. If the incident angle $\omega$ is smaller than $0.6^\circ$. the enormous increase in value of $\Delta q$ around $\alpha = 90^\circ$ for small $\omega$ does not correspond to the Bragg condition. Hence, we have discarded it from our analysis. In this central area around $90^\circ$ we have considered only the values from $\omega = 0.6^\circ$

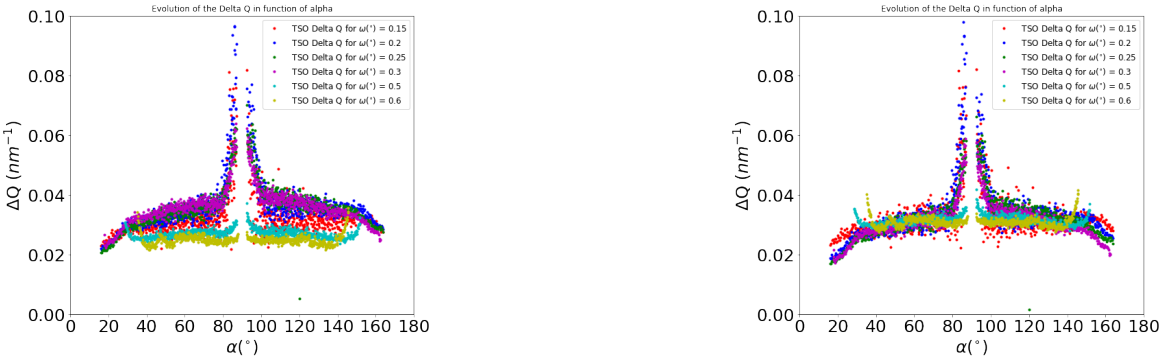


(a) (b)

Figure 3.25: Evolution of raw width ($\Delta q$ values) of the diffraction rings as a function of $\alpha$ extracted when the Eiger detector was on the position 0 (a) Evolution of the width of the diffraction rings for different incident $\omega$ after the refining procedure.

To obtain the complete profile of the curve of $\Delta q$ in Bragg condition for all $\alpha$ value we have combined the values of $\omega$ $0.25^\circ$ and $0.3^\circ$ for small $\alpha$ i.e $\alpha \leq 70$ and those from $\omega = 0.6^\circ$ for $\alpha > 70$. The resulting curve is shown in figure 3.26 below

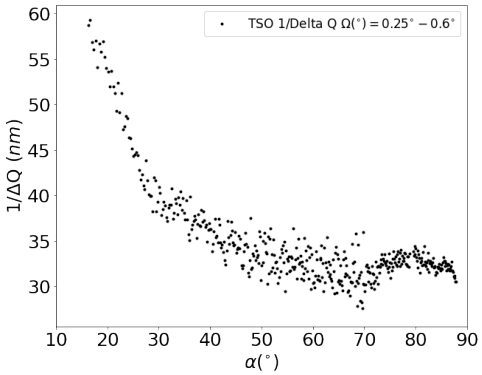


Figure 3.26: Evolution of $\Delta q$ as a function of $\alpha$ which comes from the $\mu = 0^\circ$ measurement when the Eiger detector is on position 0

The $\Delta q$ values can be due to three factors:

- Finite size effect, where in our case we are considering the variation of the number diffracting smectic layers. We will come back to this effect in chapter 4.

- The quality of order. If somewhere in the hemicylinder, there is a not too small area with varying $q$ values, it may affect the average $\Delta q$ that is measured.
- Resolution which is the length of the transfer if we convert to the size.

The experimental resolution has been calculated by the Soleil-SIXS beamline team. It is smaller than $0.015\ nm^{-1}$, a value two times smaller than the measured $\Delta q$ (figure 3.25b). Then we remain with two factors affecting our experimental $\Delta q$ notably the finite size effect and the disorder influence.

### 3.3.6 Integrated Bragg Intensity

The precise understanding of the intimate structure of the topological defect in the hemicylinders which constitute a thin smectic film confined between antagonistic anchoring requires an integrated Bragg intensity. In chapter 2, we have seen that the integrated integrated intensity is proportional to the product of the scattered Bragg intensity, $\Delta\mu$, and $\Delta q$.

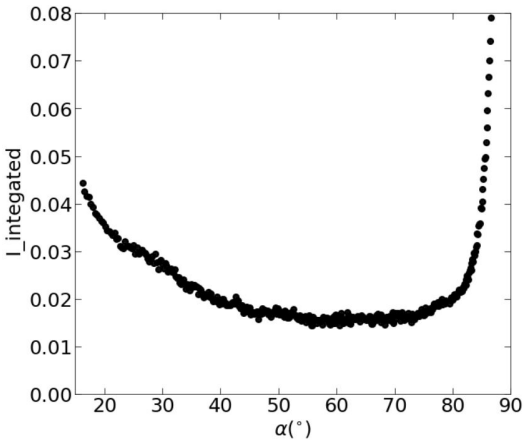


Figure 3.27: Evolution of Integrated Bragg intensity as a function of $\alpha$ from a combination of omega $0.25°$ and $0.6°$(b)

In previous sections we have shown that for small incident angle $\omega$ i.e $(0.1°, 0.15°, 0.2°, 0.25°, 0.3°$ and $0.5°$ ) the Bragg condition is satisfied only for small $\alpha$ i.e until around $70°$. For $\omega = 0.6°$ we are in Bragg condition for all $\alpha$ angle. We have then combined the data from the small omega i.e $\alpha$ values between $0°$ and $70°$ and then between $70°$ and $90°$ for $\omega = 0.6°$. The resulting Bragg intensity was multiplied by the $\Delta q$ and $\Delta\mu$ to find the integrated intensity. The profile of the obtained Integrated Bragg Intensity for the sample of thickness $180\ nm$ is shown in figure 3.27. For the reconstruction of the smectic layer structure we also need the $\Delta q$ curve in figure 3.26 and the $q$ curve in figure 3.12b.

### 3.3.7 Correction of sample misorientation-based asymmetry

We have seen in the previous sections that the scattered intensity from the hemicylinder is symmetric with respect to the position of the direct X-ray beam. For example in figure 3.22, the curves of intensity from measurement at $\mu = 0$ as well as $\mu_{scan}$ are symmetric. However, this was not always the case during our experimental measurements. We have sometime obtained asymmetric scattering rings as shown in figure 3.28. In figure 3.28 (a) and 3.28 (b), we can see that the signal below the central part of the scattering ring is not as bright and wide as the part above it. These signals are mostly from the smectic layers at the two edges of the hemicylinder, rotating around the axis of the hemicylinder. The intensities extracted from such scattering rings are shown in figure 3.29. We see that the intensity for $\alpha$ less than $90°$ is higher than those for $\alpha$ greater than $90°$.

We have also measured using TSAXS, the signals from perpendicular layers. Such signals are encircled in the black rectangle in figure 3.28(c). For a given sample, I have plotted only the signals in this black rectangle to get the real shape of the upper and the lower signals. I have then plotted the two signals in one image as shown in figure 3.30 where I have compared the two signals for different samples. For the film sample of 180 nm thickness the result are shown in figure 3.30(a). The

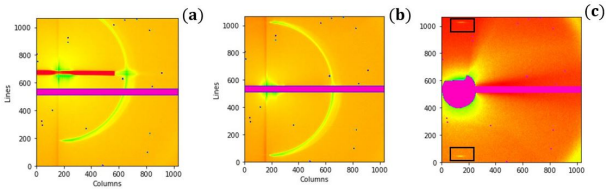


Figure 3.28: The asymmetric scattering ring from a sample of 230 nm thickness data corrected with (a) the detector displaced (b) the detector not displaced (c) The signals from perpendicular layers from a sample of 180 $nm$ thickness film with a majority of oily streaks. They are measured using TSAXS configuration.

signal in Lilas color corresponds to the upper signal whereas the green color corresponds to the lower signal. We can see that the two signals are not shifted from one another but they are instead symmetric with respect to each other. This suggests that the sample was well oriented. In contrast to this result, figure 3.30(b) which was from a film sample of 230 nm, is showing that the upper signal (in orange color) is clearly shifted i.e asymmetric with respect to the lower signal (green). This suggest that this sample was poorly oriented. When the TSAXS signals were perfectly symmetric the scattering ring from GISAXS

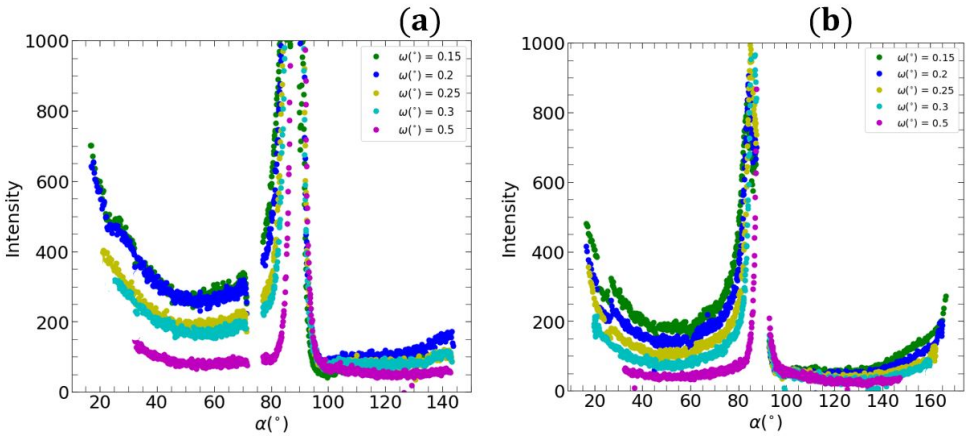


Figure 3.29: The intensity extracted from asymmetric scattering ring when (a) the detector is displaced (b) the detector is not displaced. These data were extracted from a film of 230 thickness.

was also symmetric. This confirms that a perfect $\mu$ orientation (stripes perfectly parallel to the X-ray beam for $\mu = 0^{\circ}$) is absolutely necessary to obtain symmetric rings and accurate measurements of the Bragg features. Unfortunately we did not always succeeded a perfect alignment of the stripes. The main reason was related to the large values of the $\Delta\mu$, the mosaicity, also visible in TSAXS data, leading to a difficult orientation of the stripes. This requires to apply afterward a correction using the understanding related with the $\mu_{Bragg}$ determination previously described. This correction is based on the hypothesis that an asymmetric ring corresponds to a bad initial $\mu$ alignment. This hypothesis is confirmed by $\mu_{max}$ measurements performed with the $\mu_{scan}$ for a misaligned sample (figure 3.31). This curve is not centered around $\mu = 0^{\circ}$ as it should be (see figure 3.20 instead) This kind of measurement allows to determine $\mu_o$, the value of $\mu$-alignment.

We have already seen in equation 3.26, the formulae to calculate the Bragg intensity from intensity corresponding to $\mu \neq \mu_{Bragg}$. It has been used for the measurement when $\mu$ was fixed at $0^{\circ}$ but was misaligned by $\mu_o$. The new formulae is given in equation 3.27.

$$I_{Bragg} = I_{max} e^{(\frac{\mu_{Bragg} \pm \mu_o}{\Delta\mu})^2} \tag{3.27}$$

The $+$ is for the images with detector not displaced and $-$ is for those with detector displaced. Again the $\mu_{\ Brag}$ is calculated using equation 3.25. The corrected data are shown in figure 3.32 for the two possible positions of the detector. We observe that

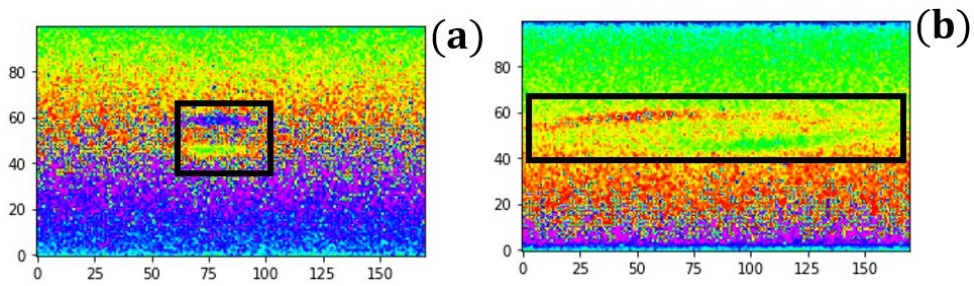


Figure 3.30: The signals from perpendicular layers measured using TSAXS configuration. (a) Well oriented in a 180 nm thick film sample (b) poorly oriented 230 thick sample.

we have been able to obtain almost perfectly symmetric intensities. This kind of corrections allowed to analyze the data of all our misaligned samples which was initially thought as impossible. To correct the asymmetric data we need to determine the value of $\mu_o$. The $\mu_o$ values obtained from the $\mu_{scans}$ (see figure3.31) values allow for a starting point of the correction. Then the $\mu_o$ value is refined to lead to a perfect symmetric intensity. For example for the figure 3.32(a) we have found the value of $\mu_o = 2.4^\circ$ and $\Delta\mu = 2.5^\circ$ for all incident angle $\omega$ (as expected) leading to the symmetric intensity shown in figure 3.32(a). It is consequently now possible to correct the data of most of the misorientated samples.

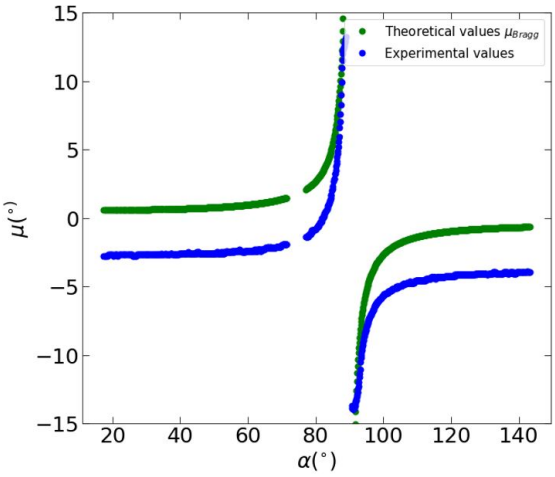


Figure 3.31: The evolution of the position of the experimental maximum intensity and the theoretical Bragg intensity for a misaligned oily streak sample of 230 $nm$

## 3.4 Conclusion

The signals scattered in Bragg condition contain information on the structure of the scattering material. It is therefore crucial to ensure that this condition is satisfied during the X-ray scattering measurements. It has been demonstrated that oily streaks intimate internal structure is made up of smectic layers rotating around the axis of the hemicylinders. To study this internal structure precisely, it is crucial to ascertain that Bragg condition is satisfied for all orientations $\alpha$ of the wave vector transfer $\vec{q}$. This $\vec{q}$ has to be parallel to the normal of the smectic layers inside the hemicylinder. For this reason, we have developed two different but complementary unprecedented theoretical and experimental techniques. The first one is the experimental $\mu_{scan}$ measurement and the theoretical formula for the position of the Bragg intensity. We have found a perfect agreement between the two. This agreement helped us to understand the critical parameter necessary to control for Bragg measurements, finally

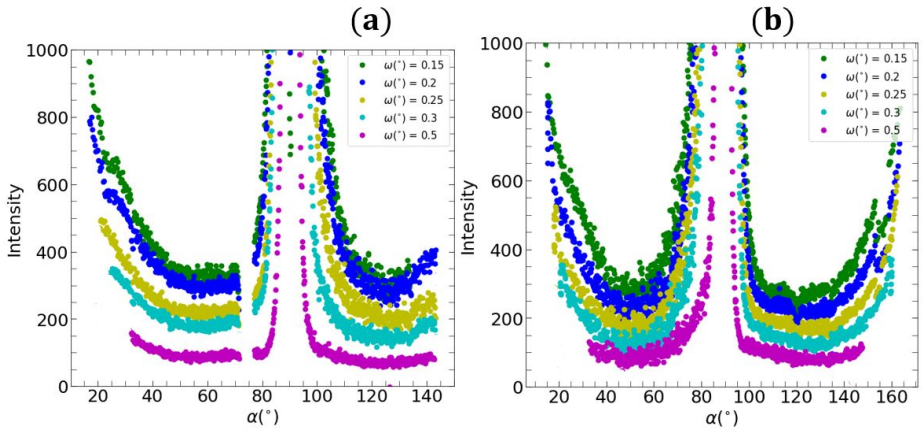


Figure 3.32: The corrected Bragg intensity extracted from asymmetric scattering ring (shown in figure 3.29) when (a) the detector is displaced (b) the detector is not displaced.

allowing to find a way to obtain Bragg conditions at $\mu = 0°$. In addition to this Bragg intensity ascertainment, in this chapter we have also presented new parameters that have not been used before in our group in the study of the intimate structure of the oily streaks. These are the $\Delta q$, the $\Delta\mu$, and the $q$ variations with $\alpha$. The former is sensitive to the presence of disorders in the inter layer spacing of the smectic layers and so it will help in chapter 4 and 5 in the localization of the defects in our system. Moreover since it is also associated with the finite size effect which is the number of scattering in our system, it will therefore play a crucial role in the determination of the number of scattering smectic layers in the next chapters. The $\Delta\mu$ is associated with the mosaicity of the hemicylinder. It signifies that due to the rubbing process the produced hemicylinder are not always perfect. Taking into account this parameter has therefore helped to take into account the effect of this mosaicity on the intensity scattered by our hemicylinders. We have performed a calculation to correct the effects of refraction in our measurement. This calculation concerns the determination of the value of the wave vector transfer $q_{film}$ inside the film. Its values are related to the interlayer spacing. We demonstrated that for the curved smectic layers, this $q_{film}$ varies as a function of its orientation $\alpha_{film}$ inside hemicylinder. This will hence be useful in the precise determination of the intimate internal structure of the hemicylinders in next two chapters. In most of the experimental measurements that we have performed, we were confronted with the issue of misorientation. We have found that the main reason was the misorientation of the $\mu_{motor}$ difficult to remove due to the large mosaicity. The effect of this was that the measured data were deviating from Bragg condition. In this chapter we have represented a technique to correct this misorientation. During this thesis we have applied it to data collected in different time and experimental campaigns and the results that we have presented have shown that its effect could be annihilated. It is therefore strongly suggests that this procedure can be used in case it becomes necessary.

# Bibliography


[1] Delphine Coursault et al. “Self-organized arrays of dislocations in thin smectic liquid crystal films”. en. In: *Soft Matter* 12.3 (2016), pp. 678–688. ISSN: 1744-683X, 1744-6848. DOI: 10.1039/C5SM02241J. URL: http://xlink.rsc.org/?DOI=C5SM02241J (visited on 01/17/2023) (cit. on p. 70).

[2] Bruno Zappone et al. “Self-ordered arrays of linear defects and virtual singularities in thin smectic-A films”. en. In: *Soft Matter* 7.3 (2011), pp. 1161–1167 (cit. on p. 70).

[3] Jean-Philippe Michel et al. “Structure of smectic defect cores: X-ray study of 8CB liquid crystal ultrathin films”. In: *Physical review letters* 96.2 (2006). Publisher: APS, p. 027803 (cit. on p. 70).

[4] M. Ambrožič et al. “Annihilation of edge dislocations in smectic- A liquid crystals”. en. In: *Physical Review E* 70.5 (Nov. 2004), p. 051704. ISSN: 1539-3755, 1550-2376. DOI: 10.1103/PhysRevE.70.051704. URL: https://link.aps.org/doi/10.1103/PhysRevE.70.051704 (visited on 07/11/2021) (cit. on p. 70).

[5] Bohdan Senyuk et al. “Shape-dependent oriented trapping and scaffolding of plasmonic nanoparticles by topological defects for self-assembly of colloidal dimers in liquid crystals”. In: *Nano letters* 12.2 (2012). Publisher: ACS Publications, pp. 955–963 (cit. on p. 70).

[6] “Composites cristaux liquides/nanoparticules, synergies entre matière molle et propriétés électroniques de nanoparticules”. PhD thesis (cit. on p. 70).

[7] Haifa Jeridi et al. “Unique orientation of 1D and 2D nanoparticle assemblies confined in smectic topological defects”. en. In: *Soft Matter* 18.25 (June 2022). Publisher: The Royal Society of Chemistry, pp. 4792–4802. ISSN: 1744-6848. DOI: 10.1039/D2SM00376G. URL: https://pubs.rsc.org/en/content/articlelanding/2022/sm/d2sm00376g (visited on 08/17/2022) (cit. on p. 70).

[8] Coursault Delphine. “Décoration de réseaux linéaires de défauts smectiques par des nanoparticules d’or.” PhD thesis. Paris: Université Pierre et Marie Curie, 2013 (cit. on p. 70).

[9] Coursault Delphine. “Composites cristaux liquides/nanoparticules, synergies entre matière molle et propriétés électroniques de nanoparticules.” PhD thesis. SORBONNE UNIVERSITÉ, 2018 (cit. on p. 70).

[10] D. Babonneau et al. “Waveguiding and correlated roughness effects in layered nanocomposite thin films studied by grazing-incidence small-angle x-ray scattering”. In: *Phys. Rev. B* 80 (15 Oct. 2009), p. 155446. DOI: 10.1103/PhysRevB.80.155446. URL: https://link.aps.org/doi/10.1103/PhysRevB.80.155446 (cit. on p. 78).

[11] Detlef-M Smilgies. “Grazing-Incidence Small-Angle Scattering (GISAXS)”. en. In: () (cit. on p. 78).

[12] P. Müller-Buschbaum. “A Basic Introduction to Grazing Incidence Small-Angle X-Ray Scattering”. en. In: *Applications of Synchrotron Light to Scattering and Diffraction in Materials and Life Sciences*. Ed. by Marian Gomez et al. Lecture Notes in Physics. Berlin, Heidelberg: Springer, 2009, pp. 61–89. ISBN: 978-3-540-95968-7. DOI: 10.1007/978-3-540-95968-7_3. URL: https://doi.org/10.1007/978-3-540-95968-7_3 (visited on 01/12/2023) (cit. on p. 78).

[13] X. Lu et al. “Grazing-incidence transmission X-ray scattering: surface scattering in the Born approximation”. en. In: *Journal of Applied Crystallography* 46.1 (Feb. 2013). Number: 1 Publisher: International Union of Crystallography, pp. 165–172. ISSN: 0021-8898. DOI: 10.1107/S0021889812047887. URL: http://scripts.iucr.org/cgi-bin/paper?db5107 (visited on 01/12/2023) (cit. on p. 78).

[14] P Busch et al. “Grazing-incidence small-angle X-ray scattering from thin polymer films with lamellar structures–the scattering cross section in the distorted-wave Born approximation”. In: *Journal of applied crystallography* 39.3 (2006), pp. 433–442 (cit. on p. 78).

[15] A.J. Leadbetter et al. “The structure of smectic A phases of compounds with cyano end groups”. en. In: *Journal de Physique* 40.4 (1979), pp. 375–380. (Visited on 05/12/2022) (cit. on pp. 81, 85).

[16] Noel A. Clark et al. “X-ray scattering study of smectic ordering in a silica aerogel”. en. In: *Physical Review Letters* 71.21 (Nov. 1993), pp. 3505–3508. ISSN: 0031-9007. DOI: 10.1103/PhysRevLett.71.3505. URL: https://link.aps.org/doi/10.1103/PhysRevLett.71.3505 (visited on 01/05/2023) (cit. on p. 81).

# Chapter 4

# Study of internal structure of a smectic A thin film of $180nm$ thickness

*"On ira d'autant plus loin dans la vie ... à condition de revenir." –*

– Docteur Robert Blacher

## Contents

## 4.1 Introduction

In chapter 1, we have seen that smectic A liquid crystal phase is characterized by a layered structure at a given temperature. Leadbetter et al. [1] have determined the interlayer spacing of the smectic layers and found it to be $d = 31.6$ Å which lead to $q_m = 1.99\ nm^{-1}$ for an 8CB molecular length of $l = 22$Å. We have confined it between homeotropic anchoring and uniform planar anchoring. This confinement induces a competition between different energy terms, namely, the two antagonistic anchoring energies, the surface energy at the air-8CB interface related to the surface curvature, the elastic and defect energy. This competition distorts the 8CB layered structure into 1D pattern, the so-called oily streaks (see section in chapter 1) [2, 3]. In this chapter, I will describe the works we have done on a sample of average thickness 180 $nm$ to study in detail the internal structure of the oily streaks. On this sample we have studied 3 zones (ribbons of length 18 $mm$ parallel to X-ray beam and of width 300 µ$m$ ). As explained in chapter 3 the thickness of each zone has been carefully determined during the analysis of optical microscopy image using the Newton tints of colors shown in the appendix A. In the following, we concentrate on the so-called $z_{mc} = -4$ of average thickness 180 $nm$. The two other zones giving similar results on this homogeneous sample. The intensity diffracted by this zone was observed on a 2D Eiger detector as a scattering ring shown in figure 4.1a in figure 3.7. For $\mu = 0$, we have done the measurement on different incident angle $\omega$ values between $0.1^\circ$ and $0.6^\circ$ that have been described in chapter 3. For each $\omega$ , we obtained a scattering ring. From each ring, we have extracted its width $\Delta q$, its radius $q$, and intensity all along this ring. All these parameters were in the function of the orientation $\alpha$ of the normal of smectic layers rotating around the axis of the hemicylinder. As we have said in chapter 2 section 2.6.2, the study and the reconstruction of the oily streaks model would need an integrated Bragg intensity which is found to be proportional to the product of the Bragg intensity, $\Delta q$ and $\Delta\mu$ as explained in chapter 3 (shown in equation 4.1). The $\Delta\mu$ is the full width at half maximum of the Bragg peak of intensities obtained through the $\mu_{scan}$ around the axis perpendicular to the sample (see chapter 3 section 3.3.3). This mosaicity comes from the rubbing process of the PVA-coated substrate: the streaks are not always perfectly orientated in the direction parallel to their axis.

$$I_{ib} = I_{Bragg}\Delta\mu\Delta q \tag{4.1}$$

In chapter 3 we saw that the Bragg condition can be satisfied for all orientations $\alpha$ for any incident angle $\omega$ either if we use the data extraction from the $\mu_{scan}$ alone or if we only use $\mu = 0$ data and combine the data from small $\omega$ values with those from $\omega_{Bragg} = 0.6^\circ$.

The corresponding profiles of the evolution of the integrated Bragg intensity $I_{ib}$, the $\Delta q$ and $\Delta\mu$ are shown in figure 4.1b, 4.2a and 4.3a respectively.

Using GISAXS and TSAXS Coursault et al. [3] have obtained the scattering ring from the 8CB smectic A liquid crystal confined between the rubbed PVA substrate and air at $\mu = 0^\circ$. The intensities extracted from the scattering ring are shown in figure 4.4a and 4.4b. The first one for film thickness $e = 100\ nm$ was obtained at incident angle $\omega = 0.2^\circ$ and is the combination of the signal from TSAXS (sample rotation was between $\alpha$ $-10^\circ$ and $20^\circ$) and GISAXS (sample rotation was between $\alpha$ $30^\circ$ and $80^\circ$ ). The second one for film thickness $e = 230\ nm$ was obtained using TSAXS only, and the sample was rotated between $\alpha = 0^\circ$ and $\alpha = 70^\circ$. I would like to highlight some issues with these intensities. Firstly, a larger part of these two curves from $\alpha = 60^\circ$ to $\alpha = 90^\circ$ doesn't satisfy Bragg's condition since they were both extracted at small omega $0.2^\circ$ for $\mu = 0^\circ$. Secondly, the data quality was not perfect. Thirdly, there is a lack of data from $\alpha = 80^\circ$ or $\alpha = 70^\circ$ to $\alpha$ $= 90^\circ$ respectively in the two samples studied. In particular, no measurement of the flat central layers was obtained. Finally, the intensity was claimed to correspond to the integrated intensity due to the hypothesis that $\Delta q$ was constant. However it is not the case as shown in figure 4.3(a).

The existing model from the 100 $nm$ should thus be re-examined. The last but not least point is that to interpret the integrated intensities, it has been hypothesized that for a given orientation $\alpha$, the integrated intensity is proportional to the number $N(\alpha)$ of diffracting smectic layers, whose normal is parallel to the wave-vector transfer $q$ orientated at $\alpha$ from the substrate. This hypothesis has been used to build the internal structure of the hemicylinder.

However, we have seen in chapter 2 that the integrated intensity is proportional to the number of scattering layers for a system of perfectly flat layered crystals. This brings the question of whether this hypothesis is still valid in case the diffracting layers are curved.

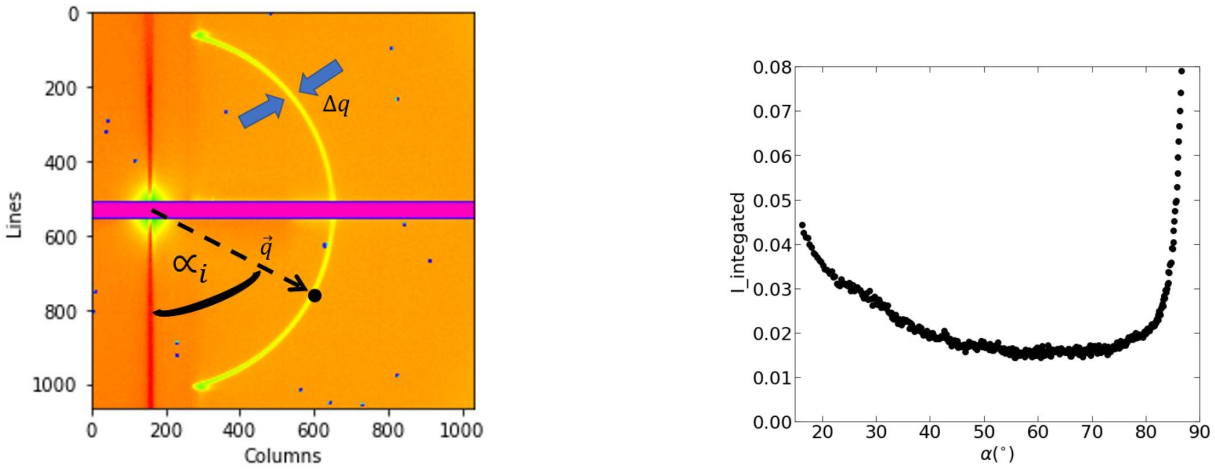


(a) (b)

Figure 4.1: (a) Scattering ring from GISAXS for $\omega = 0.25°$ (b) The experimental integrated Bragg intensity from a sample of 180 nm.

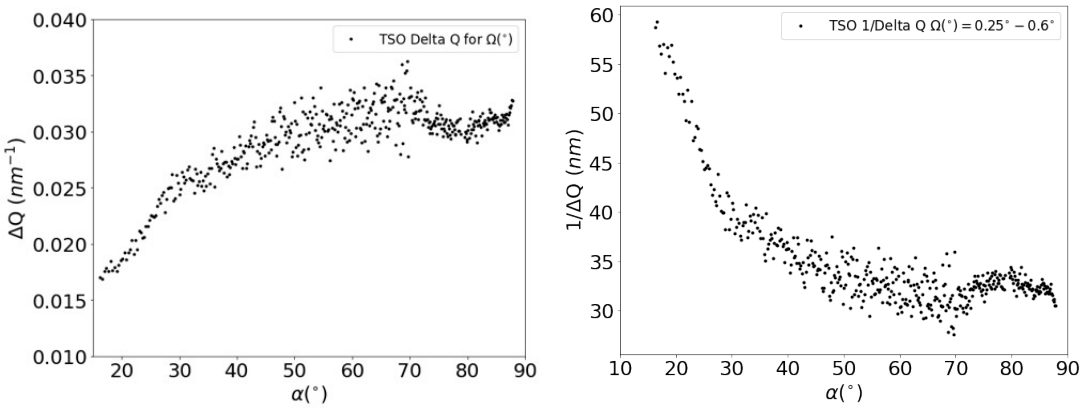


(a) (b)

Figure 4.2: (a) The evolution of the $\Delta q$ as a function of $\alpha$ .(b)Evolution of $1/\Delta q$ the inverse of the $\Delta q$ as a function of $\alpha$ .

In this chapter, we will first use the integrated Bragg intensity to calculate the number of diffracting smectic layers for a perfect flat lamellar structure. Secondly, we will calculate the relationship between the integrated Bragg intensity and the number of scatterers in curved smectic layers. This will put light on how this intensity is related to the number of diffracted layers. We will then have to conclude on the hypothesis mentioned above. The data we used in this study have high quality compared to the previous one of 2016 [3]. In addition to this, they reach $\alpha = 90°$ contrary to the previous data. We have also measured the intensity at incident angle $\omega = 0.6°$, the Bragg angle for all orientation alpha. So we got a full profile of integrated Bragg intensity using the data collected at small $\omega$ and at $\omega_{Bragg} = 0.6°$. After re-examining the above-mentioned hypothesis, we will use this new data to study and reconstruct the model of the oily streaks. This will help to ascertain whether there are other topological defects inside these oily streaks, with respect to the ones suggested in [3].

We were also interested in the understanding of the role of confinement of the 8CB layered structure on the interlayer spacing $d$. When Bragg's condition is satisfied, the value of $d$ is related to the wave vector transfer $\vec{q}$ by $d = \frac{2\pi}{q}$. It is been considered

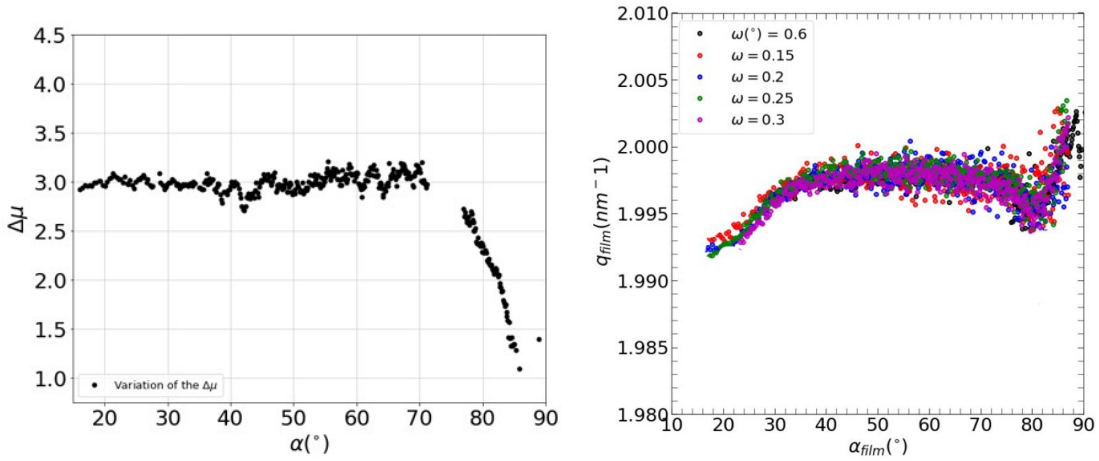


(a) (b)

Figure 4.3: (a) The evolution of the $\Delta\mu$ as a function of $\alpha$ .(b) Evolution of normalized $q_{film}$ values as a function of $\alpha$.

that $q$ is always a constant value $1.99\ nm$ for 8CB smectic A in [1]. In our data (figure 4.3b) $q$ values were extracted from the scattering ring of figure 3.7 in chapter 3.

We have leveraged the high resolution of our data (see figure 4.3b) to study how this interlayer spacing inside the linear patterns, the so-called oily streaks evolves as a function of the orientation alpha.

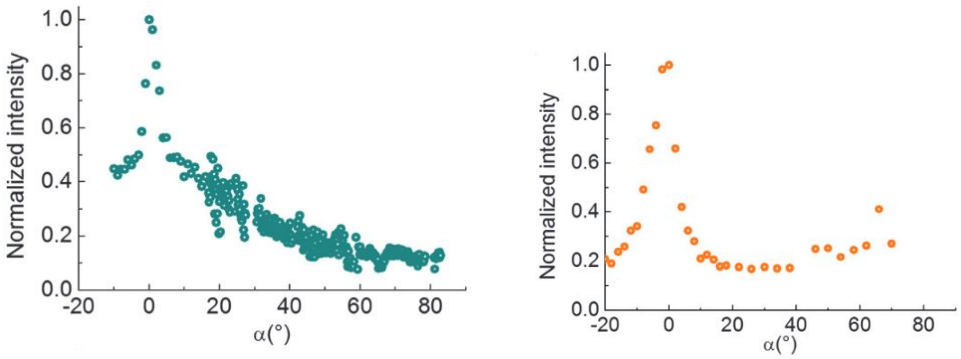


(a) (b)

Figure 4.4: (a) Normalized integrated intensity for the 8CB film of 100 $nm$ thickness, obtained by combining the GISAXS and TSAXS signals. (b) Normalized integrated intensity for an 8CB film of 230 $nm$ thickness was obtained in the TSAXS configuration [3].

## 4.2 The perfect planar stack of smectic layers

In chapter 2, section 2.2, we have seen a calculation of diffraction intensity from a stack of perfectly flat and periodic smectic layers. The number of diffracting smectic layers calculated using this intensity was proportional to the inverse of $\Delta q$.

Furthermore, the integrated intensity was proportional to $N$. So, the integrated Bragg intensity( figure 4.1b) should be directly proportional to the inverse of $\Delta q$ (figure 4.2b). To verify this proportionality, we plotted the integrated Bragg intensity as a function of the inverse of $\Delta q$ in figure 4.5. This figure evidences no proportionality. This might be due to the fact that the data we have used were from curved smectic layers. As a result, the proportionality that works for the flat layers might not work for the curved smectic layers. In the next section, we will consider the case of curved diffracting smectic layers.

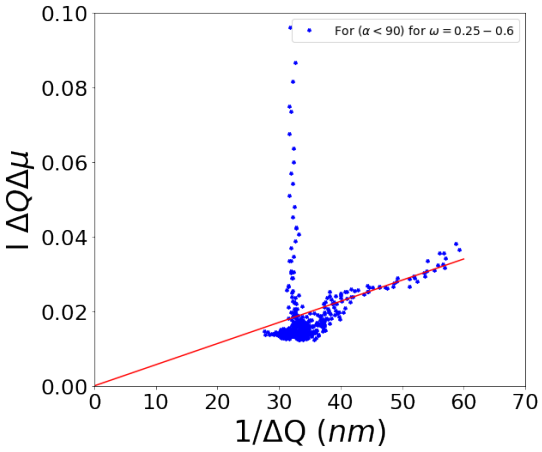


Figure 4.5: The comparison between the integrated Bragg intensity and the inverse of the $\Delta q$.

## 4.3 The curved smectic layers

In this section, we consider a perfect quarter cylinder shown in figure 4.6(a). It is made of superimposed smectic layers where $N_2$ is its total number of smectic layers and $N_1$ is the number of missing smectic layers that are supposed to be in the region very close to the curvature center due to the expected prohibitive elastic cost of these rotating layers of small curvature radius (figure 4.6 (c)). This number may be either 0 or not. Its value will be determined it in this chapter. We hypothesize that in the curved smectic layers the density of scatterers along the rotating smectic layers remains constant, i.e., the linear density remains unchanged. This is in contrast with hard crystal and is related to the fluid character of the smectic materials. Indeed we expect smectic molecules to be able to move along the layers when they are distorted.

Let's consider a triangular slab of smectic layers $\delta\alpha$ in a given orientation $\alpha$ as shown in figure 4.6(b). Let's denote the linear density of scatterers along the rotating smectic layers as $\rho$. $\delta l_i$ is the length of a single curved layer $i$ in the small slab. Its radius is the product of the inter-layer distance $d$ and $n_i$, the number of these smectic layers.

Since the whole diffracted intensity integrated onto a Brillouin zone around a diffraction peak is always proportional to the total number of scatters [4], we can write the integrated intensity as

$$\sum_{N_1}^{N_2} \rho\delta l_i \iff \delta n = \sum_{N_1}^{N_2} \rho\delta\alpha n_i d$$

$$\implies \delta I(\alpha) \propto \rho\delta\alpha d \sum_{N_1}^{N_2} n_i = \rho\delta\alpha d \left[\frac{(N_2^2 - N_1^2)}{2} + \frac{(N_2 + N_1)}{2}\right] \tag{4.2}$$

$$\delta I(\alpha) \propto \rho\delta\alpha d \left[\frac{(N_2^2 - N_1^2)}{2} + \frac{(N_2 + N_1)}{2}\right] \tag{4.3}$$

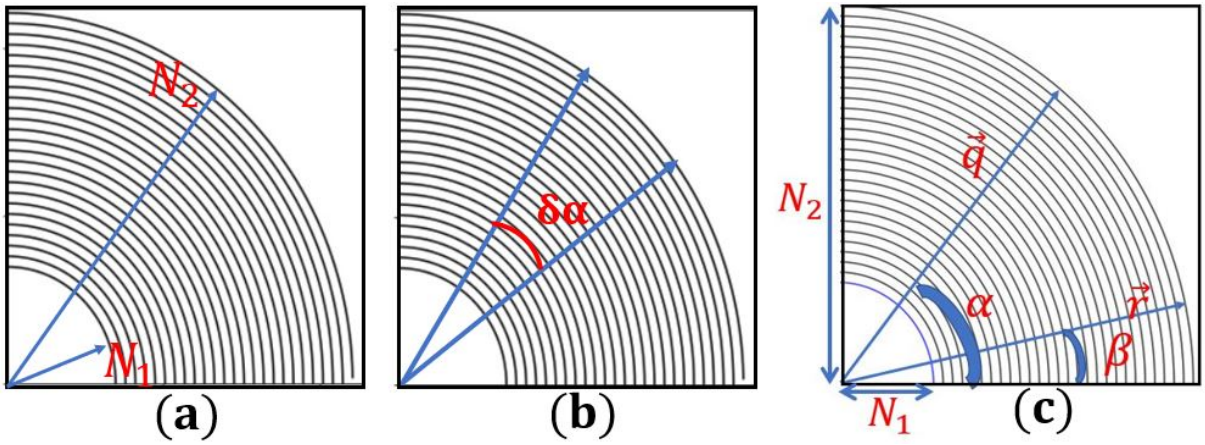


Figure 4.6: (a) The quarter of the cylinder showing the number of smectic layers being considered i.e. $N_1$ and $N_2$ (b)A quarter of perfect hemicylinder showing a triangular slab of width $\delta\alpha$.

The equation 4.3 is formed by a quadratic term and a linear term. The contribution from the quadratic term is dominating over the one from the linear term. This is an unprecedented result that the integrated intensity is not proportional to the number of curved smectic liquid crystal layers. It is due to the fluid property that is keeping the density of scatterers constant when the flat smectic layers are curved. This equation is different from the calculation we have done in section 2.2.3 of chapter 2 for flat smectic liquid crystals layers, where we have found that the integrated intensity is linearly proportional the number of the scattering layers. In section 2.6.2 of chapter 2, we have discussed the hypothesis that the integrated intensity $I(\alpha)$ diffracted by curved layers of a smectic liquid crystal material for a given orientation $\alpha$ is proportional to $N_2 - N_1$, the number of the smectic layers, whose normal, is parallel to the wave-vector transfer, $\vec{q}$ which is orientated at the angle $\alpha$ from the substrate [2, 3, 5]. However, the equation 4.3 shows that for the smectic A curved layers, the above hypothesis is incorrect. This very unusual result is directly induced by the consideration of the fluidic nature of the smectic layers. This latter indeed implies, that even when they rotate the linear density of scatterers along the smectic layers is constant, in clear contrast with hard materials.

It strongly suggests the necessity of a new calculation of the number of diffracting smectic layers that will eventually help to reconstruct a new model of oily streaks. In this chapter, we will analytically and numerically calculate the integrated intensity and $\Delta q$ in Bragg's conditions. We will then use to this number to build the new model. The experimental data that we will use were discussed in the previous chapter. They are from a smectic liquid crystal thin film sample of 180 $nm$ thickness.

## 4.4 Calculation of scattered intensity from an 8CB hemicylinder

In chapter 2 we have seen that our system is made of a 1D patterns of the so-called oily streaks where each of them is formed by an hemicylinder. The intensity scattered by these hemicylinders shown in figure 4.1b is varying as a function of the orientation $\alpha$. It contains the interference between the scattered intensities from the neighboring hemicylinders. The interpretation and make use of this experimental intensities to reconstruct the internal structure of each oily hemicylinder requires the use of the calculation of the scattered amplitude from both the single perfect quarter cylinder and the two neighboring quarter cylinders shown in the following section 4.4.1. In this section, we will firstly describe the analytical calculation of scattered amplitude from a system of a single quarter of a hemicylinder. Secondly, we will describe the system of two neighboring hemicylinders. Lastly, in subsection 4.4.2, we will focus on the numerical calculations and study the similarities and differences between the calculated scattered amplitudes from the two cases. These will be useful in the determination of the evolution of the number of scattering smectic layers $N_1$ and $N_2$ that constitute the internal structure of the hemicylinder. This will be achieved once we determine the relationship between these calculated scattered values with the experimentally scattered values as described in section 4.7.

### 4.4.1 Analytical calculation

#### Model of single perfect quarter cylinder

Our oily streaks are formed by quarter cylinder at their edges. Let's do the calculation for a single perfect quarter of the hemicylinder of length $L$ that is associated with one edge of the hemicylinder shown in figure 4.6. In figure 4.6, it can easily be seen that the more the radius of the smectic layers increases the more its length increases which implies that the number of the scatters increases. So, we can consider the quantity $r\delta r$ as a very important parameters in calculating the total scattered amplitude where we have to take into account both the $r$ and $e^{i\vec{q}.\vec{r}}$.

Let's define the density $\rho$ of scatterers at position defined by $(r, \beta)$ as shown in figure 4.6 (c)

$$\rho(r,\beta) = \sum_{N_1}^{N_2} \delta(r - nd) \tag{4.4}$$

each of the scatters gives an amplitude $e^{i\vec{q}.\vec{r}} = e^{iqr\cos(\alpha-\beta)}$, the amplitude scattered by the single perfect quarter cylinder is denoted by $A_1$ and can be obtained by

$$A_1(q,r,\alpha) = L\int_{\beta=0}^{\pi/2}\int_{r=0}^{\infty} e^{iqr\cos(\alpha-\beta)} r\rho(r,\beta)drd\beta \tag{4.5}$$

where $L$ is the length of an hemicylinder. Using 4.4 in equation 4.5 we can then get

$$\begin{cases} A_1(q,r,\alpha) = L\int_{\beta=0}^{\pi/2}\int_{r=0}^{\infty} e^{iqr\cos(\alpha-\beta)} r\sum_{N_1}^{N_2}\delta(r-nd)drd\beta & \text{(4.6a)} \\ \iff A_1(q,r,\alpha) = L\int_{\beta=0}^{\pi/2}\int_{r=0}^{\infty}\sum_{N_1}^{N_2} e^{iqr\cos(\alpha-\beta)} r\delta(r-nd)drd\beta & \text{(4.6b)} \end{cases}$$

The equation 4.6(b) is then written as

$$A_1(q,r,\alpha) = L\int_{\beta=0}^{\pi/2}\sum_{N_1}^{N_2} nde^{iqnd\cos(\alpha-\beta)}d\beta \tag{4.7}$$

This has to be simplified in a such a way that the numerical calculation will be obtained.

$$A_1(q,r,\alpha) = L\int_{\beta=0}^{\pi/2}\sum_{N_1}^{N_2}[\frac{1}{i\cos(\alpha-\beta)}\frac{\partial e^{iqnd\cos(\alpha-\beta)}}{\partial q}d\beta] \tag{4.8}$$

$$\iff A_1(q,r,\alpha) = L\int_{\beta=0}^{\pi/2}\frac{1}{i\cos(\alpha-\beta)}[\frac{\partial\sum_{N_1}^{N_2} e^{iqnd\cos(\alpha-\beta)}}{\partial q}]d\beta] \tag{4.9}$$

This sum is the basic summation for diffraction. Our next step is to operate the summation and then the derivatives which will be followed by the integral over the orientation $\beta$.

$$\sum_{N_1}^{N_2} e^{iqnd\cos(\alpha-\beta)} = \sum_{0}^{N_2} e^{iqnd\cos(\alpha-\beta)} - \sum_{N_1}^{0} e^{iqnd\cos(\alpha-\beta)} \tag{4.10}$$

Let's note $x = e^{iqd\cos(\alpha-\beta)}$,

$$\sum_{N_1}^{N_2} e^{iqnd\cos(\alpha-\beta)} = e^{iqN_1d\cos(\alpha-\beta)}[\frac{1-e^{iq(N_2-N_1)d\cos(\alpha-\beta)}}{1-e^{iqd\cos(\alpha-\beta)}}] \tag{4.11}$$

From this equation, it is easy to show that

$$\sum_{N_1}^{N_2} e^{iqnd\cos(\alpha-\beta)} = e^{iq(N_1+N_2-1)d\cos(\alpha-\beta)}[\frac{\sin\frac{qd}{2}(N_2-N_1)\cos(\alpha-\beta)}{\sin\frac{qd}{2}\cos(\alpha-\beta)}] \tag{4.12}$$

We need to do the derivation of this summation with respect to q. To achieve this, let's simplify the whole expression into small parts.

$$\begin{cases} G = e^{iq(N_1+N_2-1)d\cos(\alpha-\beta)} \\ H = \dfrac{\sin\frac{qd}{2}(N_2-N_1)\cos(\alpha-\beta)}{\sin\frac{qd}{2}\cos(\alpha-\beta)} \\ Z = \dfrac{qd}{2}\cos(\alpha-\beta) \\ M = N_2 - N_1 \\ N_2 - N_1 + 1 = 2N_1 + M - 1 \end{cases}$$

$$\frac{\partial}{\partial q}(\sum_{N_1}^{N_2} x^n) = \frac{\partial}{\partial q}(G*H) = G'H + GH'$$

where

$$H' = \frac{\frac{Z}{q}(M\cos(MZ)\sin(Z) - Z\cos(Z)\sin(MZ)}{\sin^2 Z})$$
$$G' = i(N_1+N_2-1)\frac{Z}{q} * G$$

$$\frac{\partial}{\partial q}(\sum_{N_1}^{N_2} x^n) = i(N_1+N_2-1)\frac{Z}{q} * G * H + \frac{\frac{Z*G}{q}(M\cos(MZ)\sin(Z) - \cos(Z)\sin(MZ))}{\sin^2 Z} \tag{4.13}$$

$$\frac{\partial}{\partial q}(\sum_{N_1}^{N_2} x^n) = \frac{ZG}{q}\left[\frac{(M\cos(MZ)\sin(Z) - \cos(Z)\sin(MZ))}{\sin^2 Z} + i(N_1+N_2-1) * H\right] \tag{4.14}$$

Let's divide this equation by $iq\cos(\alpha-q)$ and replace the result in equation 4.8 we get,

$$A_1(q,r,\alpha) = L\int_{\beta=0}^{\pi/2} \frac{Gd}{2}[(2*N_1+M-1)*H - i(\frac{(M\cos(MZ)\sin(Z) - \cos(Z)\sin(MZ))}{\sin^2 Z})]d\beta \tag{4.15}$$

$$A_1(q,r,\alpha) = L*\left[\int_{\beta=0}^{\pi/2} \frac{Gd}{2}[(2*N_1+M-1)*\frac{\sin(MZ)}{\sin Z}]d\beta - i\int_{\beta=0}^{\pi/2} \frac{Gd}{2}[\frac{(M\cos(MZ)\sin(Z) - \cos(Z)\sin(MZ))}{\sin^2 Z}]d\beta\right] \tag{4.16}$$

In a more simplified way, this amplitude may be written as

$$A_1(q,r,\alpha) = Re + iIm \tag{4.17}$$

where $Re = L*\int_{\beta=0}^{\pi/2}\frac{Gd}{2}[(2*N_1+M-1)*\frac{\sin(MZ)}{\sin Z}]d\beta$ and $Im = -L*\int_{\beta=0}^{\pi/2}\frac{Gd}{2}[\frac{(M\cos(MZ)\sin(Z)-\cos(Z)\sin(MZ))}{\sin^2 Z}]d\beta$

**Model of two neighboring perfect quarter cylinders.**

figure 4.7 is showing two perfect quarters (both of length $L$) to be associated with edges of two neighboring oily streaks.This figure shows also that at a given orientation of the wave vector transfer, it is possible that the scattering from one hemicylinder may affect the scattering from the other neighboring hemicylinder. So in this section we will calculate the total amplitude scattered by the two neighboring hemicylinders. In the previous subsection 4.4.1 we have calculate the amplitude scattering by the single perfect quarter on the left side (labeled by 1 in figure 4.7). In this section we will calculate the amplitude scattering by the single perfect quarter on the right side (labeled by 2 in figure 4.7). Then we will calculate the total amplitude scattered by the two neighboring perfect quarter cylinders.

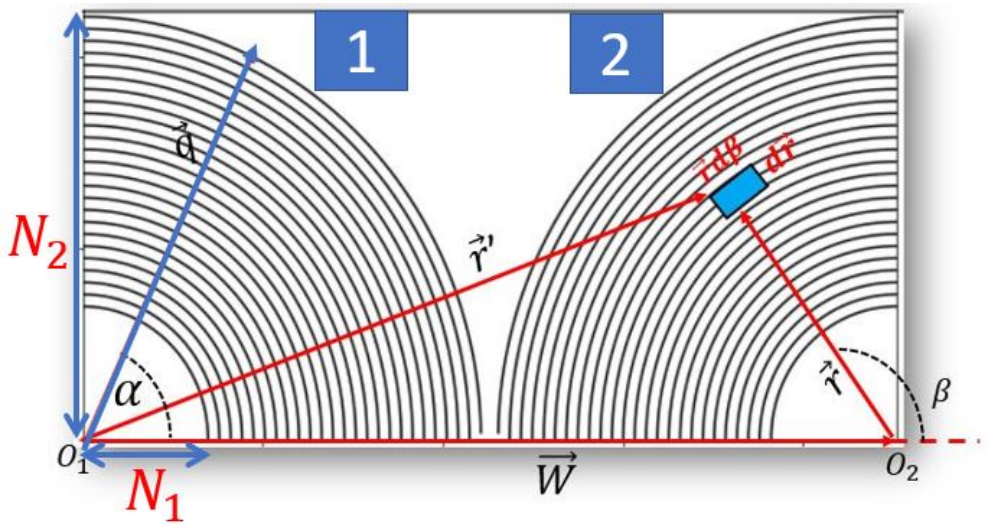


Figure 4.7: Two neighboring perfect quarter cylinders that we will use to calculate the total intensity including all possible interference from them.

$\vec{r}$ is the position of scatterers with respect to the origin $0_2$ in the quarter cylinder number 2 whereas $\vec{r'}$ is the position of scatterers with respect to the origin $0_1$ in the quarter cylinder number 1. We consider an infinitesimally small slab of volume $dV = L * r * dr * d\beta$ shown in blue color in figure 4.7 on a particular layer. The angle $\beta$ varies from 0 to $\frac{\pi}{2}$ for the quarter cylinder number 1 whereas it varies from $\frac{\pi}{2}$ to $\pi$.

The density $\rho$ of scatterers at position defined by $(r, \beta)$ as shown in figure 4.7 on the quarter cylinder number 2 is given by

$$\rho(r,\beta) = \sum_{N_1}^{N_2} \delta(r - nd) \tag{4.18}$$

Each of the scatterers in the quarter cylinder number 2 gives an amplitude $e^{(\vec{q}.r')}$ with respect to the origin $O_1$. The amplitude scattered by the quarter cylinder number 2 is given by

$$A_2(q,r) = L \int_{r=0}^{\infty} \int_{\beta=\pi/2}^{\pi} e^{(i\vec{q}\cdot\vec{r}')} \rho(r,\beta) r dr d\beta \tag{4.19}$$

by replacing the $\vec{r}'$ by $\vec{r} + \vec{W}$ based on the figure 4.7, equation 4.19 can become

$$A_2(q,r,\alpha) = L \int_{r=0}^{\infty} \int_{\beta=\pi/2}^{\pi} e^{(i\vec{q}\cdot(\vec{r}+\vec{W})} \rho(r,\beta) r dr d\beta$$

$$\implies A_2(q,r,\alpha) = L e^{(i\vec{q}\cdot\vec{W})} \int_{r=0}^{\infty} \int_{\beta=\pi/2}^{\pi} e^{(i\vec{q}\cdot\vec{r})} \rho(r,\beta) r dr d\beta$$

Then, after using the dot product, this equation becomes

$$A_2(q,r,\alpha) = Le^{(iqW\cos(\alpha))}\int_{r=0}^{\infty}\int_{\beta=\pi/2}^{\pi} e^{(iqr\cos(\beta-\alpha))}\rho'(r,\beta)rdrd\beta$$

We then replace the density by its value as given in the equation 4.18

$$A_2(q,r,\alpha) = Le^{(iqW\cos(\alpha))}\int_{r=0}^{\infty}\int_{\beta=\pi/2}^{\pi} e^{(iqr\cos(\beta-\alpha))}\sum_{N_1}^{N_2}\delta(r-nd)rdrd\beta \tag{4.20}$$

which can be written in a simplified way as

$$A_2(q,r,\alpha) = Le^{(iqW\cos(\alpha))}A_3(q,r,\alpha)$$

Where

$$A_3(q,r,\alpha) = \int_{r=0}^{\infty}\int_{\beta=\pi/2}^{\pi} e^{(iqr\cos(\beta-\alpha))}\sum_{N_1}^{N_2}\delta(r-nd)rdrd\beta \tag{4.21}$$

The detailed calculations of equation 4.21 are given in 4.5 i.e., in the same ways for a single quarter of the cylinder except that the integration is from $\beta = \pi/2$ to $\pi$ and its solution is given by 4.25 where

$$G = e^{iq(N_1+N_2-1)d\cos(\alpha-\beta)} \tag{4.22}$$

$$Z = \frac{qd}{2}\cos(\alpha-\beta) \tag{4.23}$$

$$M = N_2 - N_1 \tag{4.24}$$

where ***d*** is the interlayer spacing.

$$A_3(q,r,\alpha) = \int_{\beta=\pi/2}^{\pi}\frac{Gd}{2}[(2*N_1+M-1)*\frac{\sin(MZ)}{\sin Z}]d\beta - i\int_{\beta=\pi/2}^{\pi}\frac{Gd}{2}[\frac{(M\cos(MZ)\sin(Z)-\cos(Z)\sin(MZ))}{\sin^2 Z}]d\beta \tag{4.25}$$

The equation 4.20 can be written again in a simplified way after replacing the $A_3(q,r,\alpha)$ by its value in equation 4.25 as

$$A_2(q,r,\alpha) = Re' + iIm' \tag{4.26}$$

where

$$\begin{cases} Re' = L\times(\cos(qW\cos(\alpha))\times\displaystyle\int_{\beta=\pi/2}^{\pi}\frac{Gd}{2}[(2*N_1+M-1)\times\frac{\sin(MZ)}{\sin Z}]d\beta \\ \quad +\sin(qW\cos(\alpha))\times\displaystyle\int_{\beta=\pi/2}^{\pi}\frac{Gd}{2}[\frac{(M\cos(MZ)\sin(Z)-\cos(Z)\sin(MZ))}{\sin^2 Z}]d\beta) \end{cases} \tag{4.27a}$$

$$\begin{cases} Im' = L\times(\cos(qW\cos(\alpha))\times\displaystyle\int_{\beta=\pi/2}^{\pi}\frac{Gd}{2}[\frac{(M\cos(MZ)\sin(Z)-\cos(Z)\sin(MZ))}{\sin^2 Z}]d\beta \\ \quad -\sin(qW\cos(\alpha))\times\displaystyle\int_{\beta=\pi/2}^{\pi}\frac{Gd}{2}[(2*N_1+M-1)\times\frac{\sin(MZ)}{\sin Z}]d\beta) \end{cases} \tag{4.27b}$$

Using equation 4.17 and 4.26, we can write the real part of the total amplitude scattered by the two neighboring quarter cylinder as $Re'' = Re' + Re$ and the imaginary part as $Im'' = Im' + Im$.Hence this total amplitude can be written as

$$A_{tot}(q,r) = Re'' + iImg'' \tag{4.28}$$

where

$$\begin{cases} Re'' = L \times \Big[\cos(qW\cos(\alpha)) \times \displaystyle\int_{\beta=\pi/2}^{\pi} \frac{Gd}{2}[(2*N_1+M-1) \times \frac{\sin(MZ)}{\sin Z}]d\beta \\ \quad + \sin(qW\cos(\alpha)) \times \displaystyle\int_{\beta=\pi/2}^{\pi} \frac{Gd}{2}[\frac{(M\cos(MZ)\sin(Z)-\cos(Z)\sin(MZ))}{\sin^2 Z}]d\beta \\ \quad + \displaystyle\int_{\beta=0}^{\pi/2} \frac{Gd}{2}[(2*N_1+M-1)*\frac{\sin(MZ)}{\sin Z}]d\beta\Big] \end{cases} \tag{4.29a}$$

$$\begin{cases} Im'' = L \times \Big[\cos(qW\cos(\alpha)) \times \displaystyle\int_{\beta=\pi/2}^{\pi} \frac{Gd}{2}[\frac{(M\cos(MZ)\sin(Z)-\cos(Z)\sin(MZ))}{\sin^2 Z}]d\beta \\ \quad - \sin(qW\cos(\alpha)) \times \displaystyle\int_{\beta=\pi/2}^{\pi} \frac{Gd}{2}[(2*N_1+M-1) \times \frac{\sin(MZ)}{\sin Z}]d\beta \\ \quad - \displaystyle\int_{\beta=0}^{\pi/2} \frac{Gd}{2}[\frac{(M\cos(MZ)\sin(Z)-\cos(Z)\sin(MZ))}{\sin^2 Z}]d\beta)\Big] \end{cases} \tag{4.29b}$$

### 4.4.2 Numerical calculation

#### Determination of the theoretical Bragg intensity

We have developed Python code to perform the calculation of the scattered amplitude from both the single perfect quarter cylinder and the two neighboring quarter cylinders respectively in the equation 4.16 and 4.25. Both have $\sin(Z)$ function in the denominator. During numerical integration, we could have issues of pole or singularity of the fraction when the value of $Z$ passes through $\pi$ or $zero$. To explain this issue well, we have to note that the $Z$ in the above functions contains a $cos(\alpha-\beta)$ function which is always less than 1. If the value of $qd$ is less than 1 then $Z$ will have nonzero values which are always much less than 1 for all values of $\alpha-\beta$. The implication is that the function will never pass through the pole of the function and no singularity issue is expected for such values of $qd$. However, if $qd$ is larger than one, there will always be some value of $\alpha-\beta$ for which the value of $Z$ will pass through $\pi$ and then the singularity issue will appear. To avoid this singularity issue, we have done a second-order series expansion of the functions 4.16 and 4.25 to remove the singularities. The Python program used these new functions near the singularities whenever the **qd** value is greater than one. Otherwise, it used the original functions. When the Bragg condition is satisfied $q = q_m$ i.e $q_m = \frac{2\pi}{d_o}$. The quantity $\frac{qd}{2}$ can be written as $\frac{q}{q_m}\pi$.

We calculated the evolution of the intensity as a function of the orientation $\alpha$ that could be diffracted by both the single isolated quarter cylinder and two neighboring quarter cylinders. The thicknesses of the samples that we studied in this thesis were between 100 and 255 nm. Their corresponding total number of smectic layers is between 32 and 80. In particular, the sample we studied in this chapter had a thickness of 180 nm, that is 57 equally spaced smectic layers. We have therefore decided to vary the value of $N_2 - N_1$ between 40 and 90 for the calculation. We consider that the minimum value for $N_1$ is 1. We have then started by fixing values $N_1 = 1$, $N_2 = 40$, and the Bragg's position $\frac{q}{q_{mo}} = 1$ (inducing $\frac{qd}{2} = \pi$) on the hemicylinder.

Figure 4.8 shows the results for the real part and imaginary part of the amplitude in case of a single isolated quarter.

For both the real part and imaginary part the amplitude is constant for all $\alpha$ values far from $90^\circ$. This constant value is zero for $\alpha < 90^\circ$ when the integration is done from $\pi/2$ to $\pi$ and it is also zero for $\alpha > 90^\circ$ when the integration is done from 0 to $\pi/2$. There are high peaks of undulations of width $10^\circ$ at integration limits i.e $\alpha = 0^\circ$, $\alpha = 90^\circ$, and $\alpha = 180^\circ$. This is what we will be referring to as the effects of the integration limits. Moreover, because of the symmetry the sum of amplitudes issued from both the integral from 0 to $\pi/2$ and the integral from $\pi/2$ to $\pi$ is constant for all $\alpha$ values for the real part whereas for the imaginary part, the effects of integration limits at both $\alpha = 0$ and $\alpha = \pi$ remain. For the imaginary part the undulation at $\alpha = 90^\circ$ becomes much smaller whereas for the real part, the effect of integration limits at $\alpha = 90^\circ$ was completely removed.

The scattered intensity calculated using the total amplitude of a single perfect quarter cylinder is shown in figure 4.9 (a). It has the effect of the integration limit of width $\alpha = 0$ at both $\alpha = 0^\circ$ and $\alpha = 90^\circ$. Elsewhere, far from $\alpha = 90^\circ$ the intensity is constant.

Since we have to take into consideration the contribution from the two neighboring quarter cylinders, we have used the equation 4.25. For the latter equation, we have considered that the hemicylinders in our system are identical and are connected to each other as shown in figure 4.7, where the distance between their centers of curvature is $W = 2 * N_2$. The results are

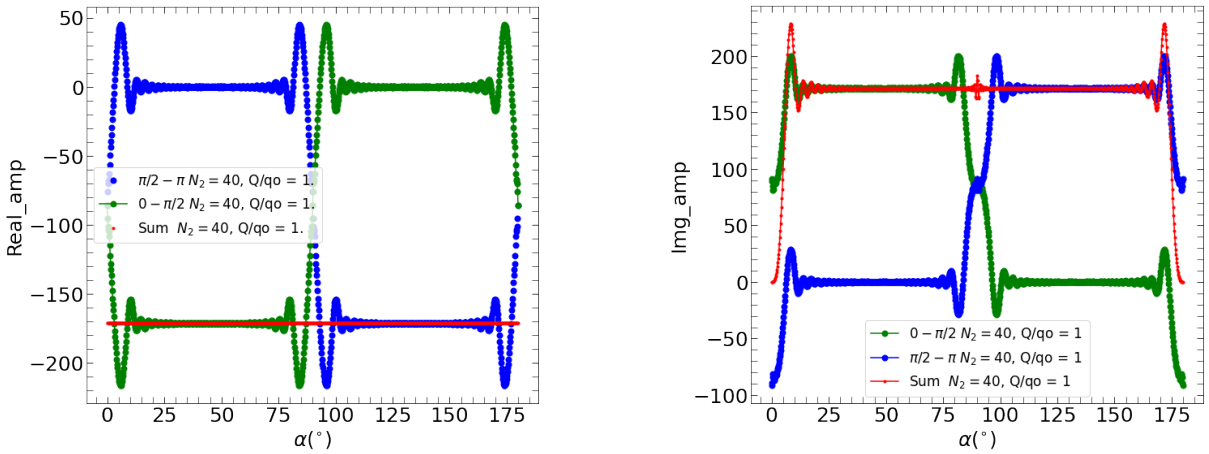


(a) (b)

Figure 4.8: The evolution of (a) the real part (b) the imaginary part of the theoretical scattered amplitude from a single quarter cylinder. The green color is for the integration from $\beta = 0$ to $\beta = \frac{\pi}{2}$, the blue color is for the integration from $\beta = \frac{\pi}{2}$ to $\beta = \pi$. The red color is the summation of these two integrations. We can see that the integration from 0 to $\pi$ is perfectly equal to the sum of the integral from 0 to $\pi/2$ and the integral from $\pi/2$ to $\pi$.

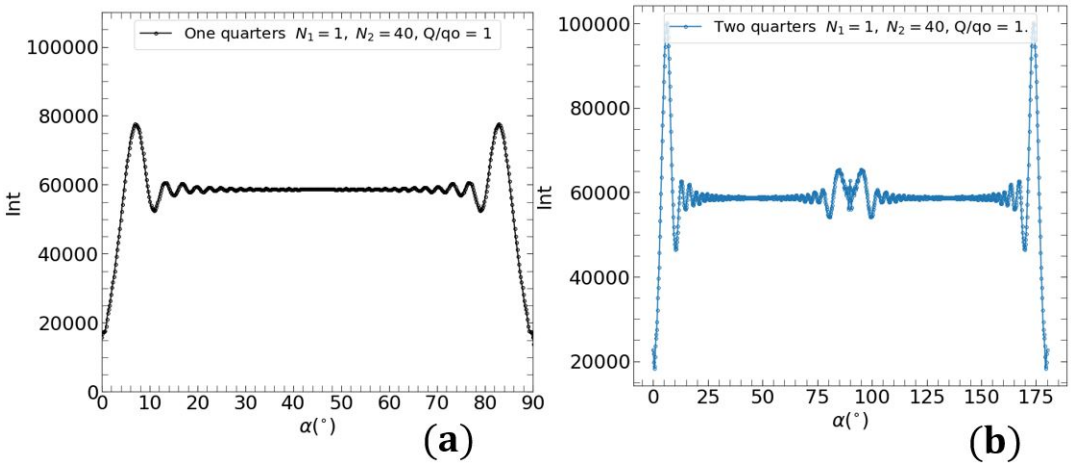


Figure 4.9: The numerically calculated Bragg intensity that can be diffracted by (a) a Single isolated quarter (b) two neighboring perfect quarter cylinders.

shown in Figure 4.9 (b). The effect of integration at $\alpha = 90^\circ$ is significantly small can be ignored which may not be the case for those at $\alpha = 0^\circ$ and $\alpha = \pi$. Most importantly, the figure 4.9 demonstrates that both the single isolated perfect quarter cylinder and the two neighboring perfect quarter cylinders have an equal constant value of intensity between $\alpha = 10^\circ$ and $= 80^\circ$. In the following most of the calculations will be performed with one single quarter cylinder. One may question on the sensitivity of $W$. This dependence can be analyzed in two steps:

1. for values of $\alpha$ far from $90^\circ$, both the real part and the imaginary part of the amplitude due to one of the two quarter cylinder is null. Therefore the sensitivity of the amplitude sum to $W$ is null.
2. for values of $\alpha$ near $90^\circ$, both the contribution of the two quarter cylinders are important but the dependence of the phase, $q \times W \times \cos(\alpha)$ on $W$ is very weak. Therefore, the fluctuation of $W$ can be neglected on the whole a domain.

We have calculated the Bragg intensity for different values of $N_2$ with a model of one single quarter. The results are shown in figure 4.10. For all orientations $\alpha$, the value of the Bragg intensity increases as $N_2$ increases. We can see that the width of the effect of integration limit is becoming slightly smaller as $N_2$ increases. The intensities are constant elsewhere except at around the integration limits. This result of constant value when $\alpha$ varies meets our expectation that the diffraction from a perfect quarter cylinder would be constant since it is formed by a constant number of scattering smectic layers that do not vary when $\alpha$ varies. In addition the increasing of the intensity when $N_2$ increases is expected due to the corresponding increase of the number of scatterers.

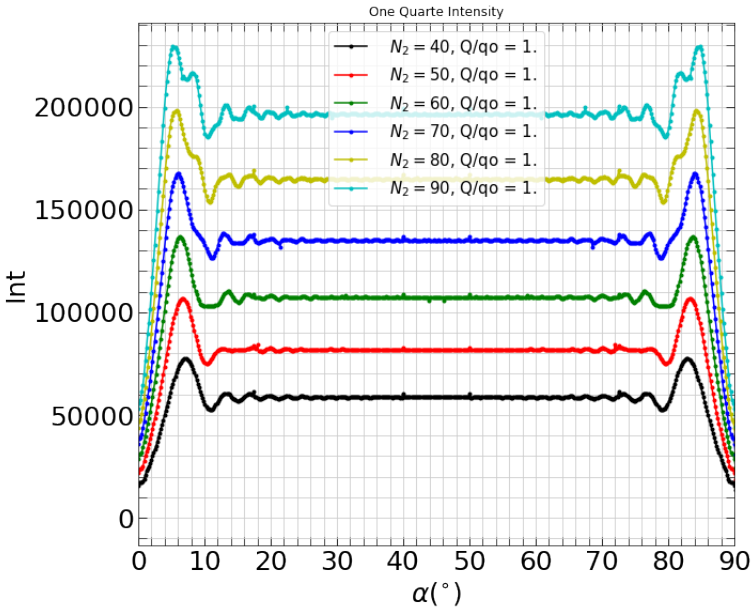


Figure 4.10: Evolution of the Bragg intensity from a single perfect quarter cylinder for different value of $N_2$. In this calculation $N_1$ was fixed at its minimum value 1. The results are always the same for other value of $N_1$.

Comparing these results to the evolution of the experimental intensity which varies as a function of $\alpha$ in figure 4.1b, we can understand that in reality the number of smectic layers inside the hemicylinder is not constant when $\alpha$ varies. It is therefore interesting to find the evolution of the number of smectic layers as a function of $\alpha$ inside this hemicylinder. This result emphasizes the importance of determining the exact relationship between the number of diffracting smectic layers and the diffracted intensity from them.

## 4.5 Determination of the theoretical integrated Bragg intensity

We have then studied the variation of the diffracted Bragg intensity as function of the number of diffracting smectic layers. Using the integration 4.16 for a single quarter cylinder and integration 4.29 for two quarter cylinders at a fixed value of $N_1 = 1$, for different values of $N_2 - N_1$ ranging between 0 and 60 we have calculated the total intensity (figure 4.10). This has been calculated for different values of $\frac{q}{q_o}$ between 0 and 2. We have then plotted for each value of $N_2 - N_1$ a curve of intensity as a function of the wave-vector transfer $q$ for all orientations $\alpha$ ( figure 4.11 is for $\alpha = 45°$, $N_1 = 1$ and $N_2 - N_1 = 60$). It leads to the peak of Bragg intensity that we always find to be positioned at $\frac{q}{q_o} = 1.$ .

By fitting this peak (figure 4.11) with a Gaussian function, we obtained the Bragg maximum intensity and the width ($\Delta q$) of the Gaussian peak as a function of $q$. The integrated Bragg intensity is the product of the maximum intensity, $\Delta q$ and $\Delta\mu$ (see 3, section 3.3.3). The latter is constant from our experimental data (see figure 4.3a). In agreement with equation 4.3, we have found that this integrated intensity is not proportional to the $N_2 - N_1$ as it was hypothesized in previous works [2, 3, 5] and calculated for flat smectic layers layers (chapter 2 2.2.3). Instead, it linearly depends on $N_2^2 - N_1^2$. This is a new result, that

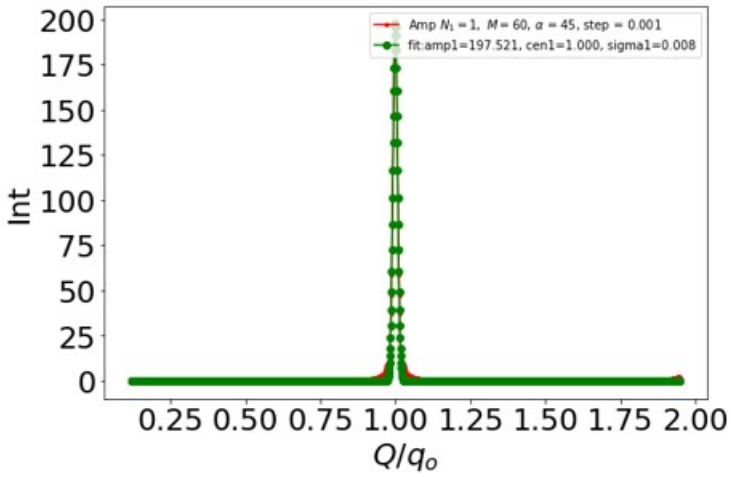


Figure 4.11: Peak of theoretical Bragg peak for a given value of $N_2 - N_1$

underlines the very specific behavior of soft matter with respect to hard matter under X-ray irradiation. Figure 4.12 shows this proportionality. We obtained identical results for the two cases, the single isolated perfect quarter cylinder and two neighboring perfect quarter cylinders in agreement with results shown in figure 4.9.

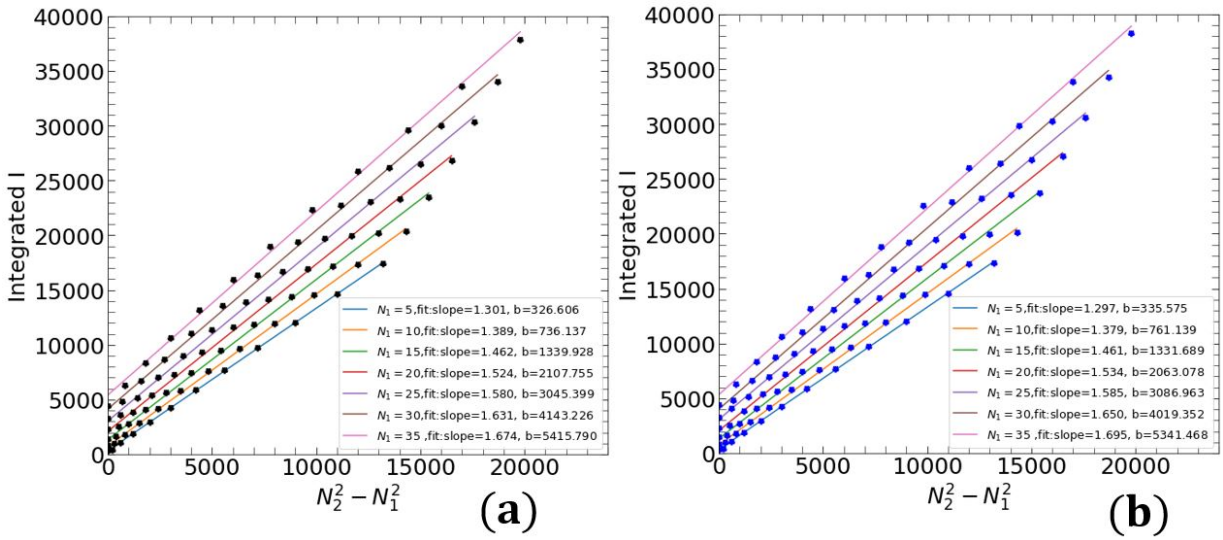


Figure 4.12: Evolution of Integrated Bragg Intensity as function of $N_2^2 - N_1^2$ for different value of $N_1$ for (a) a Single isolated quarter (b) two neighboring perfect quarter cylinders.

The general relationship between Integrated Bragg Intensity and $N_2^2 - N_1^2$ is given by equation 4.30

$$I_{ib} = I_o[A(N_1) * (N_2^2 - N_1^2) + B(N_1)] \tag{4.30}$$

The slopes (A) and the intercepts (B) of this linear relationship appear to vary quadratically as a function of $N_1$ (see appendix A). This result highlights that $N_1$ is an essential parameter for the interpretation of X-ray data.

We have also found that the Bragg peak's width $\Delta q$ varies inversely proportionality as a function of $N_2 - N_1$ as shown in figure 4.13 similarly to the case of perfectly flat smectic layers (see section in chapter 2.2 ) The general relationship between the

width and $N_2 - N_1$ is given by equation 4.31.

$$\frac{1}{\Delta Q} = [C(N_1) * (N_2 - N_1) + D(N_1)] \tag{4.31}$$

The slope (C) of this proportionality is again varying in a quadratic way as a function of $N_1$ whereas the intercept (D) varies

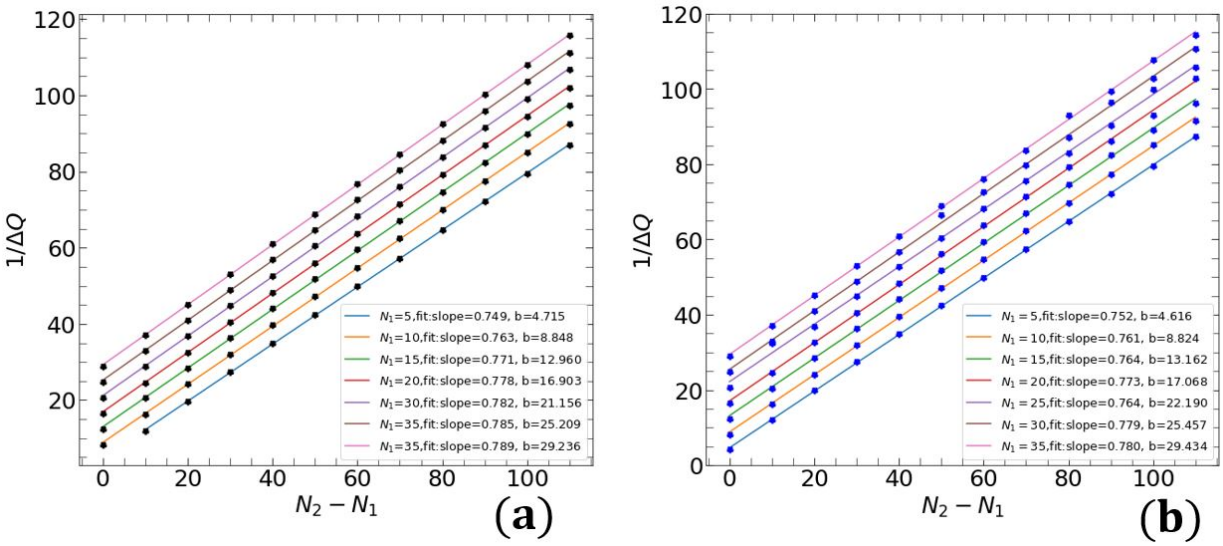


Figure 4.13: Evolution of $\Delta q$ as function of $N_2 - N_1$ for different value of $N_1$for (a) a Single isolated quarter (b) two neighboring perfect quarter cylinders.

linearly with it (see appendix A.2).

In the numerical calculation of the equation 4.25. we have considered that the hemicylinders in our system are identical and are connected to each other as shown in figure 4.7, where the distance between their center of curvature is $W = 2 * N_2$. However, in reality, two neighboring hemicylinders are connected by a curvature wall[2, 3]. The line joining the upper part of this curvature wall to the center of curvature makes a non-zero angle as described in chapter 2. We will see in the next section that no change in the results are expected because of the fact that the intensity is only locally related to the number of scattering layers as discussed below.

## 4.6 Implication of the numerical calculation

The question to be asked now is whether we can use these calculations to interpret the experimental results. To answer this question let's consider two facts. Firstly, after integrating the amplitude from $\beta = 0$ to $\frac{\pi}{2}$ and plotted it as a function of $\alpha$, we have found that it is constant everywhere except at the integration limits.

Secondly, let's consider a small triangular slab of width $\delta\alpha$ (see figure 4.14a) taken from a perfect quarter cylinder. This slab is taken around an arbitrary value of $\alpha$ (for instance we have used $45\ ^\circ$). We integrate equation 4.16 around this fixed value of $\alpha$ i.e. from $\beta = \alpha - \gamma$ to $\beta = \alpha + \gamma$. Thirdly, we did the integration at different many value of $\gamma$ (i.e varying the width of the triangular slab ) and then we plotted as function of these $\gamma$ values all the intensities as shown in figure 4.14b. We have found that the intensity is constant everywhere except within a width of $10^\circ$ which corresponds to the effect of integration limits that we have identified when the integration was done for the whole quarter cylinder. Most importantly this result is the same as those obtained for the whole single quarter cylinder. We have found similar results when the integration was made around different arbitrary values of $\alpha$ other than $45^\circ$.

From the above three points, we inferred that if the value of number $N_1$and $N_2$ of smectic layers are not varying rapidly along the edges of the hemicylinder which is not a perfect quarter cylinder as the one shown on figure 4.7 we can consider that

this edge is made of a series of connected small triangular slab like the one shown on figure 4.14a, each slab being a portion of perfect quarter of cylinders. And we can use locally the above calculation of integrated intensity and $\Delta q$ to extract the local values of $N_1$ and $N_2$ in the slab. In other word the intensity is a local quantity at the scale of $10^\circ$. In other words, the study of the variations of the intensity and the $\Delta q$ as a function of $\alpha$ should allow to appreciate the variations of $N_2$ and $N_1$ with $\alpha$ with a resolution of $10^\circ$.

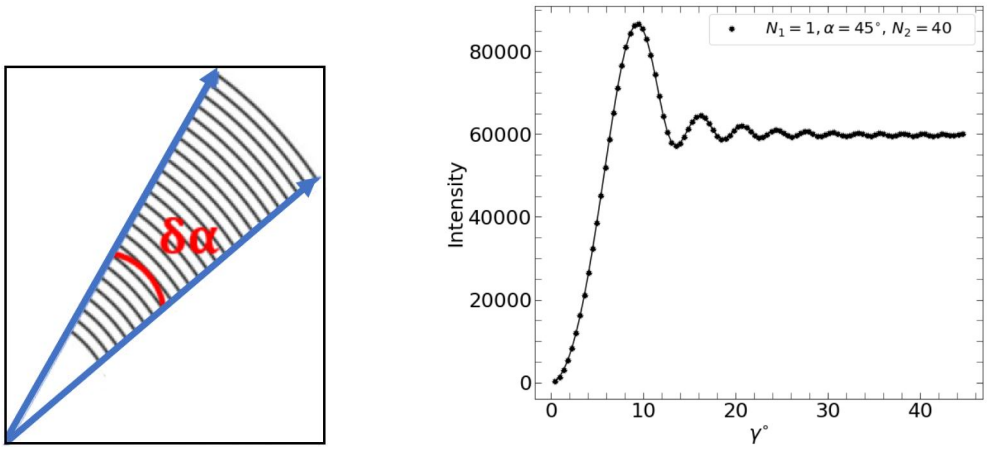


(a) (b)

Figure 4.14: (a) Single triangular slab. (b) Calculation of intensity scattered around a fixed value of $\alpha = 45^\circ$. This intensity is plotted as a function of $\gamma$.

## 4.7 Determination of the number of diffracting smectic layers $N_1$ and $N_2$

We have seen the experimental integrated Bragg intensity in figure 4.1b and the experimental $\Delta q$ in figure 4.3. During our theoretical calculation, we have found that both the integrated intensity and the $\Delta$q do not vary as a function of orientation $\alpha$ when both $N_1$ and $N_2$ are kept constant. However, they vary as a function of $N_1$ when $N_2$ is kept constant (figure 4.13 and figure 4.12) and they also vary as a function of $N_2$ when $N_1$ is kept constant ( figure 4.10 ). To reconstruct the model of the oily streaks we need the values of $N_1$ and $N_2$ as can be found using equations 4.32 and 4.33. I will use the experimental measurement of intensity and $\Delta q$ combined to the calculation of integrated Bragg intensity for fixed $N_1$ and $N_2$ and the $\frac{1}{\Delta q}$ for fixed $N_1$ and $N_2$ calculated in the case of prefect quarter cylinder. Based on the above discussion (in the section 4.6) where we have shown that the intensity is locally related to the number of scattering smectic layers, we can now consider that our real edge of quarter cylinder is made up of small triangular slabs with local values of $N_1$ and $N_2$ layers. To find the evolution of $N_1$ and $N_2$ as a function of orientation $\alpha$, at least one of them has to vary since the number of scatters would be constant if they are both constant. We had three hypotheses. The first one was to vary $N_1$ and keep $N_2$ constant for all $\alpha$ in agreement with the model initially developed in our group [2, 3]. After many attempts, it was impossible to find fully identical values of $N_2$ issued from the integrated Bragg intensity calculation (equation 4.30) or issued from $\frac{1}{\Delta q}$ calculation (equation 4.31). We have made two other hypotheses. They are based on varying $N_2$ and either keeping $N_1$ constant or varying it. For the two hypotheses, we have used the evolution of integrated Bragg intensity and $\Delta q$ given in the in equations 4.30 and 4.31 respectively, to get the evolution of $N_2$ as a function of $\alpha$ as follows

$$N_2 = \sqrt{\left(\frac{\frac{I_{ib}}{I_o} - B(N_1)}{A(N_1)}\right) + N_1^2} \tag{4.32}$$

$$N_2 = \left( \frac{\frac{1}{\Delta q} - D(N_1)}{C(N_1)} \right) + N_1 \tag{4.33}$$

where both the integrated Bragg intensity $I_{ib}$ and the width $\frac{1}{\Delta}$ are now experimental values. The key was that we had to find a value of $N_1$ that would give the same $N_2$ values from these two calculations, i.e., the curve from equation 4.32 has to superimpose the other one from the equation 4.33.

### 4.7.1 Hypothesis 1: Keeping $N_1$ constant

This hypothesis corresponds to the scheme of figure 4.15b. Starting from the hypothesis that $N_1$ is constant, we have used different $N_1$ values like $35, 30, 20, 15, 10, 8, 5$ and $1$ alongside the experimental value of both $I_{ib}$ and $\frac{1}{\Delta q}$ to calculate the value of $N_2$. Note that the coefficient of proportionality, the slope $A(N_1)$ and the intercept $B(N_1)$ for integrated Bragg intensity and slope $C(N_1)$ and intercept $B(N_1)$ for $\Delta q$ were already determined and are shown in both figures A.1 and A.2 respectively. We have to determine $N_1$ value that will give a better superimposition between the two calculations of the $N_2$ i.e. using equations 4.32 and 4.33. However, we do not expect a perfect superimposition since we also expect some disorder in our system inducing $\Delta q$ dominated by disorder effect instead of finite size, for instance. This $N_1$ determination was made in $4$ steps for each value of $N_1$. The first step is the calculation of the value of $I_o$ using equation 4.34. The curves of experimental values of integrated Bragg intensity and $\Delta q$ have constant value between $\alpha = 40°$ and $\alpha = 70°$. We expect to have a constant value of $N_2$ in this $\alpha$ interval. We have thus taken the values of experimental integrated Bragg intensity $I_{ib}$ and the $\Delta q$ which corresponds to $\alpha = 50$ °, where $N_2$ values from both the integrated Bragg intensity and $\Delta q$ are expected to be the same. I replaced them in equation 4.34 together with the chosen value of $N_1$. Secondly, the obtained value of $I_o$ is then replaced in equation 4.32 to get $N_2$. The third step is to compared the two calculations of $N_2$ (equations 4.32 and 4.33). We finally decide to retain the $N_1$ value which gives the best superimposition between the two N2 curves.

$$I_o = \frac{I_{ib}(\alpha)}{A(N_1) * \left\{ \left[ (\frac{\frac{1}{\Delta q} - D(N_1)}{C(N_1)} N_1)^2 - N_1^2 \right](\alpha) + B(N_1) \right\}} \tag{4.34}$$

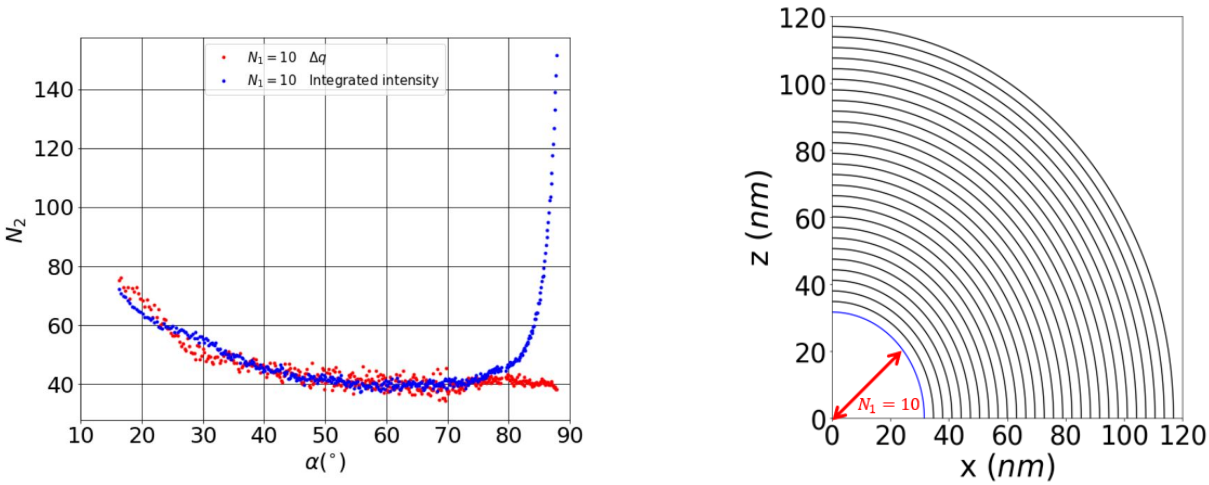


(a) (b)

Figure 4.15: (a) Evolution of the total number ($N_2$) of diffracting smectic layers at constant $N_1 = 10$ as a function of $\alpha$. The red curve was calculated using $\Delta q$ whereas the blue curve was calculated using the integrated Bragg intensity (b) quarter of the cylinder.

This procedure was done for different values of $N1$ as mentioned above. Among these $N_1$ values, only 10 gave very close superimposition of $N_2$ evolution from the integrated intensity and $\Delta q$ as it can be seen in figure 4.15a. The comparison with other $N_1$ values shown in appendix A . Although $N_1 = 10$ has given the best superimposition, it was not very different from the results of $N_1 = 3$. We could therefore suggest that $N_1 = 10 \pm 3$. We have seen in the $\Delta q$ discussion in chapter 3, section 3.3.5 that $\Delta q$ values are associated with the quality of order of diffracting smectic layers and with the finite size effect which in our case is the number of the smectic layers $N_2 - N_1$. We can see a discrepancy between the two curves at $\alpha$ values below $30^\circ$ and above $70^\circ$. This suggested that these $\alpha$ values are associated with zones in the smectic film where the disorders is so high that $\Delta Q$ is significantly increased by the corresponding variation of $q$. Figure 4.15a shows that there is a constant number of smectic layers between $\alpha = 41^\circ$ and $\alpha = 70^\circ$. It demonstrates that there are around $N_2 = 41$ layers in this $\alpha$ range. This value is logical since its corresponding thickness $(41 * 3.16\ nm)$ is quite close to the real thickness of the rotating smectic layers for our smectic system. This crucial such a direct measurement of the number of smectic layers has not been done before in our team [3, 6]. This is really because we can analyze the $\Delta q$ value for the first time that we can get quantitative information on the number of smectic layers.

Using this $N_2$ value and the constant $N_1 = 10$ , we have obtained a quarter of the cylinder with one larger disordered core area near the center of curvature of the hemicylinder shown in figure 4.15b. This is the place where curved smectic layers being very close to the center of curvature, would be the most distorted. We can understand that such layers must be very energetically expensive and thus should be removed. Therefore, for constant $N_1$ value, the scheme of the quarter cylinder is shown in figure 4.15b and would be associated with a large disordered core with $N_1 = 10$.

### 4.7.2 Hypothesis 2: Varying $N_1$ as a function of $\alpha$

This section is based on the hypothesis of keeping the value of $N_1$ varying as a function of $\alpha$. The idea is to check if it is possible to solve the above issue of prohibitive energy cost from the large disordered area through the replacement of the constant $N_1$ value was by a varying $N_1(\alpha)$. We put a connection of central non-curved smectic layers and curved smectic layers inside the hole. The former are all parallel to the substrate surface. The latter are rotating around the center of curvature as all other ones to allow for a constant interlayer spacing. This agrees with previous work [3]. We have then built a rotating grain boundary without dislocations (in red color in fig 4.16b) with a profile given by the equation 4.35 to separate the two groups of layers.

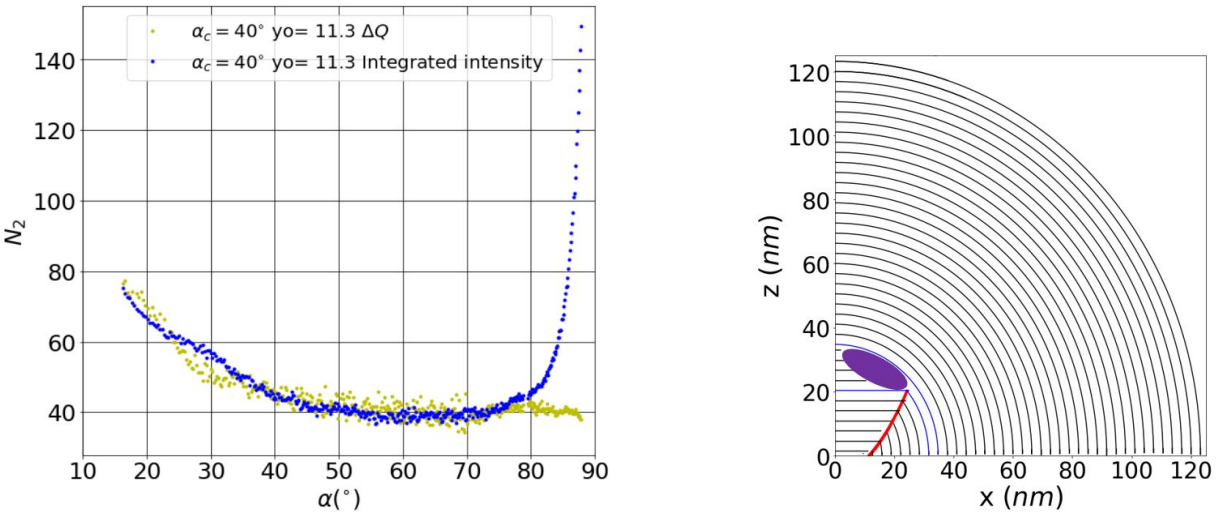


(a) (b)

Figure 4.16: (a) Evolution of the total number ($N_2$) of diffracting smectic layers with $N_1$ varying as a function of the orientation $\alpha$ of the wave vector transfer $\vec{q}$. The yellow curve was calculated using $\Delta q$ whereas the blue curve was calculated using the integrated Bragg intensity. (b) The corresponding single quarter cylinder. The red line is the rotating grain boundary without dislocation. At the top of the grain boundary, there is a dislocation defect of Burger vector 4 shown by the purple close ellipse.

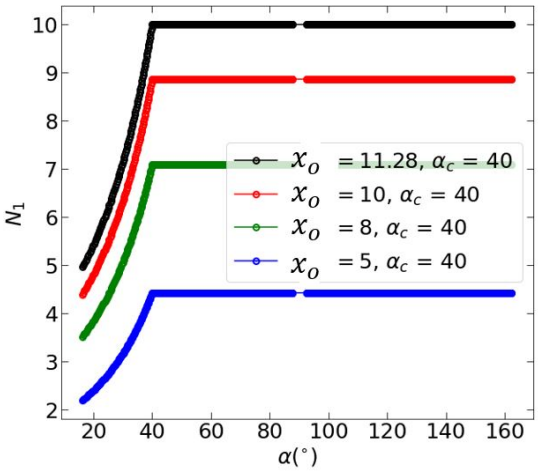


Figure 4.17: Evolution of $N_1$ for various combinations of $x_o$ and $\alpha_c$

The $x_o$ is the position of the grain boundary from the center of curvature (figure 4.16b), $r(\alpha)$ is the profile of the rotating grain boundary without dislocations.

$$r(\alpha) = \frac{x_o}{1 - \sin\alpha} \tag{4.35}$$

The evolution of $N_1(\alpha)$ was found by simply dividing the above the $r$ value given in equation 4.35 by the inter-layer distance $d = 3.16$ nm.

$$N_1(\alpha) = \frac{x_o}{d(1 - \sin\alpha)} \tag{4.36}$$

We had therefore to calculate the position $x_o$ from the curvature center of the hemicylinder and the value of the orientation $\alpha_c$, the critical $\alpha$ beyond which the number of diffracting smectic layers will remain constant. When $\alpha$ increases. $\alpha_c$ finally defines the position of the dislocation that is formed at the extremity of the rotating grain boundary. With different combinations of these two parameters, we calculated a value of $N_1$ which gave well-superimposed profiles of $N_2$ from both the integrated Bragg intensity in equation 4.32 and the full width at half maximum ($\Delta q$) of Bragg peak of intensity in equation 4.33.

The determination of the values values of $\alpha_c$ and $x_o$ was done in four steps.

Firstly, we calculated the values of $N_1$ for many different values of $x_o$ and $\alpha_c$. Example of $N_1$ evolution is shown in figure 4.17. To calculate the value of $N_2$ using the experimental value of both $I_{ib}$ and $\frac{1}{\Delta q}$ in equation 4.32 and equation 4.33, we need to calculate the coefficient of proportionality, the slope $A(N_1)$ and the intercept $B(N_1)$ for integrated Bragg intensity and slope $C(N_1)$ and intercept $B(N_1)$ for $\Delta q$.

The second step is therefore the calculation of these coefficients. We have seen that the coefficients $A(N_1)$, $B(N_1)$, and $C(N_1)$ vary quadratically as a function of $N_1$. The $D(N_1)$ is linearly related to $N_1$ and the coefficients are respectively, $0.828$ for its slop and $0.396$ for its intercept. Hence to get the evolution of $A(N_1)$, $B(N_1)$, $C(N_1)$, and $D(N_1)$ we were replacing the value of $N_1$ in these equations. Thirdly, once all these coefficients are obtained, the next step was to replace them together with the values of $N_1$ and the experimental value of the integrated Bragg intensity $I_{ib}$ and $\Delta q$ in the equations 4.32 and 4.33 to get the $N_2$ values. The value of $I_o$ was calculated as we did in the previous section 4.7.2. The fourth step was to compare the $N_2$ values obtained using integrated Bragg intensity $I_{ib}$ and $\Delta q$ in the equations. Again, we were finding the combination of $x_o$ and $\alpha_c$ that was giving the best superimposition of the $N_2$ values issued from integrated Bragg intensity $I_{ib}$ and $\Delta q$.

After attempts of many different values of $\alpha_c$ and $x_o$, we have found that the values $\alpha_c = 40^\circ$ and $x_o = 10\,nm$ have a very good agreement between the $N_2$ issued from integrated Bragg intensity $I_{ib}$ and $\Delta q$. The result is shown in figure 4.16a. This figure shows that a large part of the values of $N_2$ from the $\Delta q$ superimposes with those from integrated Bragg intensity. It gives a rotating grain boundary without dislocation on top of which there is a single small dislocation of burger vector 4 (figure 4.16b) which is less energetically expensive than the large disordered area that we have seen with the hypothesis $N_1$ constant. Figure 4.16b shows this small dislocation in the blue color with the core depicted by a purple ellipse surface. The red curve is the

rotating grain boundary without dislocation. We will discuss the systematic discrepancies for all $(x_o, \alpha_c)$ values at $\alpha$ above $70^\circ$ in the next section 4.8.2. We will as well discuss the observed $N_2$ increase for $\alpha$ below $40^\circ$ in section 4.8.3. Notwithstanding the fact that the combination ($x_o = 11.3\ nm$ , $\alpha_c = 40^\circ$) has given the best superimposition of the $N_2$ issued from integrated Bragg intensity and the $\Delta q$, it was not significantly differ from the combination ($x_o = 3\ nm$, $\alpha_c = 60^\circ$). Finally the exact shape will be refined at the end of this chapter using the result of $q_{film}\ (\alpha)$ in figure 4.29. We will confirm that the shape shown in figure 4.18b is probably close to the real one.

## 4.8 Interpretation of the evolution of the number of diffracting smectic layers for constructing the two edges of the hemicylinder.

### 4.8.1 Alpha between $40^\circ$ and $70^\circ$

As discussed above, the two hypotheses give similar result of superimposition of $N_2$ calculated from $\Delta q$ and integrated Bragg intensity. The first one has a larger disordered area which is therefore associated with a very energetically expensive model. The second one is associated with a model which has a dislocation of Burger vector 4 and a rotating grain boundary. However, there is no dislocations along this boundary and the disclination core size is significantly smaller than the large disordered area of the first hypothesis. Hence we have preferred the second hypothesis over the first one since it is associated with a model which is much less energetically expensive compared to the first one. We will come back to the choice of this second hypothesis at the end of this chapter.

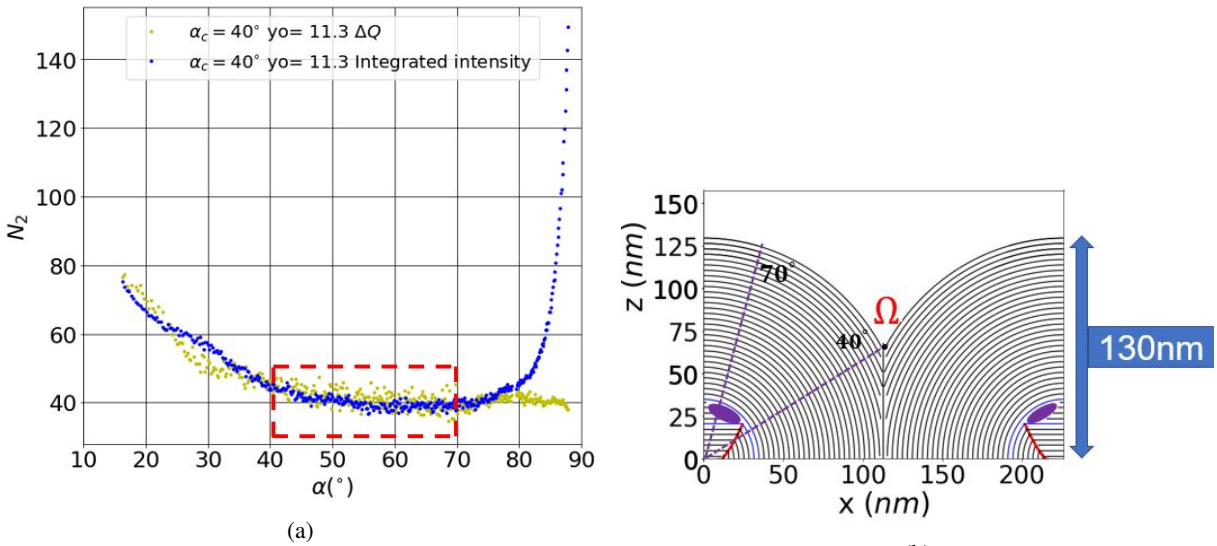


(a) (b)

Figure 4.18: (a) Evolution of total number ($N_2$) diffracting smectic layers with $N_1$ varying as a function of the orientation $\alpha$ of the wave vector transfer $\vec{q}$. The yellow curve was calculated using $\Delta q$ whereas the blue curve was calculated using the integrated Bragg intensity. (b) Two neighboring perfect quarters of 130 $nm$ thickness. The red line is the rotating grain boundary without dislocation. At the top of the grain boundary, there is a dislocation defect of Burger vector 4 shown in the purple close ellipse. The curvature wall angle omega is also indicated to be around $40^\circ$

Let's look at the evolution of the number of smectic layers from this second hypothesis. In the highlighted part between $\alpha = 40^\circ$ and $70^\circ$ in figure 4.18a, the $N_2$ issued from integrated Bragg intensity is perfectly agreeing with the $N_2$ issued from $\Delta q$. We can see that the number of smectic layers $N_2$ remains constant around 40 between $\alpha = 40^\circ$ and $70^\circ$as shown in the

highlighted part of figure 4.18a. This constant number of rotating smectic layers demonstrates that the two joined edges of the hemicylinders are made of a large slab of almost perfectly rotating smectic layers. Using the number $N_2$ of smectic layers together with the results from the varying $N_1$ we have constructed the model of two neighboring perfect quarter cylinders shown in figure 4.18b. The fact that the values of $N_2$ issued from the integrated Bragg intensity is no longer constant for $\alpha < 40^\circ$ shows that the curvature wall angle, $\Omega$ is around $40^\circ$ (this angle $\Omega$ defined by that the line between the top part of the curvature wall separating the two perfect quarter cylinder and the substrate as discussed in chapter 2). This allows to construct the model 4.18b. If we multiply this number $N_2$ of rotating smectic layers with the interlayer spacing of the 8CB smectic A liquid crystal, we find that the these rotating layers correspond to a thickness around $130\ nm$.

This result has not only allowed us to determine the structure of the model but also to get its precise thickness. This value of $N_2$ has never been determined before in any of the published works in our team. The value of the curvature wall angle, $\Omega$ of around $40^\circ$ has also never been found before, however it is not far from the published values [3]. For a $100\ nm$ thick film, the curvature wall angle, $\Omega$ was obviously found to be $30^\circ$ whereas for $230\ nm$ thick film, its value was $50^\circ$. So our value for a $180\ nm$ is $40^\circ$, in the middle of the above two previously found values.

### 4.8.2 Alpha between $70^\circ$ and $90^\circ$: Disclination areas

Using Ellipsometric measurements, our collaborator, Bruno Gallas has determined the thickness of perpendicular layers that satisfy the uniform planar anchoring on the rubbed PVA. He found that their thickness is 30 nm. This is the recent measurement that is slightly higher than the value obtain by Coursault et al. [3]. Then for our thin film sample of $180\ nm$, we have already $130\ nm$ for the rotating layers and $30\ nm$ for the perpendicular layers. So, the remaining thickness of $180 - 30 - 130 = 20$ $nm$ is equivalent to around 6 smectic layers. In this subsection we want to add these 6 layers to the model of the previous subsection 4.8.1.

As we approach the $\alpha$ range from $\alpha = 70^\circ$ to $\alpha = 90^\circ$, the number of the diffracting smectic layers from the integrated Bragg intensity increases whereas the one that comes from $\Delta q$ remains constant as underlined by the red rectangle in figure 4.19a. To understand this discrepancy, we must recall what information we can get from the integrated Bragg intensity and the $\Delta q$. In chapter 2, the calculation we made in a general way for all crystalline materials has shown that the $\Delta q$ is inversely proportional to the number of diffracting layers for all crystalline materials for strictly periodic materials. This is shown in equation 2.26. The result we have found for the smectic A material agrees with this inversely proportionality for curved smectic layers as shown in equation 4.31. However, this result responds to the strictly periodic smectic layers as well. $\Delta q$ indeed is related to the quality of order of the smectic layers. When the disorder is high, i.e., there is $q$ variation related to the presence of defects and elastic distortion, the measurement from these will dominate the average value of $\Delta q$.

This is what happens between $\alpha = 70^\circ$ and/or $\alpha = 90^\circ$. This is also because increase in the number of smectic layers that we are observing in figure 4.19a associated with the increase of the integrated Bragg intensity should induce a decrease of $\Delta q$ which may become easily dominated by elastic distortion. The results of figure 4.19a can then be explained by additional layers between $\alpha = 70^\circ$ and $\alpha = 90^\circ$ associated with $q$ variations. We need to add them to the model that we have constructed with the 40 layers between $40^\circ$ and $70^\circ$.

To do this, we will need to add convex layers where the orientation of the wave vector transfer $\vec{q}$ is varying from $70^\circ$ to $90^\circ$ only as underlined on figure 4.19b. In other words, when the smectic layers turned towards $\alpha = 70^\circ$, they must adopt a convex shape like shown on figure 4.19b in order to only present orientation of their normal between $\alpha = 70^\circ$ and $\alpha = 90^\circ$. We have already seen that around 6 smectic layers are remaining. After adding 6 convex layers as schematized on figure 4.19b we evidence a $-\frac{1}{2}$ disclination defect. Its core is shown in red point in the new model, shown in figure 4.19b. The core of this defect is between $\alpha = 40^\circ$ and $\alpha = 70^\circ$. Let's denote $z_2core$ the height position of the first layer in the disclination zone. This height is associated with $\alpha = 70^\circ$. Let's denote $z_1core$ the height of the curvature wall, on top of which the disinclination core is positioned. This height is associated with $\alpha = 40^\circ$. Though we do not know precisely how deep the first disclination layer sink in the core, we can only estimate with certainty that the size of the core of this disclination defect is less or equal to the difference $h = z_2core - z_1core = 35\ nm$ as schematized in figure 4.20. Since $z_1core$ is $30 + 130 * \sin(40)$, $z_2core$ is $30 + 130 * \sin(70)$), we find the size of the core to be smaller but close to $35\ nm$.

The strong increase of intensity most probably from $\alpha = 80^\circ$ or $\alpha = 85^\circ$ contain also contributions from the larger volume of central layers of the hemicylinder.

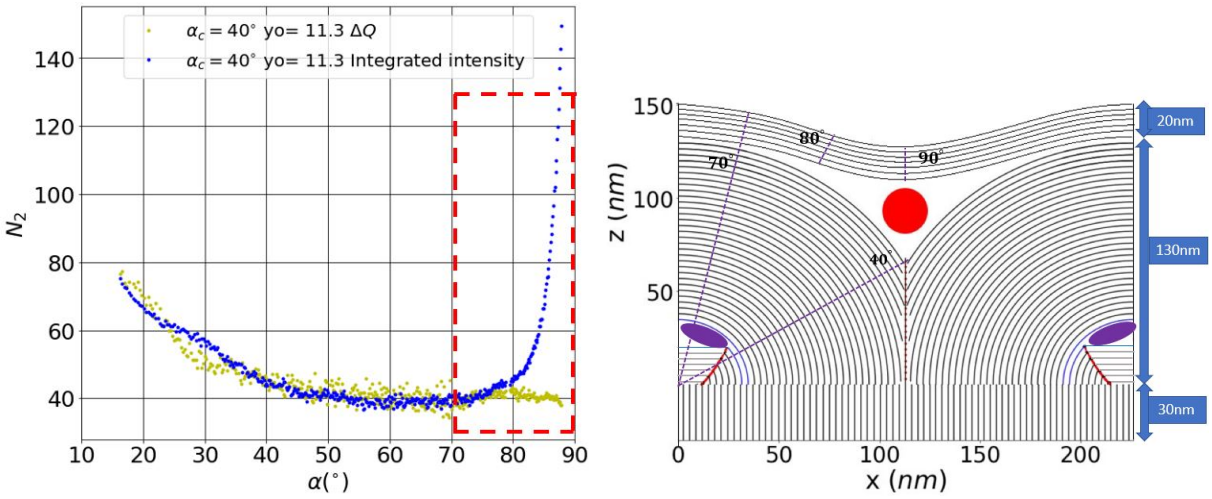


(a) (b)

Figure 4.19: (a) Evolution of total number ($N_2$) of diffracting smectic layers with $N_1$ varying as a function of the orientation $\alpha$ of the wave vector transfer $\vec{q}$. The yellow curve was calculated using $\Delta q$ whereas the blue curve was calculated using the integrated Bragg intensity. (b) Two neighboring perfect quarter cylinder of $130\ nm$ thickness. The red line is rotating grain boundary without dislocation. At the top of the grain boundary, there is a dislocation defect of Burger vector $4$ shown in the purple close ellipse. The red point is the core of the disinclination defect.

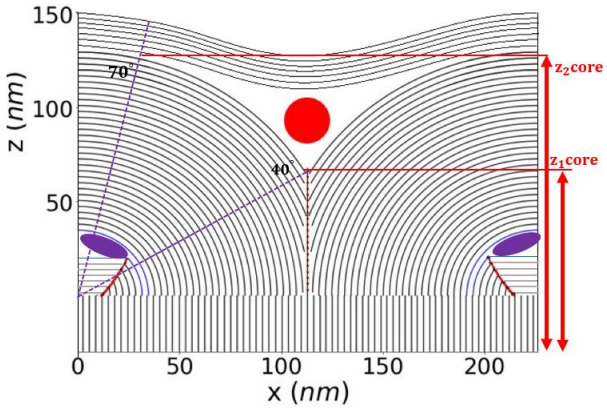


Figure 4.20: The schematized model of the disinclination defect core size

### 4.8.3 Small $\alpha$ less than $40^\circ$ and Vertical grain boundary

We observe a small disagreement between the values from integrated Bragg intensity and those from $\Delta q$ at $\alpha$ values smaller than $40^\circ$. It is due to the fact that for some orientation $\alpha$ the contribution of disorders to $\Delta q$ is significant. So this area contains some defects. We also observe on figure 4.21a that $N_2$ decreases from small $\alpha$ until around $\alpha = 40^\circ$. This $\alpha$ interval corresponds to the area of the direct junction between the two neighboring hemicylinders, i.e., along the curvature wall that separates them (see figure 4.21b). Now, if we zoom in on the area below $\alpha = 40^\circ$ in figure 4.19b, we get the figure 4.21b that shows empty gapes of different sizes along the vertical curvature wall. Figure 4.22 extracted from Williams and Kléman [7]. They considered a perfect planar sample and applied disorientation on its two edges. A small tilt creates a straight vertical curvature wall between the tilted sides with localized dilatation of layers. When the tilt angle increases, it requires a large stress associated with the

induced dilation. Such stress can be relaxed by adding extra smectic layers in the dilated areas (figure 4.22 (c)). These extra layers are associated with dislocations. We can determine the number of smectic layers to fill the gaps, shown on figure 4.21b with extra-layers in the manner shown by Williams and Kleman ( figure 4.22 [7])(c).

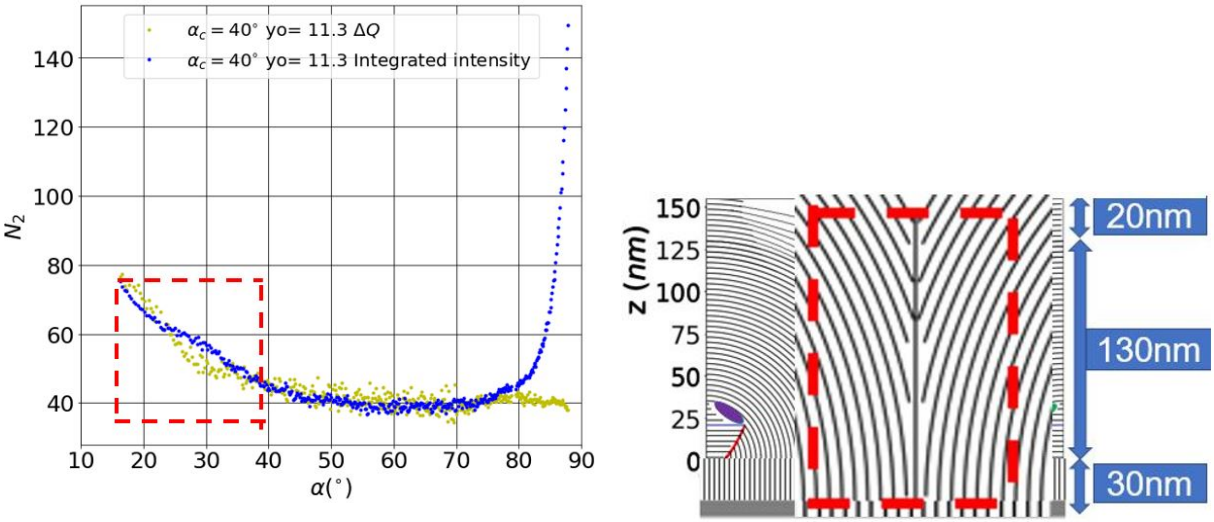


(a)

(b)

Figure 4.21: (a) Evolution of total the number ($N_2$) of diffracting smectic layers with $N_1$ varying as a function of the orientation $\alpha$ of the wave vector transfer $\vec{q}$. The yellow curve was calculated using $\Delta q$ whereas the blue curve was calculated using the integrated Bragg intensity (b) Two neighboring perfect quarter cylinder with the zoomed part along the curvature wall showing a zone possibly occupied by a chain of dislocations.

We obtained that the maximum number of smectic layers that can be added in relation with the presence of dislocation defects is 17. However, $N_2$ increases toward even larger values. This suggests that not only a possible chain of dislocations of different Burger vectors may be created along the curvature wall (since each extra added smectic layer would be associated with a dislocation) but also many distortions may occur in this localized area that we can not figure out from our data. This distortion may modify the orientation of the smectic layers depending on $\alpha$ angle. In other words, locally around the curvature wall, we may have now more regularly rotating smectic layers superimposed in the form of the perfect quarter cylinder.

It is due to this fact that we have started a collaboration with Hamdan, Abdalaziz and Scott Mac Lachlan from the university of Newfoundland. Canada, Timothy Atherton from Tufts university in Boston and Patrick Farrell from University of Oxford, UK to simulate the model of two neighboring of two quarter cylinders of imposed surface defined by the $41^{th}$ layer in our model shown on figure 4.18b. Since, the smectic order parameter is a complex quantity, it is difficult to simulate the smectic layers. In this group, they are interested in simulating distorted smectic layers in a simple system that is almost similar to our system of two neighboring perfect quarter cylinders. After many works they succeeded to obtain the simulation shown in figure 4.23. This figure is promising that we can get a lot of refined results. In this simulated model, we can see in particular that they found a quite homogeneously rotating smectic layers like in our system. Many dislocations in the region near the center of curvature and along the curvature wall, a result which is not far from our result in figure 4.21b.

In particular they found dislocated pictures like the one proposed by Williams and Kléman [7] in figure 4.22. This suggests that the structure leading to the increasing $N_2$ number when $\alpha$ decreases from $\alpha = 40°$ may be associated with particularly complex structures and that collaboration with simulators are absolutely necessary to understand really the corresponding structure. The project of collaboration consists in particular to simulate from their structure the expected diffraction in order to compare it with our experimental data.

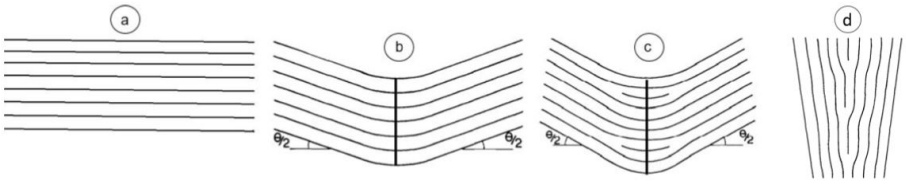


Figure 4.22: (a) Perfect planar sample before applying the stress to disorient its two edges. It is showing only dilated layers without dislocations (b) The curvature wall without dislocations after applying a small stress (c) The curvature wall with a chain of dislocations after applying a larger stress (d) the curvature wall made up of only a chain of dislocations[7]

.

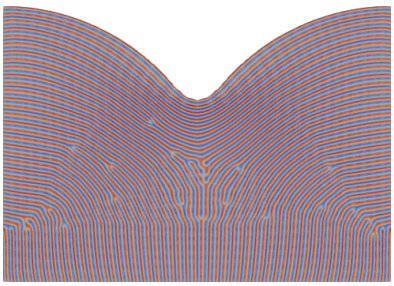

Figure 4.23: Simulation of two joined quarter of cylinders (Results from research group of Scott Mac Lachlan, Patrick E. Farrel and Timothy James Atherton).

### 4.8.4 Discussion

Confined 8CB smectic A liquid crystal has been shown to be able to produce 1D patterns of defects, the so-called oily streaks. These oily streaks are the result of the competition between anchoring energy at the boundaries of the sample, surface energy, elastic energy, and defect energy. They have been intensively studied[2, 3, 5, 6]. The former works have demonstrated that each oily streak is formed by an hemicylinder. Using a combination of optical microscopy, synchrotron X-ray diffraction and ellipsometry, Coursault et al. [3] have studied the internal structure of this hemicylinder using films of a smectic liquid crystal 8CB with thicknesses in the range of $100 - 300\ nm$ as discussed in chapter 2. In this chapter 4, I have reported the results from a $180\ nm$ thick film of 8CB deposited on the rubbed PVA. Using the hypothesis that the intensity scattered by rotating smectic layers inside the hemicylinder is approximated to the integrated Bragg intensity and thus proportional to the number $N(\alpha)$ of these layer , Coursault et al. [3] have build a model of flatten hemicylinder. However, we have demonstrated that this hypothesis is only true for perfectly flat smectic layers as in normal solid. We have demonstrated that for the case of curved or rotating smectic liquid crystal layers, the integrated intensity is instead proportional to the $N_2^2 - N_1^2$ and not to $N_2 - N_1$. This confirmed the necessity of reconstruction of the intimate internal structure of the hemicylinder.

Furthermore, experimental intensity that was used by [3] to build the model for the $100\ nm$ thick sample appeared to be not in perfect Bragg conditions. In this chapter we have used integrated Bragg intensity (as discussed in chapter 3) to determine the evolution of the number of rotating smectic layers $N_2$ and $N_1$ of missing layers close to the center of curvature as a function of $\alpha$. Similarly to the normal crystal material, we have found that the inverse of full width at half maximum $\Delta q$ is proportional to the $N_2 - N_1$. This parameter has never been used before in our group. Since it is constituted of contributions from both the disorders or fluctuations in layers and finite size effect, we have found it as an important parameter that can help to study and localize the topological defects inside the hemicylinder system. Using the calculated relationship between both the $\Delta q$ and $N_2 - N_1$ combined with the relationship between the number of scattering layers and the integrated Bragg intensity, we were able to reconstruct the model of the two neighboring quarter cylinders. This model is shown in figure 4.24.

Compared to the previously constructed models [2, 3], this new model has various unprecedented features that I am going to discuss in this section. The first feature is the rotating grain boundary without dislocations (shown in red solid line in figure 4.24). Coursault et al. [3], have reported a presence of rotating grain boundary which was formed by two parts: the lower part

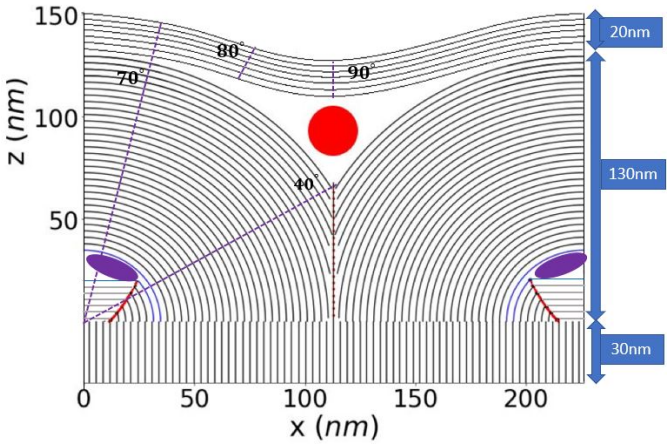


Figure 4.24: Two neighboring perfect quarter cylinder of 130 $nm$ thickness. The red line is the rotating grain boundary without dislocation. At the top of the grain boundary, there is a dislocation defect of Burger vector 4 shown in the purple close ellipse. The red point is the core of the disclination defect.

is formed by rotating grain boundary without dislocations and a upper part is formed by a number of small edge dislocations. Such grain boundary was also found for 8CB film deposited on a $MoS_2$ substrate. Like them, we have found the grain boundary without dislocations but with only one single dislocation of Burger vector (the dislocation is localized between the two layers shown in blue color and its core is shown in purple color) located on top of it. By this result we were able to minimize the number of dislocations in this area close to the center of curvature. The profile of this grain boundary is formed by a number $N_1$ of smectic layers that is changing as a function of the orientation $\alpha$. This grain boundary has two characteristic features: its position $x_o$ from the center of curvature of the quarter cylinder and the critical angle $\alpha_c$ above which the number of rotating smectic layers becomes constant. The determination of both $x_o$ and $\alpha_c$ was based on finding their combination that gives best superimposition of $N_2(\alpha)$ values calculated using the integrated Bragg intensity and those calculated using the $\Delta q$. Many combinations have given a good superimposition, however, $x_o = 11.3\ nm$ and $\alpha_c = 40^\circ$ was giving the best superimposition though not differing a lots from other combinations.

The second one is the vertical straight curvature wall that is separating the two neighboring quarter cylinders. Our results suggest a presence of a chain of dislocation defect along this curvature wall. The curvature wall angle, $\Omega$ which is the angle that the upper part of the curvature makes from the substrate was determined in [3]. For a 100 $nm$ thick 8CB film this angle was $30^\circ$. For a 230 $nm$, the angle was $50^\circ$. Through our analysis, we have found an angle around $40^\circ$ for a 180 $nm$. Based on this result, it could be possible to say that the curvature wall angle, $\Omega$ varies as a function of film thickness. However, as we will see in chapter 5, this curvature wall angle, $\Omega$ doesn't vary when the film thickness varies, the variation observed in [3] might have been caused by the fact that it was determined from the data which was not in Bragg's condition.

The third feature is the $-\frac{1}{2}$ disclination defect which has the core shown through the red point in figure 4.24. Large disorder associated with the convex layers on top of the core has been evidenced. We have demonstrated that the size of its core is of order of 35 $nm$. Since the central layers are in full rotation around the $2D$ central topological grain boundary, they form an overall $+\frac{1}{2}$ defect. Hence the newly evidence $-\frac{1}{2}$ disclination is balancing the total topological charge of the whole hemicylinder to zero. This in agreement with the model suggested by Allet, Kleman, and Vidal [8], though for their case, the central part is not flat but a normal cylinder. It is now known that the topological defects can capture and orient nanoparticles [9, 10, 11]. It would be interesting to understand how this disclination can transfer its shape to these nanoparticles.

## 4.9 Study of the central part of the hemicylinder

### 4.9.1 $\Delta\alpha$ value and Evolution of the intensity

In chapter 2 the model constructed for a very thin film of 100 $nm$ [3] lacked data associated with the central part of the hemicylinder. The lack of data was due to the beam stop hiding this central part. In addition, we have seen in chapter 3 that this data were not in Bragg condition for small incident angles like the ones used by Coursault et al. [3]. These two factors evidence the necessity of a precise study of this central part. With the collaboration of the team of SIXS beamline at Soleil Synchrotron, our team has found a new way of measuring this central part. This consists of shifting the beam stop as we have shown in figure 3.3 in chapter 3 and also displacing the detector in order to have the detector dead area (in pink color in figure 4.25(a)) positioned not in the top of the scattering ring, the resulting image on the detector is shown in figure 4.25(a).

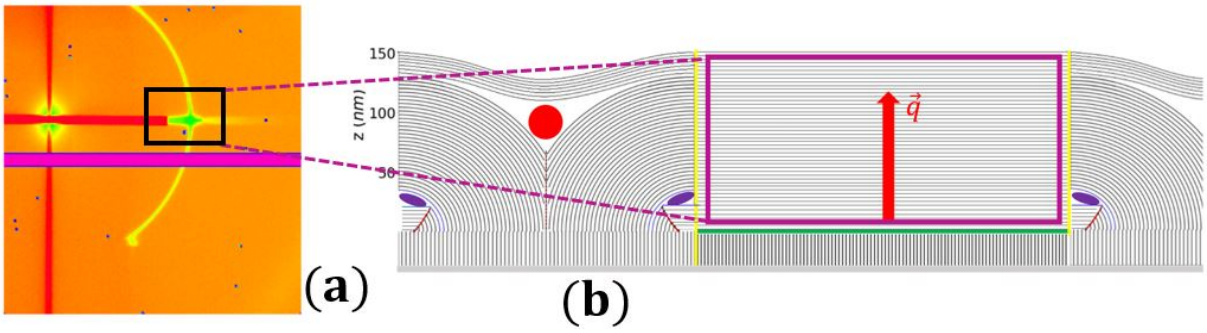


Figure 4.25: (a) Images from Eiger detector after shifting the beam stop in order to visualize signal scattered from the central part of the hemicylinder (b)) The schematized internal structure of the hemicylinder [3], the wave vector transfer $\vec{q}$ is parallel to the layer normal in the central part. The red inclined line is rotating grain boundary without dislocation. At the top of the grain boundary, there is a dislocation defect of Burger vector 4 shown in the purple close ellipse. The red point is the core of the disinclination defect.

This figure is showing the scattering ring after the shift of the beam stop. The ring is finally formed by two parts: the first part is the intensity scattered by the rotating smectic layers and the second part is the intensity scattered by the smectic layers in the central part of the hemicylinder. For a flattened hemicylinder, 8CB molecules in the central part obey the homeotropic anchoring imposed by air. The 8CB-air strong surface energy, 30 $mJm^{-2}$ [2], tends to lead to flat smectic layers. Due to the homeotropic anchoring, the central smectic layers tend to be perfectly flat with all 8CB molecules orientated in a single direction parallel to one wave vector transfer $\vec{q}$ that is perpendicular to the horizontal plane of the hemicylinder as shown in figure 4.25(b).

The large volume of the central flat smectic layers would give a single intensity peak at $\alpha = 90°$. The yellow vertical lines are the walls which are separating the rotating smectic layers and the central flat layers. The horizontal green line is depicting a 2D central grain boundary that is separating the central flat layers and the perpendicular layers on the substrate as seen in chapter 2. It has been considered as a 2D topological defect and it traps nanoparticles [3, 9]. I will come back on it later in section 4.9.9.

After zooming on the top part of the scattering ring from with Bragg incident angle $\omega = 0.6°$ we obtained the scattering as shown in (figure 4.26 (b)). Two bright peaks were observed instead of the expected single maximum at $\alpha = 90°$. The intensity extracted from these peaks gave two well-resolved peaks positioned respectively at $\alpha_1 = 89°$ and $\alpha_2 = 91°$. This implies that the two peaks are distanced by a width of $\Delta\alpha = 2°$ as shown in figure 4.26(c). Hence, the first peak is diffracted by a stack of smectic layers whose director (normal) is parallel to the wave vector transfer $\vec{q_1}$ oriented at $\alpha_1$ and the other one is diffracted by a stack of smectic layers whose director (normal) is parallel to the wave vector transfer $\vec{q_2}$ oriented at $\alpha_2$ as shown in figure 4.27. So the central part of the oily streaks in the 180 $nm$ 8CB smectic film is not formed by perfectly flattened smectic layers.

It is instead formed by a gable roof-like structure with an inclination angle of $\Delta\alpha = 2°$ at its ridge as shown in figure 4.28. The disorientation angle $\theta$ shown in this figure equal, $\frac{\Delta\alpha}{2}$ is small.

This new structure has three features. The first one is the central curvature wall (vertical line in blue color) that is induced by the disorientation applied to the two sides of the central smectic layers. It can be considered as a chevron. We have evidenced this new feature in collaboration with the group of Samo Kralj and Luka Mesarec, both from University of Maribor in Slovenia.

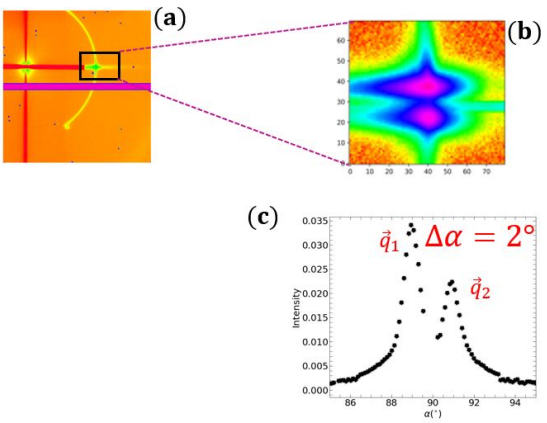


Figure 4.26: (b) zoom of the central part. The two brighter spots comes from central smectic layers which have normals orientated in different directions. (c) The Bragg intensity extracted from this central part of the hemicylinder.

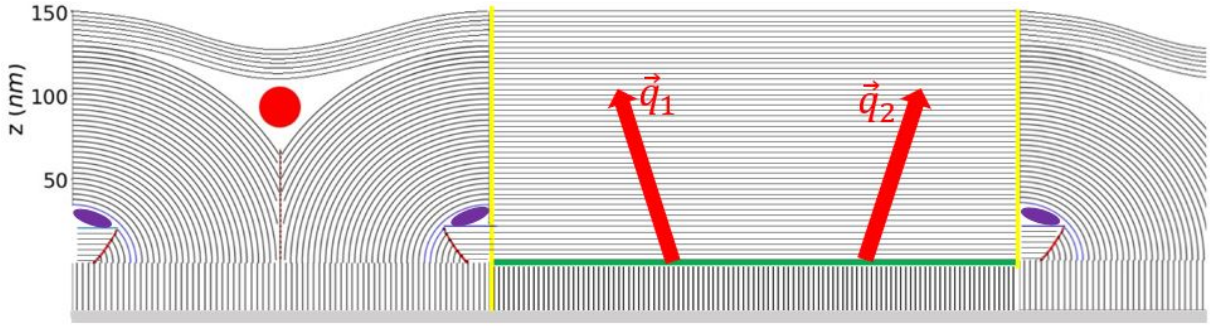


Figure 4.27: The schematized internal structure of the hemicylinder , the two wave vector transfers $\vec{q_1}$ and $\vec{q_2}$ are showing the two possible orientations of the smectic director of molecules in the central part.

The chevron structure in smectic is generally highlighted by the presence of two peaks as Takanishi et al. [12] as we discussed in chapter 2, section 2.6.3. We have seen that according to William and Kleman [7], when the disorientation angle is small, the associated stress is also small and induces curvature wall without dislocations contrary to large disorientation that induces curvature wall with a chain of dislocations along it as shown in figure 4.22(b). The second feature is that the 2D central grain boundary in figure 4.27 has became a 3D central grain boundary (in green color). The third feature is the yellow vertical line that is joins smectic layers disoriented by an angle $\theta$ from each part of this wall which has become a grain boundary. In the next section I will discuss the changes along this grain boundary between the rotating layer and the central inclined layers.

### 4.9.2 Evolution of the wave vector transfer $\vec{q}$ in the smectic oily streak

In order to understand the origin of the chevron structure (in figure 4.28) we need to finely study an experimental parameter, which is the wave vector transfer $q$. The figure 4.29 is showing the experimental values of the magnitude of wave vector transfer $q$ extracted from scattering rings obtained at different incident angle $\omega$. The way they were extracted is explained in detail in chapter 3. It is corrected from all refraction effects as described in chapter 2.

Figure 4.29 demonstrate a very clear result that the $q$ value at $\alpha = 89°$ (the $q_o$ on figure 4.29) is significantly larger than the values for all $\alpha$ between $20°$ and $85°$. The magnitude of $q$ is related to the interlayer spacing $d$, in Bragg condition, by $d = \frac{2\pi}{q}$. The values of $q_o$ are greater than those of $q'$. These values correspond respectively to the $d_o$ the average value of the interlayer spacing of in the central part and $d'$ the average value of the interlayers spacing for all $\alpha$ values which are related to the rotating

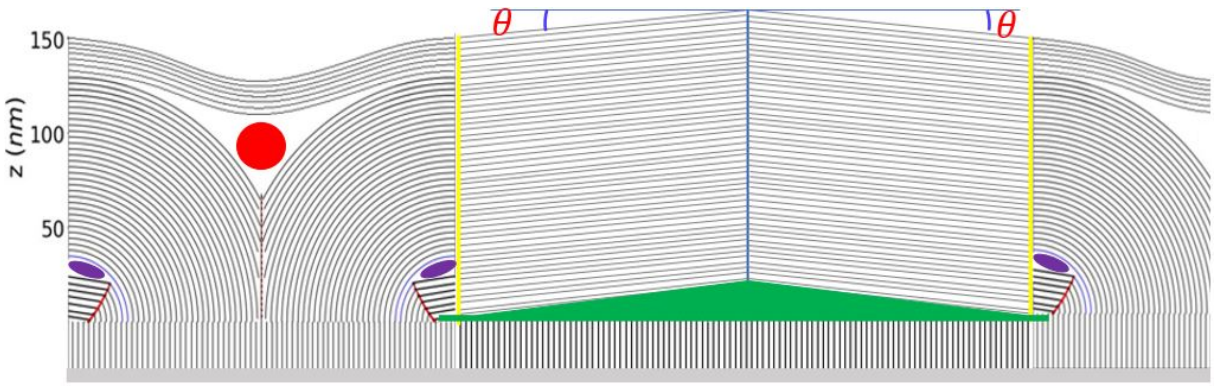


Figure 4.28: The new internal structure of the hemicylinder. The green solid triangle is a 2D topological grain boundary The red inclined line is rotating grain boundary without dislocation. At the top of the grain boundary, there is a dislocation defect of Burger vector 4 shown in the purple close ellipse. The red point is the core of the disinclination defect.

smectic layers. So, the value of $d'$, is greater than that of $d_o$. There is a dilation of rotating smectic layers with respect to the central ones.

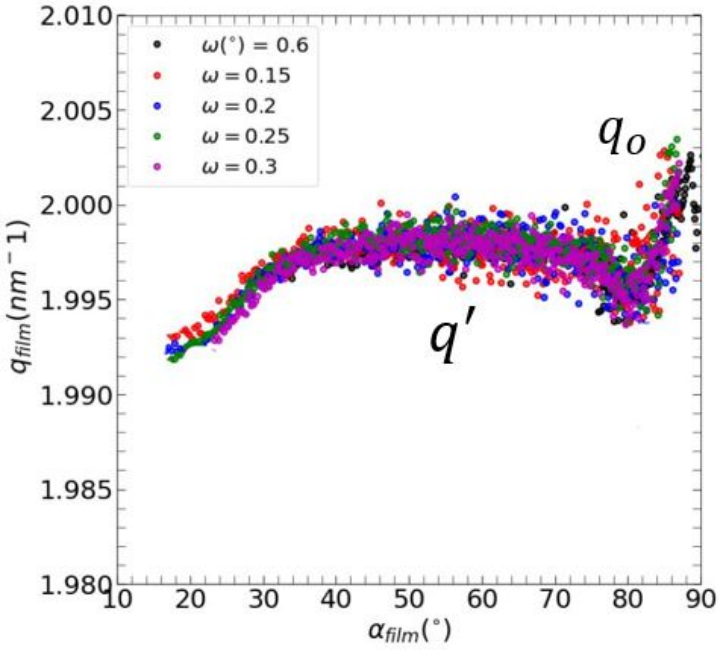


Figure 4.29: The Evolution of the wave vector transfer $\vec{q}$ as a function of orientation $\alpha$ for both rotating and central smectic layers.

If $d' > d_o$, a connection between the rotating layers and the central ones must take place around the yellow curvature plane shown on figure 4.28 a grain boundary (in yellow) must exist to connect. Geometrically, as shown in figure 4.30, a disorientation

$\theta$ between the area of the rotating layers and one of the central layers allows for a smooth connection if

$$cos(\theta) = (\frac{d_o}{d'}) \tag{4.37}$$

There is dilation (for all $\alpha$ values) of the rotating layers with respect to the central layers. The difference in the q values in the two parts is $0.005\ nm^{-1}$. Equation 4.37 finally shows that the dilation of the rotating smectic layers with respect to the central layers induces the disorientation $\theta$ of the central layers and consequently leads to the chevron in the center part of the hemicylinders as shown in figure 4.30. It is a grain boundary without dislocations formation (blue color) localized in the central part of the flattened hemicylinder in between the two tilted sides.

In addition, two other grain boundaries where the smectic layers tilt are formed and are underlined in yellow in figure 4.30 of the complete model of the internal structure of the oily streaks from a smectic A thin film of $180\ nm$ finally emerges that includes not only the two joined quarter cylinders with their defects but also the central part with 3 additional grain boundary. This structure is energetically favorable compared to the bookshelf configuration shown in figure 4.25 and that clearly appears due to the mismatch between the $d'$ and $d_o$.

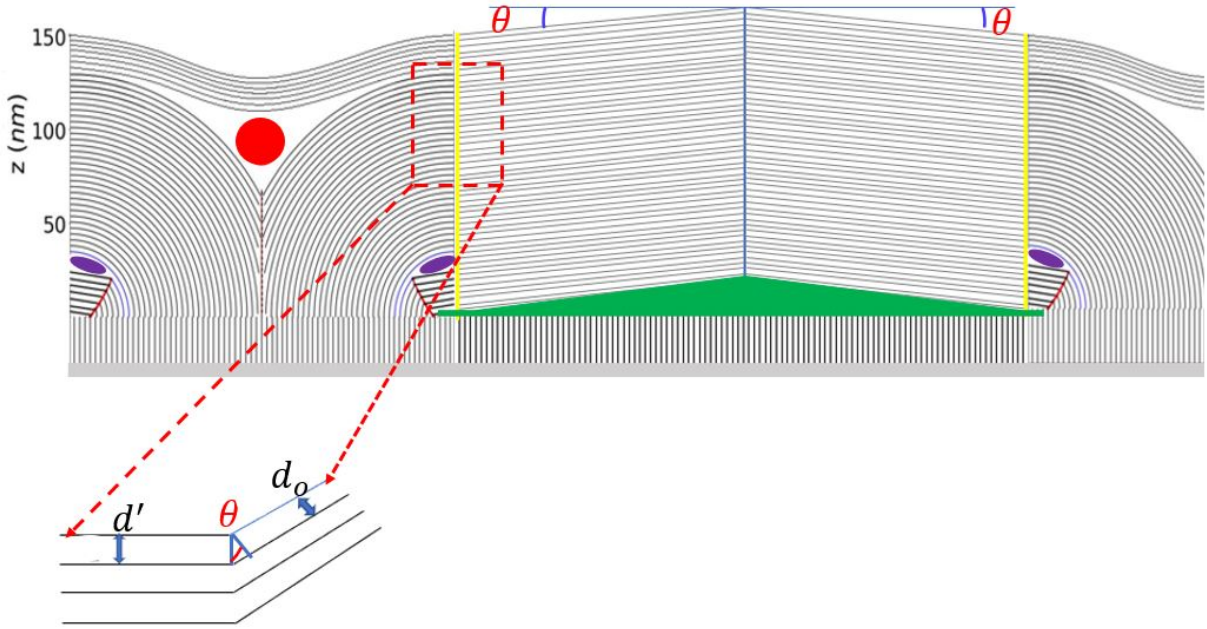


Figure 4.30: The new internal structure of the hemicylinder. The green solid triangle is aD topological grain boundary The red inclined line is rotating grain boundary without dislocation. At the top of the grain boundary, there is a dislocation defect of Burger vector 4 shown in the purple close ellipse. The red point is the core of the disinclination defect.

### 4.9.3 Energy minimization for rotating layers

To understand the origin of the observed dilation for the rotating layers in collaboration with Professor Randall R. Kamien from University of Pennsylvania, who is a leading figure in the theory of topological defects in condensed matter physics, a calculation has been performed. It relates the interlayer spacing $d'$ to the radius of curvature of the corresponding rotating smectic layer.

We have seen in chapter 1 that the 8CB in smectic A liquid crystals is characterized by a long-range orientational order of the elongated molecules, which are arranged into stacks of equally spaced fluid layers. There is a large elastic energy associated with any deformation which changes this interlayer spacing. The resulting system has to be of minimum free energy. Determination of the minimum energy can help to explain not only the above variation of the interlayer spacing but can also give more information on the structure of the hemicylinder.

Let's first recall some of the parameters that we need to do the energy minimization. We made hypothesis of extremely strong anchoring such that smectic layers geometry on the substrate and at air is fixed. We thus minimize only the elastic energy. Moreover, we can consider mostly perfectly rotating smectic layers by neglecting the area close to the curvature walls and the disclination area. So the only parameters will be $r$ in polar coordinates. From the equation 1.4 in chapter 1, we have written the relationship between the phase field $\Phi(z)$ and the average mass density $\rho(z)$ of the layer in an hypothesis of flat smectic layers perpendicular to (Oz) direction:

$$\rho(z) = \rho_o + \rho_1(z)\cos\Big\{q_o\Big[\Phi(z)\Big]\Big\} \tag{4.38}$$

where

$$\Phi(z) = z + u(z)$$

This is for the case of a planar stack of smectic layers where the local direction of layer normals is along the $z$ axis. $u(z)$ is the layer displacement from the equilibrium position $z = nd$ and the origin is chosen at $z = 0$.

However, in our case, the smectic layers are rotating and therefore the local direction of the layer normal is parallel to the radius of curvature $r$. The equation 4.38 becomes

$$\rho(r) = \rho_o + \rho_1(r)\cos\Big\{q_o\Big[\Phi(r)\Big]\Big\} \tag{4.39}$$

where

$$\Phi(r) = r + u(r) \tag{4.40}$$

The layer displacement $u(r)$ is from the equilibrium position $r = nd$ with $n$ an integer and the origin is chosen at $r = 0$.

We choose to use the free energy in term of the phase phi, written in chapter 1 in equation 4.41. This equation 4.41 will be used in polar coordinates.

$$\Upsilon = \frac{B}{2}\left\{\int d^2x\left[\frac{(\nabla\Phi)^2 - 1}{2}\right]^2 + \lambda^2(\nabla^2\cdot\Phi)^2\right\} \tag{4.41}$$

An action with Lagrangian density $\mathcal{L}$, can thus be accordingly written:

$$\mathcal{L}(\phi, \partial_i\phi, \partial_j\phi, \partial_i\partial_j\phi) = \left[\frac{(\nabla\Phi)^2 - 1}{2}\right]^2 + \lambda^2(\nabla^2\cdot\Phi)^2 \tag{4.42}$$

Using the Euler-Lagrange equation in polar coordinates to minimize the distortion free energy we obtained.

$$\nabla\left\{\nabla\phi\left[(\nabla\Phi)^2 - 1\right]\right\} - 2\lambda^2\nabla^2\nabla^2\Phi = 0 \tag{4.43}$$

where $\nabla^2 = \frac{1}{r}\frac{\partial}{\partial r}(r\frac{\partial}{\partial r})$

This leads to the following equation,

$$3(\frac{\partial\Phi}{\partial r})^2\frac{\partial^2\Phi}{\partial r^2} + \frac{1}{r}(\frac{\partial\Phi}{\partial r})^3 - \frac{\partial^2\Phi}{\partial r^2} - \frac{1}{r}\frac{\partial\Phi}{\partial r} = 2\lambda^2\left[(\frac{\partial^4\Phi}{\partial r^4} + \frac{2}{r}\frac{\partial^3\Phi}{\partial r^3} - \frac{1}{r^2}\frac{\partial^2\Phi}{\partial r^2} + \frac{1}{r^3}\frac{\partial\Phi}{\partial r}\right] \tag{4.44}$$

Using the equation 4.40 in the equation 4.44 and considering only the smallest derivative of $u(r)$ (considered to vary only slightly with $r$), we obtain the approximate equation:

$$2\left[\frac{\partial^2 u}{\partial r^2} + \frac{1}{r}\frac{\partial u}{\partial r}\right] = 2\lambda^2\left[\frac{1}{r^3}\right] \tag{4.45}$$

The solution of this equation is

$$u(r) = \frac{\lambda^2}{r} \iff \frac{\partial u}{\partial r} = -\frac{\lambda^2}{r^2} \tag{4.46}$$

The next step is to find the value of the strain. Using equations 1.16 and 4.46 we can write

$$\frac{\partial u}{\partial r} = -\frac{\lambda^2}{r^2} = (\frac{d_o - d'}{d'}) \iff d' = \frac{d_o}{1 - \frac{\lambda^2}{r^2}} \tag{4.47}$$

Therefore

$$d' = (1 + \frac{\lambda^2}{r^2}) \times d_o \tag{4.48}$$

where $d^{'}$ is the smectic interlayer spacing after the strain is applied and $d_o$ is assumed to be the natural smectic interlayer spacing. This formula 4.48 demonstrates that there will be dilation of the rotating smectic layers with respect to the radius of curvature. The dilation tends to infinity as the radius tends to zero. This agrees with the experimentally observed values in figure 4.29.

This dilation is due the bending of the rotating smectic layers. Indeed the bending energy $(\nabla^2\phi^2(r))$ increases typically as the square of the inverse of the curvature radius. It becomes increasingly expensive when the layer becomes close to the center of rotation. To decreases this elastic energetic cost, for each layer the radius has to increase through a dilation of that layer. This induces a penalty related to the first term in the equation 4.41 and finally there will be a balance between the two energy terms which lead to the observed dilation of layers. In the equation 4.48, the term of square of the ratio of the penetration depth to the curvature radius of the rotating smectic layers is always positive. Therefore this equation 4.48 is clearly showing that the interlayer spacing will always be greater or equal to the $d_o$, the natural value, i.e, it is showing that the there will always be a dilation expect when the radius of the layers is infinity. the strain depends on the square of the ratio of the penetration depth to the curvature radius of the rotating smectic layers. It increases as one approaches to the curvature center and becomes much smaller at large radius of curvature.

In figure 4.30, the layers close to the center of the hemicylinder are very energetically expensive since their radius of curvature $r$ can become very small. So, as shown in equation 4.48 they have an inter-layer distance $d^{'}$ expected to be significantly larger than the natural 8CB smectic layers distance $(d_o)$. In contrast, those far from the center of curvature are cheaper in terms of their compression energy. As the radius of curvature tends to infinity, they are expected to have an inter-layer distance very close to $d_o$. The rotating smectic layers in the figure 4.30 are consequently expected to present different intra-layer spacing for each layer. The largest dilation is expected for the layers close to the layer number $11^{th}$ (first layer fully rotating from $\alpha = 0^\circ$ to $\alpha = 90^\circ$).

Using the fact that the penetration depth $\lambda$ is approximately equal to the interlayer $d$ distance and the radius of curvature $r$ equals $d \times N$, the equation 4.48 can be written in terms of the wave vector transfer and the number of smectic layers as follow:

$$q' = (\frac{1}{1 + \frac{\lambda^2}{r^2}}) \times q_o \iff q' = (\frac{1}{1 + \frac{1}{N^2}}) \times q_o \tag{4.49}$$

The $11^{th}$ layer has thus a dilation as large as $0.83\%$. We are going to see if this experimental values of $q^{'}$ for rotating layer indeed agree with these theoretical values.

In our experiment, we do not measure this ratio $\frac{\lambda}{r}$, we instead measure the average value of the wave vector transfer $\vec{q}$.The average is over all layers starting from those with a small $r$ radius of curvature to those with a larger radius of curvature. The average $q^{'}$ is the value after the perturbation and $q_o$ is the value before perturbation or the wave vectors associated with the bulk,

### 4.9.4 Comparison experiment-theory for $\alpha$ larger than $40^\circ$

Figure 4.29 shows the evolution of the experimentally measured average values of the wave vector transfer $q$. For the smectic layers rotating between orientation $\alpha = 40^\circ$ and $\alpha = 70^\circ$ in the two edges of the hemicylinder,the wave vector transfer is constant $q' = 1.998\ nm^{-1}$. The values for the central layers is $q_o = 2.0023\ nm^{-1}$ at $\alpha = 89^\circ$ and $\alpha = 91^\circ$.

Let's take the model of two joint quarter cylinders in figure 4.31 issued from the analysis of the integrated Bragg intensity and full width at Half maximum $\Delta q$. These two experimental parameters were constant in the interval $\alpha = 40^\circ$ and $70^\circ$. So, the number of scattering smectic layers is constant in this $\alpha$ interval. These layers are from the $11^{th}$ to the $41^{st}$. The fact that

we have a constant $q'$ value between $\alpha = 40°$ and $\alpha = 70°$ fully agrees with this model. The $q'$ value of $1.998\ nm^{-1}$ is a value averaged over all superimposed smectic layers. Equation 4.49 gives the value of the wave vector transfer $q'$ associated to each of these layer numbers. This implies that the wave-vector transfer $q'$ and its inter-layer spacing vary for each layer. Then we can calculate their average value to see if it is equal or not to the constant average experimental value given in figure 4.29.

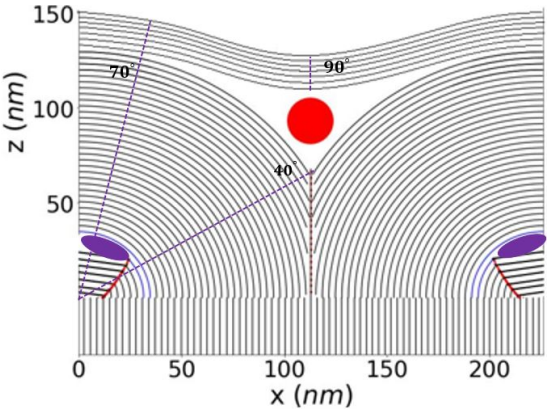


Figure 4.31: The model of two joint-quarter cylinders.

To do so we have considered $q_o = 2.0023\ nm^{-1}$ as constant and we take

$$q'_{average} = (\frac{1}{31}) * \sum_{N_i=11}^{N_i=41} \left[ (\frac{1}{1 + (\frac{1}{N_i})^2}) \times q_o \right] \tag{4.50}$$

Using equation 4.50, we have found $q'_{average} = 1.998\ nm^{-1}$, the value which is exactly equal to the experimental value. This confirms three important results. Firstly, it agrees with both the experimental integrated Bragg intensity and experimental $\Delta q$ which are constant between $\alpha = 40°$ and $70°$. This agreement between these three parameters confirms that the model of figure 4.31 is correct and in particular the presence of the 30 layers completely rotating between $\alpha = 40°$ and $70°$ is correct. We have seen in section 4.8.1 that the $N_2 = 41$ is the one that is obtained from the $\Delta q$ curve value together with the best superposition between integrated intensity and $\Delta q$, with only small variations induced when the $N_1$ model is varied. The perfect agreement revealed between the $q'$ value of figure 4.29 from alpha between $\alpha = 50°$ and $70°$ and the calculation thus confirms that the first complete smectic layer is indeed close to the $11^{th}$ one. Secondly, it confirms that the dilation of the rotating layers in figure 4.30 is induced by the radius of curvature as it was predicted by the calculation of the energy minimization in section 4.9.3. This is to say, we understand that the rotating layers are dilated due to their proximity to the curvature centers. This is expected to be a general feature of dilation of layers of small curvature radius. We must have probably for the first time, experimentally revealed the dilation phenomena associated with proximity to curvature centers that can essentially be revealed only for very thin distorted smectic films. However, in many cases the dilation must be present, for example in the well-known smectic focal conics close to the ellipse or to the hyperbola [6, 13, 14]. The last but not the least result that it is confirmed is that the central layers period is the one of the natural smectic interlayer spacing since this model predict the observed period mismatch with respect to the bulk 8CB $d_o$ and the measurement gives a mismatch with respect to the central layers. The rotating layers have to adapt to these central layers.

### 4.9.5 Implication for the tilt angle of the central layers

We have found an experimental value of tilt angle equal to $1°$. The first hypotheses we made is that the tilt angle varies from top to bottom all along the chevrons structure and the yellow grain boundary. Using equations 4.49 and 4.37, we can find the expression of the tilt angle associated with each layer:

$$\cos(\theta_{average}) = \frac{d_o}{d'} = (\frac{1}{31}) * \sum_{N_i=11}^{N_i=41} \left[ \left( \frac{1}{(1 + \frac{1}{N^2})} \right) \right] \tag{4.51}$$

The tilt angle is $7.3^\circ$ and $1.98^\circ$ for $11^{th}$ layer and $40^{th}$ layer respectively. We only measure the average value, the overall average given by the equation 4.51 is $\theta_{average} = 3.6^\circ$. We can see that both the maximum and minimum tilt angle are greater than the experimentally observed value of $1^\circ$. The calculated average value is significantly greater than the experimentally observed value.The first observed experimental result of tilt angle $1^\circ$ shows that the tilt angle $\theta$ is not given by $\cos(\theta) = \frac{d_o}{d'}$.

The second result is that we can ask a question of whether the tilt angle value varies from top to bottom. The width of the scattered intensity that we have seen in figure 4.26(c) is smaller than $1^\circ$. The $\theta$ value of $1^\circ$ is well defined and not associated with values strongly varying along the connection between rotating and central layers. If the tilt angle was varying, its variation would be of $5.32^\circ$, we could have measured it experimentally which is not the case. This evidences that in fact the smectic layers in the central part adopted a tilt angle that doesn't vary from one layer to another. Indeed the energetic cost of the associated dilation of smectic layers would have been prohibitive. However, this not varying tilt angle appears to be smaller than all required values from the one at the connection from the $10^{th}$ layer to the one at $41^{st}$ layer.

This tilt angle is imposed by a competition of three different energies. To understand it we have to look at all of them. The first one is the surface energy.When the layers are flat, the surface is of order of $p$, the width of the central part of the hemicylinder. When the layers are tilted then the surface is $\frac{p}{\cos\theta}$. So when the tilt angle increases the surface energy will increase. The surface energy tends to minimize as much as it can the value of the tilt angle $\theta$ i.e tends to keep flat the central smectic layers. The second energy that contributes to the determination of the tilt angle is the energy of the disorder of the topological grain boundary below the gable roof-like structure (in green color in figure 4.30) which has a height given by $(\frac{p}{2}) * tan(\theta)$ where $p$ is the period of the oily streak and its value is $400\ nm$ and $\theta$ is the tilt angle and height is consequently expected to be at least $3.5\ nm$. This energy increases when the tilt angle increases.

The third energy is the compression/dilation energy and curvature energy along the grain boundaries (in yellow in figure 4.30 ) that is separating the central layers from the rotating smectic ones. This grain boundary tends to have the tilt angle $\theta$ that we have calculate above. The Disclination zone has also to be taken into account. Dilation is expected in the disclination zone (see next section 4.9.6) but in the central part of the zone. At the border, the smectic layers may be following the structure of the layers below, leading to an average decrease of the induced $\theta$ angle.

The result is that we have obtained a tilt angle that is smaller than the one predicted by the grain boundary. This tilt angle $\theta$ minimized by the three global energies. In addition to this, it doesn't vary clearly to avoid the prohibitive dilation energy along the grain boundary that would be required with varying $\theta$ values along the grain boundary, in contrast with the prediction of the varying interlayer spacing $d'$. The preferable system is the one that minimizes the cost of the global energy considering all the above contributing terms, finally leading to a very small tilt.

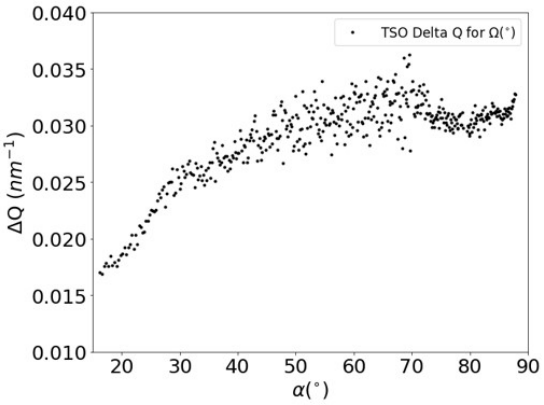


Figure 4.32: The evolution of the $\Delta q$ as a function of $\alpha$ .

### 4.9.6 Comparison experiment-theory for $\alpha$ smaller than $40^\circ$ and for $\alpha$ greater than $70^\circ$

**For $\alpha$ smaller than $40^\circ$**

Let's recall the results we have seen in section 4.7. There are two possible models of the quarter cylinder, specifically on the part close to center of curvature. These two models were based on the determination of the $N_1$. The first was that the $N_1$ number

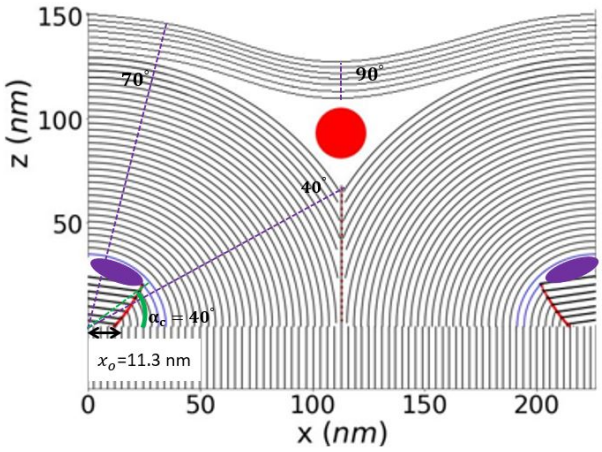


Figure 4.33: The model of two joint-quarter cylinders. The position of the rotating grain boundary (shown in red curve) is $x_o = 11.3\ nm$. The critical angle $\alpha_c = 40°$.

of smectic layers around the center of curvature was constant. For the second model, $N_1$ is changing. We have chosen the best value of $N_1$, the one that was giving the best superimposition of the $N_2$ calculated from the integrated Bragg intensity and the other one from the $\frac{1}{\Delta q}$. The distinction between the two models was not obvious. However, the second model was preferred due to low cost of elastic energy compare to the other model. Moreover, it was not obvious for the second model to choose the best $(x_o, \alpha_c)$ parameters. In this second model shown in figure 4.30, the rotating smectic layers of number smaller than the $11^{th}$ connect to the central layers at the rotating grain boundary (RGB) without dislocations (shown in the red curve ) on top of which there is one dislocation of Burger vector 4. These rotating layers can be measured only for $\alpha$ angles smaller than $\alpha_c$ as defined in section 4.7.2. We expect this $\alpha_c$ to be of the order of $40°$. This means that for $\alpha > \alpha_c$, we expect $N_1$ to be constant. For $\alpha < \alpha_c$, $N_1$ decreases. The profile of the RGB along which rotating smectic layers connect (4.33) is given by

$$r(\alpha) = \frac{x_o}{1 - \sin\alpha} \tag{4.52}$$

This allows to calculate $N_1(\alpha)$ for $\alpha < \alpha_c$ as follow:

$$N_1(\alpha) = (\frac{1}{d}) \times (\frac{x_o}{1 - \sin\alpha}) \tag{4.53}$$

where the value $x_o$ of position of the rotating grain boundary is around $11.3\ nm$ and $d = 3.16\ nm$. Using the equation 4.53, the value of $N_1$ is expected to equal to 5 and 10 respectively for $\alpha = 20°$ and $\alpha = 40°$.

If there would be no variation in $N_1$ then no further dilation of smectic interlayer spacing would be expected for $\alpha < 40°$ and according to equation 4.49 the $q'$ would remain constant with the same value as the one for $\alpha > 40°$. In contrast, we observe a clear evolution of the experimental values of $q$, in figure 4.29. A model of non-constant $N_1$ is confirmed. We now examine if the hypothesis of the presence of rotating grain boundary without dislocation is consistent with the experimental data. Already the fact that $q$, decreases when $\alpha$ is smaller than around $35°$ is consistent with $\alpha_c$ around $40°$. We have seen in section 4.9.4 that the experiment $q$ curve confirms that the $11^{th}$ smectic layer is the first complete one. If $\alpha_c$ is confirmed to be around $\alpha_c = 40°$, we can use equation 4.53 to determine $x_o$. Indeed $11 = (\frac{1}{d}) * (\frac{x_o}{(1-\sin(40))}$, leading to $x_o = 11.3$. The model that superimposes the best the two curves of $N_2$ calculated from integrated Bragg intensity and from $\Delta q$, with ($\alpha_c = 40°$; $x_o = 11.3$) is confirmed to be also consistent with the result of the $q$ curve as a function of $\alpha$.

Due to the decreasing of $N_1$ when $\alpha$ decreases below $\alpha_c = 40°$, new smectic layers must participate to the average $q'$ value for alpha values smaller than $\alpha_c$. These smectic layers are highly dilated being close to the curvature centers. They consequently decreases the $q'$ value as observed. However the calculation of the expected $q'$ is difficult. Due to the presence of the curvature wall a lack of smectic layers (a decrease of $N_2$) may be expected for $\alpha < 40°$. The value of $N_2$ may decrease along the curvature wall following the equation $N_2 = 41 * \cos(\Omega)/\cos(\alpha)$ (see the model without additional dislocation on figure 4.21b) with curvature wall angle, $\Omega$ equal $40°$ as seen in section 4.8.3. Moreover, the curves of evolution of $N_2$ calculated from the

integrated Bragg intensity and the $\Delta q$ show that an increase of number of smectic layers for $\alpha < 40^\circ$ that we attribute to the presence of additional smectic layers related to the presence of dislocations along the curvature wall (see section 4.8.3). Include these extra rotating layers around the rotating grain boundary, If we calculate the overall average $q'$ value without adding these extra layer a small value is obtained (a value $q' = 1.98\ nm^{-1}$ instead of the observed $1.992\ nm^{-1}$ is found for $\alpha = 20^\circ$ which would be associated with $N_2 = 33$ layers without extra layers). In contrast if we add these extra layers as described below, we can calculate a $q'$ value close to the experimentally observed value.

In order to calculate the new average value of $q$ for $\alpha$ smaller than $40^\circ$, for example $\alpha = 20^\circ$, equation 4.50 has thus to be changed for two features: The first one is that the starting $N$ is no more 11 but 5 for $\alpha = 20^\circ$. The $5^{th}$ to the $10^{th}$ layers are highly dilated and this leads to a decrease of the average $q'$, value. The second feature is that the ending $N_2$ has also to be changed due to the presence of the curvature wall. The analysis of the intensity and the $\Delta q$ has shown that more layers have to be added along this wall. However, the number to be added is not precisely known. This makes the second feature unclear. It may have a very small influence only if, as expected, the last layers present an interlayer spacing very close to $d_o$. Let's thus calculate with $N = 41$ and the new formula is

$$q'_{average} = (\frac{1}{37}) * \sum_{N_i=5}^{N_i=41} \left[ (\frac{1}{1 + (\frac{1}{N_i})^2}) \times q_o \right] \tag{4.54}$$

The result from this calculation using equation 4.56 is $q' = 1.992\ nm^{-1}$ a value which agrees with the experimental value in figure 4.29. This result evidences that there will always be a dilation of smectic layers which are very close to the curvature center and it indeed confirms that such layers exist. Therefore, if these layers exist then the model in figure 4.30 with a a rotating grain boundary without dislocation which stops at $\alpha = 40^\circ$ may be correct. This result implies also that we indeed have to add the above extra layers suggested by the integrated Bragg intensity.

#### For $\alpha$ greater than $70^\circ$

The evolution of the average experimental value of $q$ in figure 4.29 is showing a decreasing in its value from around $\alpha = 70^\circ$ until $\alpha = 80^\circ$. The comparison of the evolution of number of scattering layers calculated from the integrated intensity with those calculated from $\Delta q$ has shown that in this $\alpha$ interval, there is a disagreement between the $N_2$ values. This was showing that contribution from the disorder fluctuation in the interlayer spacing is large. We have then shown that this $\alpha$ value interval corresponds to the disclination zone. Dilation of smectic layers was expected in this zone. The $q$ decreasing is associated with the dilation of smectic layers in this disclination zone. If we look in the zoomed area in red rectangular, we can realize that the decreasing in the $q$ average value is almost equal to the one for the values at $\alpha < 40^\circ$. Using the $q$ value we have calculated the number of smectic layers between $\alpha = 20^\circ$ and $\alpha = 40^\circ$ and found that is around 6. This value is exactly equals to the number of smectic layer we have estimated in the disclination zone. This result shows that the dilation of the smectic layers in the disclination zone is of the same order than the one for the layers the closest to the center of curvature, that can reach $4\%$.

### 4.9.7 Implication for the full width at half maximum $\Delta q$

At the beginning of this chapter, we have done a calculation of the integrated intensity that can be scattered by a perfect quarter cylinder and its associated Bragg $\Delta q$. This calculation we have considered a system where all smectic layers have the same interlayer spacing $d$. However the results from the calculation of the minimization of the smectic distorted free energy shows that actually our system is not periodic. Every smectic layer has its own layer spacing $d$. The question comes of whether we should use the above calculation to the interpretation of the experimental results which would lead to the understanding of the internal structure of the smectic oil streaks structure ? In particular, can we use this calculation in the determination of $N_2$ ?.

To answer to this question we need to compare the theoretical width $\Delta\ q_{theo}$ due to the dilation of the smectic layers and the experimentally observed Full width at half maximum $\Delta\ q_{Exper}$. If the value of the experimental width is order of magnitude larger than the theoretical width then our Interpretation of experimental results especially the discussion of the integration Bragg intensity, the $\Delta q$ and the extraction of $(N_1, N_2)$ will be reasonable.

Let's look at the interval of $\alpha$ between $40^\circ$ and $70^\circ$. The smallest layers is the $11^{th}$.and the largest is the $40^{nd}$. According the equation 4.49,

$$\frac{1}{N^2} = \frac{q_o - q'}{q'} = \frac{d' - d_o}{d_o} \tag{4.55}$$

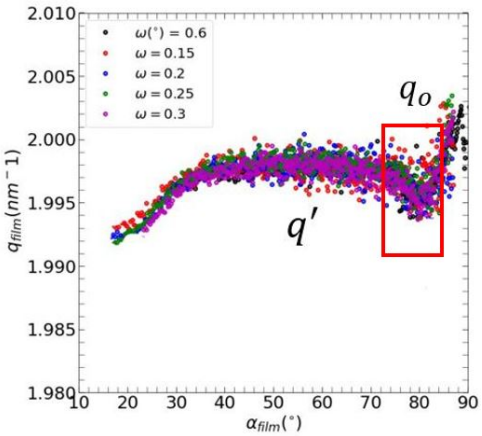


Figure 4.34: The Evolution of the wave vector transfer $\vec{q}$ as a function of orientation $\alpha$ for both rotating and central smectic layers.

For the $11^{th}$ layer which is at $\alpha = 40^{\circ}$, $\frac{1}{N^2} \approx \frac{1}{100}$ and $(q_{N1=41} - q_{N1=11})$ of the order of $0.02\ nm^{-1}$. This value is the largest possible difference between the $q$ value and is of the same order than $\Delta_{qtheor}$ for $\alpha$ between $40^{\circ}$ and $70^{\circ}$. Our calculation can thus be considered as mainly correct. It worth to use it for the comprehension of the internal structure of oily streaks for this $\alpha$ interval. However, we can see that this theoretical value becomes larger than the experimental value for $\alpha$ value less than $30^{\circ}$. In this interval we were not fully able to superimpose the curves of $N_2$ calculated from the integrated Bragg intensity and the $\Delta q$. This was because this area is at least partly dominated by dislocations defects and so their contribution to the value of $\Delta q$ is significantly large. The question to be ask here is when the measurement is dominated by this kind of disorders, where does the $\Delta q$ come from, is it from the compression or dilation of smectic layers ? Further calculation would be able needed to clarify.

### 4.9.8 Role of the substrate

Let's recall briefly what we did in the previous section. we have calculated the intensity that would be scattered by a perfect quarter of the cylinder, where we have considered that the scattering from two neighboring hemicylinders would interfere with each other. For a given orientation $\alpha$ of the wave vector transfer $\vec{q}$, we integrated over $\beta$, an orientation associated with the scatters position at a distance $r$ from the center of curvature of the quarter cylinder. We have then plotted this theoretical intensity as a function of $\alpha$ . This intensity was constant for $\alpha$ greater than $12.5^{\circ}$. Below this value there are some intensity modulations. At $\alpha = 0$, the intensity has a minimum value as shown in figure 4.38 (a). In contrast to this theoretical value, the experimental intensity at the same $\alpha$ value has a maximum value (figure 4.38 (b)). Recall that the $\alpha$ is the orientation of the smectic director which is parallel to the wave vector transfer $\vec{q}$ and it is measured from the substrate. When $\alpha = 0^{\circ}$, the molecule are orientated parallel to the substrate and the smectic layers are perpendicular to the substrate. The fact that during the theoretical calculation when these perpendicular layers are not taken into account we have obtained the minimum value at this value of $\alpha = 0^{\circ}$ confirms that the experimental maximum intensity obtained at the same $\alpha$ value was from the perpendicular layers. In the future it would be interesting to theoretically take into consideration the presence of these perpendicular layers.

Now we know that there are perpendicular smectic layers to the substrate to satisfy the uniform planar anchoring. Our first hypothesis concerning the interpretation of the observed dilation of the rotating layers for $\alpha < 40^{\circ}$ was that the interlayer spacing of the perpendicular layers on the substrate may have a larger interlayer spacing induced by the substrate. In other words the value of wave vector transfer of the perpendicular layers would be smaller than the one for both the central layers and the rotating one.

Our experimental value show that the average $q$ value of perpendicular layers $q_{per}$ is large and decreases until $\alpha = 15^{\circ}$ (figure 4.36). In other words it is larger at $\alpha = 0^{\circ}$ than until $\alpha = 35^{\circ}$ at least. In our hemicylinder model, these perpendicular layers have two contributions. The first contribution is from those which are below the rotating layers, this implies that their associated $q$ value may even be the same than for all these rotating layers. The second contribution is from those right below the central layers. So the experimental observed value is an average value from these two parts. The complete evolution

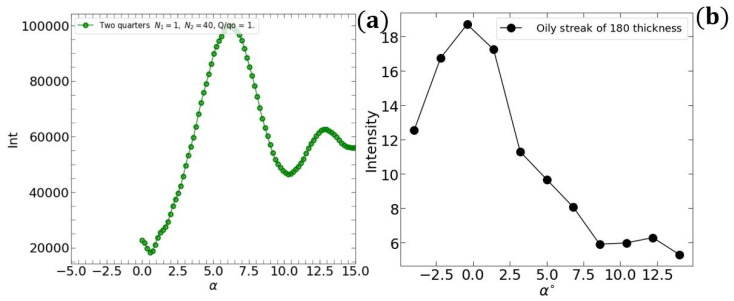


Figure 4.35: The evolution of the theoretical intensity from two neighboring perfect quarter cylinder (b) The experimental intensity measured using TSAXS configuration. The maximum value at $\alpha = 0^\circ$ was scattered perpendicular layers on the substrate

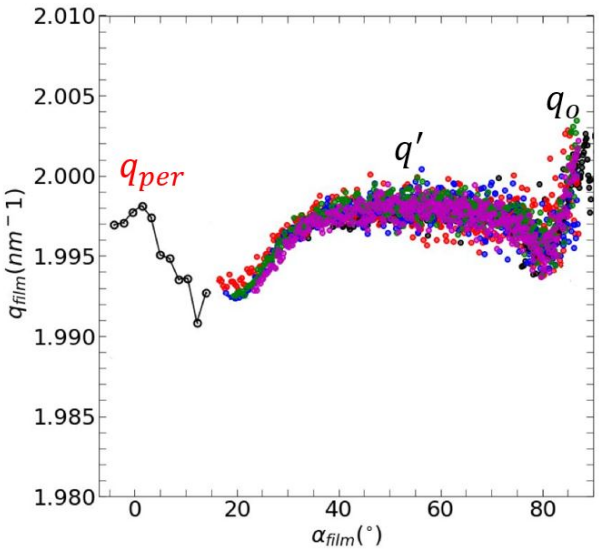


Figure 4.36: The evolution of the wave vector transfer for the whole hemicylinder. $q_{perd}$ is for perpendicular layers.

of the $q$ values as a function of orientation $\alpha$ is shown in figure 4.36. The experimental observed average value of $q_{perpe}$, for the perpendicular layers is $1.998\ nm^{-1}$. We have seen that the the number of rotating layers below $\alpha = 40^\circ$ is 41 due to the presence of the curvature wall, this corresponds to a lateral distance of $31 * d$, where 31 is the expected number of perpendicular layers below the rotating layers $(31 = 41 * \cos(40))$. Considering that the lateral size of an hemicylinder plus two quarter of hemicylinders is around $570\ nm$ which is associated with 180 perpendicular layer, we can find that the proportion of those perpendicular layers below the rotating layers for two neighboring quarter cylinders is 0.34. Now the central part of an hemicylinder is associated to approximately 118 perpendicular layers below the central layers. The proportion of these layers to the total average value of $q_{perp}$ is 0.65. The expected value of wave vector from the perpendicular below the the rotating layers is $1.984\ nm^{-1}$ can be calculated as follow:

$$q'_{average} = (\frac{1}{27}) * \sum_{N_i=5}^{N_i=31} \left[ (\frac{1}{1 + (\frac{1}{N_i})^2}) \times q_o \right] \tag{4.56}$$

where 5 is the number of layers at $\alpha = 20^\circ$

we can now calculated the expected $q'$ contribution from the perpendicular layers below the central smectic layers knowing

that the total experimentally observed average value of $q_{perp}$ is given by

$$q_{perp} = 0.65 * q_{perp_c entral} + 0.34 * q_{perp_r otate}$$

we have found $q' = 2.036$ which is around the experimentally observed $q_o$ for the central smectic layers.

Our experimental values of the wave vector transfer finally show that these perpendicular layers have a very high value of wave vector transfer vector $q_{per}$ compared to the one of the rotating smectic layers $q'$. This result evidences that it is not the substrate that imposes the compression of smectic layers in rotating layers and the central layers. It suggests that below the central defect there is no dilation as expected due to the absence of curvature. this again confirms that the observed dilation in the rotating layers is only due to the curvature and finally we may have indeed two families of perpendicular smectic layers. The first one is made by the perpendicular layers below the rotating ones of varying interlayer spacing. The second one below the central defect of constant and not dilated interlayer spacing.

### 4.9.9 Total Wall defect

We have seen that the smectic and nematic liquid crystal phases are uniaxial. However, the nematic liquid crystal phase can have two distinguished directors perpendicular to one another.[15]. Under strong enough distortion the nematic phase can exhibit biaxial order. We have also seen that confined liquid crystal can exhibit topological defects. Their defect core can be related to the structural transition between uniaxial and biaxial state [16]. N. Schopohl and T. J. Sluckin [16] have been the first to publish on such a transition.Using Landau-de-Gennes formalism, they have found that the defect core never contains isotropic matter. In the outer core, the order is asymptotically approaching the uniaxial order in the bulk. In between is a region in which the liquid crystal is biaxial. Furthermore, they have found a ring around which the biaxiality is maximum. The defect core would be fully isotropic only if this ring shrinks to a point which mean that the order completely vanishes. The transition such as the uniaxial-biaxial transition described above is called order-reconstruction (OR). This mechanism can be used to relax from the strong distortion or mechanical stress or other external perturbations in the liquid crystal system.

The result from our experimental data leads a hemicylinder model that we have discussed in detail in this chapter. The remaining part is the 2D topological grain boundary (central defect) which is separating the perpendicular layers on the substrate and the central smectic layers. The intimate structure of this defect has been a subject of collaboration between our group and the group of Samo Kralj and Luka Mesarec, both from University of Maribor in Slovenia. In this section, I will present the result of their theoretical study on this structure. The recent ellipsometric analysis have shown the thickness for the perpendicular layer is $30\ nm$. This is the position of the order reconstruction above the substrate associated with the presence of the central defect.

To understand its structure, Samo Kralj and Luka Mesarec have used the simple geometric shown in figure 4.37(a). They considered that a $180\ nm$ thick film of 8CB smectic A liquid crystal is confined between a rubbed PVA glass-coated substrate and air. They also considered that a period of smectic layers of approximately $3.16\ nm$, which means that there are $57$ smectic layers totally, $\frac{h}{d}_0 = 57$. The thickness of the film is $h$ in z-axis. The rubbed PVA glass-coated substrate-liquid crystal imposes at $z = 0$ a strong uniaxial planar anchoring along the y-axis on the 8CB molecules as we discussed in 1. The liquid crystal-air interface imposes at $z = h$, uniaxial homeotropic anchoring condition. Moreover, at lateral walls they impose free boundary conditions. For such boundary conditions the amplitudes of order parameters exhibit variations only along the z-axis. The smectic layers are orientated parallel to z-axis and y-axis respectively below and above the distance $h_w$ which is the position of the central defects. Therefore, the smectic A layer stacking exhibits discontinuous reorientation in a wall located at the distance $h_w$.

The structural changes are mainly enabled by spatial variations in the amplitudes of order parameters i.e both the nematic tensor order parameter $Q_t$ and smectic complex order parameter $\Psi$ locally within the central defect. While the smectic order parameter is one dimensional the nematic amplitude order parameters space is two-dimensional and it is described in terms of two variables $s_o$ and $\Gamma$ that measures respectively the effective nematic amplitude and the degree of biaxiality. The latter is expressed as

$$\beta_{sn}^2 = 1 - \frac{6[\mathrm{Tr}\left(Q_t^3\right)]^2}{[\mathrm{Tr}(Q_t^2)]^3} = \sin^2(3\Gamma) \in [0, 1] \tag{4.57}$$

The biaxiality is associated with $\beta_{sn} \geq 1$, and its maximum value is at $\beta_{sn} = 1$ . Nematic uniaxial state is associated $\beta_{sn} = 0$ The smectic order parameter must be melted at $z = h_w$ (i.e., $\Psi(h_w) = 0$) to reconcile different translational order above and below $h_w$. The discontinuous change in smectic translational forces nematic order to make maximum change in orientation on

the $nm$ length scale and this can be achieved either via order reconstruction or by locally melting nematic order. The later option is unfavorable since room temperature is expected to be associated with smectic A phase. Hence only the order reconstruction mechanism is preferable.

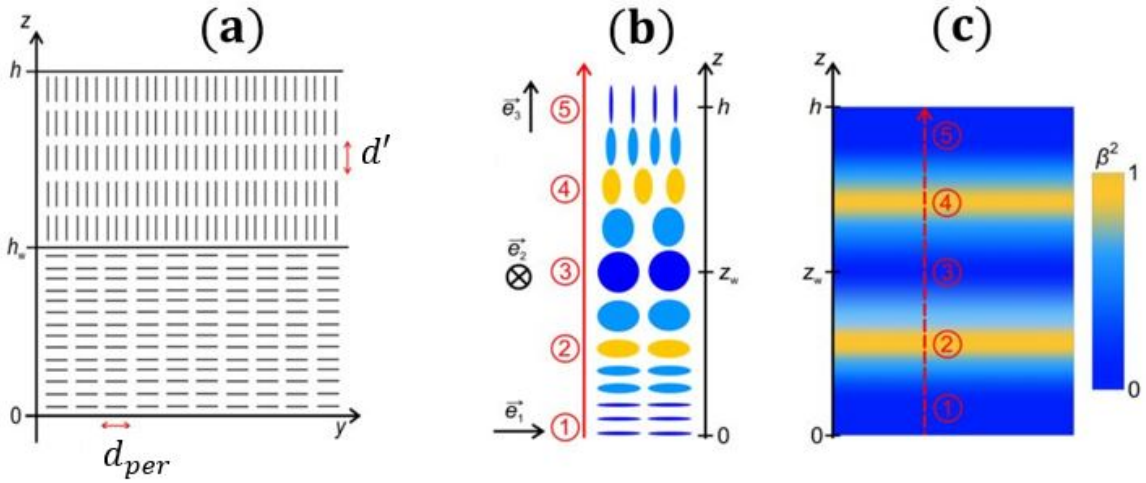


Figure 4.37: Schematic presentation of smectic A order within the cell. The frustration in translational order is resolved by forming a wall defect at z=hw. The smectic layer periodicity above and below the wall are given by $q'$ and $q_{per}$ respectively (a) Schematic geometric presentation of nematic order changes in the order reconstruction transformation (b) the corresponding degree of biaxiality $\beta^2_{sn}$ (c) .

The resulting qualitative changes in mesoscopic orientational order on traversing the central defect at $z = h_w$ are depicted in figure 4.37(b) (mesoscopic shape variations) and 4.37(c) (degree of biaxiality). The initial (1) in blue nematic state at $z = 0$ is positively uniaxial along the y-axis (the prolate mesoscopic shape). Along $z$ axis, the orientation changes from uniaxial to maximum biaxial at (2) in yellow and then at (3) blue $z = h_w$ the negative uniaxial order (resulting in cylindrically symmetric prolate mesoscopic shape) along the x-axis is realized. The orientation becomes totally biaxial at (4) and upon further increasing in $z$ (5), a positive uniaxial order is reached at $z = h$.

The nematic structure of the wall (central defect) is characterized by two planes exhibiting maximum biaxiality, enclosing the order reconstruction wall possessing negative nematic uniaxiality. Note that the outer planes exhibiting positive uniaxial order (placed at $z = 0$ and $z = h$) are enabled by strong uniaxial orientational anchoring conditions. Therefore, these states could be in real samples slightly biaxial (i.e., $0 < \beta^2 \ll 1$). Furthermore, at the order reconstruction wall the smectic order must be locally melted. Thus, the structure of the 2D topological grain boundary is singular both in nematic (if one monitors orientational order using uniaxial states) and smectic order and is therefore a Total Wall topological Defect. They have used numerically simulated this defect and the result is shown in figure 4.39. Using result in figure 4.39, we can determine the size of the total wall defect. We know that in uniaxial nematic area, the biaxiality vanishes. Figure 4.39 suggests that total wall defect appears at the $7^{th}$ layer. Its size is approximately of $5^{th}$ layer. This suggests that the defect height is even larger than the $3.5$ $nm$ estimated above.

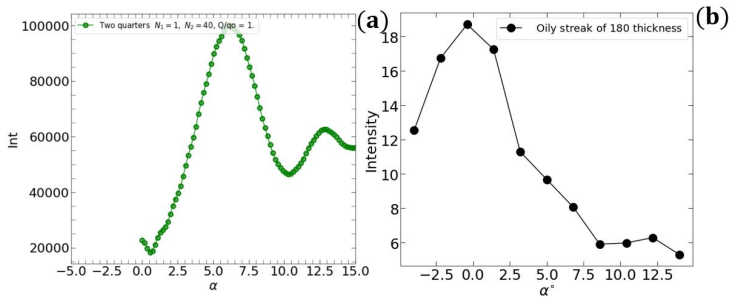


Figure 4.38: The evolution of the theoretical intensity from two neighboring perfect quarter cylinder (b) The experimental intensity measured using TSAXS configuration. The maximum value at $\alpha = 0^\circ$ was scattered perpendicular layers on the substrate

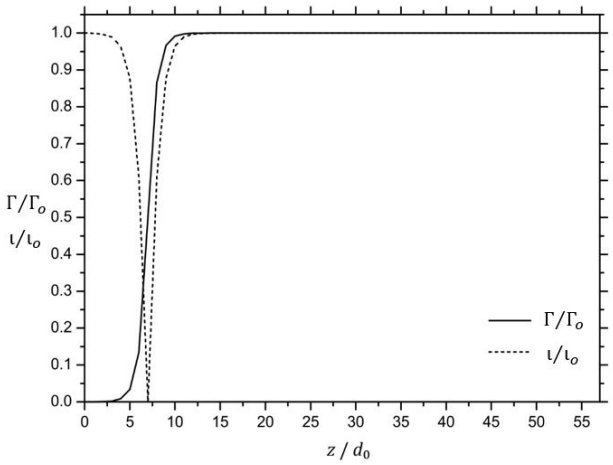


Figure 4.39: Key features of nematic and smectic A order on crossing the wall defect. At the wall center the smectic order is melted and the nematic order exhibits negative uniaxiality. The Total Wall Defect is located at $\frac{z}{d_0} = 7$, while the total sample height is set as $\frac{h}{d_0} = 57$ for sample of $180\ nm$ thickness. The solid line is for biaxiality

## 4.10 conclusion

This chapter aimed at studying and reconstructing the intimate internal structure of the oily streaks. We have presented the result from a film sample of $180\ nm$ thickness. Using the combination of experimental X-ray scattering and theoretical calculation of the intensity scattered by rotating smectic layers inside the hemicylinder, we were able to reconstruct the intimate structure of the oily streaks. A strong foundation of studied of oily streak had been laid before my thesis. [2, 3, 5, 17]. However, the results that we obtained during this thesis confirm the fact that indeed a deep analysis of this oily streak structure and of the distortion of the smectic layers was necessary. We have demonstrated that the integrated intensity scattered by this oily streak in a distorted $8CB$ smectic A material is not proportional to the number of scattering smectic layers inside the oily streak in contrast with hard crystal or perfectly flat smectic layers. Moreover, we have evidenced that this integrated intensity is linearly dependent on $N_2^2 - N_1^2$, where $N_1$ is the number of missing smectic layers very close to the center of curvature of the hemicylinder and $N_2$ is the total number of this smectic layers. We have shown that this unprecedented result is related to the fluidity of the smectic layers that leads to a constant linear density of scatterers along the smectic layers, even when they rotate. Using this relationship together with the linearly proportionality between the $\frac{1}{\Delta q}$ and the number of scattering smectic layers, we were able to determine the evolution of the number of smectic layer as a function of the orientation $\alpha$. Another new parameter that has significantly

helped to understand the oily streak structure is the wave vector transfer $q$. It is inversely proportional to the interlayer spacing. Combining the experimental results on the evolution of the integrated Bragg intensity, wave vector transfer $q$ and its width, $\Delta q$, we were able to reconstruct a new model of the intimate structure of the oily streaks with major differences with respect to the currently existing model.

The first result is that we succeeded to demonstrate the existence of almost perfectly rotating smectic layers that indeed form a large slab of a perfect quarter cylinder inside each edge of the smectic flattened hemicylinders. The closest from the center of curvature a rotating grain boundary is formed as postulated in previous works [3]. However its dimensions are now precisely determined and appear different from the previous estimations [3, 5]. We find the localization of one single dislocation of Burger vector $4$ at the extremity of a rotating grain boundary without dislocation. As a result, in the edge of the hemicylinder, the smectic layers the closest from the curvature center that fully rotate from an orientation perpendicular to the substrate to a parallel orientation may be the $11^{th}$ smectic layers.

The second result is the demonstration of a $-\frac{1}{2}$ disclination defect at the top of the curvature wall. It is made of around $6$ layers that experience a large dilation in the disclination center. We were able to estimate a large core size of the order of $35$ $nm$. Since the smectic layers rotate around the central defect, they form a topological charge of $+\frac{1}{2}$. We therefore demonstrated for the first time in our group, a topologically stable system since the $-\frac{1}{2}$ disclination balances this $+\frac{1}{2}$ topological charge.

The third result is the fact that the central part of the oily streak flattened hemicylinder is formed by a gable-roof like structure with the two tilted parts forming a chevron structure in the middle of the flattened hemicylinders. We have performed in collaboration with Randall Kamien from Pennsylvania university, a calculation on the energy minimization of the rotating smectic layers. This calculation has given us a model of how the smectic layers in the edges of the oily streak hemicylinders are dilated with respect to the central layers as a response to the very high bending energy close to the center of curvature. We obtained a quantitative expression of this dilation in agreement with the experimental data, for example associated with local dilation as high as $4\%$ for the $5^{th}$ smectic layer. This suggests that such a dilation may occur close to most of the topological defects around which smectic layers rotate with a small radius of curvature like for example close to the ellipse of focal conics. Therefore, this model allows to understand the origin of the gable roof-like structure associated with the chevron grain boundary. The tilt of the central layers is thus induced by the necessary connection between dilated rotating layers and central ones along a new grain boundary. However, whereas each rotating layers is expected to be differently dilated due to the different distance with respect to the center of curvature of each rotating layer, we show that the tilt angle remains mostly constant along the grain boundary at a smaller value than the one expected for a perfect connection between rotating and central layers. This is because of competing energies. In particular the surface energy that tends to flatten the gabble-roof like central part of the hemicylinders competes against the grain boundary energy that tend to have a perfect connection between the joined smectic layers.

The fourth result is that structure of the curvature wall between two neighboring quarter cylinders is possibly associated with a chain of dislocations of various Burger vectors. However a precise structure is yet to be produced and for this reason we have started collaboration with a group of mathematicians form Canada, UK and USA. to simulate the model of two neighboring quarter cylinders and even simulate its scattering and compare it to our experimental results and their results in order to confirm the presence of these dislocations.

The last result concerns the central topological grain boundary that separates the central smectic layers from the perpendicular layer on the substrate. We collaborate with the group of Samo Kralj and Luka Mesare from Slovenia who have demonstrated that it is a total wall defect. It is not only characterized by a local melting of a smectic order but also by a negative nematic uniaxiality associated with an order reconstruction locally induced in the defect by the melting of the smectic order. As a result the thickness of the defects could be estimated to be around $20$ $nm$.

# Bibliography


[1] A.J. Leadbetter et al. "The structure of smectic A phases of compounds with cyano end groups". en. In: *Journal de Physique* 40.4 (1979), pp. 375–380. (Visited on 05/12/2022) (cit. on pp. 98, 100).

[2] Jean-Philippe Michel et al. "Optical gratings formed in thin smectic films frustrated on a single crystalline substrate". en. In: *Physical Review E* 70.1 (July 2004), p. 011709. ISSN: 1539-3755, 1550-2376. DOI: 10.1103/PhysRevE.70.011709. URL: https://link.aps.org/doi/10.1103/PhysRevE.70.011709 (visited on 10/20/2021) (cit. on pp. 98, 102, 109, 111, 112, 120, 122, 136).

[3] Delphine Coursault et al. "Self-organized arrays of dislocations in thin smectic liquid crystal films". en. In: *Soft Matter* 12.3 (2016), pp. 678–688. ISSN: 1744-683X, 1744-6848. DOI: 10.1039/C5SM02241J. URL: http://xlink.rsc.org/?DOI=C5SM02241J (visited on 01/17/2023) (cit. on pp. 98–100, 102, 109, 111, 112, 114, 117, 120–122, 136, 137).

[4] Chang Q. Sun. "Brillouin zones, effective mass, muffin-tin potential, and work function". In: 2020. URL: https://api.semanticscholar.org/CorpusID:216497848 (cit. on p. 101).

[5] Jean-Philippe Michel et al. "Structure of smectic defect cores: X-ray study of 8CB liquid crystal ultrathin films". In: *Physical review letters* 96.2 (2006). Publisher: APS, p. 027803 (cit. on pp. 102, 109, 120, 136, 137).

[6] Bruno Zappone and Emmanuelle Lacaze. "One-dimensional patterns and topological defects in smectic liquid crystal films". en. In: *Liquid Crystals Reviews* (July 2022), pp. 1–18. ISSN: 2168-0396, 2168-0418. DOI: 10.1080/21680396.2022.2076748. URL: https://www.tandfonline.com/doi/full/10.1080/21680396.2022.2076748 (visited on 04/24/2023) (cit. on pp. 114, 120, 128).

[7] C. Williams and M. Kléman. "DISLOCATIONS, GRAIN BOUNDARIES AND FOCAL CONICS IN SMECTICS A". In: *Journal de Physique Colloques* 36.C1 (1975), pp. C1–315–C1–320. DOI: 10.1051/jphyscol:1975152. URL: https://hal.archives-ouvertes.fr/jpa-00216231 (visited on 07/27/2022) (cit. on pp. 118–120, 123).

[8] C. Allet, M. Kleman, and P. Vidal. "Striped patterns in a thin droplet of a smectic C phase". en. In: *Journal de Physique* 39.2 (1978), pp. 181–188. ISSN: 0302-0738. DOI: 10.1051/jphys:01978003902018100. URL: http://www.edpsciences.org/10.1051/jphys:01978003902018100 (visited on 04/26/2023) (cit. on p. 121).

[9] Haifa Jeridi et al. "Unique orientation of 1D and 2D nanoparticle assemblies confined in smectic topological defects". en. In: *Soft Matter* 18.25 (June 2022). Publisher: The Royal Society of Chemistry, pp. 4792–4802. ISSN: 1744-6848. DOI: 10.1039/D2SM00376G. URL: https://pubs.rsc.org/en/content/articlelanding/2022/sm/d2sm00376g (visited on 08/17/2022) (cit. on pp. 121, 122).

[10] Syou-P'heng Do et al. "Interactions Between Topological Defects and Nanoparticles". English. In: *Frontiers in Physics* 7 (2020). Publisher: Frontiers. ISSN: 2296-424X. DOI: 10.3389/fphy.2019.00234. URL: https://www.frontiersin.org/articles/10.3389/fphy.2019.00234/full (visited on 05/13/2021) (cit. on p. 121).

[11] Delphine Coursault et al. "Tailoring anisotropic interactions between soft nanospheres using dense arrays of smectic liquid crystal edge dislocations". In: *ACS nano* 9.12 (2015). Publisher: ACS Publications, pp. 11678–11689 (cit. on p. 121).

[12] Yoichi Takanishi et al. "Chevron Layer Structure in the Smectic A Phase of 8CB". In: *Japanese Journal of Applied Physics* 28.3A (Mar. 1989), p. L487. ISSN: 0021-4922, 1347-4065. DOI: 10.1143/JJAP.28.L487. URL: https://iopscience.iop.org/article/10.1143/JJAP.28.L487 (visited on 01/09/2023) (cit. on p. 123).

[13] Bruno Zappone et al. “Periodic lattices of frustrated focal conic defect domains in smectic liquid crystal films”. en. In: *Soft Matter* 8.16 (2012), p. 4318. ISSN: 1744-683X, 1744-6848. DOI: 10.1039/c2sm07207f. URL: http://xlink.rsc.org/?DOI=c2sm07207f (visited on 04/06/2023) (cit. on p. 128).

[14] Bruno Zappone and Emmanuelle Lacaze. “Surface-frustrated periodic textures of smectic- A liquid crystals on crystalline surfaces”. en. In: *Physical Review E* 78.6 (Dec. 2008), p. 061704. ISSN: 1539-3755, 1550-2376. DOI: 10.1103/PhysRevE.78.061704. URL: https://link.aps.org/doi/10.1103/PhysRevE.78.061704 (visited on 01/10/2023) (cit. on p. 128).

[15] Meina Yu et al. “Effect of biaxiality on chirality in chiral nematic liquid crystals”. en. In: *Soft Matter* 14.31 (2018), pp. 6530–6536. ISSN: 1744-683X, 1744-6848. DOI: 10.1039/C8SM00898A. URL: http://xlink.rsc.org/?DOI=C8SM00898A (visited on 06/07/2023) (cit. on p. 134).

[16] N. Schopohl and T. J. Sluckin. “Defect Core Structure in Nematic Liquid Crystals”. en. In: *Physical Review Letters* 59.22 (Nov. 1987), pp. 2582–2584. ISSN: 0031-9007. DOI: 10.1103/PhysRevLett.59.2582. URL: https://link.aps.org/doi/10.1103/PhysRevLett.59.2582 (visited on 06/07/2023) (cit. on p. 134).

[17] Bruno Zappone et al. “Self-ordered arrays of linear defects and virtual singularities in thin smectic-A films”. en. In: *Soft Matter* 7.3 (2011), pp. 1161–1167 (cit. on p. 136).

Chapter 5

# Study of the effect of variation of film thickness on the oily-streak model in smectic A sample

*After all, I thank God of my fathers, For You have given me wisdom, power and people*

– Jean de Berchmas

## Contents

## 5.1 Thicker film sample

Film thickness plays a crucial role in the determination of material properties. For example thin films of liquid crystal may have different structural properties than their bulk counterparts. In this chapter, I will report the results from the study I have done on the effect of thickness of liquid crystal thin films on the structure of the oily streak model in the 8CB smectic A sample.

We have seen in the previous chapters that the understanding of the internal structure of the oily streak necessitates the integrated Bragg intensity and the FWHM of the Bragg intensity peaks. In chapter 4, we have elaborated an unprecedented relationship between the integrated Bragg intensity and the number of smectic scattering layers that constitute the oily streak. We have also determined the relationship between this number of scattering layers and the FWHM of the Bragg peaks. In the same chapter I have focused on a thin film of 180 $nm$ thickness. In this chapter, I will describe the results on three different zones of the same sample of film thickness 200 nm, 230 $nm$ and 250 nm. I will also present the comparison of the results of these three thicknesses with respect to the previous zone of another sample of thickness 180 $nm$ .

### 5.1.1 Evolution of integrated Bragg intensity

In chapter 3, I have elucidated the experimental measurements that we have done. The data from thicker films were asymmetric as it can be seen in the scattering rings of these data shown in figure 3.28 in section 3.3.7. This figure shows an asymmetric issue that was seen on both the measurements with the detector centered (eix = 0) and when it is displaced (eix = -10) . It has caused one part of data to be out of Bragg's condition (figure3.31). The correction of these asymmetric data for different incident angles was expounded in section 3.3.7. The uncorrected data are shown in figure 3.29 and the corrected data are shown in figure 3.32 for a film of thickness of 230 $nm$. The same process was done on the other thicknesses. We have seen that the data extracted at the incidence angle $\omega = 0.6^\circ$ were in Bragg's condition for all orientation$\alpha$ of the wave vector transfer $\vec{q}$. On the other hand, the data extracted at incidence angle smaller than $\omega = 0.6^\circ$ are in Bragg condition only for $\alpha$ smaller than $70^\circ$. In order to detect the data scattered by the layers in the central part of the hemicylinder, we had to displace the detector as shown in figure 3.3.

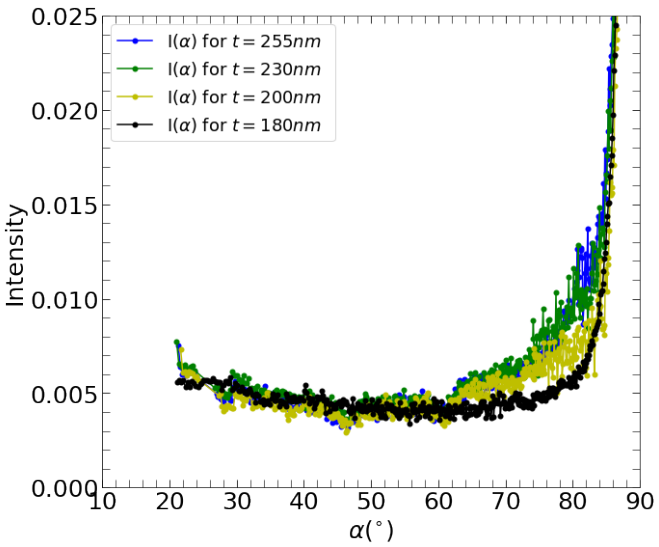


Figure 5.1: The comparison of the integrated Bragg intensity from the four films of thickness 180, 200,230,255 nm.

The combination of the data at $\omega = 0.6^\circ$ with those extracted from small $\omega$ has given us the full curves of intensity i.e for all orientation (from $\alpha = 15$ to $\alpha = 90^\circ$ ). The data resulted from this combination were multiplied by the $\Delta q$ and $\Delta\mu$ to obtain the integrated Bragg intensities. These intensities for all the film thicknesses are shown in figure 5.1, where the normalization of the integrated intensity has been performed as follow: We have first calculated the number of smectic layers $N_2$ using $\frac{1}{\Delta q}$ as shown

in equation 4.33 for all the three thicker film and compare the results to that of 180 $nm$ thick film. This calculation requires only to fix the value of $N_1$ and used the experimental values of $\Delta q$. We have found that all curves of evolution of $N_2$ were superimposed without need to normalization. This superimposition was between $\alpha = 40^\circ$ and $\alpha = 70$ and no superimposition elsewhere . This demonstrates that the value of the scattering smectic layers in this interval of $\alpha$ values doesn't vary when the film thickness changes. We can therefore expect that the scattered intensity to be the same in this $\alpha$ interval for all film thicknesses. However, the curves of evolution of intensity though have the same shape of evolution as a function $\alpha$, they were not superimposed. We have then found a factor of normalization to normalize them with respect the 180 $nm$ thickness. The result is shown in figure 5.1. This figure is showing that the integrated intensities are similar from small $\alpha$ values until $\alpha = 50^\circ$. This implies that the corresponding part of the rotating layers in the hemicylinder that we have built for the 180 $nm$ (figure 4.30) is the same for all films of different thickness. It means that is independent of the film thickness. From orientation $\alpha = 50^\circ$, we start to see the difference, which continue until $85^\circ$. In contrast to the rotating part (including the curvature wall and its associated angle $\Omega = 40^\circ$) which its similar for all film thickness the disclination zone is different. This zone is between $70^\circ$ and $85^\circ$ for the 180 $nm$ whereas for the three thicker films, between $50^\circ$ and $85^\circ$.

### 5.1.2 $N_2$ from both integrated Bragg intensity and $\Delta q$

We have seen in the previous chapter 3 that the integrated Bragg Intensity is always true regardless of whether or not there are some disorders. In contrast, the $\Delta q$ is much affected by the presence of disorder of $q$ values. Therefore, the comparison of the number of smectic layers $N_2$ calculated from both integrated Bragg intensity and the $\Delta q$ for all $\alpha$ values can reveal the areas with disorder or defects and/or areas where there is only few/no disorder or defect.

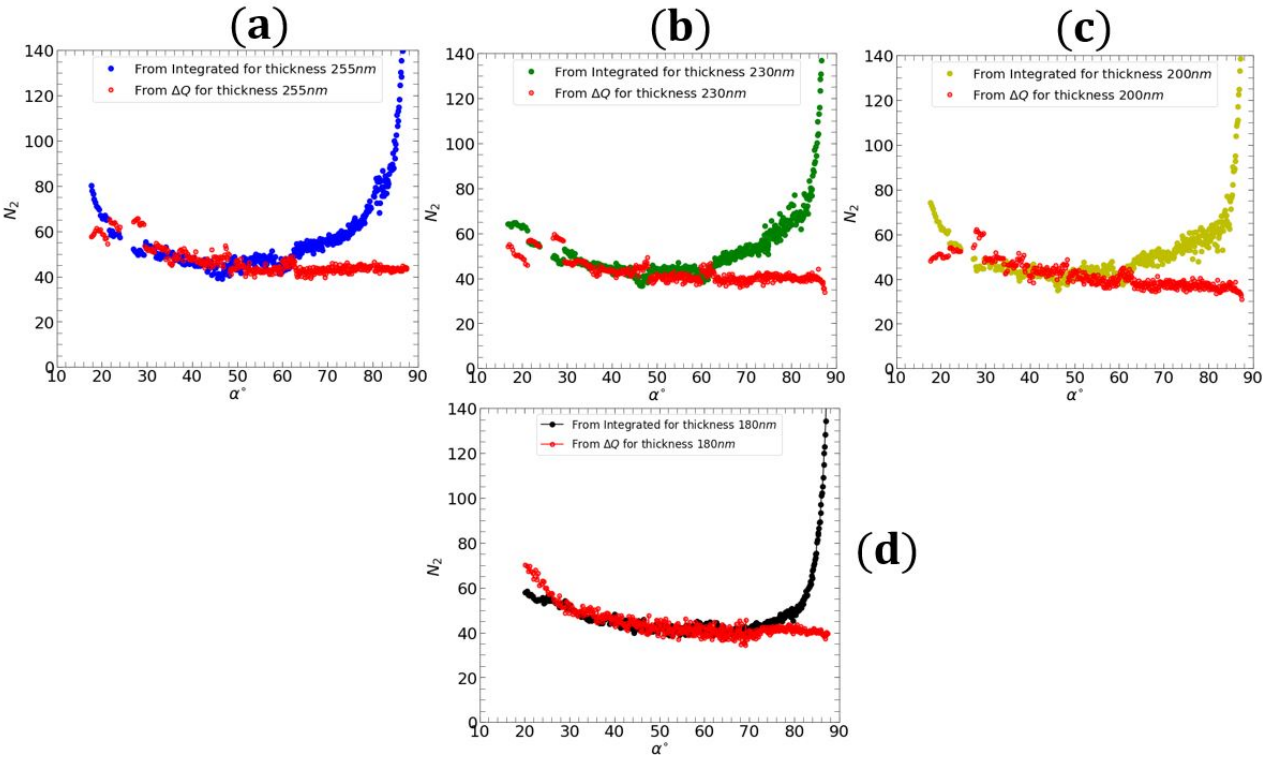


Figure 5.2: Comparison of the evolution of number of scattering layers calculated from integrated Bragg intensity and $\Delta q$ as a function of thickness

The figure 5.2 shows the comparison of the evolution of the number of smectic layers $N_2(\alpha)$ for different thicknesses. For the film of 180 $nm$ we have used the superimposition of the number of the scattering smectic layers $N_2$ calculated from both

integrated Bragg intensity and those from the $\Delta q$ for all orientation $\alpha$. Together with the curve of $q$ values, this has helped to determine the value of critical $\alpha_c$ above which the number of smectic layers does not change and the position $x_o$ of the rotating grain boundary without dislocations that is separating the central layers from the rotating smectic layers which defines the N1(alpha) curve.

The comparison shows a similar disagreement for $\alpha \leq 30^\circ$ . Around $\alpha = 30^\circ$ the $\Delta q$ is dominated by disorders similar for all thicknesses. The $N_2 = 41$ values of rotating smectic layers in the model of hemicylinder that we have evidenced in chapter 4 for the 180 $nm$ appears to be conserved for the thicker films (200 $nm$, 230 $nm$, 255 $nm$). However if the number of smectic layers is constant at $N_2 = 41$ until $\alpha = 70^\circ$ for the thickness $e = 180$ $nm$ , it is only until $\alpha = 50^\circ$ for the three other thicknesses. This is shown by the departure towards larger integrated intensities from $\alpha = 50^\circ$ for these three thicknesses (figure 5.2). The values of the angle of curvature wall which equal $40^\circ$, the critical $\alpha = 40^\circ$ and $y_o = 11.3$ $nm$ that we have found for the 180 $nm$ thick film have the same values for these thicker films. It is interesting here to notice that we clearly demonstrate that the curvature wall angle, $\Omega$, does not vary when the thickness increases, at least if the disclination is present for all thicknesses which is the case for thicknesses varying between 180 $nm$ and 255 $nm$. This is in contrast with the results claimed in [1]. This may be due to the fact that in the films as thin as 100 $nm$ that have been studied[1] the disclination may have disappeared. We may thus expect variations also of the rotating part and also of the $\Omega$ angle.

The difference between the values of $N_2$ from integrated Bragg intensity and those from $\Delta q$, become enormous at $\alpha = 50^\circ$ for all the thicker films, whereas it is only at $\alpha = 70^\circ$ for the 180 $nm$ thickness thin film. This discrepancy is due to the fact that the $\Delta q$ is dominated by the disorder. This discrepancy suggests that the disclination area and the corresponding additional layers with dilation or compression features starts earlier (at $\alpha$ around $50^\circ$ ) for these three thicknesses with respect to $e = 180$ $nm$ .This feature can be clearly seen in the figure 5.3 which is showing the comparison of the evolution of number of scattering smectic layers as a function of $\alpha$. At $\alpha = 50^\circ$, also the values of $N_2$ from the thicker films starts to differ from the value

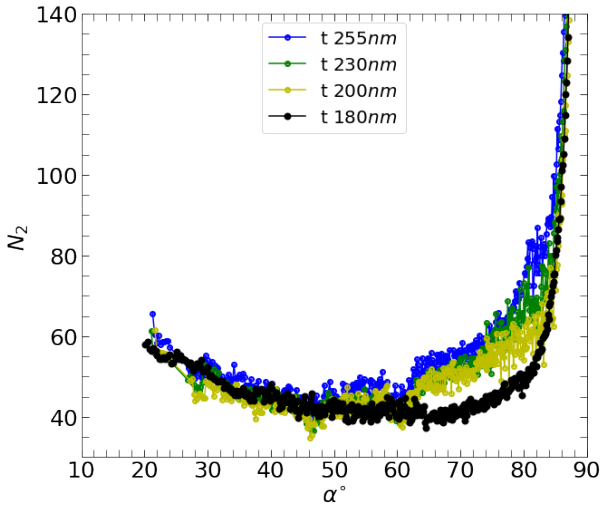


Figure 5.3: Comparison of the evolution of number of scattering layers as a function of thickness

from the 180 $nm$ film with an increasing of $N_2$ with respect to $N_2 = 41$ which occurs for all thicknesses. Together with the discrepancy between $N_2$ from integrated Bragg intensity and $N_2$ from $\Delta q$, this shows that the disclination starts at $\alpha$ value $50^\circ$ with additional layers that are measured whereas they are only measured from $70^\circ$ for the 180 $nm$ film. This disclination area continues until $85^\circ$, the value where scattering of the smectic layer in the central part starts to dominate. This figure 5.3 is also showing an increase in number of smectic layers in the disclination zone when the thickness increases from 200 to 230 and finally 250 $nm$ . In other words all additional layers related to the increase of thickness appear in the disclination area and not in the area of fully rotating smectic layers that have been described extensively in chapter 4. This shows that it is energetically cheaper to add smectic layers in the disclination area than in the rotating area of the quarter cylinders. this may be partly due to the prohibitive energy cost of these rotating layers due to bending and dilation.

These extra layers are convex as we have seen in chapter 4. Such layers are not rotating around a center of curvature as it was for the case of the perfect quarter of hemicylinder. This makes their precise determination not obvious using the $N_2$ curve

shown on figure5.3. In order to corroborate the results from the two previous sections of this chapter, we need to analyze the wave vector transfer $q$ curve as a function of the orientation $\alpha$. This will be the focus of the next section 5.1.3.

### 5.1.3 Comparison of the wave vector transfer $q$ for different film thicknesses

The extraction of the $q$ curves for these thicker films is the same as we did for the $180\ nm$ as described in chapter 2, where we have also elucidated the correction of the refraction effect that has given the $q$ values inside the film. This correction was also applied to the $q$ curves on these thicker films that I am reporting in this chapter.

For the central layers, the $q$ values ($\alpha$ between $89^\circ$ and $91^\circ$) were obtained using the measurement with the detector displaced as shown in figure 3.28(a). The rest of $\alpha$ orientations were obtained using the measurement without displacement of the detector as shown in figure 3.28(b), we normalized both of these data by putting an offset of $0.0013$ nm. We found that for almost each thickness, without any normalization the $89^\circ$ $q$ value was almost the same. This suggests that the interlayer distance of the central layers corresponding to this $q$ value is the natural value of 8CB in smectic A. Hence we have normalized all $q$ curves for $\alpha = 89^\circ$ at the $q$ value is $2.0023\ nm^{-1}$. The results of this procedure is shown in figure 5.4. The curve from the $180\ nm$ film was analyzed in details in chapter 4, precisely in sections from 4.9.2 until 4.9.4.

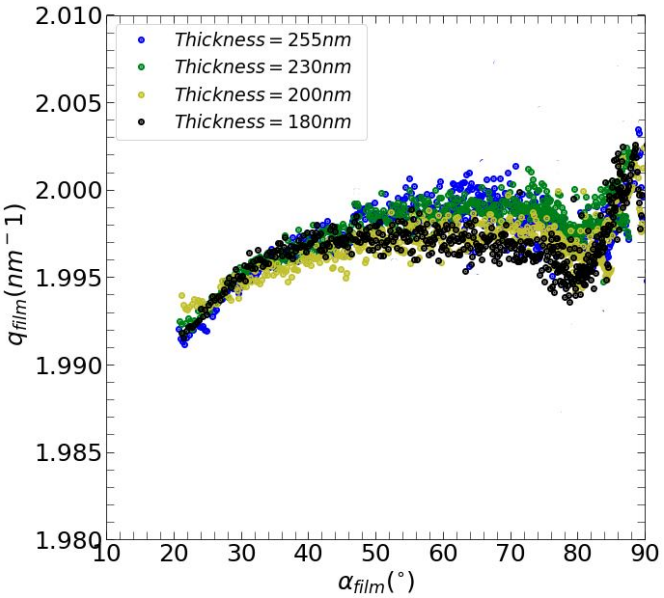


Figure 5.4: The comparison of the wave vector transfer $\vec{q}$ inside the film from four film of thickness 180, 200,230,255 nm.

#### Analysis for $\alpha < 50^\circ$

The values of the wave vector transfer $q$ shown on figure 5.4 are the average values from all smectic layers which have normals are parallel to the wave vector transfer $\vec{q}$ orientated at $\alpha$. Figure 5.4 shows that the decreasing is the same for all thicknesses in agreement with a similar number of smectic layers with similar structure and orientations of the number of scattering smectic layers. This result agrees with what we have seen in the previous subsections. The fact that all the experimental parameters agree for $\alpha$ values smaller than $50^\circ$, implies that the model we have build for the $180\ nm$ film for this region is the same for all the thicker films as shown in figure 5.5.

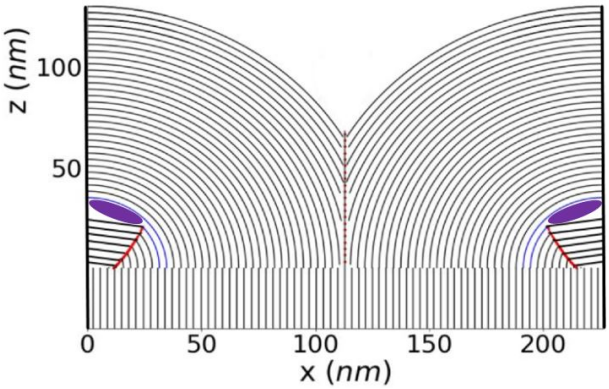


Figure 5.5: The area below the disclination zone that this the same for all the four film of thickness 180, 200,230,255 nm.

### Analysis for $\alpha > 50^\circ$

We can see that between $\alpha = 50^\circ$ and $\alpha = 80^\circ$, the $q$ values change as function of film thickness, where the thicker films are having a $q$ value larger than the one for $180\ nm$. The evolution is moreover associated with regularly increasing $q$ values when the thickness increases. Let's recall that for the film of $180\ nm$ thickness, the $q$ values between $\alpha = 35^\circ$ and $\alpha = 70^\circ$ are associated with the rotating smectic layers and are smaller than the $q = 2.0023\ nm$ value for the central layers. For this film, we have found 41 rotating smectic layers. From $\alpha = 76^\circ$, we start to see a decreasing in the $q$ value. The disclination starts at $\alpha$ around $70^\circ$ as shown by the curves of $\Delta q$ and integrated Bragg intensity. The associated decrease of average $q$ values starts at around $\alpha = 76^\circ$ where the dilation of smectic layers become large enough (see chapter 4, section 4.9.6). The $q$ values between $76^\circ$ and $80^\circ$ contain the contribution from the non-dilated smectic layers and from the dilated layers. In this interval, the evolution of the $q$ shows a decreasing for all thicknesses. This $q$ curve shows that the contribution from the dilated layers dominates, where the maximum dilation is at $80^\circ$, most probably because for larger $\alpha$ the intensity related to central layers starts to become non-negligible, this shows that for all thicknesses the maximum of dilation occurs around $\alpha = 90^\circ$ as shown in the schematized models of figure 5.7.

In Figure 5.4, the fact that the $q$ values of the thicker films are larger than the one for $180\ nm$, starting from the value $\alpha = 50^\circ$, is caused by the increase in the number of smectic layers. This agrees with the other two parameters where the number of smectic layers calculated from the integrated Bragg intensity suggests an increase in number of smectic layers starting from the value $\alpha = 50^\circ$ and those calculated from $\Delta q$ suggests a presence of a $q$ disorder in the region. Moreover, the number of scattering layers being added to the system increases as the film thickness increases. As a result, the disclination topological defect that was evidenced for the film of $180\ nm$ thickness changes when the film thickness changes. In particular, all the parameters ($N_2$ from the integrated Bragg intensity, $N_2$ from the $\Delta q$ and the $q$ evolution curves) agree with the fact that the disclination starts at $50^\circ$ for the thicker sample and $70^\circ$ for the $180\ nm$ film thickness.

### Comparison experiment-theory of the disclination zone

Both evolution of $N_2$ curves and of $q$ curves show that only the disclination zone increases its thickness when the overall thickness increases. It is thus interesting to more carefully study the $q$ curves as a function of thickness to gain information on the disclination structure. Each $q$ curve for each thickness is shown on figure 5.6. They appear characterized by an approximately constant $q$ value from $\alpha = 50^\circ$ to $\alpha = 70^\circ$, of increasing value when thickness increases. However, the shape of the curves are not perfectly similar, becoming in particular less constant with $\alpha$ when thickness increases. Together with the different $N_2$ curves, this shows that the structure of the disclinations might vary when the thickness increases. The first increasing of $q$ values that occurs between $\alpha = 50^\circ$ and $\alpha = 70^\circ$ for the three thicker samples shows that dilation is less present on the border of the disclination than in the middle. The average dilation on the total number of layers probably decreases when the thickness increases in relation with the number of layers that increases in the disclination. This is particularly obvious for the larger thickness where the average $q$ values can become as large as $q_o$. It would have been interesting to more quantitatively study

these evolutions through a more quantitative comparison between the $q$ data and the formula 4.49. The measured variations being average ones, they are very small , even less than one pixel. However due to the large width of the Gaussian fits allowing to extract $\Delta q$, we finally obtained a resolution better than one pixel as shown by the results of figure 5.4 allowing for a small discussion on the dilation features in the disclination zone.

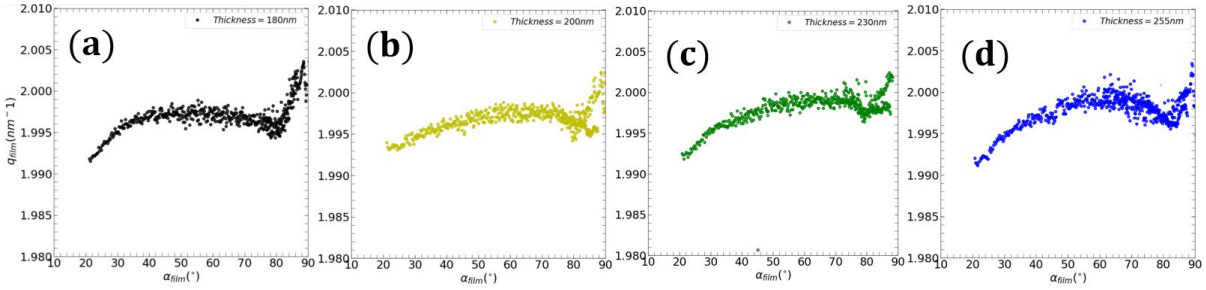


Figure 5.6: Comparison of curves of evolution the $q$ values as a function of $\alpha$ for different film thickness.

Aiming to get more precise information on these structural variations we have performed a deep analysis of each individual curve using the formulas 4.49 and 4.50 from the energy minimization that we have seen in the chapter 4, in section 4.9.3 and 4.9.4 respectively. These formulas have helped to calculate the average value of the $q$ to ensure that the theoretically predicted values agree with The experimentally observed values. In particular it allowed to confirm the size and structure of the rotating grain boundary close to the center of curvature. This has also helped to calculate the number of rotating smectic layers and the number of layers in the disinclination zone that are contributing to the average value of $q$ for the orientation $\alpha$ greater than $50^\circ$.

We started with the 255 $nm$ thick film and found that the experimental average approximately constant $q$, value is 1.9994. Using equations 4.49 and 4.50, the value that allows to obtain such average $q'$ is $N_2$ = 64 smectic layers. This number is constituted by 41 rotating layers and 23 layers supposed to have in the disclination zone. This calculation is based on the hypothesis that all these additional layers have a same period close to $d_o$ contribution to the average $q$, value. Secondly, the 230 $nm$ thick film has an average $q$ value 1.999, which corresponds to $N_2 = 58$ smectic layers. This total number is made up by the 41 rotating layers and 17 layers in the disclination zone. Finally, the 200 $nm$ thick film has an average $q$ value of 1.998, which corresponds to 46 smectic layers. This includes the contribution from the 41 rotating layers and 5 layers in the disclination zone. They also have same period and contribute to the average $q$ value.

Let's examine the implication of the above results. All these thicker films are considered as having the same number of rotating smectic layers (41) below the disclination zone(similarly to the film of 180 nm). Based on this fact the total thickness of the part below the disclination zone shown in figure 5.5 is 160 $nm$ for all films as shown by the number of rotating layers, $N_2 = 41$ and by ellipsometric measurements for the perpendicular layers [1]. Using the thickness measurements obtained by Optical Microscopy, thickness for the disclination zone is 95 $nm$ , 70 and 40 $nm$ for the 255 nm, 230, and 200 $nm$ film respectively. These thicknesses correspond to the number of smectic layers that are to be added in the disclination zone. If all these layers for each individual thickness have the same smectic period of 3.16 $nm$, then we find that the number of smectic layers in the disclination zone is of order of the 30, 22, and 12 smectic layers for the 255 $nm$, 230, and 200 $nm$ respectively. These numbers are larger than those we have found using the experimental average $q$, value.

It is clear that the thickness values measured by Optical Microscopy are not exact. This could be firstly due to the uncertainty related to the Optical Microscopy maps made during the X-ray campaign. However, the just described evolution when the Optical Microscopy determined thickness increases suggest the thickness identification, or at least its increasing, might be close to be correct. Secondly the optical index used for the thickness measurements by Optical Microscopy (see the abaque in appendix A) are $\frac{(2no+ne)}{3}$. It might be slightly overestimated and the thickness might thus be slightly underestimated. It consequently allows to conclude that the numbers of layers in the disclination zone extracted above using equation 4.49 and equation 4.50 are definitely too small for all thicknesses. This allows to conclude that the average $q$ that has been considered for the smectic layers of the disclination zone was too high. In other words, the average q of the disclination zone is associated with dilation with respect to $q_o$. Using the number of smectic layers obtained with Optical Microscopy and equation 4.49, the average dilation, considered as roughly constant from $\alpha = 50^\circ$ to $\alpha = 70^\circ$ can be estimated. It is found to be 2 $nm^{-1}$, 2.00178 and 2.00184 for thicknesses 200 nm, 230 and 250 $nm$ respectively, recalling that $q_o$is taken as 2.0023 $nm^{-1}$. The average dilation decreases when the thickness increases in agreement with a structural variation of the disclination zone when thickness increases.

As a result of the above analysis, we can propose the schematized models of the disclination zones of the oily streaks as

shown in the figure 5.7 for different film thicknesses. In this figure we can see that the part below the disclination zone (with the core shown in red) is the same for all the thickness. The difference is only in the disclination zone. The disclination core of the 180 $nm$ thick film ( figure 5.7(a)) is larger than that of the thicker films (200, 230, and 255 $nm$ as shown in figure 5.7(b), (c) and (d) respectively). The disclination core size of the these thicker films is the same as suggested by the fact that all disclinations start at the same alpha value of $50^\circ$. This indeed shows that the first smectic layer in the disclination bends until its normal is at $50^\circ$ with respect to the substrate, similarly for all thicknesses, except 180 nm. We can also see that the number of the smectic layers in the disclination is increasing as film thickness increases.

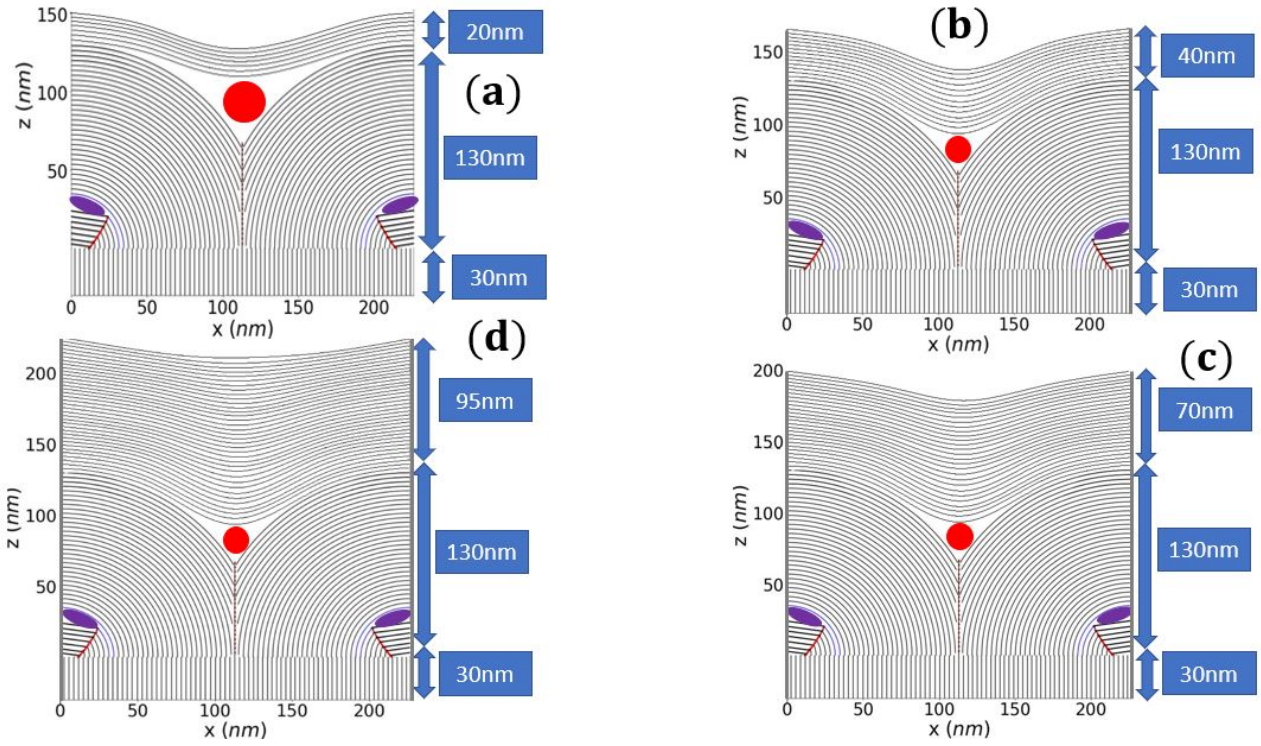


Figure 5.7: Evolution of the disclination zone as function of film thickness

### Effect of variation of film thickness on the disclination core

Now we understand that the disclination zone starts at around $\alpha = 70^\circ$ for the film of 180 $nm$ and at around $50^\circ$ for the thicker films. This result has an unprecedented implication that the disinclination core changes as a function of film thickness. To explain this, let's recall the two following features: the first one is that all the part below the disclination zone is the same for all thicknesses, even the curvature wall is the same for all films regardless of their thickness. The second fact is that we have to curve the smectic layers in the disclination zone until $50^\circ$ for the thicker sample and $70^\circ$ for the 180 $nm$ film. What does this imply ? why the 180 $nm$ thick film cannot have the disclination that starts at $50^\circ$? To respond to this questions, I have taken a prototype of the oily steak zone from the first layer in the disclination zone to the last layer which is the closest to the surface ( shown in figure 5.8). The **h** is the undulation height of the first layer. $D_2$ is the distance between this first layer to the surface, $d_2$ is the average interlayer spacing for the smectic layers in the central part of the disclination zone supposed to be larger than $d_o$ as suggested by the $q$ curves for all thicknesses where the largest dilation features appears close to $90^\circ$ (taking into account that really close to $90^\circ$, the central layer signal hides the one of the disclination). The last layer is drawn on figure is drawn on figure 5.8 as fully flat which is optimal for the surface energy. In fact it has been shown by AFM measurements with oily streaks on $MoS_2$ substrate [2] that the undulations remain always of the order of 10 nanometers, whereas here, the undulation of the top of the rotating layers can be calculated to be $41 * d_o * (1 - \sin(40)) = 46nm$. It is clear from figure5.8 that for the thicker

film if the surface undulation is smaller than h, this requires dilation in the center of the disclination zone.

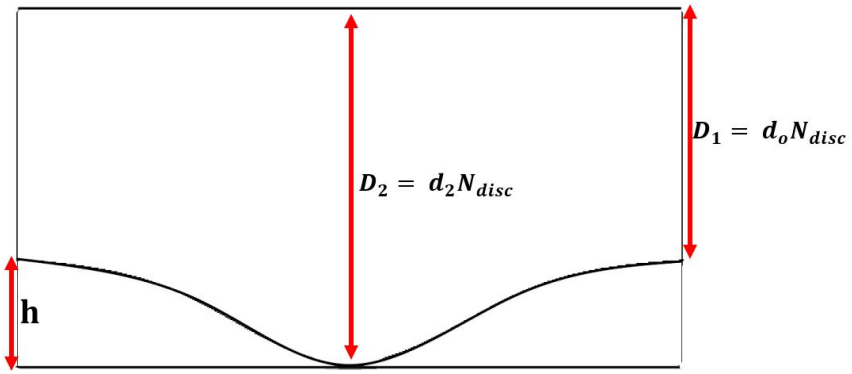


Figure 5.8: Prototype of the area in the disclination zone. The **h** is the undulation of the first layer in this zone.

If all the smectic layers $N_{disc}$ have the same period perfectly defined as $d_o$ at the border, the only way to have a flat surface is to increase the period (from $d_o$ to $d_2$) in the central part but at the same time keeping constant the $d_o$ on the left and right part of the disclination zone. This new period is given by

$$d_2 = \frac{h}{N_{disc}} + d_o \tag{5.1}$$

where $N_{disc}$ is the number of smectic layers of the disclination zone. This means that to flatten the surface with a non too high dilation ($d_2$ not too high) the distance **h** has to be the smallest as possible, and this particularly if $N_{disc}$ is small. The $N_{disc}$ layers in the center are dilated with respect to the $N_{disc}$ layers on the other two side of the disclination zone.

We have seen that the number of layers $N_{disc}$ in the disclination zone increases as the film thickness increases. This shows that for similar $D_2$, different dilation are expected as a function of thickness. This explains why we indeed observe an average dilation that decreases when the thickness increases, as extracted from the $q$ curves discussed above. If the undulation height **h** is kept constant then $d_2$ in the equation 5.1 would be smaller for the thicker films than for the 180 $nm$ film. Now we can consider the fact that all the films that we are reporting in this chapter are built on the same quarter cylinders shown on the figure 5.5 so they have the same surface below the disclination zone and lateral size. The only parameter that changes is their thickness. Therefore, their disclination core can be analyzed using the equation 5.1. For the thicker film, the value of $N_{disc}$ is larger than the one of the 180 $nm$ thick film. This means that we can expect that it would be very easier to have an almost flat surface since the $d_2$ will be smaller for the same $h$ and the dilation energy would be smaller. A critical value of $N_{disc}$ may thus exist that would lead to an decrease of $h$ to avoid a too large $d_2$ values, in other words too large dilation.. Therefore the disclination core will be similar for thicker films ($h$ is the same) but larger for the 180 $nm$ film.

It has been shown on figure 4.20 (chapter 4) that the core size is managed by the $h$ value which itself is managed by the limit angle defining the disclination ($\alpha = 70°$ for 180 $nm$, $\alpha = 50°$ for the other thicknesses). Indeed $h = h_1 + h_2$ with $h_1 = 41 * 3.16 * (1 - \sin(\alpha_d))$. $h_1 = 5$ $nm$ for 180 $nm$ and $h_1 = 30$ $nm$ for the other thicknesses. For the thick films, this leads to a core size smaller than $46 - 30 = 16$ $nm$, 46 $nm$ being the undulation of the top of the rotating layers, the exact size depending on the $h_2$ value. The available space on top of the the rotating layers to increase $h_2$ might be slightly larger for the 180 $nm$ of larger $\alpha_d$. However, if we trust AFM measurements, the top surface might not be more undulated than by 10 $nm$. $h$ would thus be at least 10 $nm$ but not much more since the dilation of some percents for 6 smectic layers may not permit an increase of much more than 1 $nm$. This would lead to a core size of the order of 35 $nm$ for 180 $nm$ with $h_2$ of the order of 6 nm. This is considerably larger than the size between16 $nm$ and 16 - h2 for the thicker films, this last one being expected not to be larger than 6 $nm$.

### 5.1.4 Study of the central part of the hemicylinder

**Evolution of the tilt angle $\Delta\alpha$**

Up to now, we have understood the part in the edges of the hemicylinder that form the oily streaks for different film thicknesses. In this section, I will describe the results on the gable roof-like central part of the hemicylinder. I will in particular focus on how the $\Delta\alpha$ ( which is twice the tilt angle $\theta$ of the smectic layers in this roof-like central part ) evolves as a function of film thickness. For a short review of the previous result in chapter 4, section 4.9, where we have reported on the study of the central part of the hemicylinder for the $180\ nm$ thick film: The $\Delta\alpha$ was $2^\circ$ i.e tilt angle of the central smectic layers was $\theta = 1^\circ$. We have seen that this tilt angle implies that the central part of hemicylinder is formed by a gable-roof like structure below which there is a 3D topological grain boundary as shown in model schematized in figure 4.28 that we show again below.

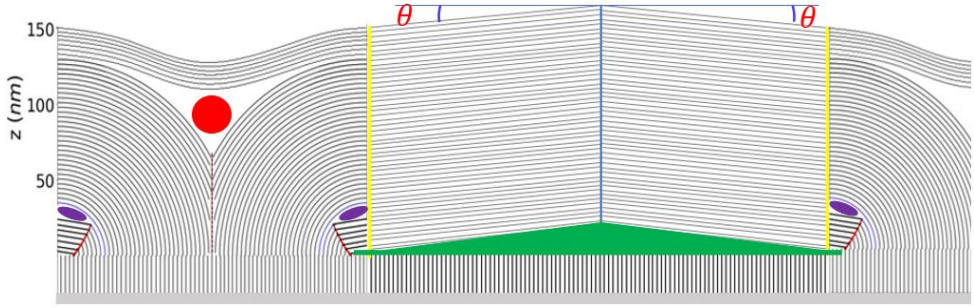


Figure 5.9: The new internal structure of the hemicylinder. The green solid triangle is a 2D topological grain boundary The red inclined line is rotating grain boundary without dislocation. At the top of the grain boundary, there is a dislocation defect of Burger vector $4$ shown in the purple close ellipse. The red point is the core of the disinclination defect.

Along the chevron-like curvature wall in this central part (shown in blue), there was no dislocation defect due to the small disorientation. Moreover, there is a grain boundary (shown in blue) that is separating the central tilted smectic layers and the rotating layers of the edges of the hemicylinder.

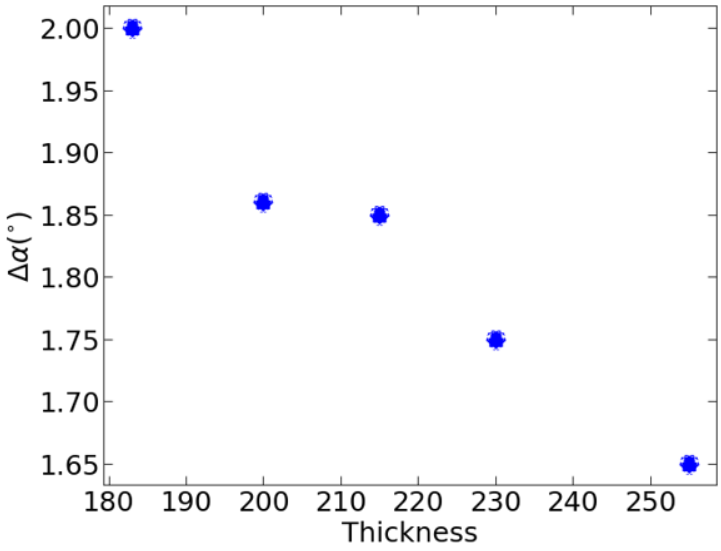


Figure 5.10: Evolution of the tilt angle for different film thicknesses

The model of the hemicylinder for the $180\ nm$ thick film and that of the thicker films present many similarities. Firstly, the quarters of cylinder below the disclination zone are the same. Secondly, they both have the gable-roof like structure in the central part since they all have a non-zero tilt angle. The evolution of this tilt angle as a function of film thickness is shown in figure 5.10. This figure shows that this angle decreases as film thickness increases. This mismatch in the interlayer distances is the origin of the chevron structure. However, the models present also some dissimilarities when the thickness varies. The upper part of the disclination zone changes for different film thickness. We have explained this in details in the previous section. In addition to this the tilt angle decreases as film thickness increases (figure 5.10). This decreasing implies that the central part of the hemicylinder varies as a function of the film thickness. Based on the fact that it is decreasing, one can anticipate that there is a thickness above which this tilt angle may completely vanish. In this case, the surface would be perfectly flat.

We have seen that this tilt angle doesn't vary from one layer to another. This tilt angle is imposed by the competition between three different energies, particularly surface energy, energy of the disorder of the topological grain boundary below the gable roof-like structure and compression/dilation energy together with curvature energy along the grain boundary that is separating the central layers from the rotating smectic ones. Whereas the rotating smectic layers are characterized by an homogeneous dilation along the layers, the dilation varies radially as shown by the model in equation 4.48, section 4.9.3 of chapter 4. In contrast, we expect the dilation to vary along the smectic layers for the convex layers of the disclination. As shown by the results of the previous section, we expect the dilation to be maximum in the center of the disclination and the interlayer spacing to be $d_o$ at the border. The result is that by unit of length along the grain boundary, the tilt angle induced by the difference of intra-layer spacing decreases when the size of the disclination increases, in other words when the thickness increases. The observed variation of the tilt angle shown on figure 5.10 is thus expected to be induced by the thickness increase of the disclination size.

## 5.2 Conclusion

In this chapter, we have reported the evolution of the structure of the oily streaks as a function of the film thickness. We have demonstrated that the disclination core size varies as film thickness changes. For $180\ nm$ it may be as high as around $35\ nm$ whereas it may decrease towards $10-16\ nm$ for the thicker films of thickness varying between 200 and $255\ nm$. This is indeed a significant contribution to the fundamental understanding of the structure of topological defects with a nanoscale resolution In addition to this, we have shown that the part below the disclination zone remains unchanged when the film thickness changes. In contrast to this part, the upper part of this zone, significantly changes when the film thickness changes. We have found that the thicker film have a larger number of the smectic layers to be added in this zone. This shows that it is energetically cheaper to add smectic layers in the disclination area than in the rotating area of the quarter cylinders. This may be partly due to the prohibitive energy cost of these rotating layers due to bending and dilation. Also the possible decreasing of surface energy when the thickness increases in the disclination zone may contribute to these observations.

We have also found that the more the film thickness increases, the more it becomes easier to obtain a flattened film surface. Furthermore, the gable-roof like structure was also found for all film thickness. The results of the analysis of this structure shows that it evolves as function of film thickness, where the thicker film may have a flat surface and the area below the roof is smaller compared to the $180\ nm$ thick film. This may be directly connected to the presence of always thicker disclination areas when the film thickness increases. Along the grain boundary the disclination area may favor no tilt of the smectic layers.

# Bibliography


[1] Delphine Coursault et al. “Self-organized arrays of dislocations in thin smectic liquid crystal films”. en. In: *Soft Matter* 12.3 (2016), pp. 678–688. ISSN: 1744-683X, 1744-6848. DOI: 10.1039/C5SM02241J. URL: http://xlink.rsc.org/?DOI=C5SM02241J (visited on 01/17/2023) (cit. on pp. 144, 147).

[2] Jean-Philippe Michel et al. “Optical gratings formed in thin smectic films frustrated on a single crystalline substrate”. en. In: *Physical Review E* 70.1 (July 2004), p. 011709. ISSN: 1539-3755, 1550-2376. DOI: 10.1103/PhysRevE.70.011709. URL: https://link.aps.org/doi/10.1103/PhysRevE.70.011709 (visited on 10/20/2021) (cit. on p. 148).

# Chapter 6

# General Summary and Perspectives

*"Beyond the impossibility line, there is an infinity possibilities, the key is in your hand if you believe it.." –*

– Jean de Dieu

One of the characteristic features of the 8CB smectic A liquid crystal is its layers structure. This allows the study of this material using X-ray diffraction. X-ray diffraction is a powerful tool. In particular, it may allow to study how topological defects appear when the thickness is small enough. Concerning X-ray diffraction of smectic 8CB distorted by antagonistic anchorings with thicknesses not larger than 1 $\mu m$, analysis using Bragg condition has been considered already in the past. Notwithstanding, interesting results that had already been obtained, they necessitate that the efforts may be continued since some questions are still pending concerning the model of the 1D pattern that had been built previously in our group [1, 2].

The patterns was known to be made of superimposed smectic layers in flattened hemicylinders but the main questions still pending were the following: What is the exact structure of the central part of the hemicylinders and in particular of the 2D grain boundary area ? where are exactly the expected dislocations close to the center of curvature ?. In the area between two neighboring hemicylinders, the bend distortion energy increases from top to bottom, this strongly suggests the appearance of topological defects along this curvature wall, however, this has not yet been studied. Are there other topological defects inside this oily streak configuration? For example what is the exact structure of the part at the top of the curvature wall between the two neighboring hemicylinders? We have seen that the film thickness affects the periodic pattern of stripes. The thickness increases can fully modify the pattern ultimately leading to a transformation into focal conics domains. It would be interesting to study the effect of the film thickness of the intimate structure on the oily streaks. My thesis aims at responding to all of these questions. The main goal was to reconstruct the intimate internal structure of the oily streaks.

To respond to this question, we have developed an unprecedented experimental and theoretical methodology that we have presented in chapter4 of this manuscript. We first performed a theoretical calculation of the integrated intensity scattered by 3D crystals and smectic liquid crystal system made up of perfectly flat layers. Similar to the 3D crystal we found that the integrated integrated intensity was proportional to the number of scattering layers. However, we have demonstrated that for the integrated intensity scattered by curved smectic liquid crystal layers, it is not proportional to the number of scattering smectic layers but instead it linearly depends on $N_2^2 - N_1^2$, where $N_2$ is the total number of rotating smectic layers. This result emanated from the fluid property of the smectic liquid crystal which keeps constant the linear density of the scatters in each smectic layer.

The signals scattered in Bragg condition contain information on the structure of the scattering material as shown by the preceding result. It is therefore crucial to ensure that this condition is satisfied during the X-ray scattering measurements. It is has been demonstrated that oily streaks intimate internal structure is made up of smectic layers rotating around the axis of the hemicylinders. To study this internal structure precisely, it is crucial to ascertain that Bragg condition is satisfied for all orientation $\alpha$ of the wave vector transfer $\vec{q}$. This $\vec{q}$ has to be parallel to the normal of the smectic layers inside the hemicylinder. For this reason, we have developed two different but complementary theoretical and experimental techniques that demonstrated the necessary orientation of the sample that allows to obtain Bragg conditions during the measurement of the scattering of the

rotating layers. In addition to this Bragg intensity ascertainment, in this chapter we have also determined new parameters that have not been used before in our group for the study of the intimate structure of the oily streaks. These are the $\Delta q$, the $\Delta\mu$, and the $q$ variations with $\alpha$, $\alpha$ being the orientation of the normal to the smectic layers, parallel to the orientation of the wave vector transfer. The former is sensitive to the presence of disorder in the inter layer spacing of the smectic layers, it has helped in the localization of the defects in our system. Moreover since it is also associated with the finite size effect which is the number of scattering smectic layers in our system, it therefore played a crucial role in the determination of the number of scattering smectic layers in the next chapters. The $\Delta\mu$ is associated with the mosaicity of the hemicylinder. Due to the rubbing process the smectic hemicylinders are not always perfect. Taking into account this parameter has therefore helped to take into account the effect of this mosaicity on the intensity scattered by our hemicylinders. We have calculated how to take into account the effect of refraction in the determination of $q$ and its variation with alpha. This allowed to obtain particularly resolved $q$ curves as a function of $\alpha$. Together with the curves of $\Delta q$ and of Integrated intensity ($I = I_{Bragg} * \Delta q * \Delta\mu$), the q curves were the basis for the deep study of the oily streak structure in the following chapters.It can also be considered that the new methodology of x-ray analysis developed in this chapter now constitutes a solid basis that may allow for a large number of future analyses of different new smectic systems (see below for the perspectives) with a particularly good resolution, in particular for smectic systems containing topological defects.

The results on the oily streak structure were presented in chapter $4$ and $5$ of this manuscript. Using the combination of experimental X-ray scattering and theoretical calculation of the intensity scattered by the rotating smectic layers inside the hemicylinder, we were able to reconstruct the intimate structure of the oily streaks.

The chapter 4 concerns the sample of thickness $180\ nm$. The first result is that we succeeded to demonstrate the existence of almost perfectly rotating smectic layers that indeed form a large slab of a perfect quarter cylinder inside each edge of the smectic flattened hemicylinders. Closer to the center of curvature a rotating grain boundary is formed as postulated in previous works [2]. However its dimensions are now precisely determined and appear different from the previous estimations [2, 3]. We find the localization of one single dislocation of Burger vector $4$ at the extremity of a rotating grain boundary without dislocation. As a result, the smectic layers the closest from the curvature center that fully rotate from an orientation perpendicular to the substrate to a parallel orientation may be the $11^{th}$ smectic layer if we count the smectic layers starting from the center of curvature.

The second result is the demonstration of a $-\frac{1}{2}$ disclination defect at the top of the curvature wall that joins two neighboring quarter cylinders. For the sample of thickness $180\ nm$, it is made of around $6$ layers that experience a large dilation in the disclination center. We were able to estimate a large core size of the order of $35\ nm$. If we consider the smectic layers that rotate around the central defect, they form a topological charge of $+\frac{1}{2}$. We therefore demonstrated for the first time in our group, a topologically stable system since the $-\frac{1}{2}$ disclination balances this $+\frac{1}{2}$ topological charge.

The third result is the fact that the central part of the oily streak flattened hemicylinder is formed by a gable-roof like structure with the two edge of the central part forming a chevron structure. We have performed in collaboration with Randall Kamien from Pennsylvania university, a calculation on the energy minimization of the rotating smectic layers. This calculation has given us a model of how the smectic layers in the edges of the oily streak hemicylinders are dilated with respect to the central layers as a response to the very high bending energy close to the center of curvature. We obtained a quantitative expression of this dilation in agreement with the experimental data, for example associated with local dilation as high as $4\%$ for the $5^{th}$ smectic layer which appears to be the first expected smectic layer at the basis of the rotating grain boundary. This suggests that such a dilation may occur close to most of the topological defects around which smectic layers rotate with a small radius of curvature like for example close to the ellipse of focal conics.

Therefore, this model allows to understand the origin of the gable roof-like structure associated with the chevron grain boundary. The tilt of the central layers is induced by the necessary connection between dilated rotating layers and central ones along a new grain boundary. However, whereas each rotating layers is expected to be differently dilated due to its different distance with respect to the center of curvature, we show that the tilt angle remains mostly constant along the grain boundary at a smaller value than the one expected for a perfect connection between rotating and central layers. This is because this tilt angle is the result of competing energies, in particular the surface energy that tends to flatten the gabble-roof like central part of the hemicylinders.

The fourth result is that the structure of the curvature wall between two neighboring quarter cylinders is possibly associated with a chain of dislocations of various Burger vectors. However a precise structure is yet to be produced and for this reason we have started collaboration with a group of simulators from Canada, UK and USA to simulate the model of two neighboring quarter cylinders. The idea is to also simulate the scattering of their simulated structure and to compare this theoretical scattering to our experimental results in order to confirm a presence of these dislocations.

The fifth result concerns the central topological grain boundary that separates the central smectic layers from the perpendicular layer on the substrate. We collaborate with the group of Samo Kralj and Luka Mesarec from Slovenia who have demonstrated that it is a total wall defect. It is not only characterized by melting of a smectic order but also by a locally negative nematic uniaxiality associated with an order reconstruction locally induced in the defect by the melting of the smectic order. As a result the thickness of the defects could be estimated to be around 20 $nm$.

The sixth result is the reconfirmation of the existence of the perpendicular layers in the oily streak on the substrate as it was demonstrated with ellipsometric study performed by Coursault et al. [2]. This comes from the comparison between the theoretical calculation of the scattered intensity from smectic A material with the experimental intensity extracted using TSAXS. The theoretical calculation was performed without considering the perpendicular layers and a minimum intensity was found on the orientation $\alpha = 0^{\circ}$. On the other side the result from the TSAXS shows a maximum intensity at this orientation. This result also suggests that a new calculation with the consideration of the presence of perpendicular layer is needed.

We have reported the evolution of the structure of the oily streaks as a function of the film thickness in chapter 5. We have demonstrated that the disclination core size varies as the film thickness changes. For 180 $nm$ it may be as high as around 35 $nm$ whereas it may decrease towards $10 - 16$ $nm$ for the thicker films of thickness varying between 200 and 255 $nm$. This is indeed a significant contribution to the fundamental understanding of the structure of topological defects with a nanoscale resolution. With a small model we have emphasized the combined role of surface energy and dilation energy to induce a critical thickness below which the disclination core size significantly increased. In addition to this, we have shown that the part below the disclination zone remains unchanged when the film thickness changes. In contrast to this part, the disclination zone on top of the curvature wall significantly changes when the film thickness changes. We have found that the thicker film have a larger number of the smectic layers to be added in this zone and that the average dilation in the disclination zone consequently decreased when the thickness was increased. This shows that it is energetically cheaper to add smectic layers in the disclination area than in the rotating area of the quarter cylinders. This may be partly due to the prohibitive energy cost of these rotating layers due to bending and dilation but the expected decreasing of surface energy when the thickness increases in the disclination zone may also contribute to these observations.

We have also found that the more the film thickness increases, the more it becomes easier to obtain a flattened film surface. The gable-roof like structure was found for all film thickness. However, the analysis of this structure shows that it evolves as function of film thickness, the chevron disorientation decreasing with the film thickness. As a consequence, we might expect that particularly thick films may even present a flat surface. This may be directly connected to the presence of always thicker disclination areas when the film thickness increases. Along the grain boundary the disclination area may favor no tilt of the smectic layers.

From a fundamental point of view, these results may contribute to a better understanding of smectic topological defects in smectic A liquid crystals. The coexistence of 1D defects such as dislocation, $-\frac{1}{2}$ disclination and the 2D defect such as the total wall defect together with two types of non topological grain boundaries all together constitute a topologically stable system. Our study of oily streaks appears possibly complete enough to try in the near future to calculate the corresponding oily streak energy, taking into account all the different distorted zones evidenced during my thesis. We would to try to interpret the observed curve of period evolution of the patterns as a function of thickness. The ultimate goal would be to understand how it is possible to stabilize such a dense array of defects and high smectic distortion. We obtained some insight on the defect core sizes. Our results have shown that the disclination zone increases and the chevron structure tends to disappear when the film thickness increases. However for a thickness as small as 180 $nm$, the disclination appears to be small, associated with around 6 layers only and with an enlarged defect core. This has been explained to be related with the necessity of keeping the surface almost flat with not too high dilation. This suggests that there might be a critical thickness beyond which not disclination or chevron structure could be found. For these small systems where the disclination may have disappeared it would be necessary to decrease as much as possible the surface energy.We might consequently expect the curvature wall to become elongated with more defects being induced and with no well-balanced topological charge.

It would be interesting in the future to carry out a study on the determination of this critical value Using the methodology developed in chapter 3. In addition to this, our preliminary data for the structure of the large stripes described in chapter 1 suggests a structure surprisingly different from the one of the oily streaks, even at the edge of the corresponding hemicylinders. The number of rotating layers for the same thickness seems to have largely decreased, deserving a deep analysis of the corresponding X-ray data to try to understand the corresponding structure[4]. We might have another thin smectic texture with large stripes associate with smaller anchoring energy able to present different kinds of topological defects, thus allowing for a study of the

role of the anchoring energy on the induced array of defects and smectic distortion. Finally,it would be interesting to study the evolution of the smectic structure in presence of nanoparticles to better understand the interaction between the defects and the nanoparticles. However, since the nanoparticle concentration is not homogeneous, this requires nano-diffraction to be performed at ESRF. On a specific area where we would identify the nanoparticle structure we would measure the smectic signal and its variations in presence of nanoparticles. Last March I participated to a first experiment at ID1 with encouraging results that now need to be confirmed by a new experiment. The good new is that we have developed already during my thesis the experimental and theoretical methodologies that are required for such studies.

# Bibliography


[1] Jean-Philippe Michel et al. “Optical gratings formed in thin smectic films frustrated on a single crystalline substrate”. en. In: *Physical Review E* 70.1 (July 2004), p. 011709. ISSN: 1539-3755, 1550-2376. DOI: 10.1103/PhysRevE.70.011709. URL: https://link.aps.org/doi/10.1103/PhysRevE.70.011709 (visited on 10/20/2021) (cit. on p. 155).

[2] Delphine Coursault et al. “Self-organized arrays of dislocations in thin smectic liquid crystal films”. en. In: *Soft Matter* 12.3 (2016), pp. 678–688. ISSN: 1744-683X, 1744-6848. DOI: 10.1039/C5SM02241J. URL: http://xlink.rsc.org/?DOI=C5SM02241J (visited on 01/17/2023) (cit. on pp. 155–157).

[3] Jean-Philippe Michel et al. “Structure of smectic defect cores: X-ray study of 8CB liquid crystal ultrathin films”. In: *Physical review letters* 96.2 (2006). Publisher: APS, p. 027803 (cit. on p. 156).

[4] Haifa Jeridi et al. “Unique orientation of 1D and 2D nanoparticle assemblies confined in smectic topological defects”. en. In: *Soft Matter* 18.25 (June 2022). Publisher: The Royal Society of Chemistry, pp. 4792–4802. ISSN: 1744-6848. DOI: 10.1039/D2SM00376G. URL: https://pubs.rsc.org/en/content/articlelanding/2022/sm/d2sm00376g (visited on 08/17/2022) (cit. on p. 157).

# APPENDIX A

# CALCULATION OF THE TOTAL DIFFRACTED AMPLITUDE FOR A SINGLE QUARTER OF HEMICYLINDER

## A.1 coefficient of proportionality for the theoretical Bragg intensity

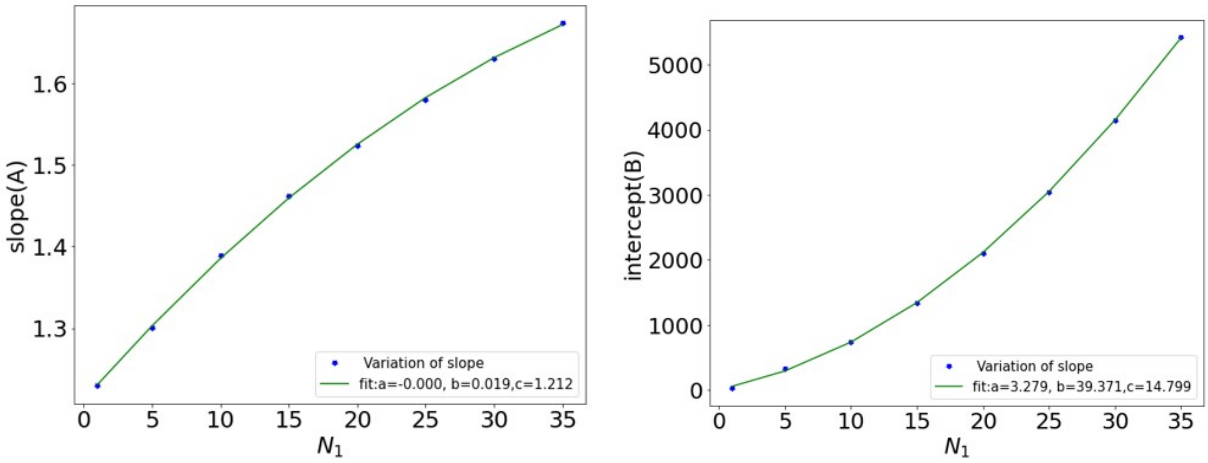


(a) (b)

Figure A.1: Evolution of the coefficient of the linear relationship between Integrated Bragg intensity and $N_2^2 - N_1^2$

## A.2 Determination of $N_1$

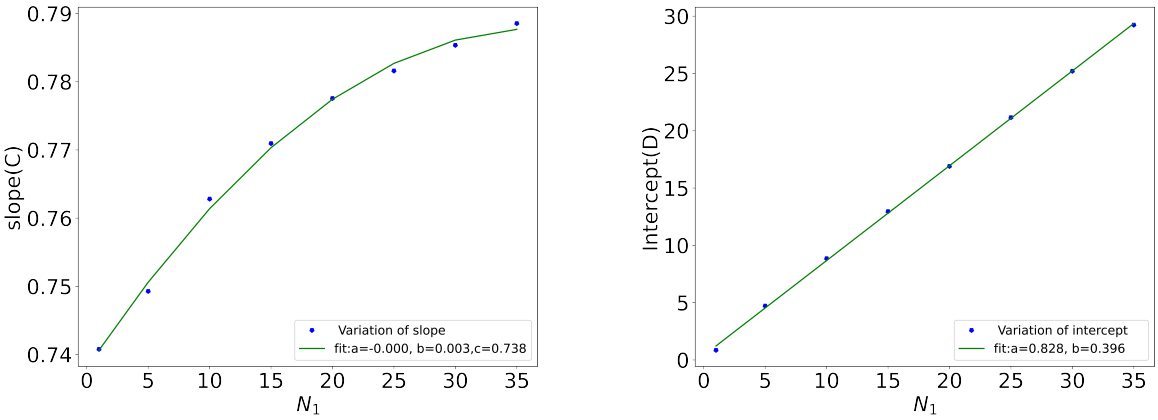


(a) (b)

Figure A.2: Evolution of the coefficient of the linear relationship between full width at half maximum and $N_2 - N_1$

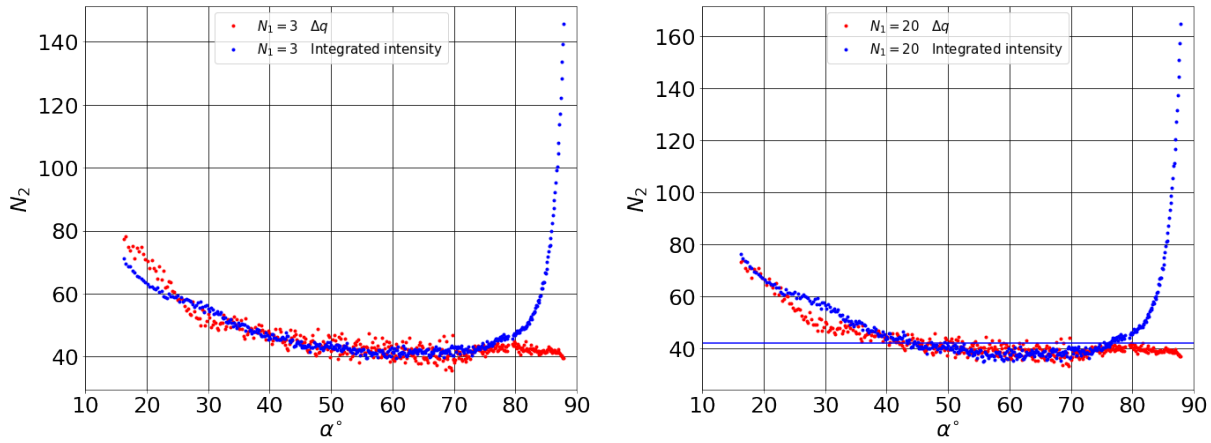


(a) (b)

Figure A.3: Evolution of the $N_2$ as a function of orientation $\alpha$ for constant $N_1$ values

Appendix A

# Newton tints of color : Evolution of colors observed in optical microscopy in parallel polarizers as a function of liquid crystal film thickness and the path difference $\delta$

| Différence de marche δ (nm) | P/A croisés | P/A parallèles | Epaisseur e (nm) |
|---|---|---|---|
| **Premier ordre** | | | |
| 0 | noir | blanc | 0 |
| 40 | gris de fer | blanc | 12,53525541 |
| 97 | gris lavande | blanc jaunâtre | 30,39799436 |
| 158 | bleu gris | blanc brunâtre | 49,51425885 |
| 218 | gris plus clair | brun jaune | 68,31714196 |
| 234 | blanc verdâtre | brun | 73,33124412 |
| 259 | blanc | rouge clair | 81,16577875 |
| 267 | blanc jaunâtre | rouge carmin | 83,67282983 |
| 275 | jaune paille pâle | brun rouge sombre teinte | 86,17988092 |
| 281 | jaune paille | violet sombre sensible | 88,06016923 |
| 306 | jaune clair | indigo | 95,89470385 |
| 332 | jaune vif | bleu | 104,0426199 |
| 430 | jaune brun | bleu gris | 134,7539956 |
| 505 | orangé rougeâtre | vert bleuâtre | 158,2575995 |
| 536 | rouge chaud | vert pâle | 167,9724224 |
| 551 | rouge plus foncé | vert jaunâtre | 172,6731432 |
| | | | |
| **Deuxième ordre** | **Teinte sensible** | | |
| 565 | pourpre | vert plus clair | 177,0604826 |
| 575 | violet | jaune verdâtre | 180,1942965 |
| 589 | indigo | jaune d'or | 184,5816359 |
| 664 | bleu de ciel | orangé | 208,0852397 |
| 728 | bleu verdâtre | orangé brunâtre | 228,1416484 |
| 747 | vert | rouge carmin clair | 234,0958947 |
| 826 | vert plus clair | pourpre teinte | 258,8530241 |
| 843 | vert jaunâtre | pourpre violacé sensible | 264,1805077 |
| 866 | jaune verdâtre | violet | 271,3882795 |
| 910 | jaune pur | indigo | 285,1770605 |
| 948 | orangé | bleu sombre | 297,0855531 |
| 998 | orangé rougeâtre vif | bleu verdâtre | 312,7546224 |
| 1101 | rouge violacé foncé | vert | 345,032905 |
| | | | |
| **Troisième ordre** | **Teinte sensible** | | |
| 1128 | violet bleuâtre clair | vert jaunâtre | 353,4942024 |
| 1151 | indigo | jaune sale | 360,7019743 |
| 1258 | bleu (teinte verdâtre) | couleur chair | 394,2337825 |
| 1334 | vert de mer | Rouge brun | 418,0507678 |
| 1376 | vert brillant | Violet teinte | 431,212786 |
| 1426 | jaune verdâtre | bleu violacé grisâtre sensible | 446,8818552 |



Figure A.1: Caption

# List of Figures